UNIVERSIDAD AUTÓNOMA DE QUERÉTARO

FACULTAD DE QUÍMICA

“Semiconductores Avanzados: Propuesta de Estructuras Metal-Orgánicas y Ftalocianinas como Capas Transportadoras de Huecos en Celdas Solares Perovskita Emergentes Libres de Plomo, y Estudio Experimental del Dopaje con Metales Alcalinotérreos en γ-In_2S_3 para Aplicaciones Fotocatalíticas”

TESIS

QUE COMO PARTE DE LOS REQUISITOS PARA OBTENER EL GRADO DE

DOCTORADO EN CIENCIAS DE LA ENERGÍA

PRESENTA

EVANGELINE LINDA

DIRIGIDA POR

Dra. LATHA MARASAMY

SANTIAGO DE QUERETARO, QUERETARO, NOVIEMBRE 2025

UNIVERSIDAD AUTÓNOMA DE QUERÉTARO
FACULTAD DE QUÍMICA

DOCTORADO EN CIENCIAS DE LA ENERGÍA

"Semiconductores Avanzados: Propuesta de Estructuras Metal-Orgánicas y Ftalocianinas como Capas Transportadoras de Huecos en Celdas Solares Perovskita Emergentes Libres de Plomo, y Estudio Experimental del Dopaje con Metales Alcalinotérreos en γ-In_2S_3 para Aplicaciones Fotocatalíticas"

TESIS

QUE COMO PARTE DE LOS REQUISITOS PARA OBTENER EL GRADO DE

PRESENTA

EVANGELINE LINDA

DIRIGIDA POR

Dra. LATHA MARASAMY

SINODALES

Dra. Latha Marasamy
Presidente

Dr. José Santos Cruz
Secretario

Dr. Francisco Javier de Moure Flores
Vocal

Dra. Aruna Devi Rasu Chettiar
Suplente

Dr. José Álvaro Chávez Carvayar
Suplente

Centro Universitario, Querétaro, Qro.
Noviembre, 2025, Mexico

Table of Contents

List of Figures

List of Tables

Resumen

Atender la creciente demanda de energía minimizando el impacto ambiental requiere desarrollo de tecnologías sostenibles y con bajas emisiones de carbono. La energía solar, ofrece una vía eficaz para la generación de electricidad, la degradación de contaminantes y la producción de hidrógeno mediante procesos fotovoltaicos y fotocatalíticos. Esta tesis presenta un estudio teórico y experimental sobre perovskitas de calcogenuro (CPs) emergentes y nanoestructuras de γ-In_2S_3 dopadas con metales alcalinotérreos, orientado al desarrollo de aplicaciones solares. En la parte teórica, se analizó el desempeño de las celdas solares $SrZrS_3$ y $BaZr_{0.96}Ti_{0.04}S_3$ empleando marcos metal-orgánicos conductores (c-MOFs) y ftalocianinas metálicas (MPcs) como capas transportadoras de huecos (HTLs) mediante simulaciones con SCAPS-1D. Los dispositivos optimizados con c-MOFs, Cu-MOF ({[Cu_2(6-mercaptonicotinate)].NH_4}$_n$), NTU-9, Fe_2(DSBDC), Sr-MOF ({[Sr(ntca)(H_2O)$_2$].H_2O}$_n$), Mn_2(DSBDC), y Cu_3(HHTP)$_2$, alcanzaron η superiores al 28%, atribuidas a una mayor separación de niveles quasi-Fermi, alta resistencia a la recombinación (1.4×10^7 Ω.cm^2), mayor potencial incorporado (~0.99V) y mejor respuesta en el infrarrojo cercano (35%). De forma similar, las HTLs de CuPc, NiPc y ZnPc en dispositivos $BaZr_{0.96}Ti_{0.04}S_3$ lograron PCE de hasta 30.12%, con un incremento del 7-9% en la eficiencia cuántica debido a barreras tipo "cliff" que favorecieron el transporte de huecos y redujeron la recombinación. La parte experimental, se sintetizaron nanoestructuras de γ-In_2S_3 puras y dopadas con Mg^{2+}, Ca^{2+} y Sr^{2+}. Los análisis de XRD, HRTEM, espectroscopía Raman, XPS y FESEM-EDS confirmaron la pureza de fase y la reducción del tamaño de cristal, la incorporación de los dopantes y una morfología tipo nanocinta, y observándose que el Ca promovió vacancias de S. Las mediciones UV-Vis, PL, M-S, EIS y efecto Hall mostraron evidenciaron la disminución del E_g (3.67 a 2.41 eV) y una mayor transferencia de carga. El material Ca:γ-In_2S_3 mostró la mejor actividad fotocatalítica, con una producción de 688 μmol·g^{-1} de H_2 y una degradación del 99.53% del herbicida 2,4-D en 240 minutos, manteniendo ~91% de eficiencia tras 10 ciclos. En conjunto, los resultados destacan el potencial de los c-MOFs y las MPcs como HTLs y el notable desempeño de las nanocintas dopadas de γ-In_2S_3, resaltando su versatilidad para mejorar la actividad fotocatalítica en semiconductores emergentes.

Palabras clave: SCAPS-1D, perovskitas de calcogenuros, estrechamiento del ancho de banda, nanocintas, dinámica de transferencia de carga

Abstract

Addressing the increasing global energy demand while minimizing environmental impact necessitates the development of sustainable, low-carbon technologies. Solar energy, owing to its abundance and versatility, offers an effective route for electricity, pollutant degradation, and H_2 fuel generation through photovoltaic and photocatalytic processes, respectively. This thesis presents a comprehensive theoretical and experimental investigation of emerging chalcogenide perovskites (CPs) and alkaline earth metal-doped γ-In_2S_3 nanostructures for next-generation solar energy applications, respectively. In the theoretical part, the performance of $SrZrS_3$ and $BaZr_{0.96}Ti_{0.04}S_3$ solar cells was systematically analyzed using conductive metal-organic frameworks (c-MOFs) and metal phthalocyanines (MPcs) as alternative hole transport layers (HTLs) through SCAPS-1D simulations. Optimized devices with c-MOFs: Cu-MOF ({[Cu_2(6-mercaptonicotinate)].NH_4}$_n$), NTU-9, Fe_2(DSBDC), Sr-MOF ({[Sr(ntca)(H_2O)$_2$].H_2O}$_n$), Mn_2(DSBDC), and Cu_3(HHTP)$_2$, achieved elevated power conversion efficiencies (PCEs) of up to >28%, attributed to enhanced quasi-Fermi level splitting, higher recombination resistance (1.4×10^7 Ω.cm^2), stronger built-in potential (~0.99 V), and a 35% improvement in near-infrared response. Similarly, CuPc, NiPc, and ZnPc HTLs in $BaZr_{0.96}Ti_{0.04}S_3$ devices yielded PCEs of 28.93%, 28.88%, and 30.12%, respectively, with 7-9% quantum efficiency enhancement due to favorable cliff-like barriers that promoted hole transport and reduced recombination. Subsequently, the experimental segment focused on synthesizing pure and Mg^{2+}, Ca^{2+}, and Sr^{2+} doped γ-In_2S_3 nanostructures. XRD, HRTEM, Raman spectroscopy, XPS, and FESEM-EDS confirmed phase purity, reduced crystallite size, successful dopant incorporation, and revealed uniform nanoribbon morphology, with Ca doping notably inducing S vacancies. UV-Vis, PL, M-S, EIS, and Hall-effect measurements demonstrated bandgap reduction from 3.67 eV to 2.41 eV and improved charge transfer upon doping. Among all samples, Ca:γ-In_2S_3 exhibited the best photocatalytic activity, producing 688 μmol·g^{-1} H_2 and achieving 99.53% 2,4-D degradation, within 240 minutes, while ~91% retention after 10 cycles. This thesis provides comprehensive theoretical insights into the potential of c-MOFs and MPcs as HTLs in emerging CP SCs, suggesting their applicability in other types of solar cells as well. Experimental outcomes highlight that Mg, Ca and Sr-doped γ-In_2S_3 nanoribbons demonstrate exceptional performance in photocatalytic 2,4-D degradation and H_2 generation, underscoring their versatility as dopants for enhancing photocatalytic efficiency in other semiconductors.

Keywords: SCAPS-1D, Chalcogenide Perovskites, Bandgap Narrowing, Nanoribbons, Charge Transfer Dynamics

Student Statement of Responsibility

I declare that the data obtained in this research were generated during the development of my thesis work in an ethical manner, and I report the necessary details so that the results of this thesis can be reproduced in future research. Finally, this thesis is an original work in which any collaboration or direct citation presented in the document has been properly declared and acknowledged.

Evangeline Linda

Dedication

"Every good and perfect gift is from above, coming down from the Father of the heavenly lights, who does not change like shifting shadows." - James 1:17

At the very outset, I bow in gratitude to God Almighty. Though there was a time I convinced myself that I did not believe, I have come to realize that His guiding hand has always been present, in moments of doubt, in seasons of struggle, and in every humble victory. Each article I published, every presentation I delivered, and every challenge I overcame was touched by His grace. With a heart full of gratitude, I thank Him for His constant presence, strength, and light throughout this journey.

This work is lovingly dedicated to my dearest family, my beloved parents, **Mr. J. Prabhu** and **Mrs. Catherine**. No words can truly capture the depth of my gratitude for all that you have sacrificed for me. Your patience, wisdom, and unwavering faith have been my pillars of strength. Thank you for standing by me through every hardship, for believing in me even when I doubted myself, and for teaching me resilience, humility, and perseverance. The values you instilled in me have shaped the person I am today and made me an independent individual, capable of facing life's challenges with courage and grace.

To my loving sister, **Ms. Eileen Mona**, my heartfelt thanks for being my constant source of inspiration and encouragement. Though younger than me, you have cared for me with the love and guidance of an elder sister. You have broken all odds to reach where you are today, and your journey has stirred immense determination and inspiration within me. Your faith in me has lifted me in moments when I felt uncertain, and your words have always reminded me that I am never alone on this path.

To my dearest grandmother, **Mrs. Maria Pushpam**, my precious *ammai*, your prayers and blessings have been my greatest treasures. The values you taught me, kindness, forgiveness, generosity, and steadfast faith, continue to guide every step I take. You have shown me what it truly means to live with grace and compassion.

To my little sunshine, **Saiparinavi**, your innocent determination and radiant smile brighten even my toughest days. Being just two years old, you amaze me with the confident ways you find to solve things on your own. Your fearless spirit reminds me to stay focused, determined, and to persevere until every task is done. You inspire me more deeply than you could ever imagine.

There is a beautiful proverb in my mother tongue, “நிறை குடம் தளும்பாது,” which means *“A person who possesses true knowledge and wisdom remains composed and humble.”* This perfectly describes my esteemed thesis supervisor, **Dr. Latha Marasamy**.

To **Dr. Latha Marasamy**, my mentor, guide, and constant source of light, words fall short in expressing the depth of my gratitude and admiration. You have been much more than an advisor; you have been a pillar of strength, a teacher of wisdom, and a compassionate presence who has shaped every part of my doctoral journey. From the very beginning, you have been guiding me through immigration procedures, the scholarship process, helping with housing arrangements, and supporting me through every challenge that comes with adapting to a new country. Your belief in me stirred the confidence I never knew I possessed. Through your patience, insight, and unwavering faith, you transformed my aspirations into meaningful achievements. I wholeheartedly say this, ma'am: you play a significant role in “I am who I am” right now.

Under your mentorship, I learned what it truly means to be a researcher, to question with purpose, to pursue truth with modesty, and to work with integrity and perseverance. Your tireless dedication, thoughtful guidance, and exceptional clarity of thought have left an enduring impact on both my academic and personal life. Even amidst your own busy schedule and health challenges, your care for my progress never weakened. I will always remember the countless hours you devoted to reviewing my work, patiently guiding me through project registration, article revisions, and results analyses, often sacrificing your own rest not just for me for all the fellow students, to ensure our growth. Your approachability, compassion, and willingness to guide me at any hour have been invaluable to me, ma’am. There are countless days when I anxiously sit, doubting myself, with a very glance you would understand my nervousness and always have stood by me with encouragement and wisdom, turning my uncertainty into motivation. Because of your unwavering belief in me, I was able to publish seven research articles and was honored with the Best Performing PhD Student Award. These milestones stand as evidence of your mentorship and unwavering support, which I would always carry with gratitude in my heart. Completing this thesis would not have been possible without your guidance, patience, and faith in me.

Being far from home, your kindness made every challenge bearable. You never allowed me to feel alone; your warmth and empathy filled every void and reminded me that I always had someone to rely on. Through moments of doubt and difficulty, you remained my guiding

compass, steering me with understanding and strength. Your mentorship has been a rare and precious gift. You have taught me that true excellence lies not only in achievement but also in character, compassion, and resilience.

This thesis is a direct reflection of your mentorship, insightful wisdom, and the faith that inspired me to persevere. My heartfelt thank you, **Dr. Latha Marasamy**, for being my mentor, my role model, and my greatest inspiration. I will forever carry your guidance, values, and the profound impact you have made on my life and career.

I am among those who think that science has great beauty. -Marie Curie, finally, I dedicate this thesis to all the women scientists who thrive against all odds, driven by passion, determination, and a relentless quest to understand science.

Acknowledgement

I would like to begin by expressing my heartfelt appreciation to the **National Council of Humanities, Science and Technology (CONAHCyT)** for their generous financial assistance and steadfast encouragement throughout the course of my doctoral studies.

My sincere gratitude also goes to the **Faculty of Chemistry, Autonomous University of Querétaro (UAQ)**, for providing an inspiring academic atmosphere, valuable resources, and unwavering guidance during my time here.

I owe my deepest respect and profound thanks to my research supervisor, **Dr. Latha Marasamy**, for her exceptional mentorship and guidance. Her insightful feedback, endless patience, and commitment to excellence have been a driving force behind this work. Her mentorship has not only influenced the direction of my research but has also greatly contributed to my development as an independent and thoughtful researcher.

I am sincerely grateful to the members of my doctoral committee, **Dr. Francisco de Moure Flores, Dr. José Santos Cruz, Dr. Aruna Devi Rasu Chettiar, and Dr. José Álvaro Chávez Carvayar**, for their constructive suggestions, thoughtful discussions, and continued support throughout my PhD journey.

To my dear best friends, **Ms. Bavya Krishnamoorthy, Mrs. Sumangi Muralitharan, Mrs. Sowmya Rajakannan, Mr. Roshan Roumanto A, Mrs. Aishwarya B.V, Mrs. Crescentia Yazhini S, Mrs. Neela M, Ms. Jayabharathi Thirumalazhagan, Ms. Priyanka Sathyamoorthy, and Ms. Antoni Snekha A**, whose enduring friendship and support have been a constant source of strength throughout this journey. Each of you has contributed in a distinct and meaningful way, offering encouragement, understanding, and inspiration whenever it was most needed. I am especially grateful for the moments when you reminded me of my purpose, particularly when I doubted my own abilities. Your unwavering belief in me has been invaluable, and I remain deeply thankful for your presence and support.

My heartfelt appreciation extends to my friends, **Valentina Sneha George** and **Roshini Ravi**, for their unwavering kindness, motivation, and care. I also wish to thank my colleagues, **Dhineshkumar Srinivasan, Kaviya Tracey, Eupsy Navis, Sathyapriya Nambirajan, and Vairamuthu Raj**, for their collaboration and constant encouragement throughout this journey.

I would also like to thank **C. Nathaly González Miranda, Lic. Arlette Torres López and Erika Vargas Mosqueira** for their dedicated assistance with administrative and academic procedures.

Special thanks to **Dr. José Álvaro Chávez Carvayar, Dr. Sergio Armando Tomas, Dr. Ángeles Mantilla, and Dr. Enrique Samaniego** for their invaluable help and support in the material characterization, which was instrumental in the completion of this thesis.

Lastly, I would like to extend my sincere appreciation to **Prof. Marc Burgelman** from **ELSI, University of Gent, Belgium**, for kindly providing access to the SCAPS-1D simulation software.

Publications in JCR-indexed Journals

1. **Linda, E**., Rasu Chettiar, Manisekaran, R., J. Á., Tomás, and Marasamy, L. (2025). Uncovering the Potential of γ-In_2S_3: Can Doping with Mg, Ca, and Sr Revolutionize Photocatalytic H_2 Evolution and 2,4-D Herbicide Degradation? *International Journal of Hydrogen Energy*. https://doi.org/10.1016/j.ijhydene.2025.151882
2. **Linda, E**., Chettiar, A.D.R. and Marasamy, L· (2024). Emerging class of $SrZrS_3$ chalcogenide perovskite solar cells: Conductive MOFs as HTLs- A game changer?. *Solar Energy Materials and Solar Cells*, *278*, 113204. DOI: http://dx.doi.org/10.1016/j.solmat.2024.113204
3. **Linda, E**., Chettiar, A.D.R. and Marasamy, L. (2024). Theoretical insights into high-efficiency $BaZr_{0.96}Ti_{0.04}S_3$ chalcogenide perovskite solar cells using phthalocyanine HTLs. *Materials Letters*, *375*, 137203. DOI: https://doi.org/10.1016/j.jphotochem.2024.115831
4. **Linda, E**., Rasu Chettiar, A.D., George, V.S., Manisekaran, R., Srinivasan, D., Martínez, A.B., Hossain, M.K., Rahman, M.F., Chávez-Carvayar, J. Á., Tomás, S.A., Mantilla, A., and Marasamy, L. (2024). Exploring the physical properties of pristine γ-In_2S_3 and its influence on Ba doping for photocatalytic degradation of 2,4-D herbicide. *Journal of Photochemistry & Photobiology, A: Chemistry* 456 115831. DOI: https://doi.org/10.1016/j.matlet.2024.137203
5. Marasamy, L., Chettiar, A.D.R., Manisekaran, R., **Linda, E**., Rahman, M.F., Hossain, M.K., García, C.E.P., Santos-Cruz, J., Subramaniam, V. and de Moure Flores, F. (2024). Impact of selenization with NaCl treatment on the physical properties and solar cell performance of crack-free Cu(In, Ga)Se_2 microcrystal absorbers. *RSC advances*, *14*(7), 4436-4447. DOI: https://doi.org/10.1039/D3RA05829H
6. Arockiadoss, K. T., Chettiar, A. D. R., **Linda, E**., & Marasamy, L. (2025). Boost efficiency with buffer and bottom stack optimization in $Cu_2BaSn(S, Se)_4$ solar cells by simulation. *Journal of Alloys and Compounds*, *1010*, 177707. DOI: https://doi.org/10.1016/j.jallcom.2024.177707
7. Arockiadoss, K. T., Rasu Chettiar, A. D., **Linda, E**., & Marasamy, L. (2025). A CdS-Free Alternative TiS_2 Buffer: Toward High-Performing Cu_2MSnS_4 (M= Co, Mn, Fe, Mg) Solar Cells. *Advanced Theory and Simulations*, 2400769. DOI: https://doi.org/10.1002/adts.202400769

1. Introduction

The increasing global energy demand, combined with the ongoing environmental crisis, presents a significant challenge to modern civilization. Currently, more than 80% of the world's energy consumption is derived from non-renewable sources, primarily fossil fuels, which account for approximately 34% from oil, 28% from coal, and 23% from natural gas. These energy sources are vital for driving industrial production, powering transportation, and advancing technology [1,2]. However, the reliance on fossil fuels, formed over millions of years, has led to their rapid depletion, while their combustion emits hazardous gases like CO_2, NO_x, and SO_x, contributing to the greenhouse effect and global warming [3,4].

To achieve long-term sustainability, it is essential to transition towards renewable energy sources. Options such as solar energy, wind energy, hydropower, and geothermal energy offer promising pathways to reduce environmental pollution, mitigate socio-economic impacts, and decrease global dependence on fossil fuels [5]. Among these, solar energy stands out as one of the most viable alternatives, owing to its abundance, accessibility, and environmental benefits [6]. Currently, humanity harnesses only about 0.014% of the total solar energy that reaches Earth annually, approximately 539 exajoules, underscoring the urgent need for innovative and efficient technologies to enhance solar energy utilization [7]. In recent years, applications of direct solar energy, including solar heating, photovoltaic (PV) systems, photocatalysis, and solar thermal power generation, have gained significant attention, reflecting a growing commitment to sustainable development [8,9].

Among the various solar technologies available, PV and photocatalysis stand out as two of the most efficient methods for converting solar energy into usable forms [10]. The origins of PV technology trace back to 1839, when Alexandre-Edmond Becquerel discovered the photoelectric effect, which enabled sunlight to be directly converted into electricity [11]. This foundational discovery paved the way for further advancements, including the creation of the first solar cell (SC) by Charles Fritts in 1883, which utilized a gold-coated selenium layer. Although its efficiency was below 1%, this innovation marked a significant step forward. Subsequent advancements in PV technology included Russell Ohl's work in 1940 and a pivotal development in 1954 by a team of scientists at Bell Laboratories, C. Fuller, G. Pearson, and D. Chapin, who developed silicon-based SCs [12,13]. Initial efficiencies of around 1% have since improved dramatically, reaching up to 26% in modern silicon SCs [14]. The extensive research in solar technologies has led to the classification of their development into distinct generations, as discussed in Section 1.1.1.1. Today, PV technologies have become a major contributor to

global renewable energy production, frequently outperforming wind power in total generation growth. By 2023, global installations of PV systems reached approximately 1.6 terawatts, with China (307 GW) and the United States (265 GW) leading the charge. Emerging countries like Mexico are also experiencing phenomenal growth, increasing from 0.4 GW in 2015 to 828 MW in 2024, largely driven by major projects such as the Villanueva Solar Park [15]. Overall, PV technology continues to play a vital role in advancing global clean energy and sustainability efforts.

On the other hand, photocatalysis, which is modeled after natural photosynthesis, utilizes light energy to drive chemical reactions, such as the breakdown of organic pollutants or the conversion of solar energy into chemical fuels [7,16]. Groundbreaking research by Fujishima and Honda in the late 1960s led to the discovery of the Honda-Fujishima effect, which significantly advanced the field of photocatalysis [17,18]. In this process, a photocatalyst absorbs light with energy equal to or greater than its bandgap, exciting electrons to transition to the conduction band (CB) and leaving holes in the valence band (VB) [19]. These photo-induced charge carriers facilitate chemical reactions critical to the production of solar fuels like green hydrogen (H_2) and the degradation of environmental pollutants. H_2 serves as a clean and efficient energy carrier, boasting high energy density, long-term storage capabilities, and zero carbon emissions [3,20]. Storage technologies for H_2 can be classified as gaseous, liquid, or solid [21]. In contrast, persistent pollutants, such as 2,4-dichlorophenoxyacetic acid (2,4-D), a common herbicide, pose serious ecological and health risks due to their stability, toxicity, and potential to form harmful by-products like 2,4-dichlorophenol (2,4-DCP) [22,23]. Photocatalytic degradation offers a sustainable method for mineralizing 2,4-D into harmless compounds such as CO_2 and H_2O, thereby mitigating its negative environmental impact [24].

The integration of PV and photocatalytic technologies represents a sustainable way to meet energy demands while addressing environmental challenges through the efficient use of solar energy. This thesis focuses on utilizing solar energy in two distinct applications: SCs and photocatalysis. Specifically, it aims to generate H_2 fuels and degrade 2,4-D through photocatalysis. Hence, our work demonstrates a commitment to advancing clean energy solutions and promoting environmental sustainability.

1.1. Renewable Solar Energy

1.1.1 Photovoltaics

1.1.1.1. Problem statement

The field of PV technology has evolved significantly since its beginning in 1839, when French physicist Alexandre-Edmond Becquerel first demonstrated that light could generate an electric current in specific materials known as semiconductors [25]. This foundational discovery initiated extensive research aimed at optimizing the conversion of solar energy into usable electricity, leading to the development of PV technologies. Despite substantial progress in enhancing the efficiency and scalability of SCs, categorized into various generations based on improvements in materials and designs (Fig. 1a), there are still critical challenges that need to be addressed. These include the reduction of production costs, enhancement of energy conversion efficiencies, and addressing the sustainability of materials used in SCs [26]. Recent efficiency charts from the National Renewable Energy Laboratory (NREL), as shown in Fig. 1b, illustrate the trajectory of power conversion efficiencies (PCE) from 1976 to the present, showcasing both the achievements within the field. As the world increasingly shifts towards renewable energy sources, understanding the complexities and future directions of PV technology becomes paramount. This knowledge is essential for both experts pushing the boundaries of solar technology and non-experts who are seeking to understand its implications for a sustainable energy future. Thus, this thesis aims to bridge the gap in knowledge regarding the technological advancements in PV systems and the associated challenges, fostering a broader understanding of their role in mitigating climate change and promoting renewable energy adoption.

First-generation SCs, known for their wafer-based technology, typically measure about 180 to 200 μm in thickness. These cells form the backbone of modern PV technology. They are primarily made from crystalline silicon, which comes in two main forms: monocrystalline and polycrystalline [14]. Due to their well-established efficiency, durability, and reliability, first-generation SCs dominate the market, accounting for over 80% of global installation capacity and about 90% market share [27]. However, the manufacturing process for these cells comes with substantial material costs. This arises from the fact that crystalline silicon has an indirect bandgap, which requires a thicker material, high purity, and a significant amount of silicon during production. Additionally, these cells are sensitive to temperature changes, have a relatively low absorption coefficient, and lack flexibility [14,28]. These limitations have

spurred the development of next-generation SCs aimed at reducing costs and enhancing efficiency while ensuring environmental sustainability.

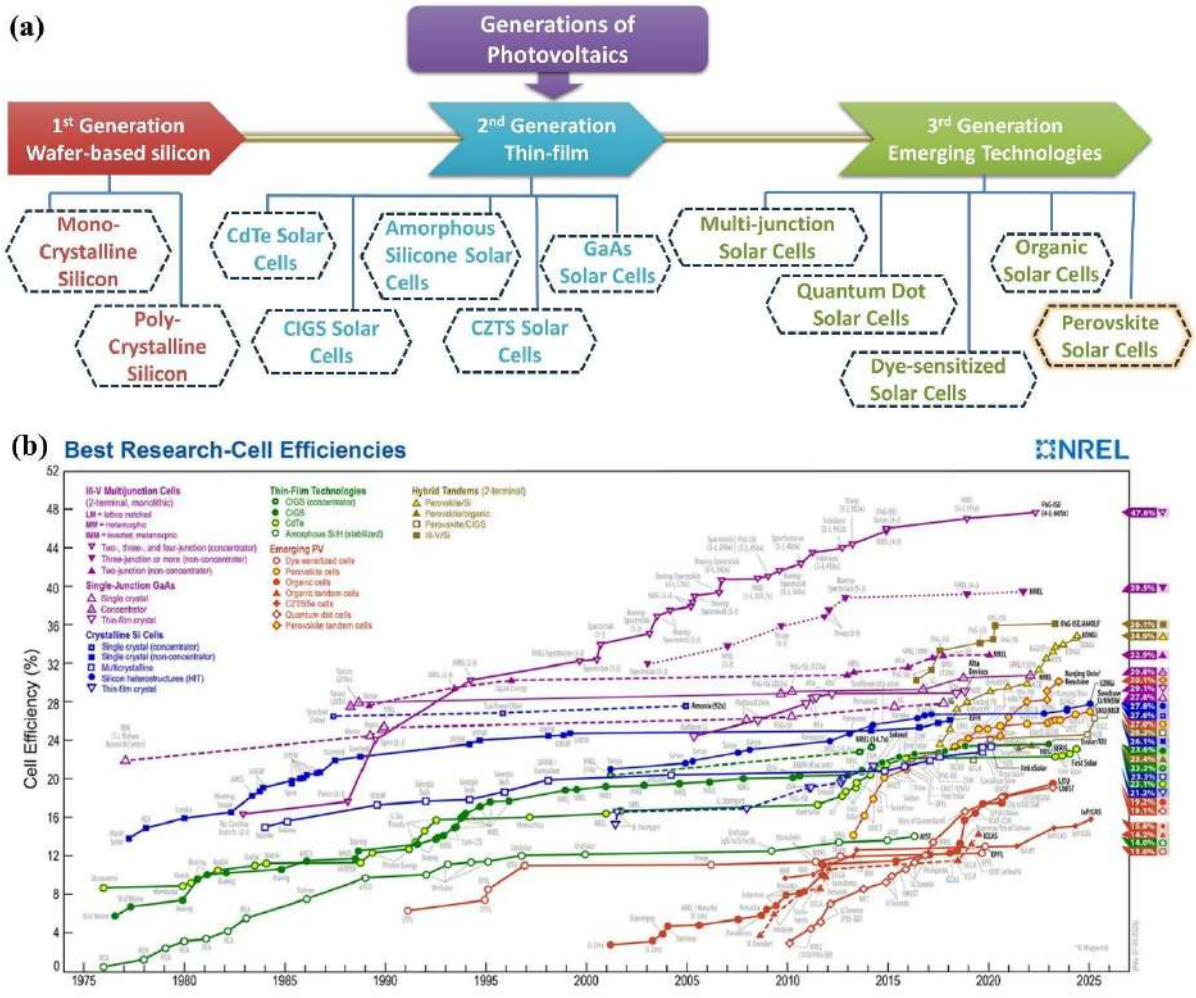

Fig. 1. (a) PV technologies categorized based on generations of SCs and (b) National Renewable Energy Laboratory (NREL) chart of the highest PCE till date.

The second generation of SCs, known as thin-film technologies, includes several light-absorbing materials such as cadmium telluride (CdTe), gallium arsenide (GaAs), copper indium gallium selenide (CIGS), amorphous silicon (a-Si), and copper zinc tin sulfide (CZTS) [14,28]. These SCs were developed to overcome the high costs and rigidity associated with traditional silicon-based SCs. Thin-film SCs are typically only around 1 µm thick, achieved by depositing multiple layers onto substrates like glass, metal, or plastic. This makes them lightweight and flexible [29]. Among these technologies, CdTe SCs are notable for their high spectral response, allowing for a thinner absorber layer of about 1 µm without significant efficiency losses. CdTe cells can achieve efficiencies exceeding 22%, making them both technically effective and economically viable [30]. However, concerns regarding the extreme

toxicity of Cd and the limited availability of Te remain critical issues [31]. In contrast, CIGS cells are recognized for their high absorption coefficients, enhanced stability, and beneficial intrinsic defects that lead to longer minority carrier lifetimes, enabling efficiencies of up to 23.6% on rigid substrates [32]. Despite these advantages, the high production costs of CIGS cells hinder widespread commercialization. a-Si cells are an abundant and inexpensive option that poses no toxicity risks and has a high absorption coefficient. However, their efficiency is relatively low due to a poor minority carrier lifetime, which limits their performance [33]. GaAs thin-film SCs have a direct bandgap of 1.43 eV and are less sensitive to temperature changes. They have achieved the highest PCE in the world, reaching up to 29.1% in single-junction systems [34]. Still, their extremely high fabrication costs remain a significant challenge. In summary, while thin-film technologies offer benefits such as direct bandgaps, high absorption coefficients, tunable bandgaps ranging from 1 to 1.7 eV, good photostability, flexibility, and scalability, their commercialization continues to face limitations. Issues such as the presence of toxic elements, reliance on rare earth metals, high material costs, and shorter lifespans compared to first-generation SCs drive ongoing research aimed at reducing costs and improving environmental safety.

The third generation of SCs marks a significant advancement in PV technology. Unlike the first and second generations, which had certain limitations, these new SCs employ innovative materials and designs to improve efficiency and performance. Key types of third-generation SCs include multi-junction cells, quantum dot solar cells (QDSCs), organic solar cells (OSCs), dye-sensitized solar cells (DSSCs), and perovskite solar cells (PSCs). These SCs aim to surpass the Shockley-Queisser limit, which sets a theoretical maximum efficiency for conventional SCs [35]. By enhancing light absorption, improving the movement of charge carriers, and maximizing the use of different light wavelengths, they strive to achieve better performance [36]. Among these options, organic and QDSCs stand out for their flexibility and lower manufacturing costs, whereas multi-junction cells excel in efficiency but come with higher production expenses [37]. PSCs are particularly promising due to their remarkable combination of high efficiency and cost-effectiveness, placing them at the forefront of solar energy research [38]. The advancements in PSCs began with groundbreaking work by Kojima et al., who achieved a PCE of 3.8% using $MAPbBr_3$ [39]. More recent developments have pushed the efficiency of single-junction PSCs to 26.7% using $FAPbI_3$, narrowing the gap with traditional silicon SCs to just 1% [40]. This progress opens doors for industrial applications. However, the commercialization of Pb-halide perovskites faces hurdles due to concerns over the toxicity

of Pb and environmental impact. Researchers have implemented various strategies to improve the stability of Pb-based PSCs, such as compositional engineering and surface passivation, but challenges related to environmental degradation persist [41]. In response to the toxicity concerns, the research community is focusing on Pb-free alternatives, particularly Sn-based perovskites. These materials demonstrate promising characteristics because their ionic radii and electronic configurations are similar to those of Pb. Initial studies on compounds like $CsSnI_3$ and $FASnI_3$ have resulted in significant efficiency gains, increasing from about 1% to over 15% through structural optimization [42]. Yet, these Sn-based perovskites also face stability challenges due to the tendency of Sn^{2+} ions to oxidize into Sn^{4+} in the presence of oxygen and moisture, creating defects that negatively affect performance [43]. Additionally, while Ge-based perovskites like $CsGeI_3$ and $MAGeI_3$ have been investigated, their high susceptibility to oxidation and cost issues limit their practical use [44]. On the other hand, mixed Sn-Ge compositions, such as $CsSnGeI_3$, show enhanced thermal and chemical stability but generally offer moderate efficiencies around 7-8% [45]. New materials involving Bi and Sb are emerging as promising Pb-free alternatives due to their chemical stability and comparable valence electron configurations. Bi-based compounds such as $Cs_3Bi_2I_9$ and $AgBi_2I_7$ demonstrate good environmental durability, though their efficiencies (1-5%) are limited by wide band gaps and lower-dimensional crystal structures [46]. Similarly, Sb-based perovskites like $Cs_3Sb_2I_9$ and $FA_3Sb_2I_9$ show potential for higher theoretical efficiencies exceeding 20%, but observed efficiencies remain below 1% [47]. Recent breakthroughs in double perovskites, where monovalent and trivalent cations (like Ag^+/Bi^{3+} or Na^+/In^{3+}) replace Pb ions, provide a pathway to achieving better thermal stability and ideal band gaps, while minimizing toxicity [48,49]. Despite these advances, Pb-free perovskites still trail behind Pb-based PSCs in terms of performance due to inherent structural limitations. Therefore, extensive research is essential to discover and develop new materials that can match the efficiencies of Pb-based PSCs while addressing critical stability and toxicity concerns.

In recent years, chalcogenide perovskites (CPs) have emerged as a promising alternative to traditional PSCs. These materials have the general formula ABX_3, where A typically represents alkaline earth metals such as Ba, Sr, or Ca; B refers to transition metals like Ti, Zr, or Hf; and X indicates chalcogen elements such as S or Se [50,51]. The unique combination of these elements leads to several key physical properties that make CPs particularly appealing for efficient solar energy conversion. One of the standout features of CPs is their high dielectric polarizability [52]. This property enhances their ability to store and manipulate electric charge,

which is crucial for high-efficiency PV devices. Additionally, CPs demonstrate remarkable thermal and chemical stability, ensuring that they can withstand various environmental conditions without degrading [53,54]. Importantly, the elemental components of CPs are non-toxic and abundant, addressing environmental concerns associated with some other SC materials discussed earlier. Theoretical studies and initial experimental findings indicate that chemical alloying within CPs can enable tunable direct bandgaps. This tunability is pivotal for optimizing the absorption of solar energy across a broad spectrum, making these materials highly suitable for a range of optoelectronic and energy-conversion technologies. Despite their promising features, CPs are still in the early phases of research. The journey from theoretical concepts to practical applications involves extensive experimental investigation and device fabrication, both of which can be resource-intensive and time-consuming. Furthermore, the reliance on sophisticated characterization tools can create barriers to accelerating research progress. To bridge these gaps, theoretical insights derived from simulation are invaluable. By utilizing tools like SCAPS-1D, researchers can model and predict the performance of emerging CP-based SCs, thus facilitating the exploration of innovative CP materials [55]. This approach aids in assessing their potential for achieving highly efficient SCs. Our thesis aims to contribute to this evolving field by leveraging numerical simulations to analyze the performance of CP materials, ultimately guiding future experimental efforts and paving the way for the development of advanced, sustainable solar energy technologies. Through this work, we hope to advance the understanding of emerging CP SCs and their performance.

1.1.1.2. Justification

The material properties of $BaZrS_3$ and $SrZrS_3$ CPs have been studied comprehensively through both experimental and theoretical approaches, revealing their potential for various applications, particularly in solar energy conversion. $BaZrS_3$ is noted for its direct bandgap of 1.72 eV, strong visible light absorption, and high chemical stability, which positions it as a prominent candidate in this field [53,56]. Importantly, the bandgap of $BaZrS_3$ can be fine-tuned through cation alloying. For instance, substituting 4% of Zr with Ti yields $BaZr_{0.96}Ti_{0.04}S_3$, resulting in a reduced bandgap of 1.51 eV that aligns well with the Shockley-Queisser limit for solar energy efficiency [57]. In parallel, $SrZrS_3$, a close analog of $BaZrS_3$, exhibits significant structural and optical versatility. Its α- and β-phases provide tunable bandgaps around 1.5 eV and 2.1 eV, respectively [58,59]. However, challenges have arisen in the synthesis of these CPs, as traditional methods often require high temperatures (900-1100 °C), which complicate solar cell fabrication due to the thermal limitations of conventional substrates and electron transport

layers [56,60]. Recent advances, such as the solution processing technique developed in 2023, have demonstrated that $BaZrS_3$ can be synthesized at much lower temperatures (500-575 °C), making it more compatible with traditional solar cell technologies like CIGS and CdTe [61].

Despite the promising characteristics of $BaZrS_3$, there has only been one report documenting the fabrication of $BaZrS_3$-based SCs, which achieved a PCE of 0.17% [62]. Theoretical predictions and device configurations for $BaZrS_3$ and $BaZr_{0.96}Ti_{0.04}S_3$ have primarily relied on conventional HTLs such as Spiro-OMeTAD, P3HT, and PTAA [63]. While these materials can improve device efficiencies, they also face challenges related to cost and stability. In contrast, various MPcs have emerged as promising alternative HTLs due to their cost-effectiveness and superior properties [64,65]. However, the applicability of MPcs has mostly been explored in the context of Pb-halide PSCs and DSSCs. To date, there have been no reports on the use of these MPcs in CP SCs, highlighting a significant opportunity for future research in this area.

Conversely, the potential of $SrZrS_3$ for PV uses is still untested experimentally. The only theoretical investigations of $SrZrS_3$ have focused on the effects of various HTLs (NiO_x, Cu_2O, and CuSCN), indicating performance improvements but also highlighting practical challenges due to high annealing temperatures or limited solubility [66]. Thus, there is a pressing need to discover new HTL materials that offer excellent hole mobility and require low-temperature processing while demonstrating enhanced stability. On this note, recent advancements highlight the promising potential of metal-organic frameworks (MOFs) in various layers of Pb-halide PSCs, including the ETL, HTL, and interfacial layers. Their unique structural and chemical properties have led to notable improvements in both device efficiency and stability [67]. In particular, when employed as HTLs, MOFs contribute to the performance enhancement via properties, such as hydrophobicity and enhanced hole conductivity [68]. Subsequently, facilitating efficient charge transport, suppressing charge recombination, improving photoresponse and light scattering, and regulating crystallization processes, ultimately resulting in larger perovskite grain sizes[69,70]. Despite these promising features, the integration of MOFs in CP SCs remains unexplored, offering a compelling direction for future research. Addressing this gap, our research investigates various c-MOFs as HTLs for $SrZrS_3$-based CP SCs. The c-MOFs being examined include Cu-MOF({[Cu_2(6-mercaptonicotinate)] $\cdot NH_4$}n), NTU-9, Fe_2(DSBDC) where ($DSBDC^{4-}$ = 2,5-disulfidobenzene-1,4-dicarboxylate), Sr-MOF ({[Sr(ntca)(H_2O)$_2$]·H_2O}n), Mn_2(DSBDC), and Cu_3(HHTP)$_2$ (HHTP=2,3,6,7,10,11-hexahydroxytriphenylene) [71–77]. This pioneering investigation aims to unlock the potential of c-MOFs to enhance the performance and versatility of $SrZrS_3$ in PV applications.

Theoretical simulations are crucial in the design of SCs, as they allow for the efficient assessment of device structures and the prediction of performance before actual fabrication. These simulations help significantly cut down on experimental costs and reduce the time required before fabrication. Among the various tools available, such as SETFOS, SILVACO-ATLAS, COMSOL, Wx-AMPS, and SCAPS-1D [78,79]. This study utilizes SCAPS-1D (version 3.3.10), which was created by Prof. Marc Burgelman at Ghent University. SCAPS-1D is selected due to its precision, intuitive interface, and capacity to conduct thorough electro-optical analyses of multilayer SCs [80]. The software facilitates the alteration of material parameters, including bandgap, carrier concentration, defect density, electron affinity, and mobility, while accommodating simulation under different illumination scenarios, for instance, AM0, AM1.5G, and even monochromatic positioning it as an excellent tool for the analysis of PV devices [80,81]. By solving fundamental equations, specifically Poisson's equation, carrier continuity, and drift-diffusion equations, SCAPS-1D effectively simulates charge transport and recombination, thereby establishing itself as a powerful and flexible tool for optimizing PV devices [31]. Moreover, this software has been extensively tested on a wide range of semiconductors, consistently showing high reliability, accurate results, and strong agreement with experimental reports [82].

In our study, using SCAPS-1D, we evaluated solar cell performance incorporating MPc (M=Cu, Ni, and Zn) based HTLs in $BaZr_{0.96}Ti_{0.04}S_3$ and various c-MOFs-based HTLs $SrZrS_3$ CP SCs, for the first time. We systematically analyzed the effects of absorber and HTL parameters, such as electron affinity, thickness, carrier concentration, and defect density, along with interfacial defects, parasitic resistance, and operating temperature. Simulations included J-V characteristics, C-V and C-F analyses, Mott-Schottky plots, generation-recombination profile, energy band alignment, and QE. Furthermore, we examined how external factors such as series resistance, shunt resistance, and operating temperature on the overall PCE. Ultimately, our findings shed light on the potential of diverse MPc (M = Cu, Ni, and Zn)-based HTLs in $BaZr_{0.96}Ti_{0.04}S_3$ and c-MOF-based HTLs in $SrZrS_3$ CP SCs demonstrate strong potential for developing non-toxic, cost-effective, and efficient thin-film SCs.

1.1.2. Photocatalysis

1.1.2.1. Problem Statement

Hydrogen (H_2) has emerged as one of the most promising energy carriers for a carbon-neutral future due to its high gravimetric energy density (about 140 MJ kg^{-1}), abundance, and

environmentally friendly nature, its only combustion product is water [21]. As a clean, flexible, and efficient energy carrier, H_2 offers immense potential for transforming various industrial sectors such as power generation, manufacturing, and transportation. A key advantage of H_2 lies in its environmental benignity; when utilized in fuel cells or combustion processes, it produces only water as a byproduct, making it a vital component in achieving global decarbonization goals. However, large-scale deployment of H_2 energy requires the development of efficient and cost-effective production and storage technologies [20]. Among the existing H_2 generation pathways, photocatalytic water splitting has attracted particular attention for its sustainability and environmental compatibility. This approach relies on semiconductor photocatalysts that harness solar radiation to split water molecules into H_2 and O_2. The method is inherently green and renewable since it utilizes sunlight, a freely available and inexhaustible energy source, to drive the reaction [83,84]. In addition, semiconductor-based photocatalysts can be engineered to enhance light absorption, charge carrier separation, and surface reactivity, thus improving the overall H_2 generation rate [4]. An overview of H_2 production methods: Focus on hydrocarbon feedstock. Beyond producing clean fuel, this technique enables decentralized H_2 generation, supports energy independence, and offers an effective strategy for storing surplus renewable energy, complementing intermittent sources such as wind and solar power. Consequently, semiconductor-driven photocatalytic H_2 production stands out as one of the most promising routes for transitioning toward a sustainable, low-carbon energy future [83].

Alongside the growing energy crisis, environmental pollution by synthetic herbicides has become a pressing global concern [85]. Herbicides have long been considered indispensable in modern agriculture due to their ability to control weeds effectively, thereby improving crop yield and quality [24]. Despite their agronomic benefits, the excessive and improper use of herbicides, particularly 2,4-dichlorophenoxyacetic acid (2,4-D), has led to growing ecological and health concerns [86,87]. As one of the most widely used organochlorine herbicides, 2,4-D constitutes a significant fraction of total pesticide usage globally and is frequently applied in both pre- and post-emergence stages of crop cultivation [86,88,89]. However, studies indicate that less than 10% of the applied herbicide actually reaches its target weeds, while the remaining fraction disperses into the environment through runoff, leaching, volatilization, and photodegradation processes.

Due to its high chemical stability and resistance to natural degradation mechanisms, 2,4-D tends to persist in soil and aquatic environments, leading to long-term contamination of

groundwater and surface water systems [90]. The compound's halogenated molecular structure contributes to its recalcitrance, making it difficult to remove through conventional treatment methods such as adsorption, thermal oxidation, electrochemical degradation, and biodegradation [87]. Prolonged exposure to 2,4-D has been associated with adverse health effects, including neurotoxicity, endocrine disruption, immune suppression, and potential carcinogenicity. Furthermore, improper handling and overuse of this herbicide have resulted in bioaccumulation within ecosystems, posing serious risks to aquatic organisms, soil microbiota, and human health [22]. Consequently, developing effective, eco-friendly, and sustainable strategies for the degradation and removal of 2,4-D from the environment has become an urgent research priority.

In this regard, a wide range of photocatalytic semiconductors has been explored for these dual applications, including metal oxides, nitrides, oxynitrides, and carbon-based materials (detailed in section 2.2). Among them, metal sulfides have gained significant attention owing to their narrow band gaps, high visible-light absorption, and efficient charge transport [91]. Unlike metal oxides, which often exhibit wide band gaps due to deep-lying oxygen 2p orbitals, metal sulfides feature shallower valence bands and lighter carrier effective masses, resulting in improved electronic conductivity and a pronounced quantum size effect [92]. Additionally, their diverse crystal structures and tunable compositions provide flexibility in adjusting optical and catalytic properties [21]. These attributes make metal sulfides suitable candidates for photocatalytic H_2 evolution and organic pollutant degradation. However, issues such as photocorrosion and limited stability continue to restrict their large-scale use, motivating the development of more robust sulfide systems [93]. To overcome these issues, dopant engineering has emerged as a promising strategy to enhance light absorption, charge separation, and durability [94]. The development of dopant-modified metal sulfide photocatalysts thus holds great potential for efficient solar-driven H_2 generation and the sustainable degradation of environmental pollutants.

1.1.2.1. Justification

Over the past few decades, considerable research efforts have focused on developing advanced semiconductor photocatalysts to enhance H_2 evolution performance and achieve an STH conversion efficiency exceeding 10% [21]. Strategies such as cation/anion doping, morphology modulation, heterojunction construction, single-atom modification, and cocatalyst loading have been explored to improve visible-light absorption, charge carrier separation, and surface reactivity [95]. Despite these advances, many existing photocatalysts still suffer from narrow

spectral response ranges, fast recombination of photogenerated charge carriers, and poor stability, which severely limit their practical applications [96]. Therefore, there is a pressing need to design novel, stable, and highly active photocatalysts that can efficiently harvest solar energy for large-scale H_2 evolution.

Subsequently, 2,4-D photodegradation, achieved by our previous work, using Ba-doped γ-In_2S_3, displayed very promising results, and it showed much higher photostability, with only minor decreases in degradation efficiency, from 77% to 73% and 94% to 93%, respectively, after four cycles, by pure and Ba-doped γ-In_2S_3. These findings highlight the significant role of Ba incorporation in enhancing both activity and durability, thereby paving the way for further exploration of other alkaline earth metal dopants to optimize the photocatalytic potential of γ-In_2S_3.

In this context, In_2S_3 has gained growing attention over the past few decades because of its unique combination of properties, including an optimal bandgap, low toxicity, high light absorption capability, excellent stability, and outstanding photocatalytic performance. These advantages stem from the presence of highly active cationic In sites and the cooperative behavior of chalcogen atoms within the structure. To date, five crystallographic polymorphs of In_2S_3 have been identified: the tetragonal β-phase, cubic α-phase, layered hexagonal γ-phase, monoclinic ε-phase, and the cubic Th_3P_4-type phase [97]. Although most previous studies have concentrated on the β-In_2S_3, recent research efforts are increasingly shifting toward exploring and developing the γ-In_2S_3 phase [98]. Its unique layered crystal structure offers abundant active sites and efficient charge transport pathways, making it highly suitable for both H_2 evolution and pollutant degradation [99]. Nonetheless, pristine γ-In_2S_3 still exhibits moderate photocatalytic activity due to limited charge separation and suboptimal band-edge alignment [100]. To overcome these challenges, doping with suitable elements has proven to be an effective strategy for modifying the electronic structure, enhancing visible-light absorption, and promoting charge mobility. On this note, a very few elements like Ba^{2+}, Sb^{3+}, As^{3+}, Ti^{4+}, V^{4+}, and Al^{3+} have been used as dopants to enhance their stability and photocatalytic performance significantly [94,99,101,102]. Thus, this creates opportunities to investigate other potential dopants.

Elements such as Mg^{2+}, Ca^{2+}, and Sr^{2+} have shown notable promise in other semiconductor systems by stabilizing crystal lattices, improving electrical transport, and reducing charge recombination. These dopants also promote band-gap narrowing, increase visible-light

absorption, and enhance ionic conductivity, key factors for optimizing photocatalytic efficiency. While Ca-doped β-In_2S_3 has been reported to exhibit improved dye degradation and H_2 evolution performance, similar studies on Mg- and Sr-doping are scarce, and no reports yet exist for their incorporation into γ-In_2S_3 [103–107].

In light of this, since our previous work identified γ-In_2S_3 and Ba-doped γ-In_2S_3 as highly efficient photocatalysts for 2,4-D degradation, we have now extended our study to further evaluate their applicability. Specifically, we intend to employ γ-In_2S_3 and its Mg-, Ca-, and Sr-doped γ-In_2S_3 for both photocatalytic H_2 evolution and 2,4-D degradation under visible-light irradiation.

2. Antecedent/Background

2.1. Basic Principles of the Photovoltaic Effect

The term *photovoltaic (PV)* refers to the generation of voltage from light energy. The concept originates from Albert Einstein's 1905 explanation of the photoelectric effect, which introduced photons as discrete packets of electromagnetic radiation [12,26]. A PV cell converts sunlight directly into electricity through semiconductor materials, where the principles of molecular orbital (MO) theory, energy band gap, electrical conductivity, crystal structure, and p-n junction behavior collectively explain the internal mechanism of solar-to-electric energy conversion [35]. Extensive research has focused on harnessing this phenomenon to develop highly efficient PV cells capable of converting solar energy into electricity effectively.

2.1.1. Working Mechanism and Device Architecture

Fig. 2a shows the typical structure of a PSC. In general, the perovskite layer, which acts as the light-absorbing layer, is sandwiched between charge transport materials. A PSC typically consists of five key layers: the transparent conductive oxide (TCO), electron transport layer (ETL), active layer (perovskite), hole transport layer (HTL), and a metal back contact [38]. Fig. 2b illustrates the working principle of a PSC, which converts sunlight into electrical energy through a sequence of steps. When sunlight enters the device, it passes through the TCO layer and the n-type ETL before reaching the perovskite absorber. In the absorber, photons with sufficient energy excite electrons from the valence band to the conduction band, leaving behind holes and generating electron-hole pairs, also known as excitons. These excitons are short-lived and must be separated quickly to prevent recombination. Thus, the ETL, with a lower electron affinity than the perovskite, facilitates the transfer of electrons, while the HTL, with a higher ionization potential, efficiently extracts holes. Subsequently, the front electrode, such as FTO

or ITO, collects electrons from the ETL, and the back electrode collects holes from the HTL. Furthermore, connecting an external circuit allows these charge carriers to flow, generating electricity, while continuous photon absorption replenishes the carriers, sustaining the operation of the solar cell as long as sunlight is available [55,108].

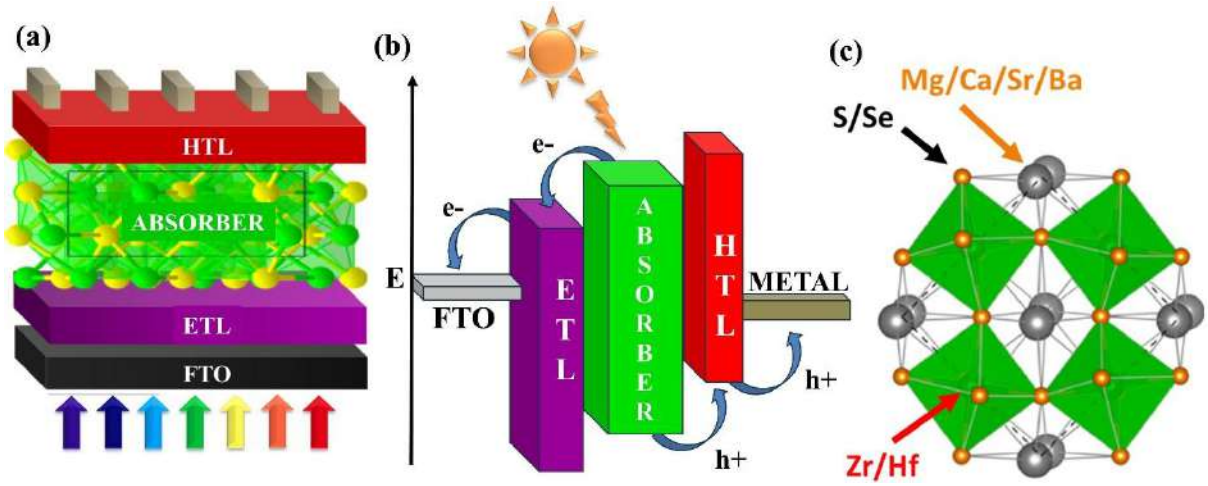

Fig. 2. (a) Typical structure of a PSC, (b) working principle of a PSC, and (c) ideal ABX_3 structure of a CP.

2.1.2. Role of Each Layer in a PSC

- **Transparent Conductive Oxide (TCO)**

TCOs play a vital role in SCs by combining high optical transparency with excellent electrical conductivity, allowing light to reach the absorber while efficiently transporting charge carriers. Commonly used TCOs include ITO, FTO, and AZO, with FTO being particularly favored for PV applications due to its exceptional thermal and chemical stability, cost-effectiveness, and comparatively high transparency. FTO also has low series resistance and offers long-term mechanical and environmental stability, making it a reliable choice for PSCs [109,110].

- **Electron Transport Layer (ETL)**

ETL is an essential part of PSCs, responsible for extracting electrons, blocking holes, and reducing recombination losses by effectively aligning energy levels. By facilitating efficient charge transfer and preventing charge recombination, the ETL plays a major role in determining the performance and durability of PSCs. For optimal operation, the conduction band minimum of the ETL must align closely with that of the perovskite layer to ensure smooth electron flow. Additionally, the ETL must resist degradation caused by light, heat, oxygen, and moisture, and remain insoluble in perovskite precursors. Thin, uniform, compact ETLs are

preferred as they promote faster electron transport and minimize energy losses. Widely used ETL materials include metal oxides such as TiO_2, SnO_2, and ZnO, which combine high transparency, moderate electron mobility, and strong environmental stability [108,111]. In our simulations, we have chosen SnO_2 as the ETL material.

- **Active Layer**

The active layer, or the absorber layer, is generally considered the heart of the solar cell device, as it absorbs light, generates charge carriers (electrons and holes), and enables the separation and transport of these carriers to the external circuit. Efforts are being made to enhance PV technology for improved cost-effectiveness and efficiency. First-generation SCs, based on crystalline silicon, dominate the market but face challenges like high cost and fabrication complexity [112,113]. Second-generation SCslike CIGS and CdTe, aim to cut costs through thin-film technology, but face obstacles related to toxicity and rare earth elements [29,35]. Third-generation SCs using PSCs have emerged as a promising solution, offering versatility in chemical and physical properties. However, concerns persist regarding Pb toxicity and halide instability [82,114]. Scientists are exploring Pb-free alternatives, particularly perovskites based on Sn^{2+} and Ge^{2+}, which offer non-toxicity, narrow band gaps, and high carrier mobility [115–117]. Nevertheless, challenges related to stability persist. Alternative strategies, such as integrating trivalent cations like Bi^{3+} and Sb^{3+} in place of Pb^{2+} ions, are being pursued [118–120]. Despite the potential, the achieved performance lags behind that of Pb-PSC due to structural constraints, necessitating the identification of new materials with similar attributes while addressing these limitations.

A promising class of materials, CPs (Fig. 2c) with the structure ABX_3 (A = Ba/Sr/Ca, B = Ti/Zr/Hf, X = S/Se), has recently emerged as a viable, stable, and non-toxic option. Over a decade ago, Sun et al. reported a theoretical investigation of 18 CPs as a potential light absorber, with material characteristics such as strong chemical bonding, favorable band gaps, and excellent optoelectronic properties [51]. Among them, $BaZrS_3$ and $SrZrS_3$ have attracted significant attention in both experimental and theoretical research due to their promising optoelectronic and structural properties [53,56]. $BaZrS_3$, in particular, is recognized as an excellent compound, featuring a direct bandgap of approximately 1.72 eV, strong absorption in the visible spectrum, and high chemical stability. Its electronic structure can be tuned via cation substitution; for example, partially replacing Zr with Ti lowers the conduction band edge, improving energy level alignment for PV applications. In this work, $BaZr_{0.96}Ti_{0.04}S_3$ was employed, where a 4% Ti substitution reduces the bandgap to around 1.51 eV, closely matching

the Shockley-Queisser efficiency limit [55]. Furthermore, $SrZrS_3$, a structurally analogous compound, has been investigated for its polymorphic flexibility and optical tunability. It exists in two main phases, α and β, with band gaps of about 1.5 eV and 2.1 eV, respectively, making it another promising material for solar energy conversion. Inspiringly, it exhibits strong light absorbance with an absorption coefficient $>10^5$ cm^{-1}, the carrier concentration $\sim10^{17}$ cm^{-3}, and the carrier mobility as high as 10^6 $cm^2V^{-1}s^{-1}$, indicating its potential as a light-absorbing material [58].

Different researchers have reported various methods for synthesis. While creating these perovskites at elevated temperatures (900 - 1100°C) for solar cell production has been difficult, material scientists have devised synthesis techniques that operate at lower temperatures [56,60]. In 2023, Agarwal and his team unveiled a method for fabricating thin films directly through a solution processing approach at temperatures ranging from 500 to 575ºC, representing a notable advancement as these processing temperatures are similar to those used for conventional solar cell absorbers (CIGS, CdTe, etc.) [61]. It took nearly ten years to overcome the temperature challenges and enhance experimental techniques. At present, there is only one documented case regarding the production of $BaZrS_3$ CP SCs, which reached a PCE of 0.17%. Conversely, the potential application of $SrZrS_3$ in PV devices has yet to be investigated experimentally.

From the reported data, $BaZr_{0.96}Ti_{0.04}S_3$ and $SrZrS_3$ stand out as potential absorber materials due to their intense light absorption, cost-efficient preparation methods, and high environmental stability, making them strong contenders for next-generation, stable, and eco-friendly SCs.

- **Hole Transport Layer (HTL)**

HTLs are essential components in solar cell structures, responsible for efficiently collecting holes from the absorber, transporting them to the back electrode, blocking electrons, and ensuring proper energy level alignment at the interface. An optimized HTL enhances charge extraction, minimizes recombination losses, and improves overall device efficiency. However, conventional HTLs often require high annealing temperatures or suffer from solubility issues, limiting their scalability and practical application. To address these challenges, new HTL materials with high hole mobility, low-temperature processability, and superior stability are being explored [121,122].

Metal phthalocyanines (MPcs), including CuPc, NiPc, and ZnPc emerging as potential HTLs, owing to their low cost, narrow bandgap, high hole mobility, excellent stability, and long

exciton diffusion length. Despite their promising characteristics, MPcs have not yet been applied to CP SCs, presenting an unexplored opportunity. Here, in this thesis, we theoretically investigated the applicability of MPc (M = Cu, Ni, Zn) HTLs in $BaZr_{0.96}Ti_{0.04}S_3$-based CP solar cells. Additionally, we proposed various conductive metal-organic frameworks (c-MOFs) as novel HTLs for $SrZrS_3$-based solar cells. Among them, Cu-MOF ({[Cu_2(6-mercaptonicotinate)]·NH_4}$_n$) with a 1.34 eV bandgap and a two-dimensional (-Cu-S-)$_n$ structure exhibited enhanced electrical conductivity and long-term stability due to improved hole mobility [71,123]. NTU-9, a titanium-based MOF with a 1.73 eV bandgap, demonstrated p-type semiconducting behavior and good thermal stability [72,124]. Fe_2(DSBDC), part of the MOF-74 family, showed excellent relative conductivity and reduced charge hopping barriers due to its high work function and the presence of β-spin Fe^{2+} electrons [73]. Sr-MOF ({[Sr(ntca)(H_2O)$_2$]·H_2O}$_n$) formed a vertically stacked π-network with strong thermal stability and notable conductivity [74,125]. Similarly, Mn_2(DSBDC) with a 2.6 eV bandgap displayed potential for high-mobility electronic applications, while Cu_3(HHTP)$_2$ (bandgap 2.75 eV) exhibited smooth morphology, high crystallinity, and p-type conductivity attributed to charge delocalization within its 2D Cu-HHTP layers [73,75]. Importantly, all these MOFs can be synthesized at temperatures below 200°C, making them suitable for low-temperature device fabrication. For example, Cu-MOF thin films were prepared by drop-coating and drying at 200°C, Sr-MOF films via spin-coating at room temperature, Cu_3(HHTP)$_2$ films by heating at 85°C, NTU-9 at 60°C, Mn_2(DSBDC) at 150°C under vacuum, and Fe_2(DSBDC) at 146°C [75,76,123–125]

Each HTL was evaluated for its energy level alignment, charge transport properties, and interfacial compatibility with the absorber. Theoretical insights from this thesis provide valuable guidance for designing optimized and stable CP-based solar cells with enhanced performance.

- **Metal Back Contact:**

Metal contacts play a pivotal role in determining the performance and reliability of SCs by facilitating charge extraction and maintaining electrical continuity. Positioned at the edges of the device, they function to collect charge carriers from transport layers, complete the external circuit, and suppress resistive losses [115]. The ideal metal contact combines high electrical conductivity with a well-matched work function, ensuring efficient and selective charge transport. It must also maintain chemical and thermal stability to prevent degradation at the interface [27].

Recent investigations have focused on metals with specific work functions to enhance charge selectivity and interfacial energetics in PSCs. Representative examples include Cu (4.6 eV), Ag (4.7 eV), Fe (4.8 eV), Cu-doped C (5.0 eV), Au (5.1 eV), W (5.22 eV), Ni (5.5 eV), Pd (5.6 eV), and Pt (5.7 eV) [50]. The alignment of these work functions with adjacent transport layers determines whether the resulting interface behaves Ohmic or a Schottky barrier. High work function metals (≥5.0 eV) are generally employed for hole-selective contacts due to their ability to enhance hole extraction and lower contact resistance, particularly in devices incorporating wide-bandgap HTLs. Furthermore, stability considerations, both thermal and chemical, are essential when selecting electrode materials for long-term operation [55].

In our theoretical evaluation, various metals were systematically studied in combination with selected HTLs, focusing on parameters such as energy level matching, interfacial recombination, and overall contact stability. The results demonstrate that carefully engineered metal contacts substantially improve PCE and operational durability, offering a clear route toward reliable and cost-effective solar technologies.

2.1.3. PV Parameters

PV parameters are critical indicators used to assess the performance and efficiency of SCs. They provide measurable insights into how well a solar device transforms incident sunlight into electrical power. The main PV parameters include the open-circuit voltage (V_{OC}), short-circuit current density (J_{SC}), fill factor (FF), and power conversion efficiency (PCE).

- **V_{OC}**

The V_{OC} represents the maximum voltage a solar cell can produce when no current is drawn, meaning the external circuit is disconnected. It is determined by the difference between the quasi-Fermi levels of electrons and holes under illumination. V_{OC} reflects the degree of charge separation achievable within the cell and is strongly influenced by recombination processes [126]. It can be estimated using the diode equation:

$$V_{OC} = \frac{nkT}{q} \ln \left[\frac{I_L}{I_0} + 1\right]$$

where n is the diode ideality factor, k is Boltzmann's constant, T is the absolute temperature, q is the elementary charge, I_L is the photocurrent, and I_0 is the reverse saturation current. A higher V_{OC} typically suggests lower recombination losses and superior material quality.

- **J_{SC}**

The J_{SC} is the current per unit area that a solar cell produces when its terminals are shorted, meaning the voltage across the cell is zero. J_{SC} reflects the efficiency with which the device generates and collects charge carriers under standard illumination conditions, typically AM1.5G at 1000 W/m^2. The performance of a solar cell depends on the dynamics of charge carriers, including their generation and transport within the device [14]. For an ideal solar cell, J_{SC} can be expressed in terms of the charge generation rate G and the diffusion lengths of electrons (L_e) and holes (L_h) as:

$$J_{SC} = qG(L_e + L_h)$$

where q is the electronic charge. This equation highlights that the J_{SC} is directly influenced by both the rate of photogenerated carriers and their ability to reach the electrodes before recombining.

- **FF**

The FF is a dimensionless metric that indicates the quality of a solar cell's output by comparing the maximum obtainable power to the theoretical power determined by the product of the V_{OC} and J_{SC} [127]. It is defined as:

$$FF = \frac{V_{MP} \cdot J_{MP}}{V_{OC} \cdot J_{SC}}$$

where V_{MP} and J_{MP} are the voltage and current density at the maximum power point. A higher FF reflects lower series resistance and better diode behavior.

- **PCE**

PCE quantifies the overall effectiveness of a solar cell in converting incident sunlight into electrical energy under standard conditions [128]. It is expressed as:

$$PCE = \frac{V_{OC} \cdot J_{SC} \cdot FF}{P_{in}} \times 100$$

where P_{in} is the incident light power density, usually 1000 W/m^2. PCE depends on all the other PV parameters, encompassing the efficiency of light absorption, charge separation, and carrier transport.

In this thesis, all PV parameters were calculated from the J-V curves obtained using numerical simulations via SCAPS-1D. These values were employed to evaluate different CP-based SC architectures, focusing on absorber materials, transport layers, and interface engineering. The relationships between V_{OC}, J_{SC}, FF, and PCE were analyzed to determine configurations that optimize efficiency while maintaining stability and scalability for practical applications.

2.2. Basic Concept Behind Photocatalysis

The term *photocatalysis* originates from the Greek words *photo* (meaning light) and *katalyo* (meaning to decompose or break apart). It refers to a light-driven process in which a semiconductor material, known as a photocatalyst, accelerates chemical reactions without undergoing any permanent change itself [129]. Solar energy, which reaches Earth as a continuous stream of electromagnetic radiation, provides the photons necessary to initiate these reactions [130]. The activation of a photocatalyst depends primarily on the wavelength of the incoming light and the material's bandgap, which is the energy difference between its valence band (VB) and conduction band (CB). When photons possessing energy equal to or greater than this bandgap strike the semiconductor surface, electrons are excited from the VB to the CB, leaving behind positive holes. These charge carriers participate in redox reactions on the surface of the photocatalyst, thereby driving a variety of chemical transformations under light irradiation [19]. Photocatalysis has been widely used in environmental and energy-related fields, such as air and water purification, self-cleaning surfaces, H_2 production, CO_2 reduction, and the breakdown of toxic organic pollutants from various sectors, such as industrial, agricultural, and medical [131]. In this thesis, photocatalysis is applied in two key areas: H_2 fuel generation and the degradation of the organic pollutant 2,4-D, which will be discussed in detail in the following sections.

2.2.1. Development of Visible Light-Driven Photocatalysts for H_2 Generation and 2,4-D Degradation

As mentioned earlier in section 1, it is imperative to switch towards clean, renewable, and sustainable alternatives. Similar to fossil fuels, H_2 is considered an equally potent energy carrier. Nevertheless, fossil fuel combustion releases an enormous amount of CO_2, while H_2 can be combusted without any pollution, just by releasing water as its byproduct, making it a promising alternative in achieving net-zero emissions by 2050 [20]. Moreover, H_2 has emerged as one of the most promising clean fuels owing to its exceptionally high energy density (140

MJ/kg), offering a sustainable pathway with immense potential for applications in fuel cells, transportation, and industrial processes [84].

H_2 production can be widely classified into two pathways: fossil fuel-dependent and renewable energy-dependent. At present, most industrial H_2 is produced using fossil-derived methods such as steam methane reforming, coal gasification, hydrocarbon pyrolysis, and partial oxidation. Although these technologies are well-established and efficient, they emit large amounts of CO_2, contributing to greenhouse gas accumulation and environmental degradation [3]. Alternatively, renewable H_2 production utilizes resources such as biomass and water. Biomass conversion can occur through thermochemical routes (including pyrolysis and gasification) or biological pathways (such as bio-photolysis and fermentation). Meanwhile, water splitting technologies, including electrolysis, thermochemical, and photocatalytic methods, rely on renewable inputs like electricity, heat, or sunlight to produce H_2 with minimal ecological impact [20].

Among these, photocatalytic water splitting has emerged as one of the most promising and environmentally benign techniques. It directly converts solar energy into chemical energy in the form of H_2 under mild reaction conditions and without the formation of harmful by-products [83,84]. Nonetheless, to produce a large amount of H_2 fuel, it is important to attain over 10% STH efficiency [21]. Achieving this remains challenging due to factors such as limited visible-light absorption, rapid recombination of photogenerated charge carriers, and insufficient long-term stability of most photocatalysts.

Since the pioneering discovery of water splitting on a TiO_2 photoelectrode in 1972, researchers have intensively explored a wide variety of semiconductor materials, including metal oxides, nitrides, oxynitrides, and carbon-based systems [132]. Among these, several metal oxides such as ZrO_2, In_2O_3, Ga_2O_3, $SrTiO_3$, and $NaTaO_3$ have demonstrated strong photocatalytic activity under UV irradiation due to their stable structures and favorable redox potentials [19]. However, their wide band gaps restrict light absorption to the UV region, which accounts for only about 4% of the solar spectrum. Consequently, even with an ideal quantum efficiency of 100%, the maximum theoretical STH conversion efficiency under UV light is only 3.3%, far below the threshold for practical solar H_2 production [129]. To overcome this limitation, researchers have turned their attention to visible-light-responsive photocatalysts, such as oxynitrides (e.g., $LaTiO_2N$, $CaTaO_2N$, and $LaTaO_2N$) and oxysulfides (e.g., $Y_2Ti_2O_5S_2$ and α-$LaOInS_2$). These materials extend light absorption into the visible region but still face challenges such as self-oxidation, limited charge transport, and complex synthesis routes [133].

Further developments have inspired the search for alternative materials that can effectively utilize a broader portion of the solar spectrum.

In this context, chalcogen-based photocatalysts, particularly binary and ternary metal sulfides, have emerged as highly promising candidates for solar-driven H_2 generation. Metal sulfides generally possess narrower band gaps, allowing efficient absorption of visible light, and exhibit suitable redox potentials for water reduction [21]. However, they also encounter issues such as photocorrosion, charge recombination, and stability under prolonged illumination. For example, MoS_2 nanosheets with mixed $1T_0$/2H phases demonstrate excellent charge separation and H_2 evolution performance due to in-plane heterojunctions, yet their oxidation kinetics remain slow, and layer restacking can limit efficiency [92]. ZnS nanoparticles achieve exceptionally high quantum yields (up to ~90% at 313 nm) and can produce H_2 even without noble metal co-catalysts, however, their wide band gap confines absorption to the UV range, and the material readily undergoes photocorrosion in the absence of sacrificial agents [132]. Similarly, CoS_2 shows high H_2 evolution rates because of its abundant active sites and good electrical conductivity, but its structural stability tends to decline during extended operation [134]. Contrastingly, SnS_2 exhibits enhanced photocatalytic activity through improved water adsorption and charge transport, yet it gradually loses activity upon long-term light exposure [21]. Cubic CdS nanocrystals possess large surface areas and strong visible-light absorption, leading to excellent H_2 evolution rates, but the risk of Cd leaching and photocorrosion remains a significant concern [135]. Other binary sulfides, such as NiS_2 and Cu_2S, combine good charge mobility and structural robustness, though their limited light absorption range and rapid electron-hole recombination can reduce efficiency [136,137].

More recently, In-based metal sulfide semiconductors have drawn increasing attention for their tunable electronic structures and strong visible-light response [138]. Compounds like $ZnIn_2S_4$ and $CdIn_2S_4$ stand out for their tunable morphologies, narrow band gaps, and strong visible-light activity [135]. These materials show efficient H_2 evolution but may still require co-catalysts (e.g., Pt, Pd, Ni etc) to maintain long-term performance and avoid photocorrosion [138]. Similarly, $CuInS_2$ and $CaIn_2S_4$ benefit from abundant active sites and broad visible-light response but possess relatively low conduction band potentials, which limit the driving force for H_2 evolution [134]. Pd-V_S-$ZnIn_2S_4$ exhibited one of the highest H_2 generation rates (185.6 μmol h^{-1}), demonstrating the strong performance of $ZnIn_2S_4$-based systems enhanced by Pd doping [139]. In binary systems, Ca-doped β-In_2S_3 co-doped with 1 wt% Pt achieved a H_2 evolution rate of 145 μmol h^{-1}, while the same material showed no activity in the absence of

Pt. Although these findings indicate that Ca-doped β-In_2S_3 can be highly efficient, its dependence on noble metal co-catalysts such as platinum raises concerns regarding cost and scalability for industrial use [140]. Other In-based ternary materials, such as $MgIn_2S_4$, have also shown promising results, producing up to 133.8 μmol h^{-1} of H_2 under optimized conditions [141]. Doped variants of $ZnIn_2S_4$, including Mo-$ZnIn_2S_4$ (92.4 μmol h^{-1}) and Ni-$ZnIn_2S_4$ (84.3 μmol h^{-1}), have delivered moderate activity, while binary systems like Pd-V_S-In_2S_4 generated approximately 58.4 μmol h^{-1} [142]. Recent progress in heterostructure engineering, which combines materials such as $ZnIn_2S_4$ and $MgIn_2S_4$ with plasmonic metals, carbon-based materials, or complementary semiconductors, has further enhanced charge separation and visible-light absorption. However, these pose several shortcomings, including fabrication complexity, material compatibility issues, poor reproducibility, the potential for interface defect formation, and thermodynamic limitations to a certain extent [143–145]. Therefore, these challenges have driven research toward developing novel, efficient, and durable semiconductor photocatalysts, particularly those employing dopant engineering, to serve as a standalone material capable of harvesting solar energy effectively for large-scale H_2 evolution.

In parallel with the energy crisis, environmental contamination from toxic organic pollutants has emerged as another major global concern. Extensive research has been devoted to the degradation of various complex contaminants, including pharmaceuticals, phenol and its derivatives, synthetic dyes, petroleum hydrocarbons, and certain agrochemicals [146,147]. Despite these efforts, persistent herbicide 2,4-dichlorophenoxyacetic acid (2,4-D) remains comparatively underexplored, even though it poses severe ecological and health risks. The widespread and continuous use of 2,4-D has substantially contributed to soil and water pollution, underscoring the urgent need to investigate effective degradation strategies for this persistent pollutant [86,88]. 2,4-D, a widely used phenoxy herbicide for controlling broadleaf weeds in crops such as wheat, rice, and sugarcane, is highly soluble, chemically stable, and resistant to biodegradation. Its persistence in the environment leads to leaching into groundwater, posing serious ecological and health hazards. Long-term exposure to 2,4-D is linked to neurological disorders, hormonal imbalance, and carcinogenic effects, prompting the World Health Organization (WHO) to set a maximum permissible concentration of 70 μg/L in drinking water [22,24,148].

Conventional treatment methods, such as adsorption, chemical oxidation, and biological degradation, are often insufficient for the complete mineralization of 2,4-D, leading to secondary contamination [149–152]. In contrast, photocatalysis offers an environmentally

friendly route capable of complete mineralization of such persistent pollutants into harmless by-products like CO_2 and H_2O [153,154].

Over the past decade, numerous photocatalytic systems have been developed to address the degradation of 2,4-D. Semiconductors such as TiO_2, ZnO, and metal sulfide-based catalysts have been investigated under both UV and visible-light irradiation to enhance degradation performance [148]. Among TiO_2-based materials, TiO_2 nanotube arrays demonstrated remarkable photocatalytic activity, achieving 97% removal of 2,4-D; however, limited to UV light [132]. Similarly, WO_3-TiO_2-SBA-15 composites exhibited rapid degradation, attaining 76% removal in 240 minutes under visible-light exposure [155]. Other TiO_2-based heterostructures, including Fe_0/TiO_2/activated carbon and $TiO_2@CuFe_2O_4$ systems, achieved degradation efficiencies ranging between 81-97%, though their performance under natural solar light was comparatively slower [22]. Later, the research interest shifted towards chalcogen-based semiconductors, particularly metal sulfides, which have attracted increasing attention because of their adjustable band gaps, strong absorption in the visible-light spectrum, and efficient charge carrier mobility [156–159]. According to reported studies, only a limited number of these materials have been explored for the degradation of 2,4-D, including $ZnIn_2S_4$ [160,161], Bi_2S_3 [162,163], Co_9S_8 [164], γ-In_2S_3, and Ba-doped γ-In_2S_3 [94], which exhibited degradation efficiencies of approximately 30%, 12%, 15%, 77%, and 94%, respectively. Among these, $ZnIn_2S_4$ demonstrated poor long-term performance, as its degradation efficiency dropped significantly from 30% to 3% after five consecutive cycles, indicating limited stability. In comparison, our earlier work revealed that γ-In_2S_3 and Ba-doped γ-In_2S_3 displayed much higher durability, with only minor decreases in degradation efficiency, from 77% to 73% and 94% to 93%, respectively, after four cycles. These encouraging results inspired us to further investigate the incorporation of other alkaline earth metals as dopants in γ-In_2S_3, aiming to develop promising photocatalysts capable of achieving both efficient H_2 evolution and effective degradation of 2,4-D.

2.2.2. Photocatalytic H_2 Evolution Mechanism

The general mechanism of photocatalytic H_2 evolution involves a series of reactions as illustrated in Fig. 3a. Briefly, when the catalyst absorbs photons (hν), e^- are excited from the VB to the CB, leaving behind h^+ in the VB. These charge carriers migrate to the surface of the photocatalyst, where the photogenerated electrons reduce protons (H^+) to form H_2 gas through the H_2 evolution, and the h^+ oxidize water to produce O_2 via the O_2 evolution. For this process to proceed, the conduction band minimum (CBM) must be more negative than the H^+/H_2

potential (0 V vs. NHE) and the valence band maximum (VBM) more positive than the O_2/H_2O potential (+1.23 V vs. NHE), ensuring the thermodynamic feasibility of both half-reactions. An overpotential is also required to overcome kinetic barriers [132]. The photocatalytic process can be summarized by the following reactions:

$$\text{Photocatalyst} + h\nu \rightarrow \text{Photocatalyst}\ (e^- + h^+)$$

$$2H^+ + 2e^- \rightarrow H_2$$

$$2H_2O + 4h^+ \rightarrow O_2 + 4H^+$$

$$2H_2O \rightarrow 2H_2 + O_2 \qquad (\Delta G_r = 273\ kJ \cdot mol^{-1},\ T = 298\ K)$$

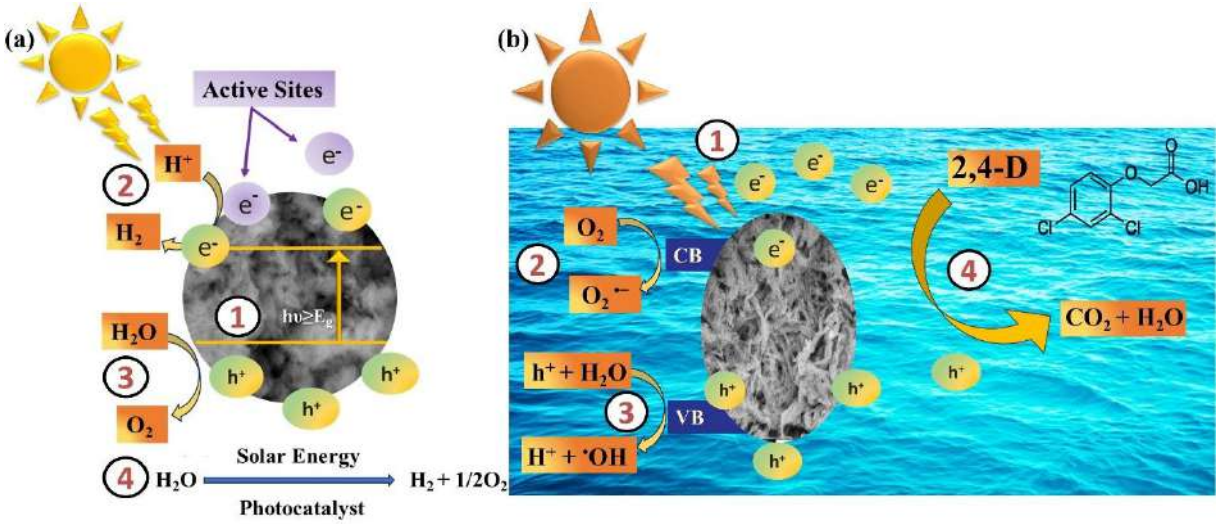

Fig. 3. General mechanism of photocatalytic (a) H_2 evolution and (b) 2,4-D degradation

2.2.3. Photocatalytic 2,4-D Degradation Mechanism

The photocatalytic degradation process generally involves the activation of a semiconductor material by an energy source with energy greater than its band gap. This excitation promotes the formation of electron-hole pairs, which can either recombine or interact with the surrounding substances. These substances may act as electron donors (e.g., •OH) or acceptors (e.g., $O_2^{\bullet-}$). As a result, highly reactive species such as hydroxyl and superoxide radicals are generated, which attack and decompose organic pollutants, thereby purifying the water.

In the case of 2,4-D degradation through photocatalysis, the mechanism is based on the excitation of electrons from the VB to the CB of the photocatalyst under light irradiation. This photoexcitation produces electron-hole pairs, which migrate to the catalyst surface and participate in redox reactions that lead to the breakdown of 2,4-D molecules [141,165,166].

The initial reactions in this process can be divided into four main steps, as illustrated in Fig. 3b.

1. **Photoexcitation:** When the photocatalyst is exposed to light, it absorbs photons and generates electrons and holes, as shown in Eq. (a):

$$\text{Photocatalyst} + h\upsilon \rightarrow \text{Photocatalyst}\ (e^- + h^+) \qquad (a)$$

2. **Formation of superoxide radicals:** The photoexcited electrons in the CB react with dissolved oxygen in water to form superoxide anions (Eq. (b)):

$$e^- + O_2 \rightarrow O^{2\bullet-} \qquad (b)$$

3. **Generation of hydroxyl radicals:** The holes in the VB oxidize water molecules, producing protons and hydroxyl radicals (Eq. (c)):

$$h^+ + H_2O \rightarrow H^+ + \bullet OH \qquad (c)$$

4. **Degradation of 2,4-D:** The reactive species (H^+, $O^{2\bullet-}$, and •OH) attack the 2,4-D molecules, resulting in their oxidation and eventual mineralization, as represented in Eq. (d):

$$H^+ + O_2^{\bullet-} + \text{2,4-D} \rightarrow CO_2 + H_2O + \text{byproducts} \qquad (d)$$

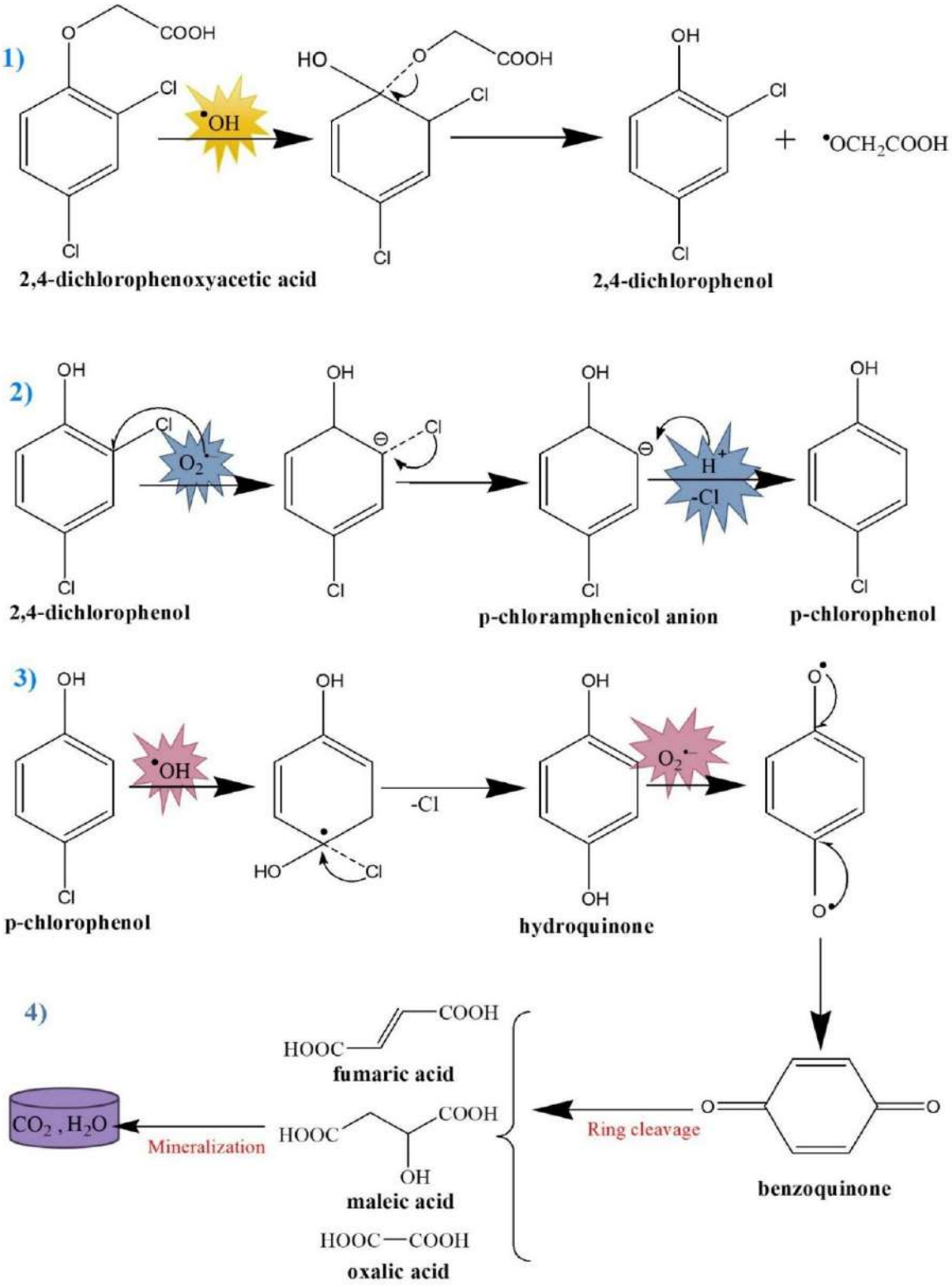

Fig. 4. Possible pathway for the photocatalytic degradation of 2,4-D using γ-In_2S_3.

According to previous studies, the reactions illustrated in Fig. 4 represent a plausible pathway for the photocatalytic degradation of 2,4-D using γ-In_2S_3 [87,160,162,165,167,168]. The overall degradation proceeds through multiple intermediate steps. Initially, 2,4-D (1) interacts

with •OH radicals, which preferentially attack the carbon atom linked to the -OCH_2COOH group due to the substituent positions on the aromatic ring. This produces 2,4-dichlorophenol (2) as the first intermediate. Next, an electrophilic substitution occurs at the meta-position of the ring, influenced by the hydroxyl group at the ortho-position, leading to the formation of the p-chloramphenicol anion (3). Protonation of this anion yields p-chlorophenol (4). The electron-donating nature of the hydroxyl group in p-chlorophenol facilitates an additional •OH attack at the para-position, resulting in hydroquinone (5). Hydroquinone subsequently reacts with superoxide radicals ($O_2^{\bullet-}$) to produce an intermediate that transforms into benzoquinone (6). Finally, benzoquinone undergoes ring cleavage, forming short-chain organic acids such as fumaric, maleic, and oxalic acids (7), which are ultimately mineralized into CO_2 and H_2O (8). This sequence of reactions demonstrates the complete mineralization pathway of 2,4-D under photocatalytic conditions.

3. Hypothesis

Rationally engineered conductive MOF and phthalocyanine-based HTLs with their ambipolar π-conjugated charge transport would enhance hole mobility and suppress interfacial recombination, boosting the performance of chalcogenide perovskite solar cells, whereas alkaline earth metal doping of γ-In_2S_3 modulates its band structure, improves charge carrier dynamics, and induces sulfur vacancies, yielding superior visible-light photocatalytic activity.

4. Objectives

4.1. General Objective

To design and assess advanced solar energy materials by introducing conductive Metal-Organic Framework and phthalocyanine-based hole transport layers for lead-free chalcogenide perovskite solar cells, alongside experimentally investigating the effect of alkaline earth metal doping in γ-In_2S_3 nanostructures on its photocatalytic performance toward 2,4-D degradation and H_2 fuel evolution, with the principal goal of achieving high-efficiency, stable, and environmentally sustainable energy conversion systems.

4.2. Specific Objective

1. To develop and optimize Pb-free $SrZrS_3$ chalcogenide perovskite solar cells employing diverse conductive metal-organic framework-based HTLs and assess their impact on device performance to identify configurations that maximize energy conversion efficiency.

2. To explore the underlying mechanisms contributing to performance enhancement through analyses including Nyquist plots, quantum efficiency, and energy band alignment studies, while investigating the effects of different metal back contacts, interface properties, parasitic resistances, and operating temperatures.
3. To evaluate the effectiveness of metal phthalocyanine-based HTLs in eco-friendly $BaZr_{0.96}Ti_{0.04}S_3$ chalcogenide perovskite solar cells, focusing on their impact on the built-in electric field, quantum efficiency, charge carrier generation rates, and recombination resistance.
4. To synthesize phase-pure γ-In_2S_3 and its Mg, Ca, and Sr doped counterparts, performing comprehensive structural, morphological, compositional, optical, and electrical characterization to elucidate the impact of dopants on the intrinsic properties of γ-In_2S_3.
5. To assess the photocatalytic potential of the Mg, Ca, and Sr doped γ-In_2S_3 nanomaterials for H_2 fuel evolution and the degradation of persistent herbicide 2,4-dichlorophenoxyacetic acid under different experimental conditions, linking dopant effects to enhanced photocatalytic efficiency.

4.3. Summary of the Objectives

4.3.1. Objectives 1 and 2

Detailed methodologies are presented in Section 5.1.1, while a comprehensive discussion on the results obtained is elucidated in Section 6.1. In the pursuit of fulfilling proposed specific objectives 1 and 2, we designed and optimized Pb-free $SrZrS_3$-based CP SCs employing conductive metal-organic framework (c-MOFs) as HTLs through SCAPS-1D theoretical simulation. For the first time, we introduced diverse c-MOFs, namely, Cu-MOF ({[Cu_2(6-mercapto nicotinate)]·NH_4}n), NTU-9, Fe_2(DSBDC), Sr-MOF ({[Sr(ntca)(H_2O)$_2$]·H_2O}n), Mn_2(DSBDC), and Cu_3(HHTP)$_2$, as promising alternatives to traditional HTLs for a novel $SrZrS_3$ absorber. This marks a pioneering advancement in the development of next-generation Pb-free PSCs via SCAPS-1D. We examined a total of 193 distinct device configurations, systematically optimizing various electrical and structural parameters, including thickness, carrier concentration, defect density, and interface properties of the absorber and HTL. This optimization resulted in significant improvements in device performance. Comparative analyses employing J-V characteristics, QE measurements, Nyquist Plots, Mott-Schottky analysis, and generation-recombination profile provided deep insights into the mechanisms driving performance enhancements. Additionally, we investigated the effects of metal back contacts, interface properties, parasitic resistances, and operating temperatures, highlighting

the interconnected effects of structural, electronic, and environmental factors on solar cell performance. *This research has been published:* **Linda, E**., Chettiar, A.D.R. and Marasamy, L. (2024). Emerging class of $SrZrS_3$ chalcogenide perovskite solar cells: Conductive MOFs as HTLs- A game changer?. **Solar Energy Materials and Solar Cells**, 278, 113204. **DOI: http://dx.doi.org/10.1016/j.solmat.2024.113204.**

4.3.2. Objective 3

Systematic methodology is presented in Section 5.1.2, while a comprehensive analysis of the results is presented in Section 6.2. To achieve the specific objective 3, we explored the potential of metal phthalocyanine (MPc)-based HTLs in eco-friendly $BaZr_{0.96}Ti_{0.04}S_3$ chalcogenide perovskite solar cells, utilizing SCAPS-1D theoretical simulation. This work represents one of the first systematic evaluations of copper phthalocyanine (CuPc), nickel phthalocyanine (NiPc), and zinc phthalocyanine (ZnPc) as HTLs in $BaZr_{0.96}Ti_{0.04}S_3$ solar cells. In our simulations, we analyzed device structures of FTO/SnO_2/$BaZr_{0.96}Ti_{0.04}S_3$/MPc (M=Cu, Ni, Zn)/C. We optimized these device structures by varying crucial parameters of the absorber and HTL's thickness, defect density, and carrier concentration. Wherein, the optimized devices demonstrated notable enhancements in QE, improved charge carrier generation at the absorber-HTL interface, and higher recombination resistance. These findings indicate reduced carrier losses and enhanced charge extraction. In a nutshell, this work not only establishes MPc as effective and environmentally benign HTLs but also positions $BaZr_{0.96}Ti_{0.04}S_3$ as a strong candidate for next-generation sustainable photovoltaic technologies. *This work has been published:* **Linda, E**., Chettiar, A.D.R. and Marasamy, L. (2024). Theoretical insights into high-efficiency $BaZr_{0.96}Ti_{0.04}S_3$ chalcogenide perovskite solar cells using phthalocyanine HTLs. **Materials Letters**, 375, 137203. DOI: **https://doi.org/10.1016/j.jphotochem.2024.115831**.

4.3.3. Objectives 4 and 5

Detailed methodologies for synthesis, characterization, and photocatalytic applications, specifically the photodegradation of 2,4-D and H_2 fuel evolution, are presented in Section 5.2. Comprehensive analyses and discussions of the results can be found in Sections 6.3 and 6.4. To achieve objectives 4 and 5, for the first time, we successfully synthesized phase-pure γ-In_2S_3 nanoribbons and systematically doped them with Mg^{2+}, Ca^{2+}, and Sr^{2+} ions using a straightforward heating-up method. We conducted structural, morphological, compositional, surface charge, optical, and electrical investigations to elucidate the intrinsic effects of dopant

incorporation on the γ-In_2S_3 crystal lattice. Characterization techniques such as XRD, HRTEM, and Raman spectroscopy confirmed the formation of single-phase γ-In_2S_3 and the maintenance of phase purity upon doping. FESEM micrographs revealed a distinct nanoribbon morphology for undoped and Mg-doped samples, whereas Ca and Sr-doping showed dense aggregation. EDS and XPS analyses confirmed the estimated stoichiometry of 2:3 for In:S, with approximately 2 at% of dopants incorporated. Additionally, the BET isotherm analysis indicated a notable increase in the surface area of all the doped samples. Optical studies, including UV-Vis spectroscopy and PL measurements, revealed a redshift upon doping, effectively narrowing the bandgap from UV to the visible region. Electrical analyses, comprising Mott-Schottky, EIS, and Hall measurements, confirmed improved charge transfer dynamics, reduced recombination rates, and extended carrier lifetimes. Subsequently, we systematically evaluated the photocatalytic activities of the synthesized nanoribbons for H_2 fuel evolution and 2,4-D degradation under various experimental conditions. Among the synthesized photocatalysts, Ca: γ-In_2S_3 exhibited the most outstanding performance, achieving an H_2 evolution of 688 μmol g^{-1} and a 2,4-D degradation efficiency of 95.47% within 4 hours. Further optimization of experimental conditions, including scavenger types, catalyst dosage, initial 2,4-D concentrations, and solution pH, yielded maximum degradation of 99.53% at pH 3 using 40 mg catalyst and 60 ppm 2,4-D, while maintaining excellent recyclability with over 91% activity retention after 10 cycles. *This research has been published:* **Linda, E**., Rasu Chettiar, Manisekaran, R., J. Á., Tomás, and Marasamy, L. (2025). Uncovering the Potential of γ In_2S_3: Can Doping with Mg, Ca, and Sr Revolutionize Photocatalytic H_2 Evolution and 2,4-D Herbicide Degradation? **International Journal of Hydrogen Energy**, 185, 151882. **DOI: https://doi.org/10.1016/j.ijhydene.2025.151882**.

5. Methodology

5.1 Theoretical Simulation

Several software programs are available for simulating the characteristics of SCs based on their structural inputs. Commonly used software includes SETFOS, SILVACO-ATLAS, COMSOL, Wx-AMPS, and SCAPS-1D [78,79,169,170]. In this study, SCAPS-1D (version 3.3.10), a one-dimensional, steady-state simulation program developed by Professor Marc Burgelman at Ghent University, Belgium, was utilized [31,171]. This software offers advantages such as being user-friendly, free of cost, capable of analyzing up to seven layers, and supporting in-depth batch analysis with high consistency [80,172]. It allows researchers to adjust critical

parameters such as bandgap (E_g), carrier concentration, defect density, electron affinity, density of states (DOS), mobility, and more. Additionally, the software provides various illumination settings, including AM0, AM1.5G, and monochromatic light, making it ideal for detailed solar cell performance evaluation [80,81,173]. Most of all, SCAPS-1D operates by solving fundamental semiconductor equations like Poisson's equation, the carrier continuity equation, and the drift-diffusion equation, calculating current within specified limits based on the solar cell's structural configuration and input material parameters [55,174–176].

5.1.1. Computation Framework and Device Configuration of Pb-free $SrZrS_3$ CP SCs

In this work, we initially developed a benchmark device with a superstrate configuration (FTO/SnO_2/$SrZrS_3$/Cu-MOF/Ni) featuring a novel $SrZrS_3$ CP absorber and c-MOFs as HTLs for the first time, as depicted in Fig. 1(a). Profoundly, in the context of solar cell devices, light penetrates through FTO and traverses the ETL (SnO_2) to reach the absorber. Owing to the built-in potential (V_b) in the p-n junction, charge carriers are generated, segregated, and collected at their respective contacts. The initial parameters for simulating each layer of the solar cell are outlined in Table 1 and were obtained entirely from existing literature. Table 1 provides values for d, E_g, χ, ε_r, N_c, N_v, μ_n, μ_p, N_D, N_A, and N_T representing thickness, bandgap, electron affinity, dielectric permittivity, effective density of states in the conduction band, effective density of states in the valence band, electron mobility, hole mobility, donor concentration, acceptor concentration, defect density, respectively. The thermal velocity of electrons and holes was consistently set at 10^7 cm/s across all layers, and a flat band condition was applied on the front contact. The simulations were conducted under AM 1.5G spectral irradiance at a temperature of 300 K. Additionally, neutral defects were incorporated at the interfaces of SnO_2/$SrZrS_3$ and $SrZrS_3$/HTL to emulate accurate conditions of SCs, following the specifications detailed in Table 2.

Herein, the device structure, as illustrated in Fig. 5(a), was initially used to simulate the first solar cell device. Afterward, the study focused on investigating the properties of each layer by varying material parameters such as d, χ, N_D, N_A, and N_T. As a result, the solar cell parameters, including V_{OC}, J_{SC}, FF, and PCE, were obtained. After optimizing each layer in the initial device, the study delved into the impact on the PCE of diverse c-MOFs as HTLs. Following this, the analysis explored the impact of back contact by adjusting the back metal work function (BMWF) from 4.5 eV to 5.7 eV. Finally, among 193 devices, the one with the highest PCE was selected, and their performances were examined by varying defect density in the ETL/absorber and absorber/HTL interface, series resistance (R_S), shunt resistance (R_{Sh}), and

operating temperature (10^{10} to 10^{20} cm^{-3}, 1 to 10 Ω cm^2, 10 to 10^7 Ω cm^2, and 300 to 400 K, respectively). The material properties were elucidated using J-V, C-V, QE, Nyquist plot, Mott Schottky, and generation/recombination profiles from SCAPS-1D.

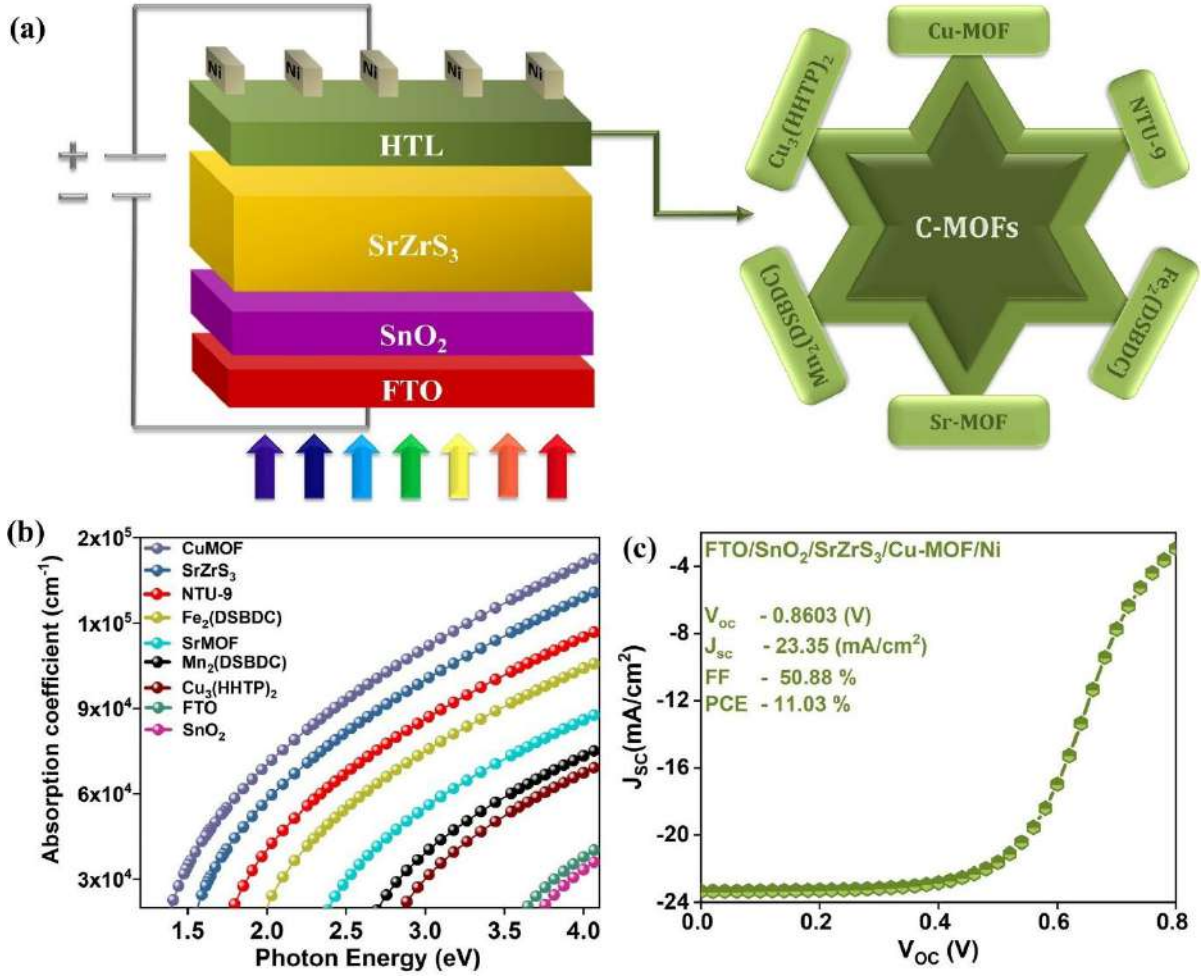

Fig. 5. (a) Solar cell structure with varying c-MOFs as HTL, (b) absorption coefficient, and (c) Initial J-V characteristics of novel $SrZrS_3$ solar cell with Cu-MOF as HTL.

Table 1. Input parameters of different layers of novel $SrZrS_3$ solar cell with c-MOFs as HTL [55,66,71–76,123–125,177,178].

Parameter	FTO	SnO_2	$SrZrS_3$	Hole Transport Layers					
				Cu-MOF	NTU-9	Fe_2(DSBDC)	Sr-MOF	Mn_2(DSBDC)	Cu_3(HHTP)$_2$
d (µm)	0.05	0.02	0.4	0.06	0.04	0.06	0.04	0.07	0.04
E_g (eV)	3.5	3.6	1.52	1.34	1.72	1.92	2.3	2.6	2.85
χ (eV)	4	3.9	4.3	4	3.8	3.6	3.4	2.5	2.8
ε_r	9	9	9.6	9.2	8	9	9.8	10	9.6

N_C (cm^{-3})	2.20E+18	2.20E+18	2.20E+18	1.00E+18	1.00E+20	1.00E+18	1.00E+20	1.80E+18	1.00E+20
N_V (cm^{-3})	1.80E+19	2.20E+19	1.80E+19	6.15E+18	6.15E+20	6.15E+19	6.15E+21	9.15E+19	6.15E+20
μ_n (cm^2/ Vs)	2.00E+01	1.00E+02	1.88E+01	1.00E+07	5.00E+01	1.00E+07	1.00E+07	1.00E+07	1.00E+07
μ_h (cm^2/ Vs)	1.00E+01	2.50E+01	6.81E+00	1.00E+07	2.00E+04	8.00E+02	1.00E+02	1.00E+02	8.00E-01
N_A (cm^{-3})	1.00E+18	1.00E+14	0	0	0	0	0	0	0
N_D (cm^{-3})	0	0	1.00E+14	1.00E+13	1.00E+16	1.00E+14	1.00E+15	1.00E+14	1.00E+16
N_t (cm^{-3})	1.00E+15	1.00E+16	1.00E+16	1.00E+17	1.00E+15	1.00E+16	1.00E+14	1.00E+15	1.00E+14

Table 2. SCAPS-1D simulation parameters at the SnO_2/$SrZrS_3$ and $SrZrS_3$/Cu-MOF interface.

Parameters	**SnO_2/$SrZrS_3$ interface**	**$SrZrS_3$/Cu-MOF interface**
Defect density (cm^{-3})	1.00E+10	1.00E+11
Defect type	Neutral	Neutral
Capture cross section for electrons (cm^2)	1.00E-19	1.00E-19
Capture cross-section for holes (cm^2)	1.00E-19	1.00E-19
Energetic distribution	Single	Single
Energy level with respect to valence band maximum (eV)	0.600	0.600

5.1.2. Modeling and Device Engineering of Eco-Friendly $BaZr_{0.96}Ti_{0.04}S_3$ CP SCs

To investigate the performance of $BaZr_{0.96}Ti_{0.04}S_3$ SCs concerning diverse MPc (as ZnPc, NiPc, and CuPc) HTLs at 300 K under AM 1.5G (100 mW/cm^2, one sun) spectral irradiance. The initial devices (Fig. 6) were configured with a structure FTO/SnO_2/$BaZr_{0.96}Ti_{0.04}S_3$/MPc/C,

utilizing the input parameters provided in Table 3, and the achieved PCEs are shown in Table 4. Later, the absorber properties, including N_A (10^{12} to 10^{20} cm^{-3}), N_T (10^{12} to 10^{20} cm^{-3}), and thickness (100 to 800 nm), were tuned. Further, HTL properties such as thickness (40-200 nm), χ for CuPc (3.3-3.6 eV), NiPc (2.8-3.1 eV), ZnPc (3.8-4.1 eV), and N_A (10^{12} to 10^{20} cm^{-3}) were optimized. The study aims to investigate the performance of $BaZr_{0.96}Ti_{0.04}S_3$ SCs with various metal phthalocyanine (MPc) HTLs, specifically Zinc Phthalocyanine (ZnPc), Nickel Phthalocyanine (NiPc), and Copper Phthalocyanine (CuPc). All experiments were conducted at a constant temperature of 300 K under standard solar illumination conditions, simulating AM 1.5G spectral irradiance at an intensity of 100 mW/cm², equivalent to one sun. The initial device configurations were established using the input parameters detailed in Table 3, which outlines the foundational characteristics of the SCs. The performance metrics, particularly the PCEs, are compiled in Table 4, providing a clear depiction of the efficiency gains associated with each HTL material. Following the initial assessment, several absorber properties were systematically varied to evaluate their influence on solar cell performance. Key parameters included the electron concentration (N_A) and trap concentration (N_T), both ranging from 10^{12} to 10^{20} cm^{-3}, alongside the absorber thickness, which was adjusted between 100 nm and 800 nm. Additionally, the properties of the HTLs were also optimized. The thickness of the HTLs was methodically tailored within a range of 40 nm to 200 nm. The work function (χ) of the different MPcs was scrutinized, revealing values for CuPc ranging from 3.3 to 3.6 eV, NiPc from 2.8 to 3.1 eV, and ZnPc from 3.8 to 4.1 eV. Furthermore, the electron concentration for each HTL was similarly optimized within the range of 10^{12} to 10^{20} cm^{-3}.

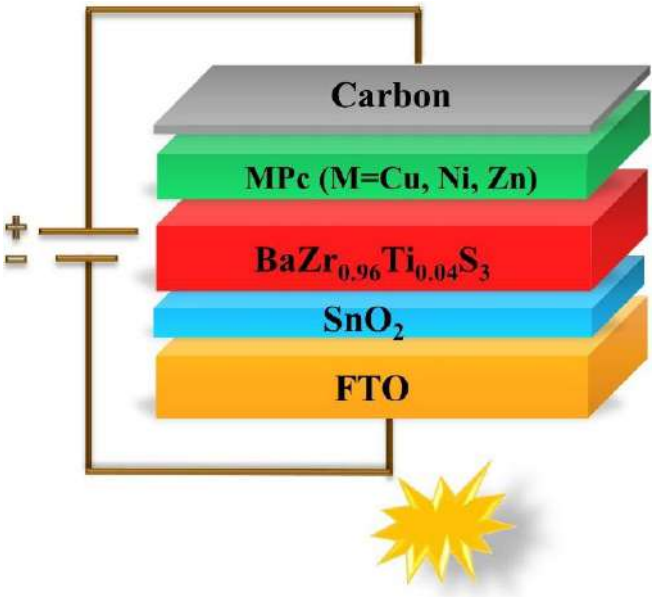

Fig. 6. $BaZr_{0.96}Ti_{0.04}S_3$ device structure with varying MPcs as HTL.

Table 3. Input parameters for the initial device.

Parameter	FTO	SnO_2	$BaZr_{0.96}Ti_{0.04}S_3$	Hole Transport Layers		
				CuPc	NiPc	ZnPc
Thickness (μm)	0.200	0.020	0.300	0.160	0.120	0.120
E_g (eV)	3.5	3.6	1.51	1.70	2.2	1.39
χ (eV)	4	3.9	4.37	3.5	3	3.9
ε_r	9	9	9.6	9.2	6.392	3.5
N_C (cm^{-3})	2.20E+18	2.20E+18	2.20E+18	1.00E+19	1.00E+19	1.00E+19
N_V (cm^{-3})	1.80E+19	2.20E+19	1.80E+19	1.00E+19	6.15E+19	9.13E+19
μ_n (cm^2/Vs)	2.00E+01	1.00E+02	16.8	2.00E-06	3.00E+01	1.00E+05
μ_h (cm^2/Vs)	1.00E+01	2.50E+01	2.6	5.00E-03	1.00E-01	7.60E-05
N_A (cm^{-3})	1.00E+18	1.00E+18	0	0	0	0
N_D (cm^{-3})	0	0	1.00E+14	1.00E+13	9.00E+16	9.00E+14
N_t (cm^{-3})	1.00E+15	1.00E+13	1.00E+16	1.00E+17	1.50E+15	1.00E+15
References	[1]	[1]	[2]	[3,4]	[4,5]	[6]

Table 4. Obtained PV parameters of initial devices.

S.No.	Initial Devices	V_{OC} (V)	J_{SC} (mA/cm^{-2})	FF (%)	PCE (%)
1	$FTO/SnO_2/BaZr_{0.96}Ti_{0.04}S_3/CuPc/C$	1.0722	13.84	82.02	12.17
2	$FTO/SnO_2/BaZr_{0.96}Ti_{0.04}S_3/NiPc/C$	0.9353	22.21	64.01	13.30
3	$FTO/SnO_2/BaZr_{0.96}Ti_{0.04}S_3/ZnPc/C$	0.9607	23.59	63.91	14.49

5.2 Experimental Section

5.2.1. Chemicals and Reagents

Indium (III) chloride (In_2Cl_3 98%), magnesium chloride ($MgCl_2$- 99.9%), calcium chloride dihydrate ($CaCl_2.2H_2O$), strontium chloride hexahydrate ($SrCl_2.6H_2O$), ethylenediaminetetraacetic acid tetrasodium salt dihydrate (EDTA-2Na 98.5%), isopropanol

(C_3H_8O 70% in H_2O), 1,4-benzoquinone (≥98%), oleylamine (technical grade 70%), triethanolamine (TEOA ≥99.0 %), NaOH solution (98 %), sodium sulfide (Na_2S, 98.0 %), and sodium sulfate (Na_2SO_4, 99.0%), were purchased from Sigma-Aldrich. Sulfur powder (precipitated, 99.5%) was ordered from Thermo Scientific Chemicals. Lactic acid (LA, 85%), methanol (Absolute, 99.8%), ethanol (Absolute, 99.8%), and chloroform (≥99.8%, containing about 1% ethanol as a preservative) were brought from J.T. Baker. 2,4-D ($C_8H_6Cl_2O_3$, 98%) was purchased from Alfa Aesar. All chemicals were used as received without further purification.

5.2.2. Characterization Techniques

The crystal structure and orientation of the samples were investigated by X-ray diffraction (XRD; Smart Lab, RIGAKU) using Cu-Kα radiation (λ = 1.5406 Å) with a step size of 0.04° at 20 mA and 45 kV. Raman microscopy (DXR3, Thermo Scientific) was used to obtain Raman spectra of the samples at room temperature (RT) with an excitation wavelength of 546 nm. Field emission scanning electron microscopy (FESEM) images were recorded using a JSM-7401F (JEOL) instrument at an operating voltage of 5 kV. The chemical composition of the samples was analyzed by energy dispersive X-ray spectroscopy (EDS) at 6 kV using an XFlash 5010 detector (BRUKER) coupled with FESEM. The morphology and size of the particles were assured using HRTEM (JEM-ARM200F) analysis with an accelerating voltage of 200kV. The samples were prepared by drop casting the samples dispersed in ethanol on a 200-mesh nickel grid (Ted Pella, Inc). The optical properties of the samples were determined using a Shimadzu UV2450 UV-Vis spectrophotometer at RT. UV-Vis absorption spectra were obtained by dispersing ~0.05 mg of the samples in 2 ml hexane thiol via sonication for 3 min at 25 Hz. Photoluminescence (PL) spectra were recorded at room temperature using an excitation wavelength of 300 nm. The chemical state, bonding environment, and the position of the valence band maximum (VBM) were determined using X-ray photoelectron spectroscopy (XPS) using a Thermo Scientific K-Alpha spectrometer supplied with a monochromatic Al Kα X-ray source (1486.6 eV). All spectra were calibrated using the C 1s reference peak at 284.8 eV to account for any charging effects. The specific surface area was analyzed using N_2 adsorption/desorption isotherms with a Quantachrome NOVA 4200e instrument. Before the analysis, the samples were degassed at 120°C for 10 hours under liquid nitrogen at 200°C. Electrochemical impedance spectroscopy (EIS) measurements were conducted over a frequency range of 10 MHz to 100 kHz, with an applied amplitude of 10 mV, to obtain the electrical measurements. Electrochemical tests were conducted in a three-

electrode system, with a Pt sheet serving as the counter electrode, an Ag/AgCl electrode as the reference electrode, and the prepared samples as the working electrodes. 0.1 M Na_2SO_4 solution was employed as an electrolyte. Hall measurements were conducted to determine the electrical properties, including the carrier concentration, mobility, and resistivity. Typically, these measurements were carried out using a Van Der Pauw configuration with a magnetic field of 5000 G and an applied current of 5×10^{-4} A in a typical Hall measurement setup.

5.2.3. Synthesize phase-pure γ-In_2S_3 and its Mg, Ca, and Sr doped counterparts

In our experiment, pure γ-In_2S_3 and its Mg, Ca, and Sr doped variants were synthesized using a simple one-pot heating-up method, as shown in Fig. 7. Following a procedure similar to our previous work, 2 mmol of $InCl_3$, 3 mmol of elemental sulfur, and 20 ml of oleylamine were placed in a three-neck round-bottom flask under an N_2 atmosphere. The reaction was conducted at 200°C for 2 hours with continuous stirring. During the process, the solution underwent a rapid color change from transparent brown to colloidal bright yellow, indicating the successful formation of pure γ-In_2S_3. The reaction was then terminated, and the mixture was purified and dried. Further, to synthesize Mg, Ca, and Sr doped γ-In_2S_3, the same procedure was followed by adding 2 at % of $MgCl_2$, $CaCl_2.2H_2O$, and $SrCl_2.6H_2O$, respectively. The respective samples were labeled as Mg: γ-In_2S_3, Ca: γ-In_2S_3, and Sr: γ-In_2S_3. The optical images of these synthesized materials are depicted in Fig. 7.

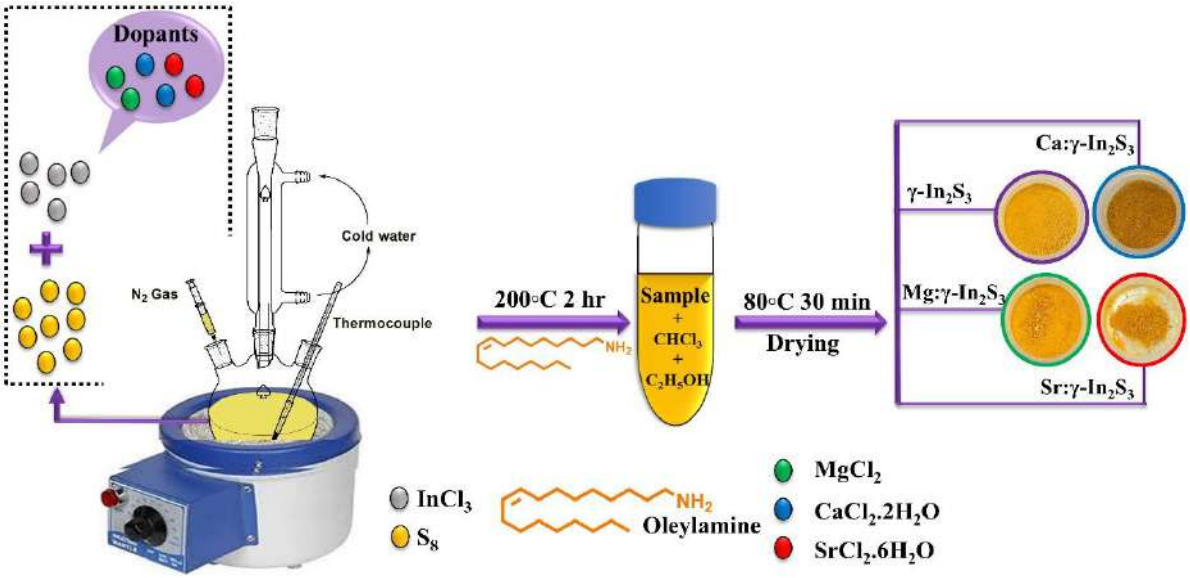

Fig. 7. Schematic illustration of the synthesis methodology of pure γ-In_2S_3 and its doped variants.

5.2.4. Photocatalytic H_2 Evolutions

In a typical experiment, 25 mg of pure γ-In_2S_3 was dispersed in 100 mL of an aqueous solution containing 20% triethanolamine (TEOA) as a sacrificial agent. This dispersion was transferred to a Pyrex glass reactor, where it was purged with ultrapure argon (Ar) gas for at least 20 minutes to remove any residual air. Prior to initiating the photocatalytic reaction, a 300 W Xe lamp with a 420 nm cut-off filter was preheated for 30 minutes to stabilize the light output. During the reaction, the temperature of the solution was maintained at 5°C using a cooling water circulation system, while a magnetic stirrer positioned beneath the reaction cell ensured consistent dispersion of the photocatalyst. The H_2 produced was analyzed every 30 minutes over a total reaction time of 240 minutes, using a gas chromatograph (Gow-Mac 580) equipped with a molecular sieve 5Å column, a thermal conductivity detector (TCD), and high-purity Ar as the carrier gas. The same procedure was applied for the photocatalytic H_2 evolution using Mg: γ-In_2S_3, Ca: γ-In_2S_3, and Sr: γ-In_2S_3. With the best-performing sample, the apparent quantum yield (AQY) and solar-to-hydrogen (STH) conversion were determined using equations 1 and 3 with a 300 W Xe lamp as the light source. Experiments were conducted at 5 °C under monochromatic irradiation at different wavelengths (λ = 400, 420, 450, 500, 550, and 600 nm, each with a ±15 nm bandpass). The photon flux at each wavelength was determined using an optical power meter. Illumination was provided over a circular area of 34.5 cm² (radius = 3.24 cm). All reported AQY values were derived from the average of four independent measurements, with standard deviations used to estimate the experimental error.

AQY was measured according to the following equation (Eq. 1):

$$AQY\ (\%) = \frac{2 \times the\ number\ of\ evolved\ H_2\ molecules}{the\ number\ of\ incident\ photons} \times 100\% \qquad (1)$$

The number of incident photons was obtained according to:

$$N = \frac{IAt\lambda}{hc}\% \qquad (2)$$

where I is the incident light intensity, A is the illuminated surface area (3.45×10^{-3} m^2), t is the irradiation time, λ is the excitation wavelength, h is Planck's constant, and c is the speed of light.

The STH efficiency was calculated using the following formula (Eq. 3):

$$\mathrm{STH\%} = \frac{\text{Hydrogen evolution rate(mol/s)}}{\text{Incident optical density } (\mathrm{mW/cm^2})} \times 100\% \quad (3)$$

Furthermore, for scavenging tests, the TEOA was replaced with other hole scavengers: 0.25 M Na_2S/0.35 M Na_2SO_3, 20% lactic acid (LA), and 20% methanol (MeOH). Additionally, cyclic experiments were performed to assess the stability of H_2 evolution. After each cycle, the photocatalyst was thoroughly washed and dried, and the system was purged with Ar for 20 minutes to remove any dissolved gases before being reused for up to five cycles.

5.2.5. Photocatalytic 2.4-D Degradation

To evaluate the photocatalytic performance of the samples, we conducted a series of experiments focused on the degradation of 2,4-D in an aqueous solution under simulated solar conditions. The experiments were carried out using a 300 W xenon lamp equipped with a D65 filter, which simulates the full spectrum of solar UV-Vis radiation. The experimental setup featured a closed system, where a 300W xenon lamp focused on a securely clamped quartz tube. In the experimental procedure, we initially suspended 30 mg of pure γ-In_2S_3 in a cylindrical quartz tube containing 60 ml of a 2,4-D solution with an initial concentration of 40 ppm. To ensure proper adsorption-desorption equilibrium, the suspension was continuously stirred in darkness for 60 minutes. After achieving equilibrium, the light irradiation was commenced. During the light exposure, 3 ml aliquots of the solution were periodically withdrawn using a syringe equipped with a micropore filter. These aliquots were then centrifuged for 10 minutes at 4500 rpm to remove any photocatalyst particles that could interfere with subsequent absorbance measurements. The degradation of 2,4-D in the presence of pure γ-In_2S_3 under UV-Vis light was monitored by tracking changes in the absorbance intensity of characteristic peaks specific to 2,4-D. Additional experiments were conducted following the same methodology, with targeted modifications to examine various factors influencing photocatalytic degradation efficiency. Initially, we evaluated the photocatalytic performance of pure γ-In_2S_3 after doping it with Mg^{2+}, Ca^{2+}, and Sr^{2+}. Then, using the best-performing photocatalyst among the doped variants, along with pure γ-In_2S_3, an additional set of experiments was conducted under varying conditions, as mentioned below. Herein, the inclusion of the undoped catalyst under identical conditions served as a control, enabling a direct background comparison and validation of the intrinsic activity of the doped material. Moreover, all photocatalytic degradation efficiencies were calculated as the average of four independent experiments conducted under identical conditions, with standard deviations used to estimate the experimental error.

Initially, the investigation of the involvement of different reactive species in the photocatalytic process was conducted by introducing specific scavengers. Isopropanol (IP) was employed to neutralize hydroxyl radicals (•OH), benzoquinone (BZ) was used for superoxide radicals ($O_2^{\bullet-}$), and ethylenediaminetetraacetic acid disodium salt (EDTA-2Na) targeted holes (h^+), all at a concentration of 5 mM. Following this, we explored the effect of varying the dosage of the optimal photocatalyst on degradation efficiency, with amounts ranging from 20 to 50 mg. Additionally, the influence of different initial concentrations of 2,4-D on the degradation process was assessed using concentrations of 40, 60, and 80 ppm. The impact of the solution's pH on photocatalytic degradation was also examined by adjusting the pH to 1, 3, 5, 7, 9, and 11 using 0.1 M HCl and 0.1 M NaOH solutions. Lastly, the reusability of the best-performing photocatalyst was evaluated over four cycles under optimal conditions. After each cycle, the catalyst was extracted, rinsed with distilled water, and dried at 70°C under vacuum in preparation for subsequent use.

The degradation efficiency (η) for the whole set of experiments was finally determined using Eqn. (4) [107].

$$\eta = \left\{1 - \left(\frac{C_t}{C_0}\right)\right\} \times 100\% \qquad (4)$$

Here, C_0 (mg/L) represents the initial 2,4-D concentration, while C_t denotes the concentration at time t.

6. Results and Discussion

6.1. Role of Conductive Metal-Organic Framework-based HTLs and Back Contacts Engineering in $SrZrS_3$ SCs

This section presents the thorough simulation results addressing **Objectives 1 and 2**. **Sections 5.1.1, 6.1.1, and 6.1.2** describe the baseline device performance and optimization limits owing to absorber and charge transport layers via parametric modulations. **Section 6.1.3** provides an in-depth analysis of the $SrZrS_3$ absorber layer, while **Sections 6.1.4 to 6.1.5** evaluate the PV characteristics of the Cu-MOF-based HTL. **Section 6.1.6** extends this analysis to diverse conductive MOF-based HTLs. Subsequently, **Sections 6.1.7 to 6.1.9** explore the mechanistic insights behind performance enhancement by comparing initial and optimized devices using the Nyquist Plot, QE spectra, and energy band alignment analysis. **Sections 6.1.10 to 6.1.12** further investigate the influence of various metal back contacts, interface properties, parasitic

resistances, and operating temperature on device performance. Finally, **Section 6.1.13** discusses the comparison of optimized device performance with existing literature reports, highlighting the advancements achieved through the proposed design and optimization strategies.

6.1.1. Baseline Device Performance

In pursuit of understanding the synergistic effects of c-MOFs employed as HTL and novel CP as an absorber, we formulated an initial device structure denoted as FTO/SnO_2/$SrZrS_3$/Cu-MOF/Ni, illustrated in Fig. 3(a). Subsequently, Fig. 3(b) depicts the absorption coefficients (α) across photon energies within layers, including FTO, ETL, absorbers, and MOF-based HTLs obtained from SCAPS 1D simulation software. In the realm of solar cell technology, the α of a material denotes its effectiveness in capturing light, a critical aspect of enhancing PCE. Therefore, a heightened α is eagerly pursued for superior performance in solar cell applications [82,117]. The internal absorption model in SCAPS-1D employs the algebraic expression, $\sqrt{h\nu - E_g}$ [117]. Interestingly, from Fig. 3(b), $SrZrS_3$ displayed a prominent peak in the band-edge region, surpassing 10^5 cm^{-1}, indicating its significant light absorption ability, which aligned with prior research findings. Similarly, within the realm of MOFs, Cu-MOF displayed a conspicuous peak preceding the absorber, attributable to its narrower bandgap of 1.3 eV. This reveals that materials with narrower band gaps inherently exhibit greater capacity for photon absorption compared to those with wider band gaps [179]. Simulations, based on parameters from Table 1, yielded J-V characteristics and PV parameters depicted in Fig. 3(c), revealing an initial PCE of 11.03%. To further enhance performance, we systematically optimized the electron affinity, carrier concentration, defect density, and thickness of the ETL, absorber, and HTL properties, detailed in the following sections.

6.1.2. Parametric optimization of ETL, Absorber, and HTL: Influence of Electron Affinity, Carrier Concentration, Defect Density, and Thickness

The ETL and HTL are widely acknowledged for their requisite functions in PSCs. They efficiently transport photo-generated charge carriers from the absorber to their contacts while acting as barriers against electrons and holes. This study employed 6 HTLs (Cu-MOF, NTU-9, Fe_2(DSBDC), Sr-MOF, Mn_2(DSBDC), and $Cu_3(HHTP)_2$, SnO_2 ETL, and $SrZrS_3$ CP absorber to optimize the SC structures' PV outputs. Initial optimization of SnO_2 ETL involved fine-tuning parameters like electron affinity, carrier concentration, defect density, and thickness. Noteworthy is the absence of significant changes in the PV parameters for ETL

(Table 5). Then, we optimized the absorber as it is crucial for SC performance, so we explored its influence by tuning carrier concentration (10^{12} cm^{-3} to 10^{20} cm^{-3}), defect density (10^{12} cm^{-3} to 10^{18} cm^{-3}), and thickness (100 nm to 1000 nm) as presented in Table 6. Followed by the optimization of HTL, similarly varying electron affinity (3.7 eV to 3.85 eV), carrier concentration (10^{14} cm^{-3} to 10^{20} cm^{-3}), defect density (10^{12} cm^{-3} to 10^{20} cm^{-3}), and thickness (40 nm to 200 nm) systematically, as illustrated in Table 7. The outcomes of these comprehensive optimizations are elucidated in the subsequent sections.

Table 5: Optimization of ETL's thickness, defect density, and carrier concentration.

ETL optimization (SnO_2)						
Parameters	**Range**	**Voc (V)**	**Jsc (mA/cm^2)**	**FF (%)**	**PCE (%)**	
Thickness (nm)	10	0.8639	23.35	55.78	11.25	Cu-MOF:1
	20	0.8640	23.34	55.80	11.25	Cu-MOF:2
	30	0.8640	23.32	55.80	11.24	Cu-MOF:3
	40	0.8640	23.32	55.80	11.24	Cu-MOF:4
	50	0.8640	23.31	55.80	11.24	Cu-MOF:5
	60	0.8639	23.31	55.80	11.24	Cu-MOF:6
	70	0.8639	23.31	55.80	11.24	Cu-MOF:7
	80	0.8639	23.30	55.80	11.23	Cu-MOF:8
	90	0.8639	23.30	55.80	11.23	Cu-MOF:9
	100	0.8639	23.30	55.80	11.23	Cu-MOF:10
Defect Density N_T (cm^{-3})	10^{12}	0.8640	23.34	55.80	11.25	Cu-MOF:11
	10^{13}	0.8640	23.34	55.80	11.25	Cu-MOF:12
	10^{14}	0.8640	23.34	55.80	11.25	Cu-MOF:13
	10^{15}	0.8640	23.34	55.80	11.25	Cu-MOF:14
	10^{16}	0.8640	23.34	55.80	11.25	Cu-MOF:15
	10^{17}	0.8640	23.34	55.80	11.25	Cu-MOF:16
	10^{18}	0.8640	23.34	55.80	11.25	Cu-MOF:17
Carrier Concentration N_A (cm^{-3})	10^{12}	0.8628	23.36	55.56	11.20	Cu-MOF:18
	10^{13}	0.8628	23.36	55.56	11.20	Cu-MOF:19
	10^{14}	0.8628	23.36	55.56	11.20	Cu-MOF:20
	10^{15}	0.8628	23.36	55.56	11.20	Cu-MOF:21
	10^{16}	0.8628	23.36	55.57	11.20	Cu-MOF:22

	10^{17}	0.8632	23.36	55.64	11.22	Cu-MOF:23
	10^{18}	0.8640	23.34	55.80	11.25	Cu-MOF:24
	10^{19}	0.8642	23.31	55.85	11.25	Cu-MOF:25
	10^{20}	0.8643	23.31	55.87	11.25	Cu-MOF:26

Table 6: Optimization of absorber's carrier concentration, defect density, and thickness.

Absorber Optimization ($SrZrS_3$)						
Parameters	**Range**	**Voc (V)**	**Jsc (mA/cm^2)**	**FF (%)**	**PCE (%)**	
Carrier Concentration N_A (cm^{-3})	10^{12}	0.8641	23.34	55.78	11.25	Cu-MOF:27
	10^{13}	0.8641	23.34	55.79	11.25	Cu-MOF:28
	10^{14}	0.8640	23.34	55.80	11.25	Cu-MOF:29
	10^{15}	0.8629	23.34	56.00	11.28	Cu-MOF:30
	10^{16}	0.8687	23.35	61.69	12.52	Cu-MOF:31
	10^{17}	0.9185	20.29	73.51	13.70	Cu-MOF:32
	10^{18}	0.9926	14.98	81.22	12.08	Cu-MOF:33
	10^{19}	1.1242	13.61	65.11	9.96	Cu-MOF:34
	10^{20}	1.2217	6.26	57.20	4.38	Cu-MOF:35
Defect Density N_T (cm^{-3})	10^{12}	0.9378	23.42	83.22	18.28	Cu-MOF:36
	10^{13}	0.9377	23.42	83.11	18.25	Cu-MOF:37
	10^{14}	0.9361	23.41	81.99	17.97	Cu-MOF:38
	10^{15}	0.9240	23.41	73.90	15.98	Cu-MOF:39
	10^{16}	0.8641	23.34	55.78	11.25	Cu-MOF:40
	10^{17}	0.8510	22.62	47.83	9.21	Cu-MOF:41
	10^{18}	0.8432	14.16	46.96	5.96	Cu-MOF:42
Thickness (nm)	100	0.9253	16.24	82.59	12.41	Cu-MOF:43
	200	0.9337	20.82	83.05	16.15	Cu-MOF:44
	300	0.9378	23.42	83.22	18.28	Cu-MOF:45
	400	0.9401	24.96	83.30	19.55	Cu-MOF:46
	500	0.9413	25.93	83.34	20.34	Cu-MOF:47
	600	0.9421	26.56	83.36	20.86	Cu-MOF:48
	700	0.9427	26.99	83.37	21.21	Cu-MOF:49

	800	0.9430	27.29	83.36	21.46	Cu-MOF:50
	900	0.9433	27.51	83.35	21.63	Cu-MOF:51
	1000	0.9435	27.67	83.33	21.76	Cu-MOF:52

Table 7. Optimization of HTL's (Cu-MOF, NTU-9, Fe_2(DSBDC), Sr-MOF, Mn_2(DSBDC), and Cu_3(HHTP)$_2$) defect density, electron affinity, carrier concentration, and thickness

HTL 1 Optimization (Cu-MOF)						
Parameters	**Range**	**Voc (V)**	**Jsc (mA/cm^2)**	**FF (%)**	**PCE (%)**	
Defect Density N_T (cm^{-3})	10^{12}	0.9957	26.57	80.10	21.19	Cu-MOF:53
	10^{13}	0.9957	26.57	80.10	21.19	Cu-MOF:54
	10^{14}	0.9955	26.57	80.12	21.19	Cu-MOF:55
	10^{15}	0.9933	26.57	80.28	21.18	Cu-MOF:56
	10^{16}	0.9798	26.57	81.23	21.14	Cu-MOF:57
	10^{17}	0.9421	26.56	83.36	20.86	Cu-MOF:58
	10^{18}	0.8896	26.55	84.55	19.97	Cu-MOF:59
Electron Affinity (eV)	3.7	0.9957	26.57	80.10	21.19	Cu-MOF:60
	3.75	1.0457	26.57	80.78	22.44	Cu-MOF:61
	3.8	1.0955	26.56	81.42	23.69	Cu-MOF:62
	3.85	1.1447	26.56	82.05	24.95	Cu-MOF:63
Carrier Concentration N_A (cm^{-3})	10^{14}	1.1447	26.56	82.05	24.95	Cu-MOF:64
	10^{15}	1.1447	26.56	82.05	24.95	Cu-MOF:65
	10^{16}	1.1447	26.56	82.05	24.95	Cu-MOF:66
	10^{17}	1.1446	26.56	82.01	24.94	Cu-MOF:67
	10^{18}	1.1442	26.56	82.45	25.06	Cu-MOF:68
	10^{19}	1.1447	26.56	85.67	26.05	Cu-MOF:69
	10^{20}	1.1684	26.56	88.43	27.45	Cu-MOF:70
Thickness (nm)	40	1.1684	26.56	88.43	27.45	Cu-MOF:71
	80	1.1696	27.47	88.42	28.41	Cu-MOF:72
	120	1.1705	28.26	88.41	29.24	Cu-MOF:73
	160	1.1713	28.94	88.41	29.97	Cu-MOF:74
	200	1.1720	29.54	88.40	30.60	Cu-MOF:75
HTL 2 Optimization (NTU-9)						

Parameters	Range	Voc (V)	Jsc (mA/cm^2)	FF (%)	PCE (%)	
Defect Density N_T (cm^{-3})	10^{12}	1.2350	25.46	89.91	28.27	NTU-9: 1
	10^{13}	1.1540	22.34	88.55	22.82	NTU-9: 2
	10^{14}	1.1491	21.77	88.39	22.11	NTU-9: 3
	10^{15}	1.1473	21.54	88.31	21.82	NTU-9: 4
	10^{16}	1.1464	21.41	88.27	21.66	NTU-9: 5
	10^{17}	1.1458	21.32	88.25	21.56	NTU-9: 6
	10^{18}	1.1455	21.27	88.23	21.49	NTU-9: 7
Electron Affinity (eV)	3.75	1.2971	25.55	87.48	28.99	NTU-9: 8
	3.8	1.2350	25.46	89.91	28.27	NTU-9: 9
	3.85	1.1890	24.69	89.41	26.25	NTU-9: 10
	3.9	1.1551	22.46	88.59	22.99	NTU-9: 11
Carrier Concentration N_A (cm^{-3})	10^{14}	1.2971	25.55	87.48	28.99	NTU-9: 12
	10^{15}	1.2979	25.57	88.10	29.24	NTU-9: 13
	10^{16}	1.2986	25.58	88.42	29.37	NTU-9: 14
	10^{17}	1.2993	25.59	88.64	29.47	NTU-9: 15
	10^{18}	1.3000	25.59	88.81	29.55	NTU-9: 16
	10^{19}	1.3006	25.59	88.95	29.61	NTU-9: 17
	10^{20}	1.3011	25.60	89.06	29.66	NTU-9: 18
Thickness (nm)	40	1.3011	25.60	89.06	29.66	NTU-9: 19
	80	1.3012	25.66	89.06	29.74	NTU-9: 20
	120	1.3013	25.72	89.06	29.78	NTU-9: 21
	160	1.3013	25.76	89.06	29.78	NTU-9: 22
	200	1.3014	25.80	89.06	29.78	NTU-9: 23
HTL 3 Optimization (Fe_2(DSBDC))						
Parameters	**Range**	**Voc (V)**	**Jsc (mA/cm^2)**	**FF (%)**	**PCE (%)**	
Defect Density N_T (cm^{-3})	10^{12}	1.0723	25.54	81.21	22.24	Fe_2(DSBDC):1
	10^{13}	1.0723	25.54	81.21	22.24	Fe_2(DSBDC):2
	10^{14}	1.0723	25.54	81.21	22.24	Fe_2(DSBDC):3
	10^{15}	1.0723	25.54	81.21	22.24	Fe_2(DSBDC):4
	10^{16}	1.0723	25.54	81.21	22.24	Fe_2(DSBDC):5
	10^{17}	1.0723	25.54	81.21	22.24	Fe_2(DSBDC):6
	10^{18}	1.0723	25.54	81.21	22.24	Fe_2(DSBDC):7

Electron Affinity (eV)	3.2	1.0723	25.54	81.21	22.24	Fe_2(DSBDC):8
	3.25	1.1222	25.54	81.82	23.45	Fe_2(DSBDC):9
	3.3	1.1717	25.54	82.41	24.66	Fe_2(DSBDC):10
	3.35	1.2207	25.54	82.95	25.86	Fe_2(DSBDC):11
Carrier Concentration N_A (cm^{-3})	10^{14}	1.2207	25.54	82.95	25.86	Fe_2(DSBDC):12
	10^{15}	1.2207	25.54	82.95	25.86	Fe_2(DSBDC):13
	10^{16}	1.2207	25.54	82.96	25.87	Fe_2(DSBDC):14
	10^{17}	1.2207	25.54	83.01	25.88	Fe_2(DSBDC):15
	10^{18}	1.2211	25.54	83.72	26.11	Fe_2(DSBDC):16
	10^{19}	1.2251	25.54	86.33	27.01	Fe_2(DSBDC):17
	10^{20}	1.2491	25.54	88.50	28.23	Fe_2(DSBDC):18
Thickness (nm)	40	1.2491	25.54	88.50	28.23	Fe_2(DSBDC):19
	80	1.2491	25.57	88.50	28.26	Fe_2(DSBDC):20
	120	1.2491	25.59	88.50	28.29	Fe_2(DSBDC):21
	160	1.2491	25.61	88.50	28.31	Fe_2(DSBDC):22
	200	1.2492	25.62	88.50	28.33	Fe_2(DSBDC):23
HTL 4 Optimization (Sr-MOF)						
Parameters	**Range**	**Voc (V)**	**Jsc (mA/cm^2)**	**FF (%)**	**PCE (%)**	
Defect Density N_T (cm^{-3})	10^{12}	1.1325	25.52	81.93	23.68	Sr-MOF:1
	10^{13}	1.1325	25.52	81.93	23.68	Sr-MOF:2
	10^{14}	1.1325	25.52	81.93	23.68	Sr-MOF:3
	10^{15}	1.1325	25.52	81.92	23.68	Sr-MOF:4
	10^{16}	1.1325	25.52	81.92	23.68	Sr-MOF:5
	10^{17}	1.1325	25.52	81.92	23.68	Sr-MOF:6
	10^{18}	1.1325	25.52	81.92	23.68	Sr-MOF:7
Electron Affinity (eV)	2.95	1.0828	25.52	81.32	22.47	Sr-MOF:8
	3	1.1325	25.52	81.93	23.68	Sr-MOF:9
	3.05	1.1821	25.52	82.50	24.89	Sr-MOF:10
	3.1	1.2306	25.52	83.05	26.08	Sr-MOF:11
Carrier Concentration N_A (cm^{-3})	10^{14}	1.2306	25.52	83.06	26.08	Sr-MOF:12
	10^{15}	1.2306	25.52	83.06	26.08	Sr-MOF:13
	10^{16}	1.2306	25.52	83.06	26.08	Sr-MOF:14

	10^{17}	1.2306	25.52	83.09	26.09	Sr-MOF:15
	10^{18}	1.2307	25.52	83.76	26.31	Sr-MOF:16
	10^{19}	1.2340	25.52	86.45	27.22	Sr-MOF:17
	10^{20}	1.2583	25.52	88.53	28.43	Sr-MOF:18
Thickness (nm)	40	1.2583	25.52	88.53	28.43	Sr-MOF:19
	80	1.2583	25.52	88.53	28.43	Sr-MOF:20
	120	1.2583	25.53	88.53	28.44	Sr-MOF:21
	160	1.2583	25.53	88.53	28.44	Sr-MOF:22
	200	1.2583	25.54	88.53	28.45	Sr-MOF:23
HTL 5 Optimization (Mn_2(DSBDC)						
Parameters	**Range**	**Voc (V)**	**Jsc (mA/cm^2)**	**FF (%)**	**PCE (%)**	
Defect Density N_T (cm^{-3})	10^{12}	1.0520	25.52	80.94	21.72	Mn_2(DSBDC):1
	10^{13}	1.0520	25.52	80.94	21.72	Mn_2(DSBDC):2
	10^{14}	1.0520	25.52	80.94	21.72	Mn_2(DSBDC):3
	10^{15}	1.0520	25.52	80.94	21.72	Mn_2(DSBDC):4
	10^{16}	1.0520	25.52	80.94	21.72	Mn_2(DSBDC):5
	10^{17}	1.0520	25.52	80.94	21.72	Mn_2(DSBDC):6
	10^{18}	1.0520	25.52	80.94	21.72	Mn_2(DSBDC):7
Electron Affinity (eV)	2.5	1.0520	25.52	80.94	21.73	Mn_2(DSBDC):8
	2.55	1.1020	25.52	81.55	22.93	Mn_2(DSBDC):9
	2.6	1.1516	25.52	82.16	24.14	Mn_2(DSBDC):10
	2.65	1.2010	25.52	82.71	25.35	Mn_2(DSBDC):11
	2.7	1.2488	25.52	83.25	26.53	Mn_2(DSBDC):12
Carrier Concentration N_A (cm^{-3})	10^{14}	1.2488	25.52	83.25	26.53	Mn_2(DSBDC):13
	10^{15}	1.2488	25.52	83.25	26.53	Mn_2(DSBDC):14
	10^{16}	1.2488	25.52	83.25	26.53	Mn_2(DSBDC):15
	10^{17}	1.2488	25.52	83.28	26.54	Mn_2(DSBDC):16
	10^{18}	1.2489	25.52	83.95	26.75	Mn_2(DSBDC):17
	10^{19}	1.2521	25.51	86.57	27.66	Mn_2(DSBDC):18
	10^{20}	1.2762	25.51	88.45	28.80	Mn_2(DSBDC):19
Thickness (nm)	40	1.2762	25.51	88.45	28.80	Mn_2(DSBDC):20
	80	1.2762	25.52	88.45	28.80	Mn_2(DSBDC):21

	120	1.2762	25.52	88.45	28.80	Mn_2(DSBDC):22
	160	1.2762	25.52	88.45	28.80	Mn_2(DSBDC):23
	200	1.2762	25.52	88.45	28.80	Mn_2(DSBDC):24
HTL 6 Optimization ($Cu_3(HHTP)_2$)						
Parameters	**Range**	**Voc (V)**	**Jsc (mA/cm^2)**	**FF (%)**	**PCE (%)**	
Defect Density N_T (cm^{-3})	10^{12}	1.0425	25.52	80.81	21.50	$Cu_3(HHTP)_2$:1
	10^{13}	1.0425	25.52	80.81	21.50	$Cu_3(HHTP)_2$:2
	10^{14}	1.0425	25.52	80.81	21.50	$Cu_3(HHTP)_2$:3
	10^{15}	1.0425	25.52	80.81	21.50	$Cu_3(HHTP)_2$:4
	10^{16}	1.0425	25.52	80.81	21.50	$Cu_3(HHTP)_2$:5
	10^{17}	1.0425	25.52	80.81	21.50	$Cu_3(HHTP)_2$:6
	10^{18}	1.0425	25.52	80.81	21.50	$Cu_3(HHTP)_2$:7
Electron Affinity (eV)	2.25	0.9924	25.52	80.14	20.29	$Cu_3(HHTP)_2$:8
	2.3	1.0425	25.52	80.81	21.50	$Cu_3(HHTP)_2$:9
	2.35	1.0923	25.51	81.45	22.70	$Cu_3(HHTP)_2$:10
	2.4	1.1422	25.51	82.05	23.91	$Cu_3(HHTP)_2$:11
	2.45	1.1914	25.51	82.63	25.12	$Cu_3(HHTP)_2$:12
	2.5	1.2399	25.51	83.15	26.30	$Cu_3(HHTP)_2$:13
Carrier Concentration N_A (cm^{-3})	10^{14}	1.2399	25.51	83.15	26.30	$Cu_3(HHTP)_2$:14
	10^{15}	1.2399	25.51	83.15	26.31	$Cu_3(HHTP)_2$:15
	10^{16}	1.2399	25.51	83.15	26.31	$Cu_3(HHTP)_2$:16
	10^{17}	1.2399	25.51	83.20	26.32	$Cu_3(HHTP)_2$:17
	10^{18}	1.2402	25.51	83.88	26.54	$Cu_3(HHTP)_2$:18
	10^{19}	1.2438	25.51	86.49	27.45	$Cu_3(HHTP)_2$:19
	10^{20}	1.2677	25.51	88.48	28.62	$Cu_3(HHTP)_2$:20
Thickness (nm)	40	1.2677	25.51	88.48	28.62	$Cu_3(HHTP)_2$:21
	80	1.2677	25.51	88.48	28.62	$Cu_3(HHTP)_2$:22
	120	1.2677	25.51	88.48	28.62	$Cu_3(HHTP)_2$:23
	160	1.2677	25.51	88.48	28.62	$Cu_3(HHTP)_2$:24
	200	1.2677	25.51	88.48	28.62	$Cu_3(HHTP)_2$:25

6.1.3. Optimization of Absorber Carrier concentration, Defect density, and Thickness

Absorber carrier concentration significantly impacts SCs' electrical conductivity, charge separation efficiency, and stability. It is necessary to pinpoint the optimal carrier concentration of the absorber to achieve outstanding solar cell performance. In this study, the carrier concentration in $SrZrS_3$ was systematically varied from 10^{12} cm^{-3} to 10^{20} cm^{-3}, and the corresponding variations in V_{OC}, J_{SC}, FF, and PCE are illustrated in Fig. 8(a) and (b). Notably, both V_{OC} and J_{SC} exhibited relative constancy up to 10^{16} cm^{-3}. Beyond this range, V_{OC} showed an increasing trend, while J_{SC} exhibited a decreasing trend. On the other hand, both the FF and PCE remained consistent from 10^{12} cm^{-3} to 10^{15} cm^{-3}. Subsequently, FF increased up to 10^{17} cm^{-3}, while PCE increased up to 10^{18} cm^{-3}, and then both decreased further. Here, the improvement in V_{OC} can be attributed to the enhanced V_b of the device, as shown in the Mott-Schottky plots (Fig. 8(c)) [30]. Specifically, V_b increased from 0.66 V to 0.94 V as carrier concentrations changed from 10^{12} cm^{-3} to 10^{17} cm^{-3}. Furthermore, the elevated carrier concentrations caused an upward movement of both the conduction band (E_C) and the valence band (E_V) (Fig. 8(d)). Importantly, the absorber's E_V moved towards the quasi-Fermi level of holes (F_P), thereby improving conductivity and charge carrier transport [31,180]. Moreover, the observed increase in the separation of quasi-Fermi levels for electrons and holes in the absorber region at 10^{17} cm^{-3} markedly enhanced V_{OC}, leading to better overall solar cell performance [66,181]. However, the observed decrease in J_{SC} was attributed to the absorber's elevated carrier concentrations, which caused the depletion region at the ETL/absorber interface to mainly occupy the ETL, reducing its width in the absorber [119]. This limits photon absorption within the absorber, lowering QE [182]. To summarize, a rise in the absorber's carrier concentrations shifted energy band positions and boosted both quasi-Fermi level splitting and V_b, thereby enhancing the PCE of solar cell devices [183]. Nevertheless, although elevated carrier concentrations were often linked to better solar cell performance, they also posed a risk of Auger recombination [184]. This effect can obstruct hole transport because of higher recombination and impurity scattering in the absorber, potentially counteracting the advantages and leading to a reduction in FF and PCE after 10^{17} cm^{-3}. To fabricate efficient CP SCs based on p-n heterojunctions, carrier concentrations equal to or below 10^{17} cm^{-3} are desirable. Hence, 10^{17} cm^{-3} emerged as the optimum choice for subsequent simulations.

The regulation of interfacial recombination, carrier lifetime, and material doping levels is significantly influenced by defects, which can arise from uncoordinated atoms, non-stoichiometry, and other sources. These defects are predominantly situated at the interface,

surface, or grain boundaries [119,185]. Therefore, effectively controlling absorber defects is crucial for achieving optimal solar cell performance. To investigate this in detail, we systematically adjusted the defect density of $SrZrS_3$ from 10^{12} cm^{-3} to 10^{18} cm^{-3} to scrutinize its detailed impact. The variations in V_{OC}, J_{SC}, FF, and PCE concerning absorber defect density are illustrated in Fig. 8(e) and (f). Specifically, as the defect density increased from 10^{12} cm^{-3} to 10^{18} cm^{-3}, all four PV parameters declined. This substantial reduction was attributed to the increased recombination sites along the path of photogenerated charge carriers with rising defects, leading to a shortened diffusion length and lifetime [186]. Typically, the minority carrier lifetime (τ) was computed using equation 5, [117,182] given by

$$\tau = \frac{1}{(\sigma \upsilon_{th} N_t)} \qquad 5$$

In this equation, σ represents the capture cross-section of the charge carrier, v_{th} is the thermal velocity, and N_t is the defect density.

The diffusion length of charge carriers is expressed as $L = \sqrt{D\tau}$, with L and D denoting the minority carrier diffusion length and diffusion coefficient, respectively [182]. In this context, the values of L and τ were obtained from SCAPS-1D for various defect densities of the absorber, with a thickness of 400 nm (Fig. 8(g)). When the defect density was raised from 10^{12} cm^{-3} to 10^{18} cm^{-3}, τ experienced a considerable decrease from 1.00E+05 to 1.00E-01 ns. L underwent a drastic reduction from 1.70E+00 µm to 1.70E-03 µm. Furthermore, the observed decrement in L and τ led to an increased recombination rate of charge carriers, ultimately resulted in poor solar cell performance [187]. Likewise, Fig. 8(h) illustrated a significant increase in the recombination rate of charge carriers corresponding to defect density 10^{18} cm^{-3}, hindering their collection at the respective contacts. This hindrance diminished the separation and collection of holes from the absorber to the back contact, negatively impacting PCE [82]. However, the shear and Young's moduli of $SrZrS_3$ were higher, suggesting enhanced shear and tensile deformation resistance. Furthermore, its ductile nature implied that any strain-induced defects at the interface, particularly during deposition on substrates, might relax over a short distance [53,188]. Moreover, CPs were generally identified as defect-tolerant due to their high formation energy, surpassing deep-level defects [55,189]. Therefore, from an experimental perspective, a defect density of 10^{12} cm^{-3} was chosen as the optimal value for the $SrZrS_3$ absorber.

The thickness of the absorber layer is a crucial factor influencing SC performance through enhanced photon absorption and device efficiency [190]. The $SrZrS_3$ absorber layer thickness was adjusted from 100 nm to 1000 nm for optimization. A thin absorber partially absorbs photons, transmitting most light and reducing charge carrier generation. Conversely, a thick absorber may impede solar cell performance due to constraints in charge carrier diffusion length [117]. Therefore, optimizing the absorber thickness is vital for achieving maximum PCE. The $SrZrS_3$ perovskite absorber thickness ranged from 100 nm to 1000 nm, with all solar cell parameters increasing with an increase in the absorber thickness (Fig. 8(i) and (j)). Specifically, enhancements from 100 nm to 1000 nm resulted in decreased V_{OC} but an increased J_{SC} and PCE from 16.24 mA/cm^2 to 27.67 mA/cm^2 and 12.41% to 21.75%,

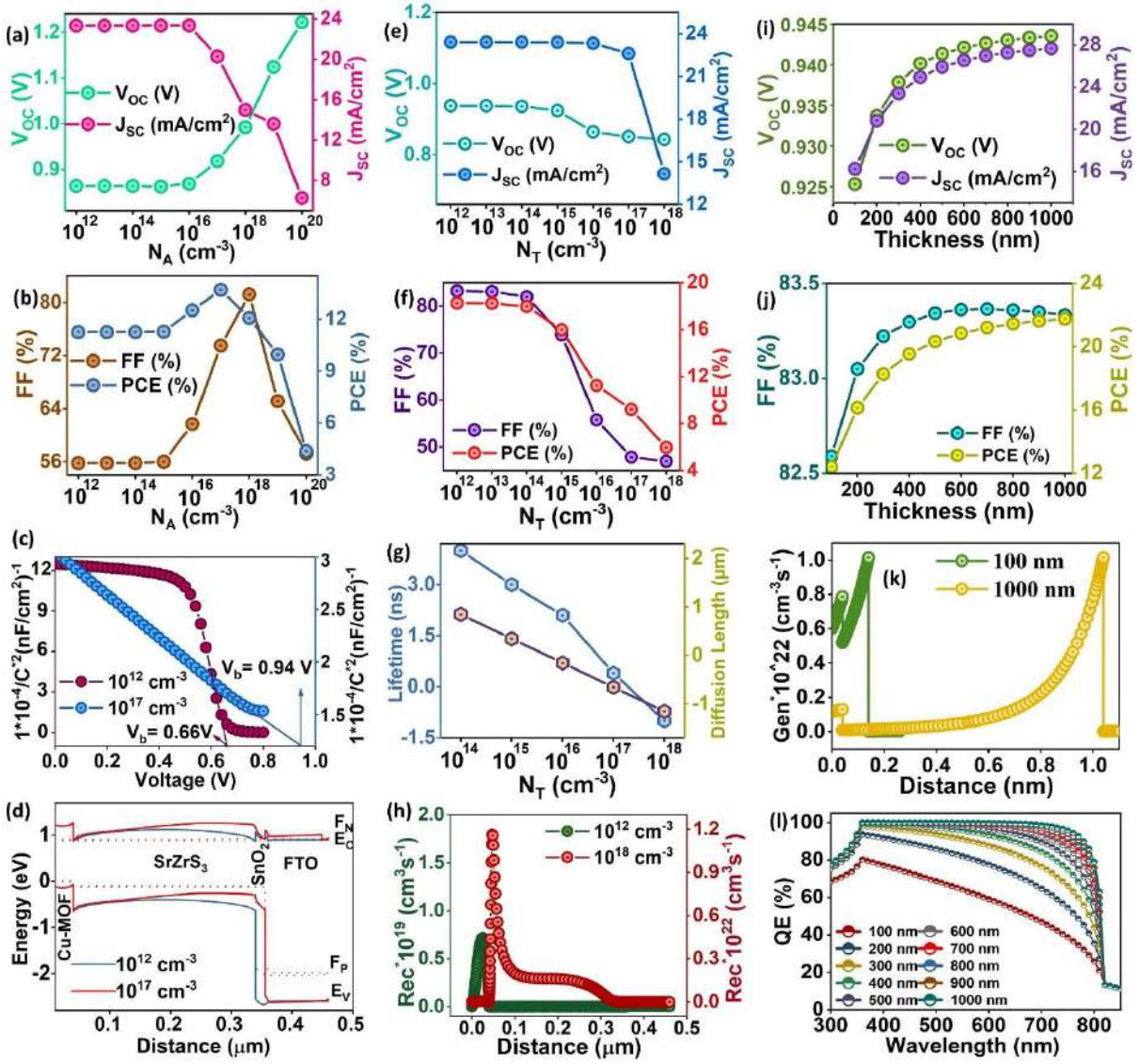

Fig. 8. Variations in (a) Voc, Jsc, (b) FF, PCE, (c) Mott-Schottky, and (d) Energy band diagram as a function of the absorber's carrier concentration. Variations in (e) Voc, Jsc, (f) FF, PCE,

(g) lifetime, diffusion length, and (h) recombination rate as a function of the absorber's defect density. Variations in (i) Voc, Jsc, (j) FF, PCE, (k) generation rate, and (l) QE as a function of the absorber's thickness.

respectively. Notably, the PCE increment was around 8.44% from 100 nm to 600 nm, whereas it was merely less than 1% when extended from 600 nm to 1000 nm. The rise in J_{SC} at the optimum thickness contributed to an increased FF. However, beyond 600 nm, the absorber thickness accelerated charge carrier depletion, leading to an elevation in R_s and a subtle reduction in the FF [191]. Additionally, the PCE of the device was influenced by both light absorption and carrier transport. A thin absorber absorbed a small portion of light and transmitted the unreflected remaining incident light, leading to significant absorption in the HTL [82,192]. Subsequently, charge carriers accumulated near the back contact, intensifying recombination in the device. With increasing thickness, more light was absorbed in the absorber layer, diminishing the build-up of charge carriers in the back contact [185]. This behavior can be seen in Fig. 8(k), illustrating the charge carrier generation rate at two distinct thicknesses, 100 nm and 1000 nm. At 100 nm, the generation rate was higher in the HTL region than in the absorber, indicating a substantial accumulation of charge carriers, while at 1000 nm, it was more prominent in the absorber region, revealing increased photon absorption in the absorber and resulting in enhanced device performance. Moreover, the QE measurements presented in Fig. 8(l) revealed a rise in the integral area of QE absorption from 52.41% to 83.4% as the thickness expanded from 100 nm to 1000 nm. Considering PCE, QE measurements, and manufacturing cost, the optimized thickness for $SrZrS_3$ was determined to be 600 nm.

6.1.4. Optimization of HTL Defect density and Electron affinity

Positioning an HTL between the absorber layer and the back contact can optimize hole transport and prevent electrons from reaching the back contact, thereby reducing interfacial recombination in SCs [57,115,193]. Consequently, it is essential to study how the HTL's characteristics influence the solar cell's performance. Initially, we varied the HTL's defect density from 10^{12} cm^{-3} to 10^{18} cm^{-3}. The results obtained, as portrayed in Fig. 9(a) and (b), revealed V_{OC}, J_{SC}, and PCE until 10^{16} cm^{-1}, beyond which a sharp decline was observed. Conversely, FF remained steady until 10^{15} cm^{-1}, followed by a substantial increase and marginal decrease. The presence of defects introduced nonradiative recombination pathways, converting light energy into heat instead of electrical energy [128,194]. Particularly,

recombination centers impede photogenerated carriers before reaching contacts, thereby diminishing carrier lifespan [195]. Fig. 9(c) supported this conclusion, illustrating that the recombination at the $SrZrS_3$/Cu-MOF interface was much more evident at a defect density of 10^{18} cm^{-3} compared to 10^{12} cm^{-3}. Thus, minimizing defects was crucial for enhancing device performance. The decline in PV parameters at higher defect densities was attributed to reduced carrier diffusion length, leading to increased recombination rates at the $SrZrS_3$/Cu-MOF interface [196,197]. Consequently, an HTL defect density of 10^{12} cm^{-3} was considered optimal for further simulations.

To optimize the performance of PSCs, it is crucial to adjust the electron affinity of the HTL to reduce energy barriers at the HTL/absorber interface [63]. We varied the electron affinity of the Cu-MOF from 3.7 eV to 3.85 eV in increments of 0.05 eV to determine the best value for enhancing hole migration. Fig. 9(d) and (e) presented PV parameter analysis, which showed a consistent performance increase with rising electron affinity. The effectiveness of a solar cell device depends on maintaining a high conduction band offset (CBO) and a low valence band offset (VBO) at the $SrZrS_3$/Cu-MOF interface to ensure efficient hole transport and limit electron flow [181,198]. Thus, the CBO and VBO at the interface, corresponding to the HTL affinity values, were calculated using equations (6-7) [187,199].

$SrZrS_3$/Cu-MOF interface:

$$\mathrm{CBO} = \chi_{Absorber} - \chi_{HTL} \qquad 6$$

$$VBO = \left(E_{gHTL} + \chi_{HTL}\right) - \left(E_{gAbsorber} + \chi_{Absorber}\right) \qquad 7$$

This involves varying χ_{HTL} from 3.7 eV to 3.85 eV while keeping the values of $\chi_{Absorber}$, $E_{gAbsorber}$, and E_{gHTL} constant at 4.1 eV, 1.52 eV, and 1.39 eV, respectively.

It is noteworthy that within the $SrZrS_3$/Cu-MOF interface, a cliff-like barrier (negative VBO) was observed, as shown in Table 8, indicating that the valence band maximum (VBM) of the HTL was higher than that of the absorber. When the χ_{HTL} increased from 3.7 eV, there was a corresponding increase in V_{OC}. This could be attributed to the improved activation energy relative to the absorber's bandgap. Interestingly, a similar trend was seen in the FF, pointing to the formation of a cliff-like barrier in the VBO. As a result, the PCE improved with the increase in the electron affinity of the HTL. This configuration established a significant barrier for electrons and a smaller barrier for holes, facilitating better hole transport through the HTL [185]. Therefore, the optimal VBO at the $SrZrS_3$/Cu-MOF interface was identified as -0.43 eV.

The optimal VBO at the $SrZrS_3$/Cu-MOF interface was -0.43 eV. The changes in energy band offset relative to the HTL's electron affinity were clearly depicted in the energy band diagram in Fig. 9(f).

Table 8. Variation in CBO and VBO relating to electron affinity of Cu-MOF.

Electron Affinity (eV)	**3.7**	**3.75**	**3.8**	**3.85**
CBO (eV)	0.4	0.35	0.3	**0.25**
VBO (eV)	-0.58	-0.53	-0.48	-0.43

To delve into the details of charge carrier transportation and recombination concerning the HTL's electron affinity, we utilized C-F measurements to construct a Nyquist plot depicted in Fig. 8(g). Typically, Nyquist plots of SCs displayed two semicircles across different frequency ranges. The low-frequency semicircle corresponded to the recombination resistance (Rrec) at the ETL/absorber interface, while the high-frequency semicircle represented the resistance to hole transfer at the absorber/HTL interface [200–202]. Interestingly, in this case, a single semi-circle was observed across the entire frequency spectrum. The lack of high-frequency semicircles indicated negligible hole transfer resistance in this solar cell [201]. The large semi-circle at 3.85 eV signified a high R_{rec} in the device, attributed to the appropriate VBO at the absorber and HTL interface. Conversely, the increase in the semi-circle's size for affinity values above 3.7 eV suggested decreased recombination rates of charge carriers owing to inadequate interface barriers. This was further validated by the Mott-Schottky plot in Fig. 8(h), demonstrating an increase in the V_b, facilitating the effective separation and collection of generated carriers at the contacts without recombination [203,204]. These findings underscore the importance of maintaining an appropriate VBO at the $SrZrS_3$/Cu-MOF interface for effective charge carrier transportation and reduced recombination. Thus, to achieve a high PCE, an electron affinity of 3.85 eV was identified as the optimal value for enhancing device performance. It is crucial to acknowledge that the type of barrier (spike or cliff) and the optimal barrier height in SCs also depend on factors such as carrier concentration and thickness; therefore, we proceeded with the optimization of carrier concentration and thickness.

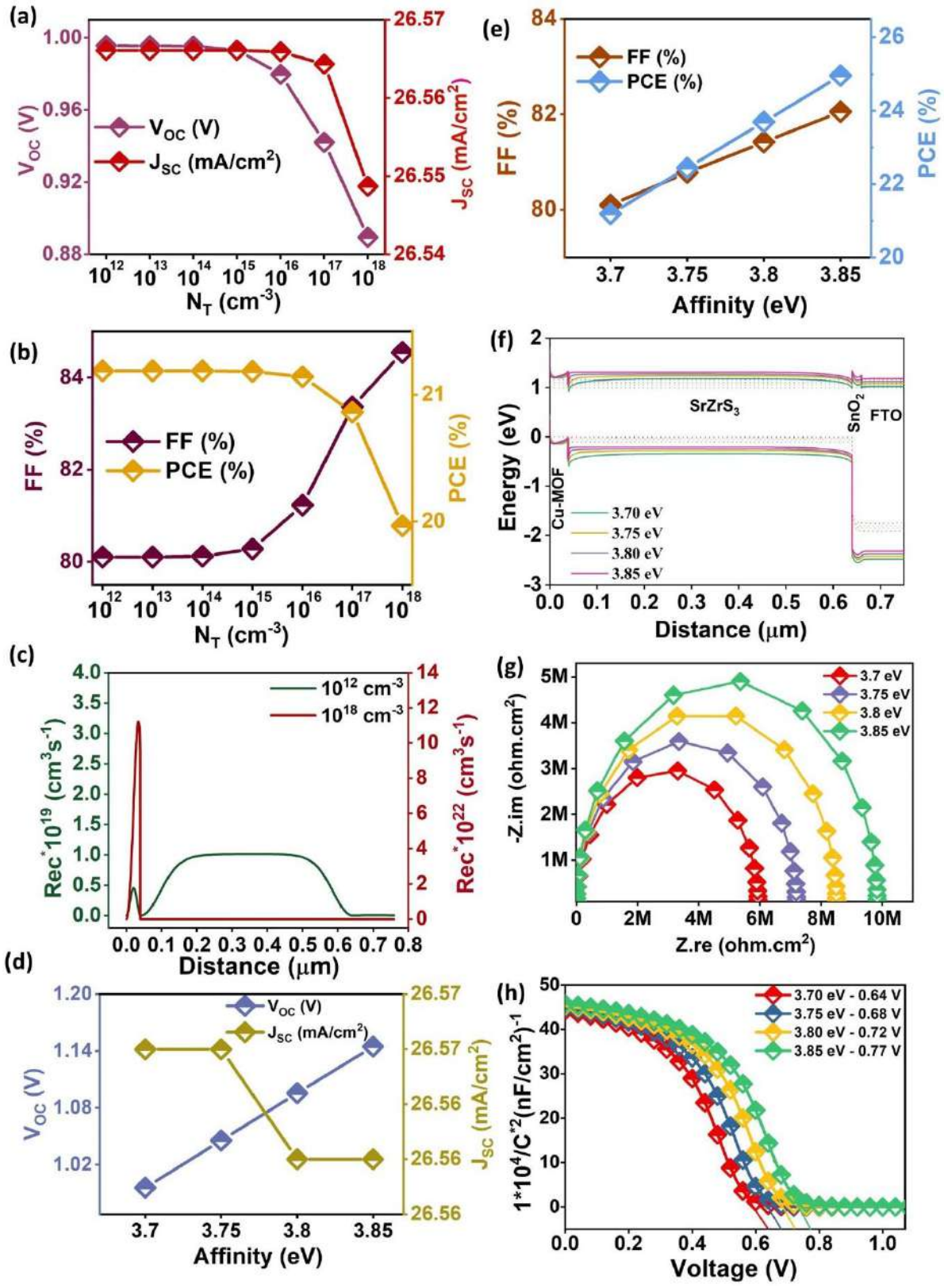

Fig. 9. Variations in (a) Voc, Jsc, (b) FF, PCE, and (c) Recombination rate as a function of the HTL's defect density. Variations in (d) Voc, Jsc, (e) FF, PCE, (f) Energy band diagram, (g) Nyquist Plot, and (h) Mott−Schottky as a function of HTL's electron affinity.

6.1.5. Optimization of HTL Carrier concentration and Thickness.

Investigations into the impact of the HTL's carrier concentration, spanning from 10^{14} cm^{-3} to 10^{20} cm^{-3}, revealed variations in V_{OC}, J_{SC}, FF, and PCE, as shown in Fig. 10(a) and (b). It was observed that while J_{SC} remained constant, V_{OC}, FF, and PCE showed improvement beyond a certain carrier concentration. This trend was attributed to the reduction of the hole barrier and the improvement of the electron barrier as the carrier concentration rose, which caused shifts in the energy bands [199,205]. When the carrier concentration of HTL matched or was lower than that of the absorber, there was no change in the energy bands, keeping the solar cell's performance steady up to 10^{17} cm^{-3}. Additionally, significant barriers for holes at the absorber/HTL interface and the back contact served as recombination centers, obstructing the flow of charge carriers to the contacts [206,207]. However, if the HTL's carrier concentration surpassed that of the absorber, energy band shifts occurred, alleviating the barriers at both interfaces. This was supported by the Nyquist plot (Fig. 10(c)), which showed an increase in the semicircle size with higher carrier concentrations, indicating decreased recombination rates [194]. The Mott-Schottky plot (Fig. 10(d)) further corroborated these results by showing enhanced transport efficiency, conductivity, and V_b of the solar cell [208]. Thus, a carrier concentration of 10^{20} cm^{-3} was identified as optimal for further investigation.

Investigations into thickness variations revealed that increasing the thickness led to improvements in all PV parameters (Fig. 10(e) and (f)), while V_{OC} remained stable, indicating no shifts in the energy band positions and Fermi levels with HTL thickness changes [115]. The J_{SC} enhanced from 26.56 mA/cm^2 to 29.78 mA/cm^2, attributed to better light absorption in devices with thicker HTLs, as evidenced by QE measurements (Fig. 10(g)). Photons with energy below the absorber's bandgap passed through to the HTL, causing a drop in QE around 800 nm, followed by additional absorption until 920 nm [209]. This slight absorption occurred in the NIR region, corresponding to the low bandgap HTL (1.34 eV), which absorbed low-energy photons transmitted from $SrZrS_3$. Increasing the thickness from 40 nm to 200 nm resulted in a notable improvement in QE in the NIR region, rising from 14% to 45%. This trend was also evident in the generation rate graph (Fig. 10(h)), showing that thicker HTL promoted charge carrier generation in that region. Results suggested that Cu-MOF functioned as both a partial light absorber and a hole transporter, enhancing solar cell performance. However, a decrease in FF was observed due to increased R_S and power dissipation at greater thicknesses [119]. Despite this, a thicker HTL boosted photon absorption, making 200 nm the optimal thickness for further optimization.

6.1.6. Systematic study on the influence of diverse c-MOFs as HTL in the optimized device

In our research, we extensively optimized each layer of our device, focusing on the ETL, absorber layer, and HTL (Cu-MOF). To achieve this, we fine-tuned parameters such as electron affinity, carrier concentration, defect density, and thickness. When we were exploring the best HTLs for novel $SrZrS_3$ solar cell devices, we kept the optimized ETL and absorber constant while testing six different c-MOFs as HTLs: Cu-MOF:1, NTU-9:1, Fe_2(DSBDC):1, Sr-MOF:1, Mn_2(DSBDC):1, and $Cu_3(HHTP)_2$:1. For each of these, we optimized parameters such as electron affinity, carrier concentration (ranging from 10^{14} cm^{-3} to 10^{20} cm^{-3}), defect density (10^{12} cm^{-3} to 10^{20} cm^{-3}), and thickness (40 nm to 200 nm) to find the most effective device configuration. Overall, this extensive optimization process resulted in 193 distinct device configurations, as detailed in Tables 5, 6, and 7. We identified the devices with the highest PCE for each of the studied c-MOFs. The top-performing devices were: Cu-MOF:75 with a PCE of 30.60%, NTU-9:22 with a PCE of 29.78%, Fe_2(DSBDC):21 with a PCE of 28.29%, Sr-MOF:22 with a PCE of 28.44%, Mn_2(DSBDC):22 with a PCE of 28.80%, and $Cu_3(HHTP)_2$:24 with a PCE of 28.62%. Fig. 11(a) and (b) showed the J-V plots comparing the performance of the initial and optimized devices. Additionally, the bar graphs in Fig. 11(c) to (h) illustrate the improvements in PV parameters for the six best-performing solar cell devices before and after optimization. Notably, all optimized solar cell devices achieved a PCE exceeding 28%, highlighting the significant enhancement resulting from the optimization process.

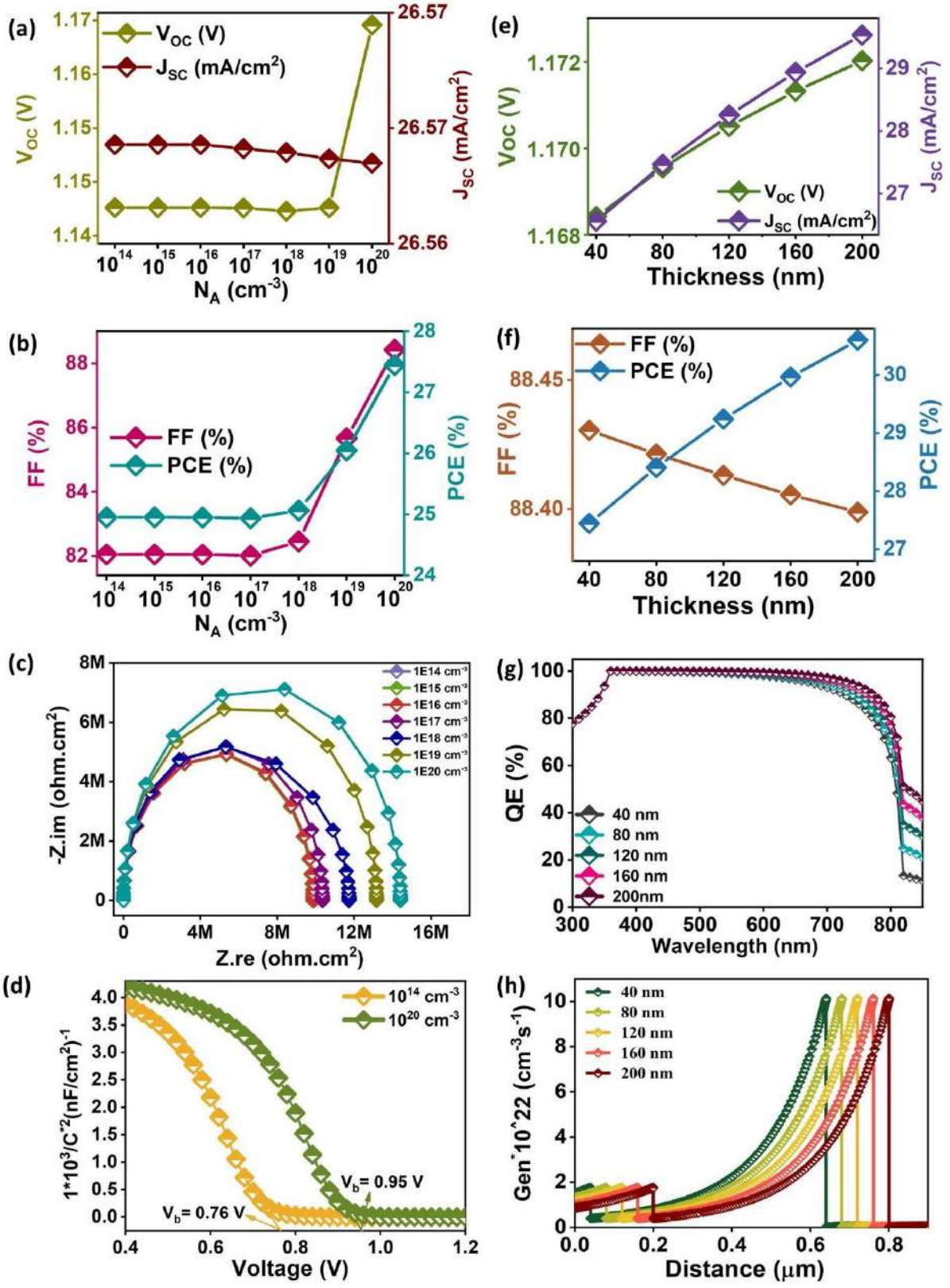

Fig. 10. Variations in (a) Voc, Jsc, (b) FF, PCE, and (c) Nyquist Plot (d) Mott-Schottky as a function of the HTL's carrier concentration. Variations in (e) Voc, Jsc, (f) FF, PCE, (g) QE, and (h) Generation rate as a function of HTL's electron affinity.

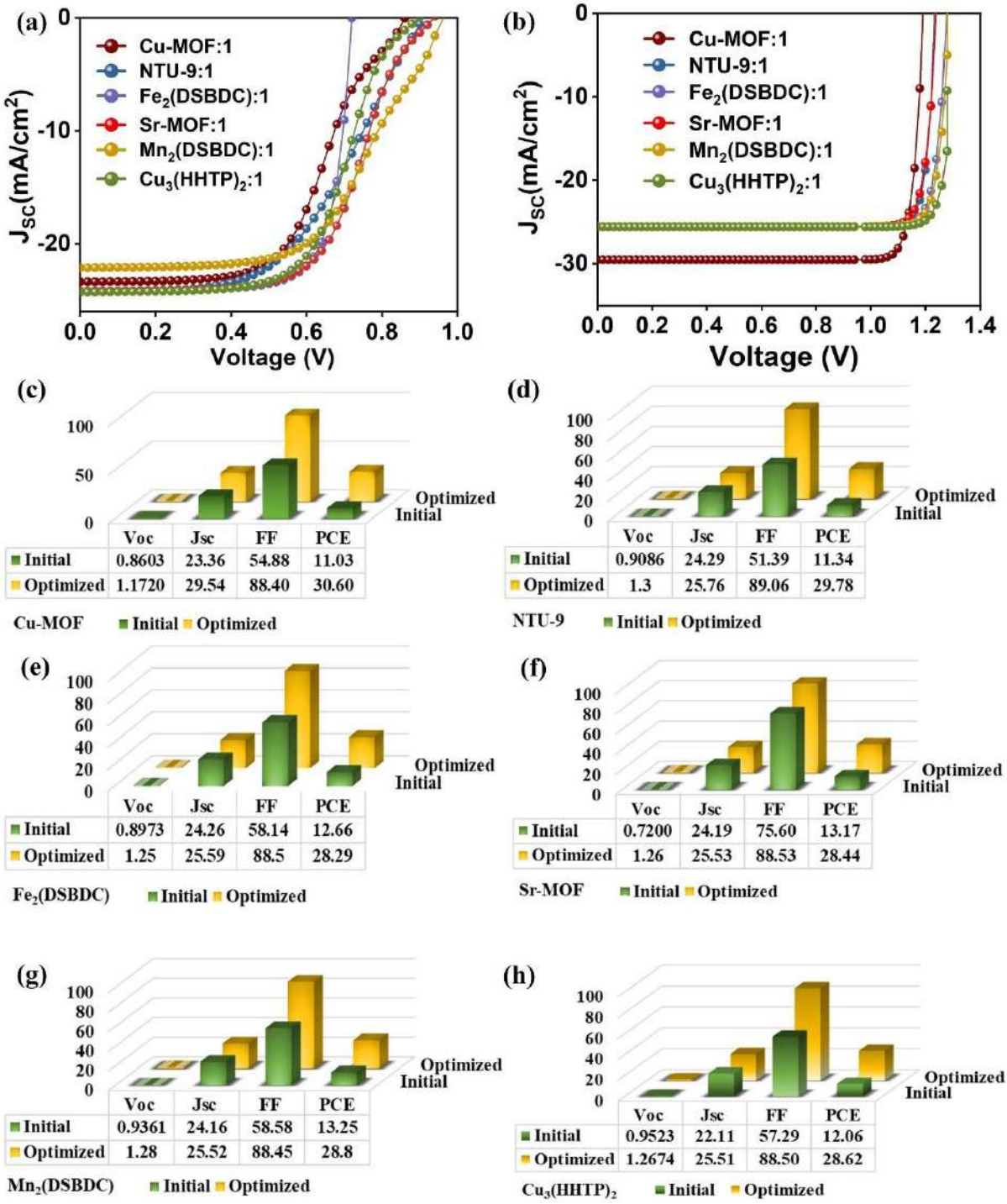

Fig. 11. J-V characteristics of novel $SrZrS_3$ solar cell devices with different c-MOFs as HTLs, (a) initial and (b) after optimization. PV parameters of the corresponding initial and optimized devices (c) Cu-MOF, (d) NTU-9, (e) Fe_2(DSBDC), (f) Sr-MOF, (g) Mn_2(DSBDC), and (h) $Cu_3(HHTP)_2$.

6.1.7. Nyquist plot measurements for initial and optimized solar cell devices.

Impedance spectroscopy emerges as a pivotal tool in studying SCs, unraveling the details of charge carrier transport, and shedding light on their functioning mechanisms [182,210]. Accordingly, Nyquist plots, derived from C-F measurements, precisely portrayed the behaviors of initial (optimized) SCs, namely: Cu-MOF:1 (Cu-MOF:75), NTU-9:1 (NTU-9:22), Fe_2(DSBDC):1 (Fe_2(DSBDC):21), Sr-MOF:1 (Sr-MOF:22), Mn_2(DSBDC):1 (Mn_2(DSBDC):22), and $Cu_3(HHTP)_2$:1 ($Cu_3(HHTP)_2$:24) in Fig. 12(a-f) respectively, each manifesting a distinctive semi-circular plot highlighting the competence of their depletion regions. As mentioned in section 6.1.4, traditionally, Nyquist plots outlined two semicircles at distinct frequency bands, with the low-frequency arc signifying recombination resistance and the high-frequency counterpart denoting resistance to charge transfer [200].

Intriguingly, our investigation exposed a singular semi-circle primely across the entire frequency spectrum, emphasizing the predominance of recombination resistance and minimal resistance to charge transfer within the SCs [82,193]. Moreover, the amplified semi-circle observed in the optimized SCs compared to their initial counterparts highlighted an augmented recombination resistance in the former, facilitating a more efficient separation and collection of photogenerated charge carriers without recombination, thus enhancing their overall PCE [211]. Specifically, the heightened V_{OC} of the optimized SCs expedited charge carrier separation, ensuring their collection at contacts before recombination, thereby bolstering solar cell performance. Specifically, the best-performing devices: Cu-MOF:75, NTU-9:22, Fe_2(DSBDC):21, Sr-MOF:22, Mn_2(DSBDC):22, and $Cu_3(HHTP)_2$:24 demonstrated enhanced recombination resistances of 1.4×10^7 $\Omega.cm^2$, 6.2×10^6 $\Omega.cm^2$, 1.6×10^7 $\Omega.cm^2$, 1.6×10^7 $\Omega.cm^2$, 1.5×10^7 $\Omega.cm^2$, and 1.7×10^7 $\Omega.cm^2$, respectively. Conversely, the diminished recombination resistance in the initial SCs accelerated the rate of charge carrier recombination, resulting in inferior performance.

6.1.8. QE measurements for initial and optimized solar cell devices.

QE measurements serve as a crucial tool for assessing the maximum current output of a solar cell under varying photon flux [208,212,213]. These measurements offer profound insights into fundamental processes like photon absorption and the generation-separation of charge carriers [214]. Fig. 13 depicts comprehensive QE measurements conducted on initial and optimized $SrZrS_3$ SCs equipped with different HTLs across a spectrum of incident wavelengths. Notably, in the initial devices, NTU-9:1's absorption began to decrease at 750 nm, while Cu-MOF:1,

Fe_2(DSBDC):1, Sr-MOF:1, Mn_2(DSBDC):1, and $Cu_3(HHTP)_2$:1 initiated at 480 nm. Across all six devices, absorption ceased at 815 nm, indicating the absorption edge of $SrZrS_3$ with a bandgap of 1.52 eV. However, in Cu-MOF, absorption extended to 910 nm due to additional absorption in the HTL region, owing to its lower bandgap compared to the absorber. It was crucial to note that photons with energy lower than the active layer's bandgap could not be absorbed and were transmitted to the HTL. Consequently, QE dropped to 30% at 815 nm, corresponding to the 1.52 eV bandgap of $SrZrS_3$. Furthermore, QE remained at 15% in the 815-910 nm range, indicating minimal light absorption in the HTL. Remarkably, post-optimization, QE in the NIR region enhanced from 15% to 35%. Specifically, since the HTL's bandgap was 1.34 eV, it absorbs low-energy photons transmitted from $SrZrS_3$, extending absorption to longer wavelengths. Hence, the Cu-MOF HTL operated dually by absorbing light and facilitating hole transportation. Nevertheless, optimized devices (Cu-MOF:75, NTU-9:22, Fe_2(DSBDC):21, Sr-MOF:22, Mn_2(DSBDC):22, and $Cu_3(HHTP)_2$:24) exhibited a consistent spectral response up to 850 nm. This enhanced performance, marked by ~30% increased light absorption for optimized NTU-9:22 and ~7% for Fe_2(DSBDC):21, Sr-MOF:22, Mn_2(DSBDC):22, and $Cu_3(HHTP)_2$:24), relative to respective initial SCs, arose as a result of systematic optimization, extending absorption to the NIR region (700 - 850 nm) with 100 % QE. This suggested that $SrZrS_3$ absorbed photons across the visible (400 - 700 nm) and NIR regions, yielding a significant number of charge carriers collected at corresponding contacts due to proper energy band alignment, thereby fostering high-performance SCs.

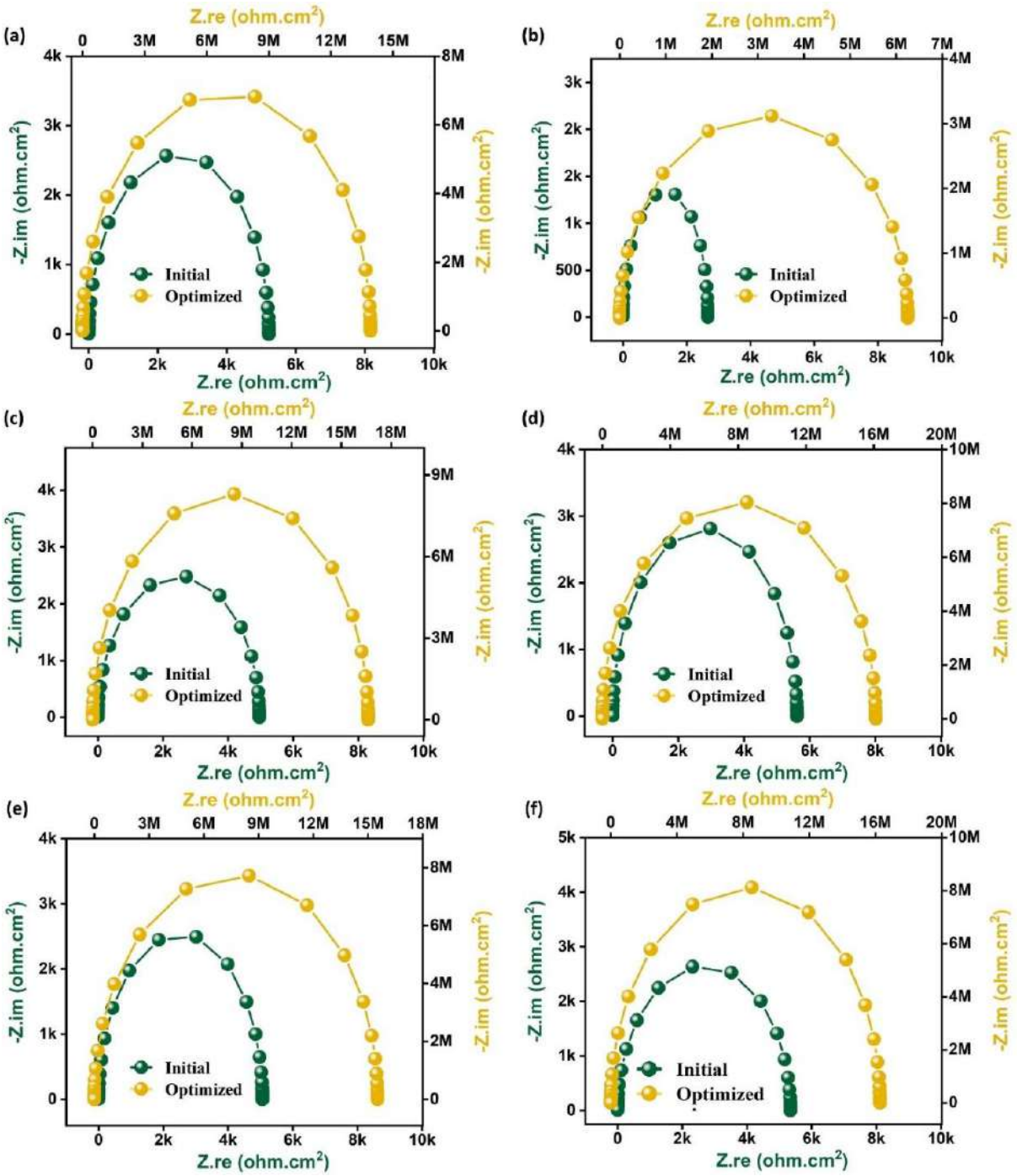

Fig. 12. Nyquist plots of initial and optimized novel $SrZrS_3$ solar cell devices with different c-MOFs as HTLs (a) Cu-MOF, (b) NTU-9, (c) Fe_2(DSBDC), (d) Sr-MOF, (e) Mn_2(DSBDC), and (f) $Cu_3(HHTP)_2$.

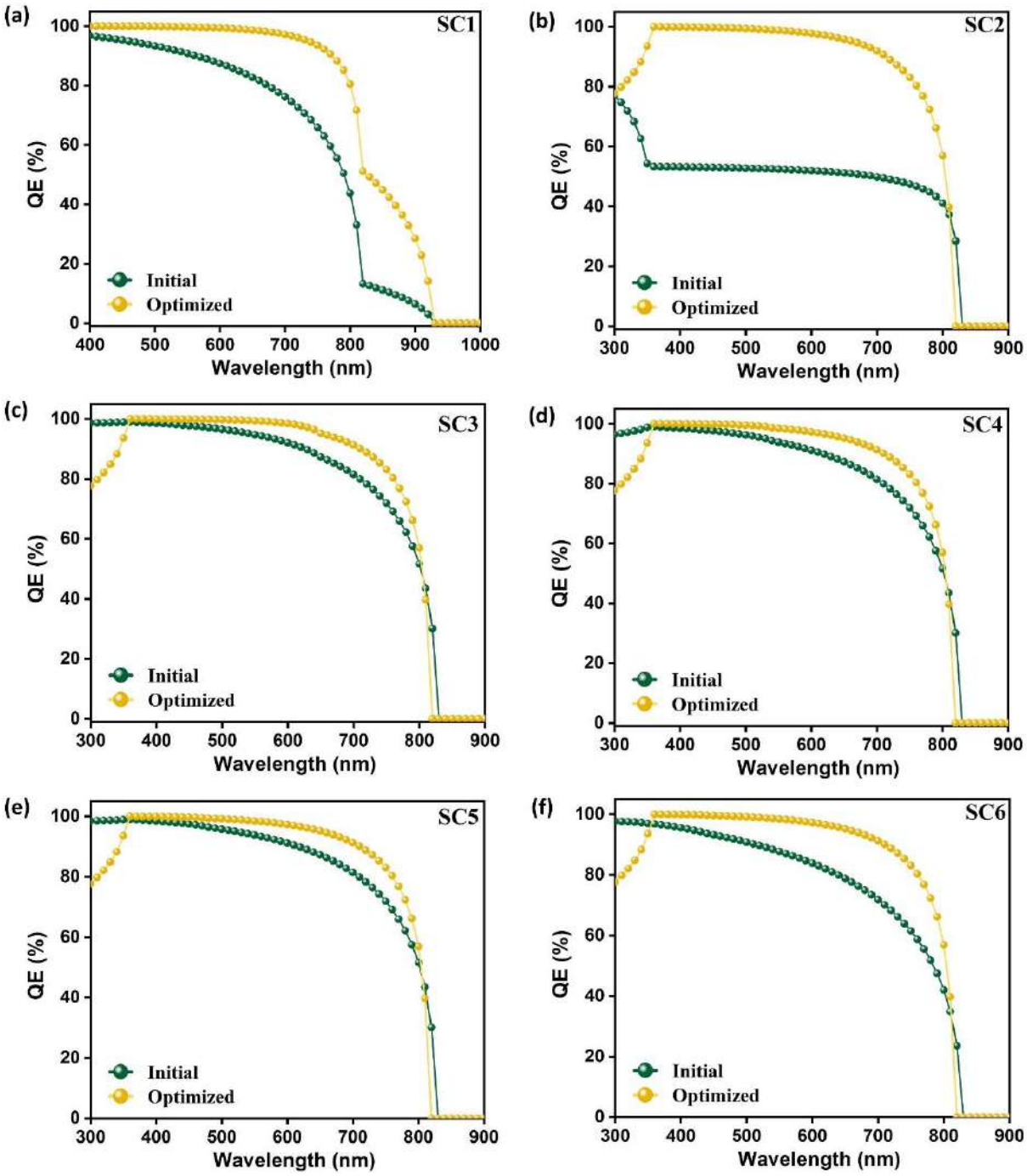

Fig. 13. QE measurements of initial and optimized novel $SrZrS_3$ solar cell devices with different c-MOFs as HTLs (a) Cu-MOF, (b) NTU-9, (c) Fe_2(DSBDC), (d) Sr-MOF, (e) Mn_2(DSBDC), and (f) $Cu_3(HHTP)_2$.

6.1.9. Energy band diagram for initial and optimized solar cell devices.

The device's performance hinges on the precise alignment of energy bands across its constituent parts: the absorber, ETL, and HTL. Specifically, the mismatch in energy bands at the interfaces of ETL/absorber and absorber/HTL significantly impacts the device's efficiency by influencing

interfacial recombination [215,216]. Therefore, it is crucial to precisely adjust the electronic properties of ETL, HTL, and absorber materials. This fine-tuning primarily targets the band offsets at the ETL/absorber (CBO) and absorber/HTL (VBO) interfaces, which are pivotal in facilitating electron transport while impeding hole transport and vice versa in the latter by effectively decreasing the interfacial barriers [27,200,217]. To shed more light on it, the CBO value is the difference between the CBM of the absorber and that of the ETL, while the VBO is the difference between the valence band maximum of the HTL and the absorber. When the CBO is negative, it indicates a configuration where the CBM of the ETL lies below that of the absorber, creating a "cliff-like barrier." Conversely, a positive CBO signifies a "spike-like barrier," where the CBM of the ETL is higher than that of the absorber. Similarly, the VBO reflects the difference between the VBM of the HTL and the absorber. A negative VBO suggests a "cliff-like barrier," with the VBM of the HTL higher than that of the absorber, while a positive VBO implies a "spike-like barrier," where the VBM of the HTL falls below that of the absorber [218]. Therefore, to exclusively investigate how band alignment affected the performance of simulated SCs, the energy band diagrams of Cu-MOF:1, NTU-9:1, Fe_2(DSBDC):1, Sr-MOF:1, Mn_2(DSBDC):1, and $Cu_3(HHTP)_2$:1 and (Cu-MOF:75, NTU-9:22, Fe_2(DSBDC):21, Sr-MOF:22, Mn_2(DSBDC):22, and $Cu_3(HHTP)_2$:24) were examined. The band diagrams are depicted in Fig. 14(a) to (f) (initial SCs) and Fig. 15(a) to (f) (optimized best performing SCs), followed by Table 9, providing the calculated CBO and VBO values for each configuration, along with the activation energy (E_a) at the HTL/absorber interface.

Table 9. Band offsets at ETL/absorber interface and absorber/HTL interface along with activation energy at absorber/HTL interface for both initial and optimized devices.

Devices		**CBO at ETL/Absorber Interface (eV)**		**VBO at Absorber/HTL Interface (eV)**		**Ea at Absorber/HTL Interface (eV)**	
Initial	**Optimized**	**Initial**	**Optimized**	**Initial**	**Optimized**	**Initial**	**Optimized**
Cu-MOF:1	Cu-MOF:75	-0.2	-0.2	-0.28	-0.42	1.22	1.35
NTU-9:1	NTU-9:22	-0.4	-0.4	-0.28	-0.3	1.72	1.92
Fe_2(DSBDC):1	Fe_2(DSBDC):21	-0.2	0.01	-0.48	-0.3	1.92	1.92
Sr-MOF:1	Sr-MOF:22	-0.2	-0.2	-0.3	-0.22	2.30	2.30
Mn_2(DSBDC):1	Mn_2(DSBDC):22	-0.2	-0.2	-0.3	-0.32	2.60	2.60
$Cu_3(HHTP)_2$:1	$Cu_3(HHTP)_2$:24	-0.3	-0.18	-0.15	-0.27	2.85	2.85

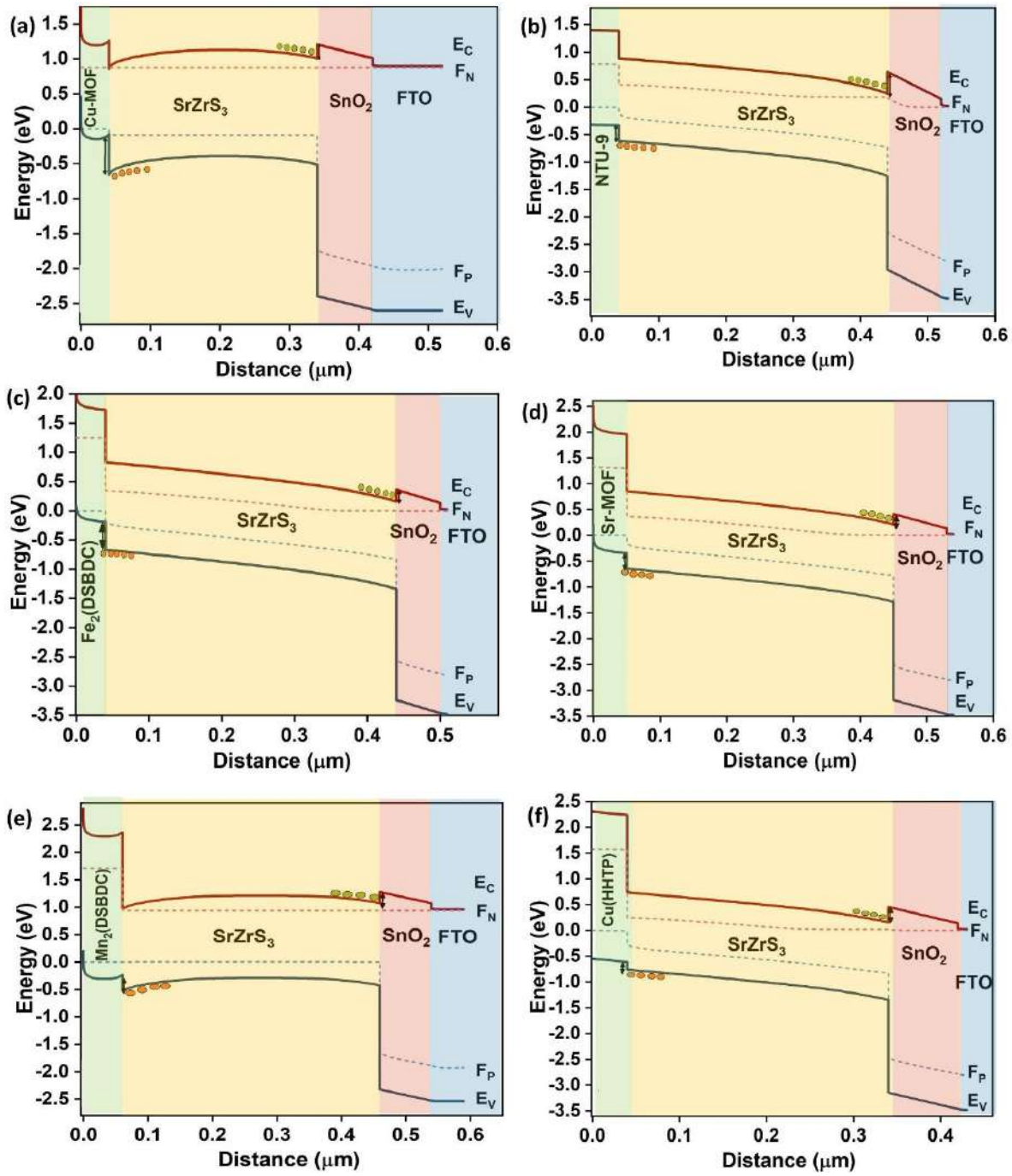

Fig. 14. Energy band diagram of initial solar cell devices (a) Cu-MOF:1, (b) NTU-9:1, (c) Fe_2(DSBDC):1, (d) Sr-MOF:1, (e) Mn_2(DSBDC):1, and (f) Cu_3(HHTP)$_2$:1.

Clearly, the arrangement of the conduction band (E_C) and valence band (E_V) at both the ETL/absorber and absorber/HTL interfaces demonstrated a consistent trend among all initial SCs. This uniformity resulted from the utilization of the same absorber ($SrZrS_3$) and ETL (SnO_2). Notably, in all instances, a negative CBO was observed at the ETL/absorber interface, while a negative VBO was evident at the absorber/HTL interface. These characteristics denoted the presence of cliff-like barriers in both cases. Noteworthy is to mention that the activation

energy (E_a) evaluated carrier recombination at both interfaces [219]. When CBO values aligned with the absorber's bandgap (1.52 eV), E_a mirrored this value. Here, at the absorber/HTL interface, E_a varied from 1.22 to 2.85 eV for devices Cu-MOF:1, NTU-9:1, Fe_2(DSBDC):1, Sr-MOF:1, Mn_2(DSBDC):1, and $Cu_3(HHTP)_2$:1, respectively.

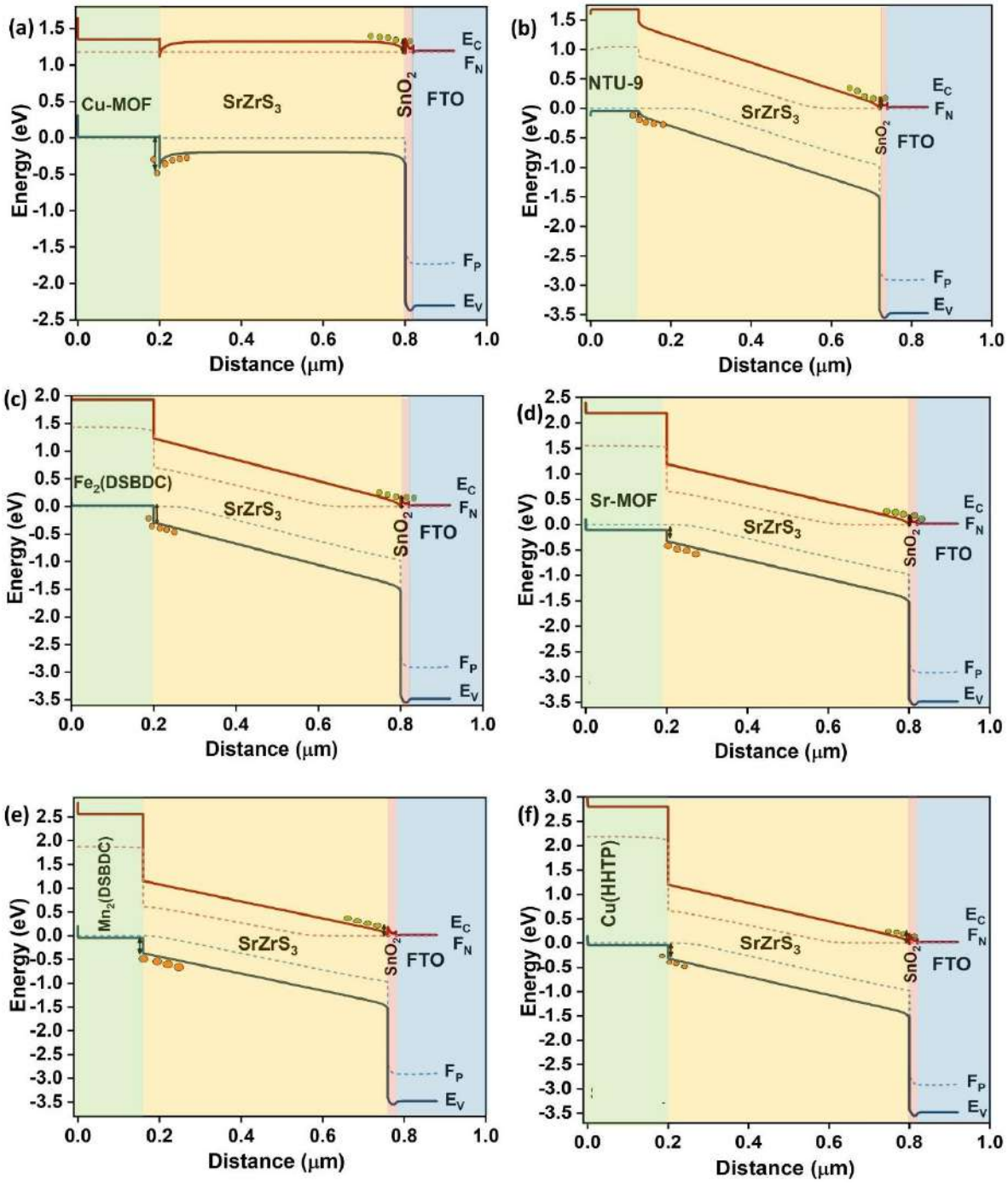

Fig. 15. Energy band diagram of optimized solar cell devices (a) Cu-MOF:75, (b) NTU-9:22, (c) Fe_2(DSBDC):21, (d) Sr-MOF:22, (e) Mn_2(DSBDC):22, and (f) $Cu_3(HHTP)_2$:24.

When E_a was smaller than the bandgap of the perovskite, it signified that interface recombination predominantly influenced the recombination mechanism. Moreover, when E_a was markedly lower than the absorber's bandgap, carriers were more inclined to undergo recombination. However, except Cu-MOF:1, the remaining exhibited E_a above the bandgap of the absorber. Still, we meticulously optimized each layer to overcome barriers and enhance device efficiencies. Subsequently, in the optimized devices, the CBO remained the same as the initial except for Fe_2(DSBDC):21 and $Cu_3(HHTP)_2$:24, with a decrease in CBO (-0.19 and -0.12). On the other hand, the VBO likewise experienced an adequate amount of change, as can be seen in the band diagrams, holding both negative values. However, the decrement in the barrier height enhanced the hole transportation towards the back metal contact.

The E_a showed an elevation at 1.35 eV and 1.92 eV for Cu-MOF:75 and NTU-9:22, respectively, while it remained constant for Fe_2(DSBDC):21, Sr-MOF:22, Mn_2(DSBDC):22, and $Cu_3(HHTP)_2$:24. A detailed analysis revealed a consistent shift in the quasi-Fermi levels (F_p and F_n) across all devices. This shift indicated an upward movement in the energy bands, leading to increased separation and splitting of the quasi-Fermi levels. This phenomenon contributed significantly to the enhancement of the V_{OC} in SCs. Consequently, this robustly improved the conductivity of the SCs, resulting in superior solar cell performance.

6.1.10. Impact of Metal Back Contacts

The choice of back contacts with appropriate work functions is crucial for ensuring efficient hole transportation and maximizing the V_b in PSCs [115,220]. The energy gap separating the Fermi energy from the vacuum level is represented as the work function [27]. To this end, metals like Cu/Mo, Ag, Fe, Cu-doped C, Au, W, Ni, Pd, and Pt, with varying work functions ranging from 4.6 eV to 5.7 eV, were evaluated for their suitability in Cu-MOF:75, NTU-9:22, Fe_2(DSBDC):21, Sr-MOF:22, Mn_2(DSBDC):22, and $Cu_3(HHTP)_2$:24 SCs. Fig. 16 illustrates the variation in V_{OC}, J_{SC}, FF, and PCE with respect to the BMWF in a heatmap. It was evident that all PV parameters generally improved with increasing work function. However, upon closer examination, it was observed that the PCE stabilized after surpassing certain BMWF thresholds. Specifically, for Cu-MOF:75, the PCE plateaued after a BMWF of 5.2 eV, while for NTU-9:22, it stabilized after 5.5 eV. Similarly, for Fe_2(DSBDC):21, Sr-MOF:22, Mn_2(DSBDC):22, and $Cu_3(HHTP)_2$:24, the PCE remained constant after a BMWF of 4.8 eV. Notably, back contacts with lower work functions like Cu (4.6 eV) and Ag (4.7 eV) resulted in PCE >25% for Fe_2(DSBDC):21, Sr-MOF:22, Mn_2(DSBDC):22, and $Cu_3(HHTP)_2$:24, rendering them suitable for the device architecture in terms of cost efficiency. Fig. 17 depicts

this behavior, particularly highlighting Cu-MOF:75 with a high PCE to showcase the impact of varying work functions. In instances where the work function was low, the Fermi level of the metal aligns in close proximity to the E_C of the HTL (Scenario 1). This configuration erected a substantial barrier known as the Schottky barrier, hindering the transfer of holes from the HTL to the metal contact, thereby impeding efficient hole transportation [55]. Conversely, the low barrier for electrons facilitated their transfer between the E_C conduction band of the HTL and the metal contact, or vice versa, amplifying the probability of recombination within the solar cell [115]. In contrast, with a higher work function, the Fermi level is aligned nearer to the E_V of the HTL, thereby diminishing the Schottky barrier for hole transfer and facilitating their migration to the metal contact (Scenario 2). Consequently, the improvement in solar cell performance with increasing work function can be attributed to the shift of the metal's Fermi level towards the valence band of the HTL [221,222].

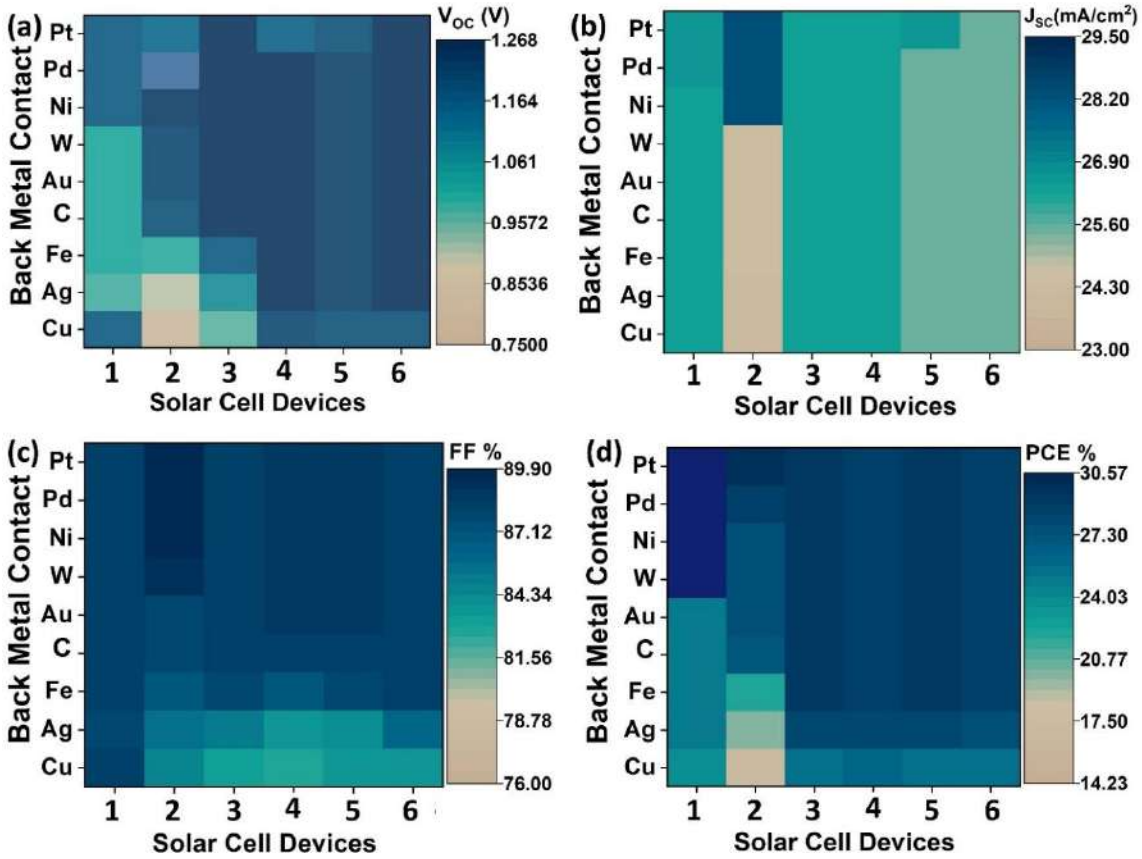

Fig. 16. Variation in PV parameters as a function of metal work function (a) V_{OC}, (b) J_{SC}, (c) FF, and (d) PCE. The SCs 1-6 represents Cu-MOF:75, NTU-9:22, Fe_2(DSBDC):21, Sr-MOF:22, Mn_2(DSBDC):22, and Cu_3(HHTP)$_2$:24, respectively.

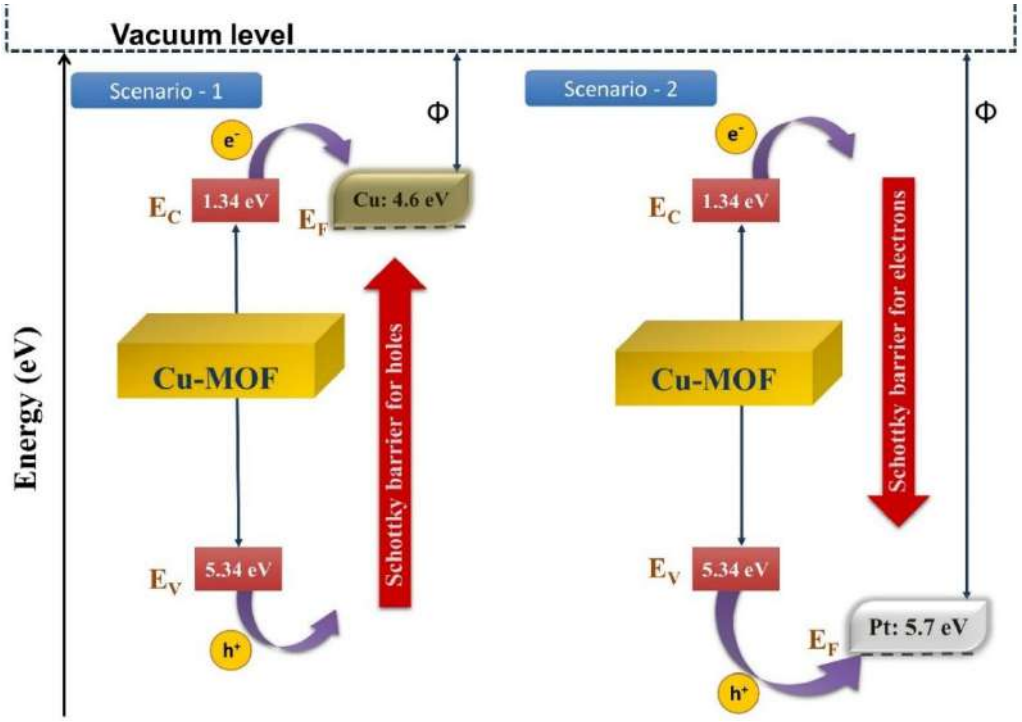

Fig. 17. Impact of the lowest and highest BMWFs on the device performance.

The Nyquist plot in Fig. 18, corresponding to the best-performing solar cell devices, displayed a single semicircle representing recombination resistance. It was evident that the semicircle widened as the BMWF increased, and eventually, the semicircles aligned on par with the aforementioned phenomenon. To summarize, Cu-MOF:75 and NTU-9:22, respectively, achieved the highest PCE of 30.60% and 29.78% with a BMWF of 5.2 eV and above. Fe_2(DSBDC):21 exhibited its peak PCE of 29.28% with a BMWF of 5.1 eV, while Sr-MOF:22, Mn_2(DSBDC):22, and $Cu_3(HHTP)_2$:24 showed maximum PCE values of 28.43%, 29.22%, and 28.62% after reaching a BMWF of 5 eV. These findings indicated that for Cu-MOF:75 and NTU-9:22, metals such as W, Ni, Pd, and Pt served as suitable ohmic contacts at the HTL/back contact interface, facilitating efficient hole transport while introducing a Schottky barrier to electrons. Conversely, for Fe_2(DSBDC):21, Sr-MOF:22, Mn_2(DSBDC):22, and $Cu_3(HHTP)_2$:24, metals, including Fe, Cu-doped C, and Au, as well as W, Ni, Pd, and Pt, were also viable options for ohmic contacts. Considering both cost efficiency and PCE, Ni was the most suitable back contact for Cu-MOF:75 and NTU-9:22, while Fe was the preferred choice for Fe_2(DSBDC):21, Sr-MOF:22, Mn_2(DSBDC):22, and $Cu_3(HHTP)_2$:24.

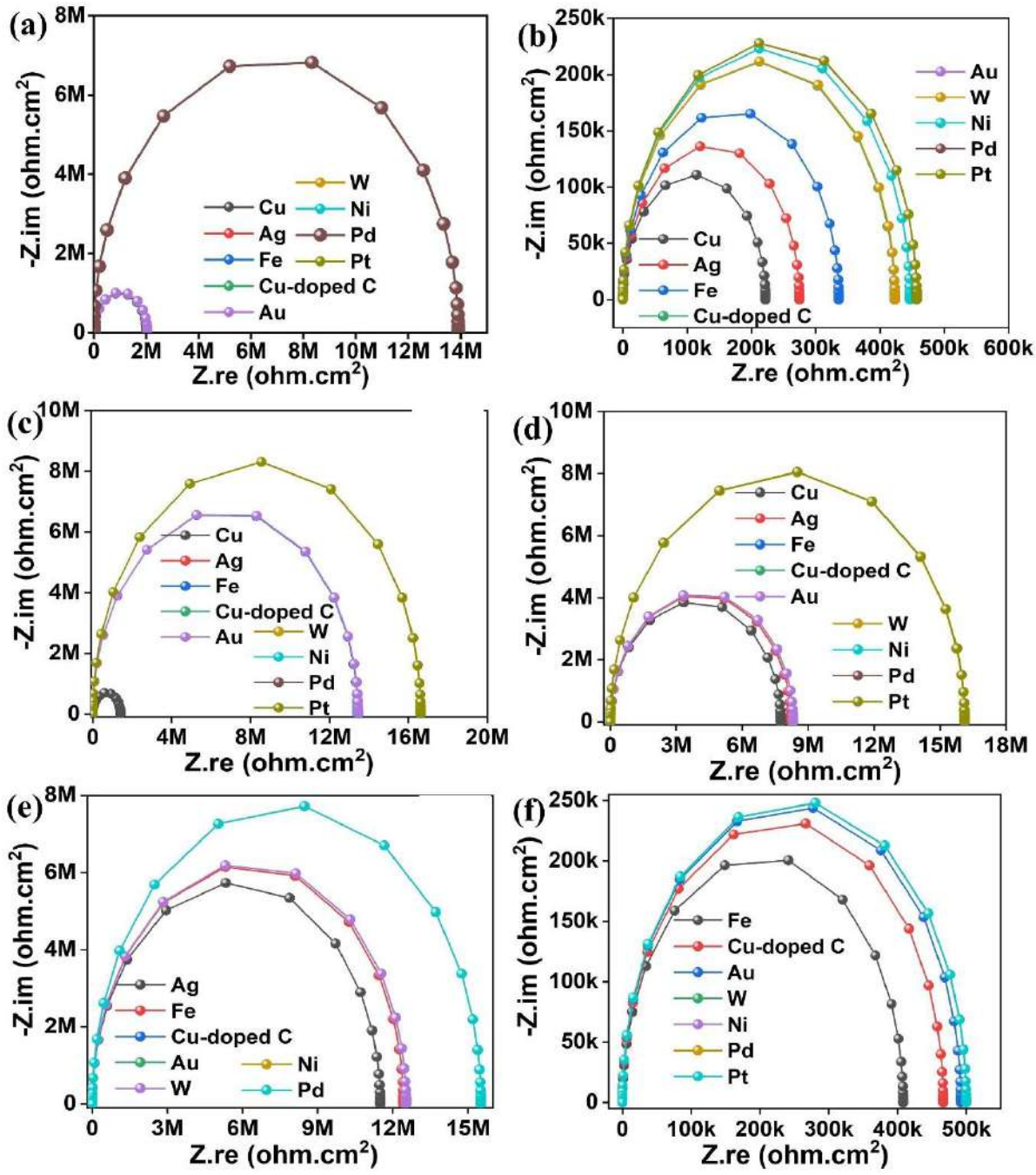

Fig. 18. Impact of various metal contacts on Nyquist Plot (a) Cu-MOF:75, (b) NTU-9:22, (c) Fe_2(DSBDC):21, (d) Sr-MOF:22, (e) Mn_2(DSBDC):22, and (f) $Cu_3(HHTP)_2$:24.

6.1.11. Influence of Interface Properties

Structural imperfections known as interface defects are intrinsic to SCs and arise during fabrication, significantly amplifying charge carrier recombination at interfaces and consequently reducing solar cell efficiency [207,223]. Hence, a comprehensive analysis of these defects and their influence on SCs is imperative to determine the optimal defect density for practical fabrication [223]. In this study, we investigated the interface defects of the Cu-

MOF:75 (highest PCE) solar cell, maintaining a neutral defect density of 10^{12} cm^{-3} at the $SnO_2/SrZrS_3$ and $SrZrS_3$/Cu-MOF interfaces. The interface defect density was varied from 10^{10} cm^{-3} to 10^{20} cm^{-3} and its effects on PV parameters were observed. The results, illustrated in Fig. 19(a) and (b), showed that the V_{OC} remained constant until 10^{14} cm^{-3}, decreasing sharply after that. The J_{SC} remains relatively stable until 10^{16} cm^{-3}, with a subtle decline beyond this threshold. Similarly, the FF remains unchanged until 10^{15} cm^{-3}, decreasing slightly afterward. Nevertheless, the reduction in J_{SC} and FF is less pronounced compared to V_{OC}. Furthermore, the PCE followed a similar trend as V_{OC} reduction, suggesting that changes in V_{OC} largely dictated the overall performance, with minimal influence from J_{SC} and FF at the $SnO_2/SrZrS_3$ interface. The PCE experienced a sharp decline from 30.60% to 24.52% within the defect density range of 10^{10} to 10^{20} cm^{-3}, indicating the sensitivity of $SrZrS_3$-based SCs to $SnO_2/SrZrS_3$ interface defects. The degradation in solar cell performance due to interface defects was attributed to increased trap-assisted recombination of photogenerated electrons at the $SnO_2/SrZrS_3$ interface, hindering their flow towards the front contact [224,225]. Consequently, an optimal defect density of 10^{14} cm^{-3} was identified at the $SnO_2/SrZrS_3$ interface to achieve maximum solar cell performance, outperforming defect densities previously noted at comparable interfaces. In the same way, altering the defect density at the $SrZrS_3$/Cu-MOF interface within the range of 10^{10} to 10^{20} cm^{-3} (as shown in Fig. 19(c) and (d) resulted in a consistent decline in all PV parameters, with saturation observed beyond the threshold values, respectively. Specifically, V_{OC} and J_{SC} decreased from 1.17 to 0.78 V and 26.34 to 22.44 mA/cm^2, respectively, while FF and PCE dropped from 88.61 to 80.57% and 30.60 to 15.76%, respectively. This decline in solar cell performance suggested that heightened interface defects at the $SrZrS_3$/Cu-MOF interface increased the likelihood of hole trapping or recombination during their transit from the absorber to HTL. The findings underscore the necessity of maintaining a defect density between 10^{10} cm^{-3} to 10^{12} cm^{-3} at this interface for optimal solar cell performance. In essence, the study emphasized the crucial role of interface defects in solar cell efficiency, advocating for the adoption of effective deposition techniques and integration strategies such as etching, post-heat treatment, and passivation layer incorporation to mitigate these defects.

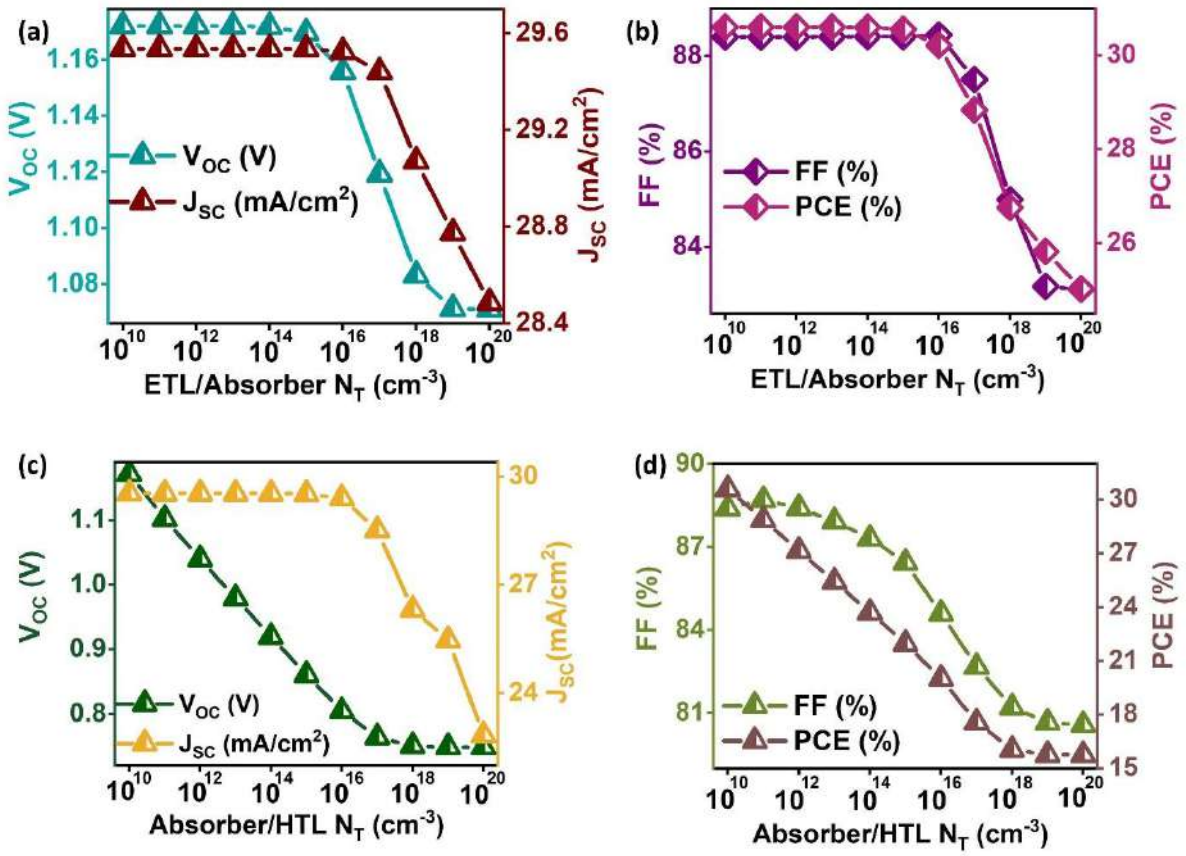

Fig. 19. Variations in (a) Voc, Jsc, and (b) FF, PCE, as a function of interface defect at the ETL/absorber. Variations in (c) Voc, Jsc, (d) FF, PCE, as a function of interface defect at the absorber/HTL.

6.1.12. Impact of Series Resistance (R_S), Shunt Resistance (R_{Sh}), and Operating Temperature

The efficiency of solar devices hinges significantly on two key factors: series resistance (R_S) and shunt resistance (R_{Sh}). These resistances play crucial roles in shaping J-V curves and identifying inefficiencies within the device. R_S typically increases due to resistance at metal contacts (front and back) and transport layers, along with electrical dissipation in the absorber [218]. Conversely, R_{Sh} mainly arises from reverse saturation current induced by manufacturing flaws in SCs [179].

In our investigation using SCAPS-1D, we analyzed the impact of R_S and R_{Sh} on the performance parameters of high-efficiency solar cell Cu-MOF:75. Initially, R_S was varied from 1 to 10 Ωcm^2, with corresponding values of V_{OC}, J_{SC}, FF, and PCE illustrated in Fig. 20(a). Notably, V_{OC} and J_{SC} remained almost consistent across the range, while FF exhibited a

significant decline from 85.87% to 64.88%. This decline is attributed to substantial power loss (P_{loss}) within the SCs as R_S increases, as indicated by the equation (8) [213]

$$P_{loss} = I_{sc}^2 R_s \qquad 8$$

Since P_{loss} was directly proportional to R_S, an increase in R_S amplifies P_{loss} within the device, impacting FF and ultimately reducing overall performance, leading to a deterioration in PCE from 29% to 22%. Therefore, maintaining a low R_S of 1 Ωcm^2 was essential for ensuring efficient solar cell operation. Similarly, R_{Sh} was adjusted from 1000 to 5000 Ωcm^2 to investigate its impact on solar cell performance (Fig. 20(b)). The results revealed that J_{SC} and V_{OC} remain unchanged while FF and PCE improved with increasing R_{Sh}. However, the difference in PCE between 1000 Ω cm^2 and 5000 Ωcm^2 was minimal, indicating that the influence of R_{Sh} on solar cell performance was negligible compared to R_S. Thus, a low R_S of 1 Ωcm^2 was highly recommended for the efficient functioning of these novel $SrZrS_3$ SCs.

The temperature at which SCs operate was of paramount importance, especially considering their exposure to open atmospheric conditions where long-term stability was crucial. Thus, it was imperative to understand the degradation processes that occur in SCs under ambient conditions. In this regard, we varied the operating temperature of the best-performing SCs with a PCE of 30.60% from 300 K to 400 K (Fig. 20(c)) to assess its impact comprehensively. As temperatures rise, electrons gain greater thermal energy, leading to a narrowing of the bandgap and an increase in photocurrent. However, despite this phenomenon, the proposed device structure (Cu-MOF:75) suggested that the J_{SC} remained constant as the temperature increased. The decline in V_{OC} values, on the other hand, could be attributed to several factors. The temperature dependence of the V_{OC} had been extensively studied to understand the link between recombination-associated V_{OC} deficit, as shown in Fig. 17. The V_{OC} vs. temperature behavior could be described by the following equation (9) [200],

$$V_{OC} = \frac{E_a}{q} - \frac{MkT}{q} ln \frac{j_{00}}{j_{PD}} \qquad 9$$

where T represents temperature, M is the ideality factor, E_a is the recombination activation energy, q is the elementary charge, k is Boltzmann's constant, J_{00} is a prefactor, and J_{PD} is the photocurrent density.

If M, J_{00}, and J_{PD} are assumed to be independent of temperature, the plot of V_{OC} as a function of T should produce a straight line. By extrapolating this line to T = 0 K, one could determine

the E_a [226]. If the extracted E_a was smaller than the absorber bandgap, it suggested that interface recombination, occurring at the ETL/absorber or absorber/HTL junctions, dominated. On the other hand, when E_a was close to or equal to the absorber's bandgap, the primary recombination mechanism was typically Shockley-Read-Hall (SRH) recombination within the absorber's space charge or neutral region [227,228]. As shown in Fig. 21, for the Cu-MOF:75 device, the E_a was found to be lower than the absorber's bandgap (1.34 eV). This indicated that recombination at the interface caused by poor energy level alignment and defects at the interfaces was the main reason for substantial V_{OC} losses. Furthermore, the adverse impact of rising temperatures on the mobility of charge carriers, carrier concentration, and other physical parameters directly affected charge carrier transport efficiency, consequently diminishing the device FF. The simultaneous decrease in V_{OC} and FF consequently results in a drop in PCE from 30.60% to 28.4%. However, the reduction in PCE with increasing temperature is minimal, indicating that the device was highly stable.

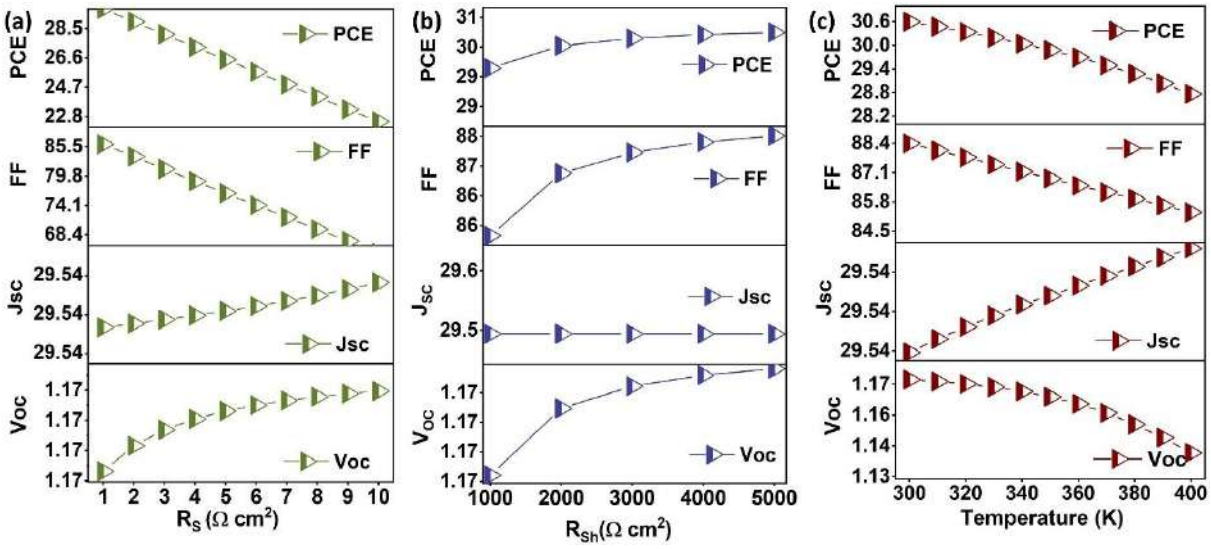

Fig. 20. Variations in PV parameters with respect to (a) R_S, (b) R_{SH}, and (c) operating temperature.

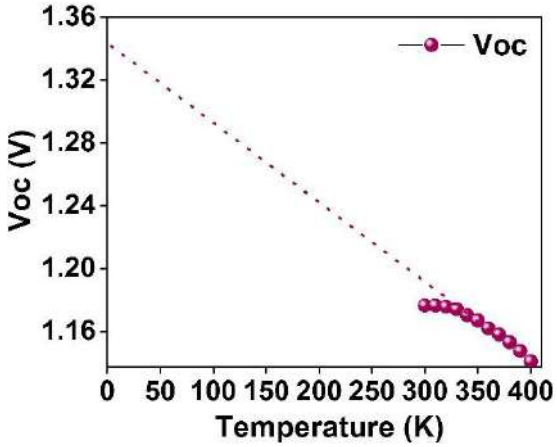

Fig. 21. Temperature dependence of the V_{OC} for Cu-MOF:75, with a linear fit used to determine the activation energy at 0 K.

6.1.13. Comparison of Performance of CP SCs in The Literature

Table 10. Compilation of CP-Based SCs (theoretical and experimental).

Solar cell device structure	**V_{OC} (V)**	**J_{SC} (mA/cm^2)**	**FF (%)**	**PCE (%)**	**Ref**
FTO/TiO_2/$BaZrS_3$/Spiro-OMeTAD/Au	1.21	16.54	86.26	17.29	[229]
FTO/TiO_2/$BaZrS_3$/Cu_2O/Au	1.16	12.24	87.13	12.42	[82]
FTO/ TiO_2/$BaZrS_3$/$CuSbS_2$/W	1.00	22.57	73.70	17.13	[103]
FTO/TiO_2/$BaZrS_3$/Spiro-OMeTAD/Au	0.70	22.00	79.40	12.12	[190]
AZO/i-ZnO/CdS/$BaZrS_3$/a-Si	1.31	19.08	78.88	19.72	[186]
FTO/TiO_2/$BaZrSe_3$/Spiro-OMeTAD/Au	0.72	46.65	77.32	25.84	[190]
FTO/ZrS_2/$BaZrS_3$/SnS/Pt	1.18	29.74	80.15	28.17	[55]
FTO/TiO_2/$BaZrS_3$/Pt	0.39	0.71	63.00	0.17	[25]
FTO/TiO_2/$Ba(Zr_{0.87}Ti_{0.12})S_3$/$Cu_2O$/Metal	1.09	26.57	85.78	24.86	[180]
AZO/i-ZnO/CdS/$Ba(Zr_{0.95}Ti_{0.05})S_3$/a-Si	1.26	27.06	88.47	30.06	[186]
FTO/ZrS_2/$Ba(Zr_{0.96}Ti_{0.04})S_3$/SnS/ Pt	1.18	32.26	84.94	32.58	[55]
FTO/SnO_2/$BaZr_{0.96}Ti_{0.04}S_3$/ZnPc/C	1.27	26.62	88.81	30.12	[230]
FTO/ZnO/$SrZrS_3$/NiO/Ni	1.18	26.13	84.29	25.97	[66]
FTO/SnO_2/$SrZrS_3$/Cu-MOF/Ni	1.17	29.54	88.40	30.60	This work
FTO/SnO_2/$SrZrS_3$/NTU-9/Ni	1.30	25.76	89.06	29.78	
FTO/SnO_2/$SrZrS_3$/Fe_2(DSBDC)/Fe	1.25	25.59	88.50	28.29	
FTO/SnO_2/$SrZrS_3$/Sr-MOF/Fe	1.26	25.53	88.53	28.44	

FTO/SnO_2/$SrZrS_3$/Mn_2(DSBDC)/Fe	1.28	25.52	88.45	28.80	
FTO/SnO_2/$SrZrS_3$/$Cu_3(HHTP)_2$/Fe	1.27	25.51	88.48	28.62	
* Represents experimental work					

Table 10 displays a summary of both theoretical and experimental studies on CP absorbers. It is worth noting that the majority of the entries in the table are focused on $BaZrS_3$, followed by $BaZr_{0.96}Ti_{0.04}S_3$. There is only one report addressing $SrZrS_3$. Despite the advantageous characteristics of $SrZrS_3$, such as its low band gap of 1.52 eV, superior mobility, and low recombination rate, $BaZrS_3$ has received the most attention. A recent report by N. Chawki et al. presented a device with the configuration FTO/ZnO/$SrZrS_3$/NiO/Ni, achieving a PCE of 25.97%. The table also shows that all the devices utilize traditional organic and inorganic HTLs. Organic HTLs, including PEDOT: PSS, Spiro-OMeTAD, and P3HT, offer advantages such as adjustable bandgaps and high-quality film formation [114,187,231]. However, their limited hole mobility and vulnerability to moisture absorption hinder effective hole transport and device stability. On the other hand, traditional inorganic HTLs like NiO_x, Cu_2O, and CuSCN exhibit superior long-term stability and hole mobility, but their practical application is often hindered by high annealing temperatures, prolonged processing times, and limited solubility, constraining their use in large-scale and flexible device configurations. Therefore, there is a clear need for a more efficient HTL that can overcome these limitations.

The important thing to note is that there is only one experimental report available for the fabrication of CP SCs since the prediction of these materials, which was almost a decade ago. Creating SCs using CP absorbers is still in its early stages and remains challenging. The primary issue has been the high processing temperature of the material (900 to 1100ºC), as the substrates and ETLs were unable to withstand these temperatures [232]. Recently, a solution process for creating thin films at lower temperatures (500 to 575ºC) has been developed. However, the achieved PCE is only 0.17%, which is very low. This emphasizes the need for proper device design, including optimizing the absorber and finding suitable transport layers, as well as front and back contacts.

The experimental proof for $SrZrS_3$ CP SCs in the early stages of development can be challenging. Therefore, it is important to have theoretical guidelines to gain experimental insights in the near future. In this regard, we have explored the solar cell performance of $SrZrS_3$ by introducing diverse c-MOFs as HTLs via SCAPS-1D for the first time. It is worth noting

that the achieved PCEs surpass those in the literature, highlighting the potential of these c-MOFs. The introduction of c-MOFs not only aims to improve the performance of these devices but also offers a new direction in SCs technology. We believe that this innovation could be a game-changer in the realm of SCs, sparking significant interest among material scientists worldwide and opening promising opportunities for fabricating highly efficient CP SCswith diverse c-MOFs as HTLs in addition to $SrZrS_3$. This work sets a new standard in the field and paves the way for innovative advancements in PV technology.

6.2 Influence of Dopant-free Phthalocyanine-based HTLs on the Performance of $BaZr_{0.96}Ti_{0.04}S_3$ CP SCs

This section highlights the simulation studies conducted to achieve **Objective 3**, focusing on the impact of dopant-free phthalocyanine HTLs on the performance of $BaZr_{0.96}Ti_{0.04}S_3$ chalcogenide perovskite SCs. In **Section 6.2.1**, the performance of the benchmark device and its baseline characteristics are presented. **Section 6.2.2** systematically optimizes the $BaZr_{0.96}Ti_{0.04}S_3$ absorber layer. In **Section 6.2.3**, we examine the device performance when incorporating the proposed dopant-free phthalocyanine-based HTL, while **Section 6.2.4** consolidates the findings through a comparative analysis with reported studies. Finally, **Section 6.2.5** discusses experimental considerations necessary to achieve a highly efficient $BaZr_{0.96}Ti_{0.04}S_3$ device using dopant-free phthalocyanine HTLs.

6.2.1. Performance Benchmark Device

SCAPS-1D (version 3.3.10) was used to investigate the performance of $BaZr_{0.96}Ti_{0.04}S_3$ SCs concerning diverse MPc HTLs at 300 K under AM 1.5G (100 mW/cm², one sun) spectral irradiance. The initial devices (Fig. 6) were configured utilizing the input parameters provided in Table 3, and the achieved PCEs are shown in Table 4. Later, the absorber properties, including N_A (10^{12} to 10^{20} cm^{-3}), N_T (10^{12} to 10^{20} cm^{-3}), and thickness (100 to 800 nm) were tuned. Further, HTL properties such as thickness (40-200 nm), χ for CuPc (3.3-3.6 eV), NiPc (2.8-3.1 eV), ZnPc (3.8-4.1 eV), and N_A (10^{12} to 10^{20} cm^{-3}) were optimized as detailed in the upcoming sections.

6.2.2. Optimization of Absorber's N_A, N_T, and Thickness

Fig. 22(a&b), all three HTLs show a significant increase in V_{OC} after reaching specific N_A thresholds: 10^{16} cm^{-3} for CuPc and NiPc and 10^{14} cm^{-3} for ZnPc. Initially, J_{SC} remains constant up to these thresholds, then drops sharply. FF and PCE are relatively stable until 10^{14} cm^{-3}, increase up to 10^{16} cm^{-3}, and subsequently decline with further increases in N_A. These changes

are attributed to higher electric fields, as shown in the inset (Fig. 22(c-e)) at the ETL/absorber interfaces, which increases recombination rates [55], as can be evidenced in Fig. 22(c-e). Furthermore, at elevated N_A, the depletion region shifts predominantly into the ETL, reducing the depletion width in the absorber. This reduction in depletion width decreases absorption, resulting in a sharp decline in J_{SC}. Overall, surpassing the optimal N_A (10^{16} cm^{-3}) dramatically increases charge carrier recombination, adversely affecting device performance.

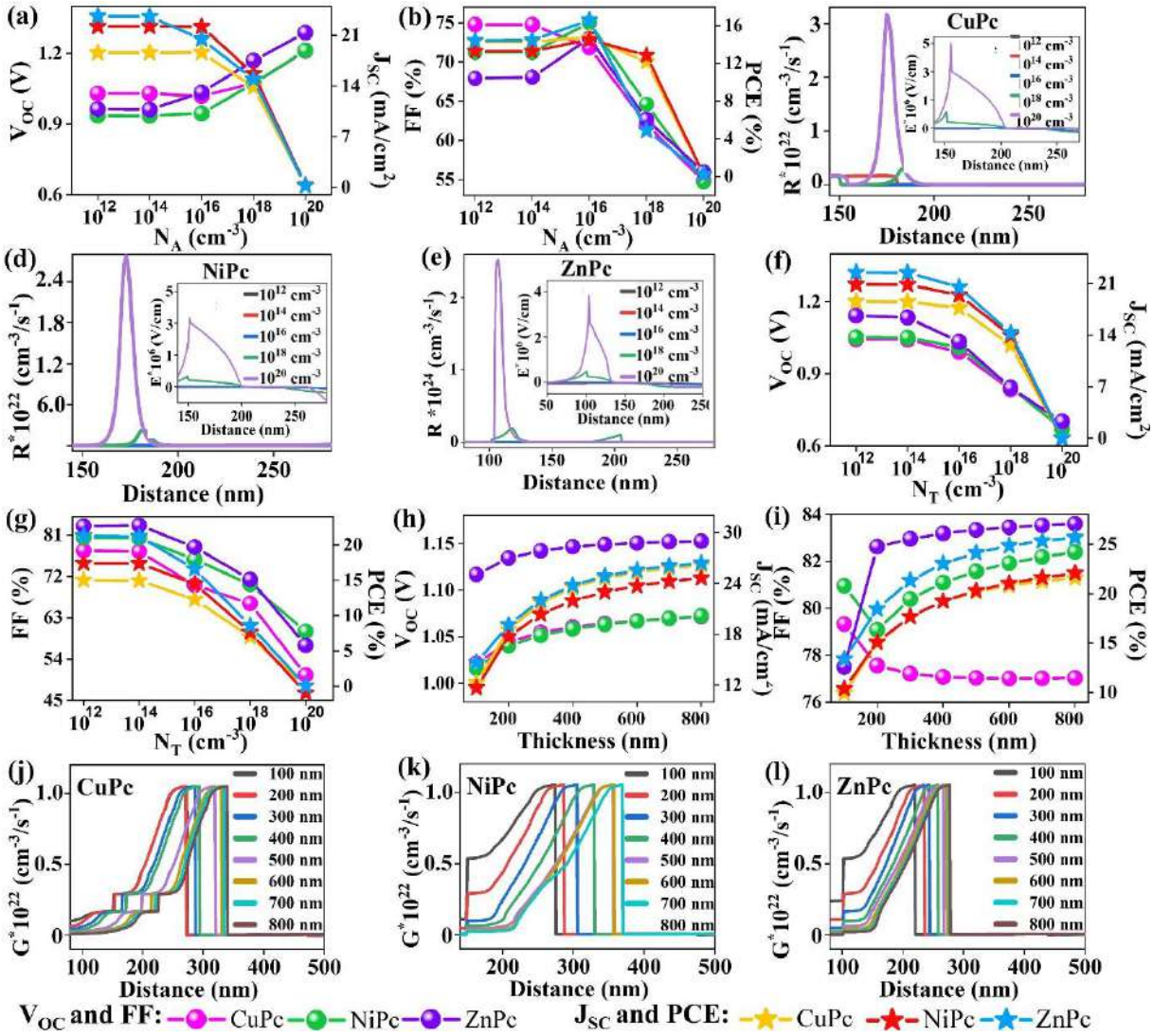

Fig. 22. Changes in (a) V_{OC}, J_{SC} (b) FF, PCE (c,d,e) Recombination rate (electric fields are shown in the inset) concerning absorber NA with diverse HTL (f) V_{OC}, J_{SC} (g) FF, PCE concerning absorber N_T with diverse HTL (h) V_{OC}, J_{SC} (i) FF, PCE (j,k,l) Generation

Upon further investigation, it was found that the absorber's characteristics remain stable until an N_T of 10^{14} cm^{-3}, after which they decline significantly (Fig. 22(f&g)). This decline is due to defects that trap photogenerated charge carriers, reducing their diffusion length and lifetime

(Fig. 23 (a-c)) [82]. For upcoming simulations, an optimal absorber N_T of 10^{14} cm^{-3} is selected for all three HTLs.

Thereafter, the influence of thickness was studied. The V_{OC} of all SCs, as depicted in Fig. 22(h), improves up to a thickness of 300 nm and then stabilizes. This improvement is due to better quasi-Fermi level splitting and increased charge carrier generation, while the stabilization is caused by rising dark saturation current [182]. Fig. 22(i) shows that for thicknesses beyond 200 nm, devices with HTLs NiPc and ZnPc experience a drop in series resistance (R_S), resulting in an elevated FF, whereas devices with CuPc exhibit the opposite behavior. Fig. 22(h&i) demonstrates that J_{SC} and PCE follow a similar trend. J_{SC} increases dramatically up to 600 nm, followed by smaller improvements concerning diverse HTLs. This leads to a higher PCE, as increased thickness improves photon absorption and charge carrier generation, as demonstrated in Fig. 23(d-f) and Fig. 22(j-l). Thus, we further consider 600 nm as the optimal absorber thickness.

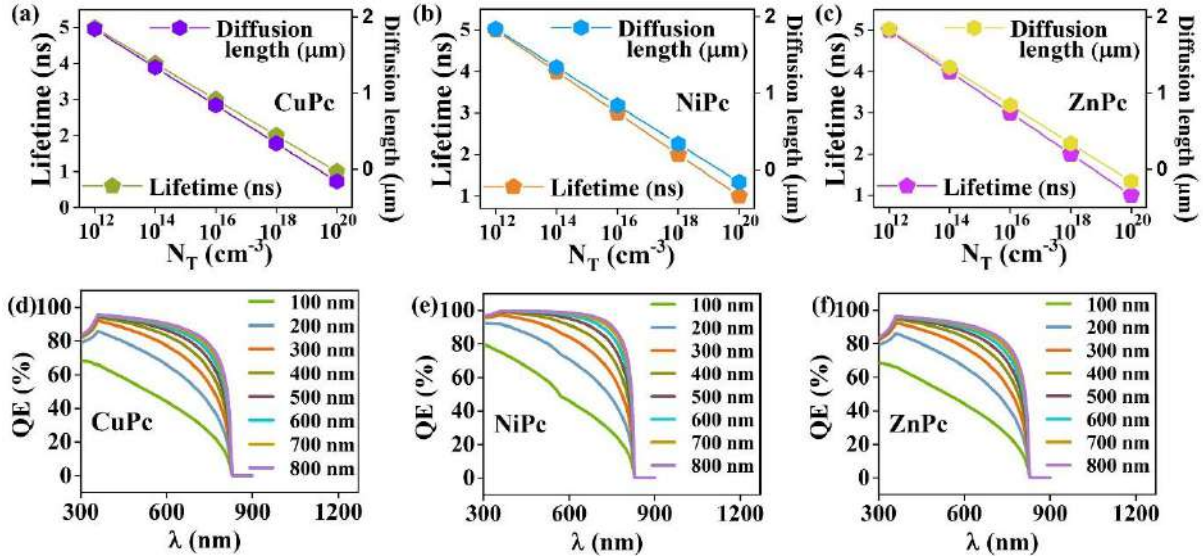

Fig. 23. Variation in lifetime and diffusion length of (a) CuPc, (b) NiPc, and (d) ZnPc with respect to the absorber's N_A.

6.2.3. Optimization of HTLs' Thickness, χ, and N_A

Fig. 24(a&b) shows that varying the HTL thickness impacts PV parameters similarly across different devices. However, with CuPc, as the R_S increases, the FF and PCE decrease, leading to a reduction in QE (Fig. 24(c)) [233]. The HTL should be thicker than the ETL to synchronize charge carrier arrival and reduce recombination, but a thicker HTL can also lead to

recombination due to reduced shunt resistance [16]. Hence, thicknesses of 80 nm (NiPc and ZnPc) and 40 nm (CuPc) were selected.

Fig. 24(d&e) demonstrates that increasing χ improves PV parameters in all the devices. Low χ creates a high VBO (spike-like barrier), increasing recombination, while higher χ lowers the VBO (cliff-like barrier), reducing recombination. In our case, higher χ facilitates hole transport and reduces recombination [200]. Nyquist plots (Fig. 24(f-h)) show that higher recombination resistance improves charge carrier separation and transport. Hence, the optimized χ values were 3.6 eV (CuPc), 3.1 eV (NiPc), and 4 eV (ZnPc).

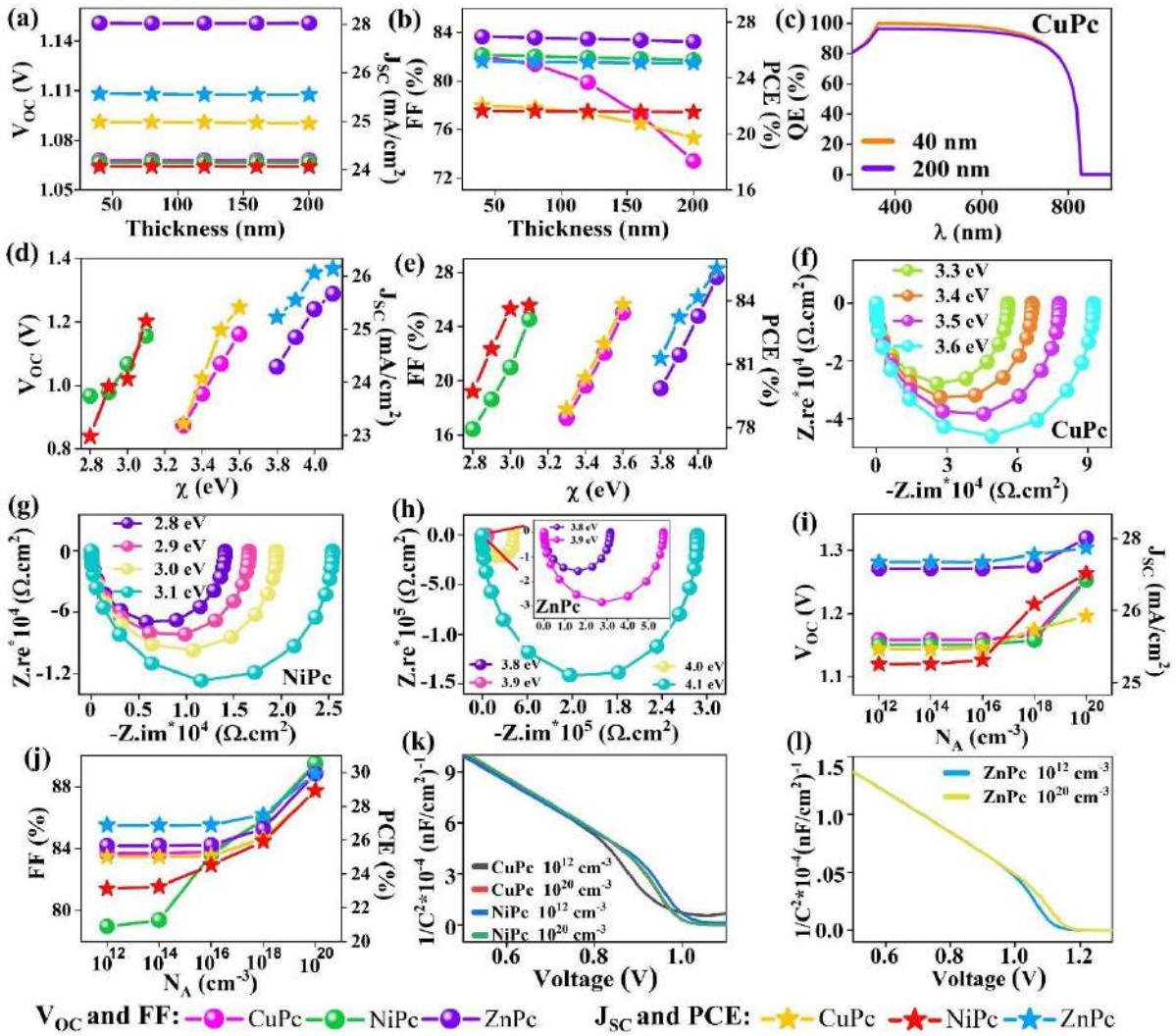

Fig. 24. Changes in (a) V_{OC}, J_{SC} (b) FF, PCE (c) QE concerning diverse HTL thickness (d) V_{OC}, J_{SC} (e) FF, PCE, (f, g, h) Nyquist concerning diverse HTL χ (i) V_{OC}, J_{SC} (j) FF, PCE (k,l) Mott-Schottky concerning diverse HTL N_A.

The influence of increasing the HTL N_A on device performance was studied (Fig. 24(i&j)). In all devices, increasing the N_A tends to increase PV parameters after a threshold point. This is

due to the upward shift of energy bands, which enhances hole movement, limits electron flow, and reduces recombination [182]. Mott-Schottky plots (Fig. 24(k&l)) show an increase in built-in potential with higher N_A. Hence, an optimal N_A of 10^{20} cm^{-3} is recommended for enhancing device performance.

To sum up, we have compared the performance of the initial and optimized devices. J-V plots (Fig. 25(a&b)), displayed remarkable enhancements in both V_{OC} and J_{SC} in the optimized devices, attributed to enhanced light absorption and effective generation of charge carriers, as evidenced by the QE and generation rate in Fig. 26(a-f).

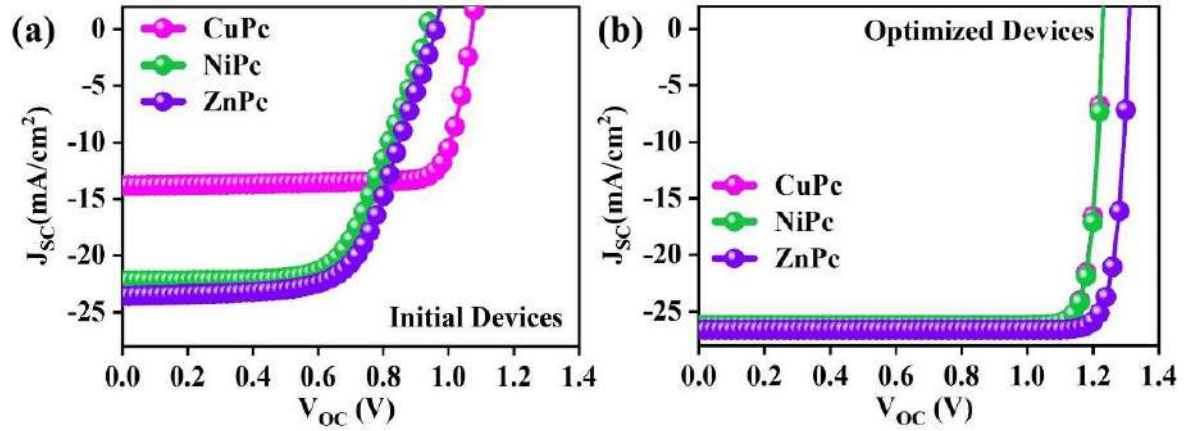

Fig. 25. (a-b) J-V characteristics of the initial and optimized devices

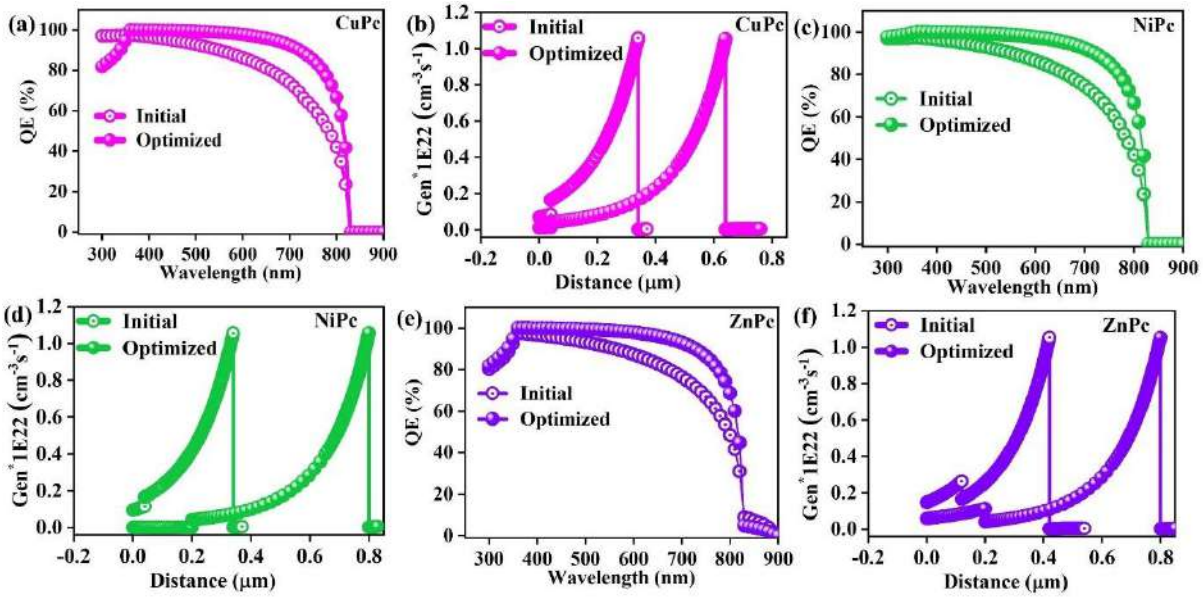

Fig. 26. (a-b) QE and generation plots for CuPc, (c-d) QE and generation plots for NiPc, and (e-f) QE and generation plots for ZnPc.

6.2.4. Comparison of significant outcomes with the literature

Table 11 summarizes theoretical and experimental studies on CP absorbers. It is evident that all SCs use organic and inorganic HTLs. However, the limited hole mobility, lower stability, high processing temperature, etc., often restrict their use in large-scale and flexible devices. This emphasizes the need for more efficient HTLs that can overcome these challenges. Therefore, for the first time, our work introduces MPcs HTLs, and the resulting PCEs are similar to or higher than those in the literature. These significant findings underscore the potential of these HTLs to produce highly efficient $BaZr_{0.96}Ti_{0.04}S_3$ SCs.

Table 11. Comparison of the performance of CP SCs in the literature.

Device structure	**V_{OC} (V)**	**solar cell (mA/cm^2)**	**FF (%)**	**PCE (%)**	**Ref**
FTO/TiO_2/$BaZrS_3$/Spiro-OMeTAD/Au	1.21	16.54	86.26	17.29	7
FTO/TiO_2/$BaZrS_3$/Cu_2O/Au	1.16	12.24	87.13	12.42	8
FTO/ TiO_2/$BaZrS_3$/$CuSbS_2$/W	1.00	22.57	73.70	17.13	9
FTO/TiO_2/$BaZrS_3$/Spiro-OMeTAD/Au	0.70	22.00	79.40	12.12	10
AZO/i-ZnO/CdS/$BaZrS_3$/a-Si	1.31	19.08	78.88	19.72	11
FTO/TiO_2/$BaZrSe_3$/Spiro-OMeTAD/Au	0.72	46.65	77.32	25.84	10
FTO/ZrS_2/$BaZrS_3$/SnS/Pt	1.18	29.74	80.15	28.17	1
FTO/TiO_2/$BaZrS_3$/Pt	0.39	0.71	63.00	0.17	12*
FTO/TiO_2/$Ba(Zr_{0.87}Ti_{0.12})S_3$/$Cu_2O$/Back contact	1.09	26.57	85.78	24.86	13
AZO/i-ZnO/CdS/$Ba(Zr_{0.95}Ti_{0.05})S_3$/a-Si	1.26	27.06	88.47	30.06	14
FTO/ZrS_2/$Ba(Zr_{0.96}Ti_{0.04})S_3$/SnS/ Pt	1.18	32.26	84.94	32.58	[55]
FTO/ZnO /$SrZrS_3$/NiO/Ni	1.18	26.13	84.29	25.97	15
FTO/SnO_2/$BaZr_{0.96}Ti_{0.04}S_3$/CuPc	1.23	26.33	89.41	28.94	Present work
FTO/SnO_2/$BaZr_{0.96}Ti_{0.04}S_3$/NiPc	1.23	26.22	89.51	28.89	
FTO/SnO_2/$BaZr_{0.96}Ti_{0.04}S_3$/ZnPc	1.31	26.62	88.81	30.12	
* Represents experimental work					

6.2.5. Experimental suggestions to accomplish highly efficient $BaZr_{0.96}Ti_{0.04}S_3$ SCs using MPcs HTLs

Controlling the elemental composition when preparing the $BaZr_{0.96}Ti_{0.04}S_3$ absorber is crucial, as S-rich Zr-poor compositions exhibit p-type conductivity with an optimal N_A (10^{15} cm^{-3}),

while S-poor Zr-rich compositions show unfavorable properties. One of the key advantages of this material is its high formation energy, which helps achieve lower N_T [189]. The thickness of the material can be adjusted by varying experimental conditions, such as time and temperature. The N_A and χ of MPcs strictly depend on the π-π stacking of the peripheral ring and the d-d transition of the metal center. It has been demonstrated that N_A and χ can be tuned by adding dopants, while the thickness can be changed by modifying synthesis methods and processing conditions [234,235]. According to the literature, there is a high chance of achieving the optimal values of N_A, N_T, thickness, and χ of $BaZr_{0.96}Ti_{0.04}S_3$, and MPcs as predicted in this work. This information will aid experimental scientists in fabricating high-performing SCs.

6.3. Systematic Analysis of Structural, Morphological, Compositional, Surface, Optical, and Electrical Properties of Synthesized Pure and Mg, Ca, and Sr Doped γ-In_2S_3

This section outlines the comprehensive characterization of the synthesized γ-In_2S_3 and its Mg, Ca, and Sr-doped counterparts, addressing **Objective 4**. **Sections 6.3.1 and 6.3.2** delve into structural characterization performed using XRD, HRTEM, and Raman Spectroscopy, confirming the phase purity and crystallinity of all the samples. In **Section 6.3.3**, we focused on morphological and elemental analyses employing FESEM, EDS, EDS mapping, BET isotherm, and XPS to elucidate surface morphology, composition, and chemical states. Lastly, **Sections 6.3.4 and 6.3.5** present a thorough examination of the optical and electrical properties, incorporating UV-Vis spectroscopy, PL, XPS-Valence band analysis, Hall measurements, EIS, and Mott-Schottky studies to collectively provide insights into the electronic structure and charge transport behavior of the synthesized material.

6.3.1. Crystal phase and structural analysis

The XRD patterns, depicted in Fig. 27a, were analyzed to understand the crystalline structure and orientation of pure γ-In_2S_3 and its doped forms with Mg^{2+}, Ca^{2+}, and Sr^{2+}. The synthesized products exhibited distinct XRD peaks at 2θ angles of 19.30°, 27.44°, 30.80°, 47.96°, and 55.96°, corresponding to the (012), (110), (113), (300), and (1010) crystal planes, respectively. These peaks match the hexagonal γ-In_2S_3 structure as referenced in the JCPDS database (Card No. 33-0624), manifesting the phase purity of the products [99,236]. Notably, the broadening observed in the (113) plane peak is a characteristic feature of the γ-phase of In_2S_3, consistent with earlier reports [100,236,237]. Doping γ-In_2S_3 with Mg^{2+}, Ca^{2+}, and Sr^{2+} did not introduce additional peaks, which would suggest the absence of other phases such as CaS, MgS, or SrS, thus confirming the high purity of the samples. The slight shifts in peak positions, compared to

the standard diffraction pattern, further verify successful doping [238]. Fig. 27b and Fig. 27c present magnified views of the (110) and (300) reflections within the 2θ ranges of 27-33° and 45-51°, respectively, revealing systematic peak shifts upon doping. Specifically, in the (300) plane peak, for Mg: γ-In_2S_3, the diffraction peaks shifted slightly to higher 2θ angles (47.93° to 48.02°), while for Ca: γ-In_2S_3 (47.93° to 47.74°) and Sr: γ-In_2S_3 (47.93° to 47.80°), the peaks shifted to lower 2θ angles. These shifts reflect lattice distortions caused by residual stress associated with ionic substitution [103]. For example, the minor blue shift in Mg: γ-In_2S_3 is due to the slight difference in ionic radius between Mg^{2+} (0.79 Å) and In^{3+} (0.81 Å). In contrast, the redshift observed with the introduction of Ca^{2+} (0.99 Å) and Sr^{2+} (1.13 Å) is due to lattice expansion, further demonstrating that the dopants successfully occupied the lattice sites rather than interstitial sites in pure γ-In_2S_3 [239,240].

The HRTEM analysis (Fig. 27d) reveals that pure γ-In_2S_3 has interplanar spacings of 0.32 nm and 0.19 nm, corresponding to the (110) and (300) planes, respectively. Upon doping, subtle changes were observed: Mg: γ-In_2S_3 showed lattice spacings of 0.31 nm for the (110) plane and 0.17 nm for the (300) plane. In the case of Ca: γ-In_2S_3, the spacings were 0.34 nm (110) and 0.21 nm (300), while Sr-doped γ-In_2S_3 exhibited spacings of 0.36 nm (110) and 0.23 nm (300), as illustrated in Figs. 27(e-g). These variations in lattice spacings are consistent with the differing ionic radii of Mg^{2+}, Ca^{2+}, and Sr^{2+} compared to In^{3+}, which induces lattice strain. This further confirms their successful incorporation into the γ-In_2S_3 lattice through substitutional doping [138,241]. Additionally, the SAED patterns (insets of Figs. 27(d-g)) for both pure and doped samples display concentric diffraction rings. Pure γ-In_2S_3 shows d-spacings that match the most intense XRD reflections: d = 0.32 nm at 27.44°, d = 0.26 nm at 30.80°, and d = 0.19 nm at 47.96°. The systematic variations in d-spacings upon doping, as observed in HRTEM, correlate excellently with the XRD results, further validating the phase purity of the materials in addition to confirming substitutional doping.

Table 12 presents the structural parameters, including crystallite size (D), dislocation density (δ), and micro-strain (ε), for both pure γ-In_2S_3 and the doped variants, focusing on the prominent (300) plane. The D of the synthesized materials was estimated using the Debye-Scherrer formula (Eqn. 9) [103] :

$$D = \frac{0.89\lambda}{\beta cos\theta} \qquad (9)$$

where λ is the X-ray wavelength of 1.5405 Å, β is the full width at half maximum (FWHM) in radians, and θ is the diffraction angle in degrees. The pure γ-In_2S_3 exhibits the largest crystallite

size (36.73 nm) while doping with Mg, Ca, and Sr results in a reduction in crystallite size due to the lattice distortions induced by the incorporation of dopant ions. Among the doped samples, Sr: γ-In_2S_3 demonstrates the largest crystallite size (31.57 nm), followed by Mg: γ-In_2S_3 (30.94 nm), and Ca: γ-In_2S_3 (28.10 nm), indicating variations in the effect of different dopants on lattice dynamics.

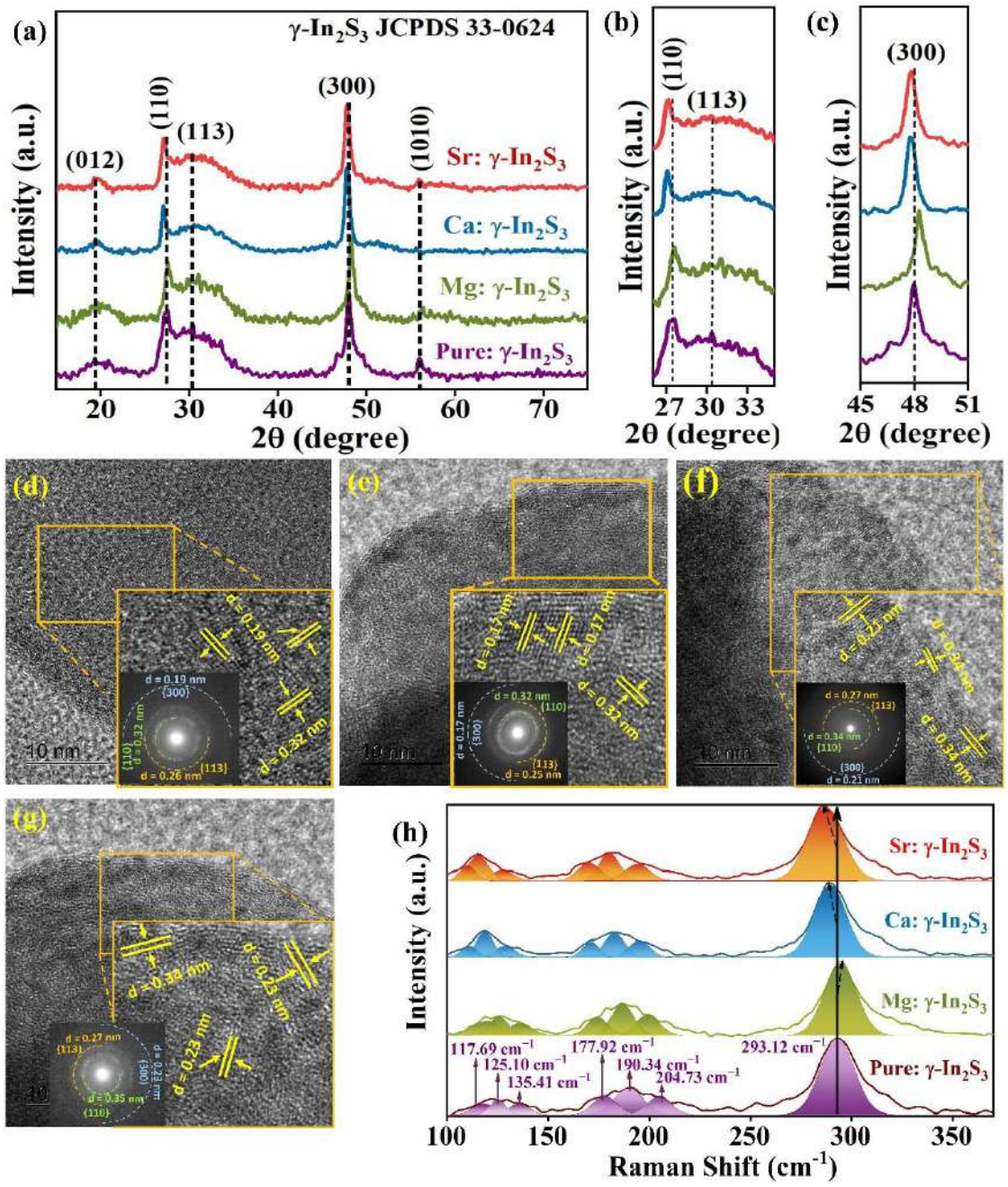

Fig. 27. Pure γ-In_2S_3 and Mg, Ca, and Sr doped γ-In_2S_3 (a) XRD patterns (b-c) Magnified view of the (110) and (300) plane (d-g) HRTEM images with SAED patterns in insets, and (h) Raman spectra at room temperature**.**

The dislocation density (δ), representing the defect density within the crystal lattice, was estimated using Eqn. 10 [242]:

$$\delta = \frac{1}{D} lines/m^2 \qquad (10)$$

Pure γ-In_2S_3 has the lowest dislocation density, while doped samples exhibit higher values due to increased lattice imperfections caused by dopant incorporation. Similarly, the microstrain (ε), which accounts for distortions in lattice spacing due to structural imperfections, was calculated using Eqn. 11 [242]:

$$\varepsilon = \frac{\beta cos\theta}{4} \qquad (11)$$

The microstrain (ε) also increases upon doping, with pure γ-In_2S_3 having the lowest value (0.94). Among the doped samples, Ca: γ-In_2S_3 exhibits the highest ε (1.23). Overall, the data presented in **Table 12** clearly demonstrate the inverse relationship between D and both δ and ε, as expected. A decrease in D leads to higher δ and ε, indicating the presence of certain lattice distortions.

Table 12. Structural parameters of pure γ-In_2S_3, Mg, Ca, and Sr doped γ-In_2S_3.

Samples	**D (nm)**	**δ (lines/m^2)**	**ε**
Pure γ-In_2S_3	36.73	0.74	0.94
Mg: γ-In_2S_3	30.94	1.04	1.12
Ca: γ-In_2S_3	28.10	1.27	1.23
Sr: γ-In_2S_3	31.57	1.00	1.10

6.3.2. Raman spectroscopy

In Fig. 27h, the Raman spectrum provides insights into the pure γ-In_2S_3, revealing three characteristic peaks at 125.10 cm^{-1}, 190.34 cm^{-1}, and 293.12 cm^{-1}, corresponding to the hexagonal vibrational modes. It is worth mentioning that the γ-In_2S_3 exhibits a specific crystallographic symmetry, belonging to the $R\bar{3}C$ space group and D_{3d} point group symmetry [100]. Further focusing on the Raman spectrum within the framework of D_{3d} point group symmetry, we can anticipate the presence of 7 vibrational modes [236]. Based on theoretical insights, the irreducible representations for these modes are listed in **Table 13**. Of these, only two modes are Raman-active, while the others are Raman-inactive. To shed more light, the principle of group theory justifies this: the $^2A_{1u}$ and ^4E_u modes are Raman-inactive due to the

absence of a center of symmetry, and the $^3A_{2g}$ and $^2A_{2u}$ modes are Raman-inactive because there is no perpendicular mirror plane applicable to the principal axis. Consequently, the Raman spectrum displays two Raman-active vibrations associated with the A_{1g} mode and five Raman-active vibrations associated with the E_g mode, resulting in a total of seven Raman-active vibrations. These vibrations are marked by the observed peaks in Fig. 27h, which align with the theoretical predictions. The Raman spectrum also exhibits notable shifts in peak positions upon doping. A red shift is observed for Ca^{2+} and Sr^{2+} doped γ-In_2S_3, reflecting an extension of the In-S bonds due to the incorporation of larger dopant ions [243]. In contrast, Mg: γ-In_2S_3 shows a blue shift, indicating a shortening of the In-S bonds caused by the smaller ionic radius of Mg^{2+} [243]. These shifts signify changes in the vibrational modes due to the incorporation of dopants into the crystal framework, leading to the formation of new bonds with S^{2-} ions [244]. The resulting structural modifications reaffirm the successful experimental synthesis and doping of Mg^{2+}, $Ca^{2+,}$ and Sr^{2+} into the γ-In_2S_3 lattice, consistent with observations from XRD analysis.

Table 13. Irreducible representations of D_{3d} framework with respect to point group theory.

Vibrational modes	Raman active	Raman inactive	Number of modes
A_{1g}	✓		2
A_{1u}		✓	2
A_{2g}		✓	3
A_{2u}		✓	2
E_u		✓	4
E_g	✓		5

6.3.3. Morphological and elemental analysis

The morphology of pure γ-In_2S_3 and its doped counterparts (Mg: γ-In_2S_3, Ca: γ-In_2S_3, and Sr: γ-In_2S_3) was examined using FESEM, as illustrated in Fig. 24. Distinct morphological differences were observed between the pure and doped samples. The low-magnification FESEM images (Figs. 28a and 28c) show that both pure γ-In_2S_3 and Mg: In_2S_3 exhibit a nanoribbon structure with irregular aggregation. High-magnification images (Figs. 28b and 28d) provide a detailed view of these structures. The nanoribbons in pure γ-In_2S_3 have an average thickness of 90 nm, which decreases to c.a. 50 nm upon doping with Mg^{2+}. In contrast,

doping with Ca^{2+} and Sr^{2+} induces significant morphological changes. Low-magnification FESEM images (Figs. 28e and 28g) reveal that Ca: γ-In_2S_3 and Sr: γ-In_2S_3 adopt a densely gathered, cloud-like structure. High-magnification images (Figs. 28f and 28h) further show that these samples still contain tiny nanoribbons, with thicknesses of approximately 20 nm for Ca: γ-In_2S_3 and 16 nm for Sr: γ-In_2S_3. These substantial changes upon doping highlight the influence of dopant ions on the morphological properties of γ-In_2S_3. Notably, the smaller nanoribbon size in Ca: γ-In_2S_3 enhances surface interaction, suggesting its potential as an effective photocatalytic active site compared to other dopings. This finding underscores the critical role of morphology in determining the material's functional properties.

Furthermore, to gain deeper insights into the specific surface area, the BET isotherm method using nitrogen adsorption-desorption measurements at 77 K was performed, as it plays a critical role in analyzing the catalyst performance by influencing the number of accessible active sites and the efficiency of interfacial charge transfer [245,246]. Generally, a higher surface area leads to increased exposure of active sites, thereby improving charge-transfer processes and enhancing catalytic activity [247]. A linear plot of BET multipoint analysis of $[1/W ((P_o/P)-1)]$ vs P/P_o is presented in Fig. 29. The surface area calculations were based on data collected within the relative pressure (P/P_o) interval of 0.05 to 0.30, which is widely recognized as the reliable range for BET multipoint analysis due to the exclusion of capillary condensation effects that typically become significant above $P/P_o = 0.5$ [97]. To ensure the validity of the method, at least three data points within this range were used to establish a linear multipoint BET plot with a positive slope, consistent with expected multilayer adsorption behavior. All samples demonstrated good linearity in this region, confirming the suitability of the BET multipoint model. Comparative analysis revealed that Ca: γ-In_2S_3 achieved the highest specific surface area (79.36 m^2g^{-1}), followed sequentially by Mg: γ-In_2S_3 (55.23 m^2g^{-1}), Sr: γ-In_2S_3 (38.21m^2g^{-1}), and the pure γ-In_2S_3 (17.23 m^2g^{-1}). The observed increase in surface area upon doping suggests that the incorporation of alkaline earth metals enhances surface texturing, thereby providing more active sites that facilitate improved charge transfer processes and improve overall catalytic activity.

Fig. 30 presents the elemental mapping for pure γ-In_2S_3 and its doped counterparts, illustrating the uniform distribution of elements in these materials. Figs. 30a, 30d, 30h, and 30l show the selected areas analyzed for pure γ-In_2S_3, Mg: γ-In_2S_3, Ca: γ-In_2S_3, and Sr: γ-In_2S_3, respectively.

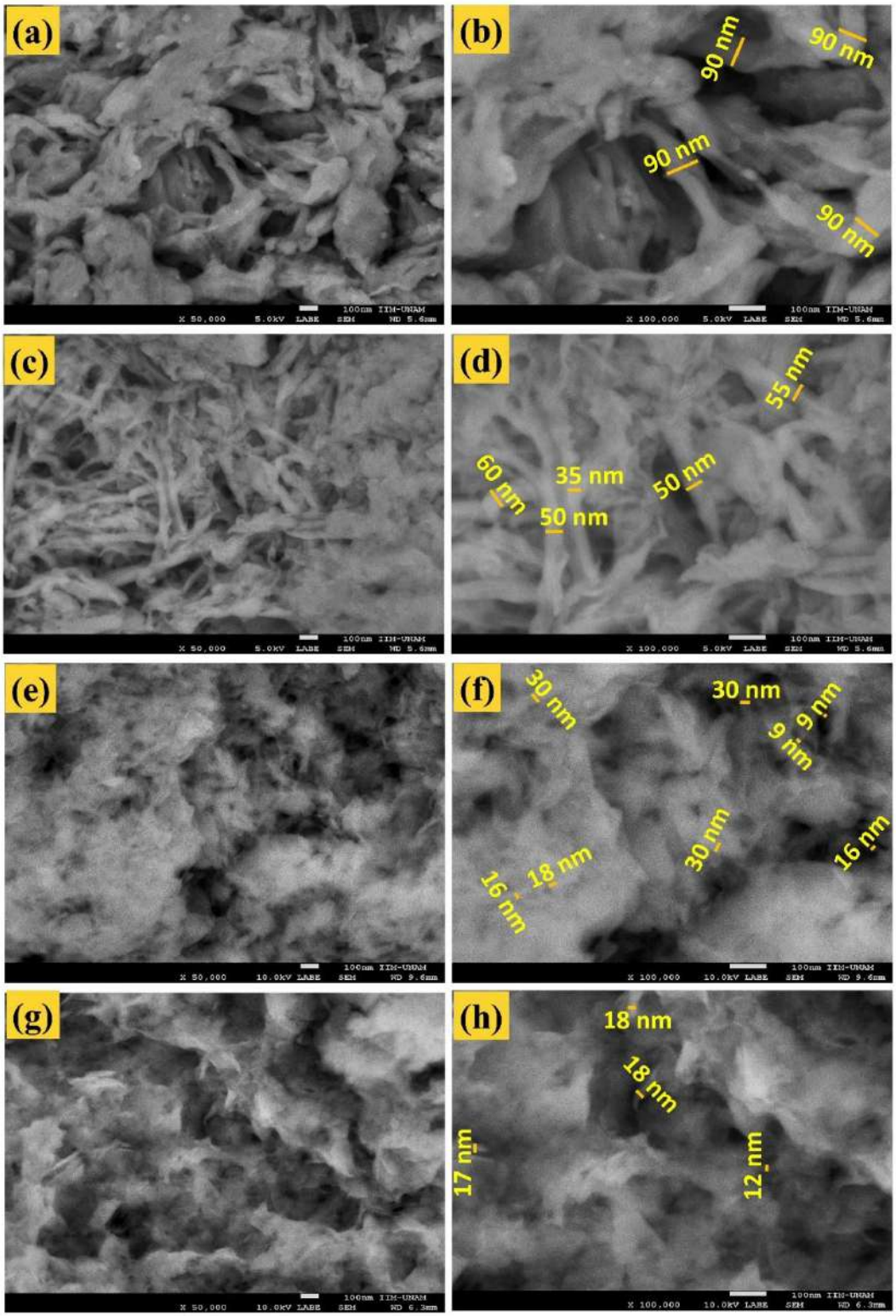

Fig. 28. Typical FESEM micrographs of (a-b) pure γ-In_2S_3, (c-d) Mg: γ-In_2S_3, (e-f) Ca: γ-In_2S_3, and (g-h) Sr: γ-In_2S_3.

For pure γ-In_2S_3, Figs. 30b and 30c confirm the uniform distribution of In and S throughout the analyzed area. Similarly, the doped samples Mg: γ-In_2S_3 (Figs. 30e - 30g), Ca: γ-In_2S_3 (Figs.

30i - 30k), and Sr: γ-In_2S_3 (Figs. 30m - 30o) demonstrate a homogeneous distribution of their respective dopants alongside In and S within the selected regions.

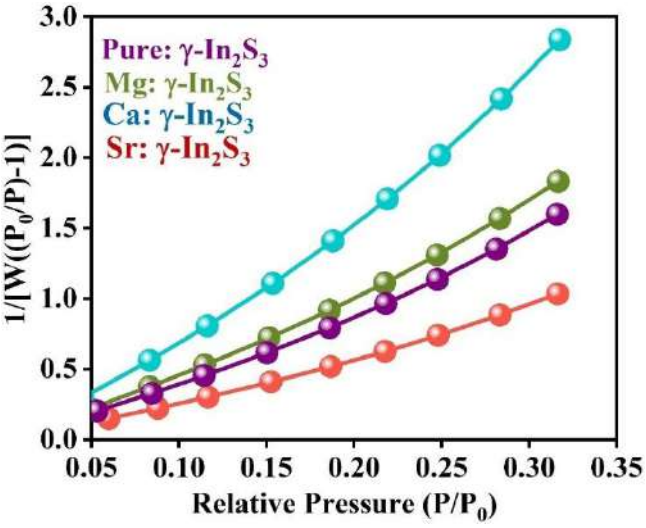

Fig. 29 BET Multipoint plots of pure γ-In_2S_3 and its doped variants.

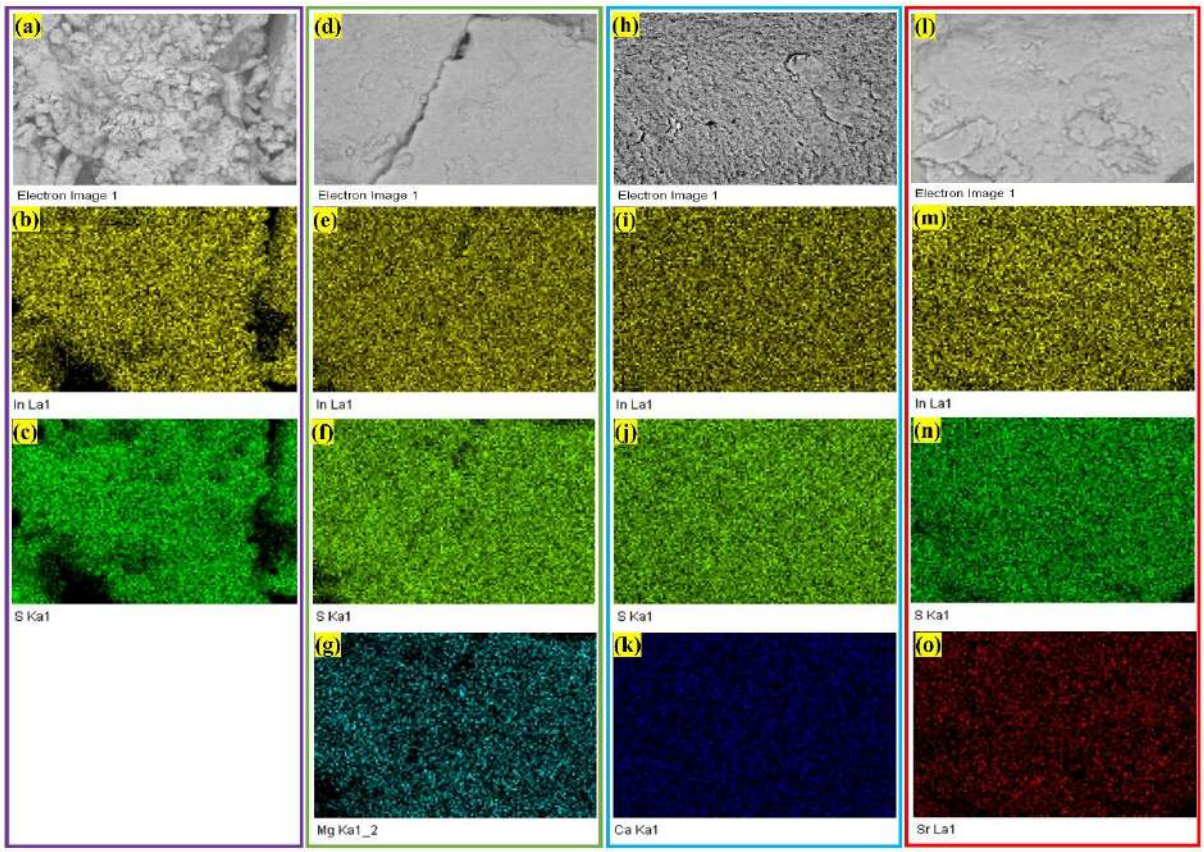

Fig. 30. Elemental mapping of (a-c) pure γ-In_2S_3, (d-g) Mg: γ-In_2S_3, (h-k) Ca: γ-In_2S_3, and (l-o) Sr: γ-In_2S_3.

The phase composition of pure γ-In_2S_3 and its doped variants, expressed in atomic percentages, is summarized in **Table 14**. For pure γ-In_2S_3, the analysis revealed an atomic ratio of 41.01% In and 59.99% S, aligning closely with the expected In:S molar ratio of 2:3. This confirms the purity and stoichiometric integrity of the γ-In_2S_3 phase. In the case of Mg: γ-In_2S_3, EDS results indicate the presence of 1.95% Mg, accompanied by a reduction in the In content to 38.44%. This suggests that Mg^{2+} ions have been successfully incorporated into the crystal lattice, likely substituting for In sites. For Ca: γ-In_2S_3, the analysis identifies 2.10% Ca, with S and In percentages of 57.34% and 40.56%, respectively. These results confirm the incorporation of Ca^{2+} ions into the lattice, accompanied by the introduction of S vacancies, while maintaining the overall phase composition. Similarly, Sr: γ-In_2S_3 displays 1.89% Sr, along with S and In percentages of 60.10% and 38.01%, respectively. This affirms the successful doping of Sr^{2+} ions into the crystal structure. Herein, S vacancies play a significant role by introducing localized electronic states that enhance the material's optical and electronic properties, particularly in Ca: γ-In_2S_3 [138]. Overall, the consistent elemental distributions observed in the doped samples confirm the precise and successful incorporation of dopant ions into the γ-In_2S_3 lattice via substitutional doping, validating the synthesis approach and ensuring the integrity of the doped structures.

Table 14. Elemental composition of Pure γ-In_2S_3 and its doped variants acquired from EDS analysis.

Pure γ-In_2S_3		**Mg: γ-In_2S_3**		**Ca: γ-In_2S_3**		**Sr: γ-In_2S_3**	
Element	**At %**	**Element**	**At %**	**Element**	**At %**	**Element**	**At %**
S K	59.99	**S K**	59.61	**S K**	57.34	**S K**	60.10
In L	41.01	**In L**	38.44	**In L**	40.56	**In L**	38.01
		Mg K	1.95	**Ca K**	2.10	**Sr K**	1.89

Subsequently, XPS was employed to analyze the chemical composition and electronic structure of the synthesized samples, facilitating a precise verification of the substitutional incorporation of dopants into the γ-In_2S_3 lattice [97,248]. The XPS survey spectra, as depicted in Fig. 31a, confirm the presence of characteristic peaks for S 2p, In 3d, Mg 1s, Ca 2p, and Sr 3d, affirming their inclusion in the structure. In Fig. 31b, the Mg 1s peak, deconvoluted at 1303.59 eV, indicates the presence of magnesium in the +2 oxidation state [249]. The Ca 2p region, as shown in Fig. 31c, reveals two peaks at 347.58 eV (Ca $2p_{3/2}$) and 351.13 eV (Ca $2p_{1/2}$) with an

energy separation of 3.55 eV, consistent with the typical values for Ca^{2+}, thereby confirming successful calcium doping in the lattice [140,250]. For the Sr: γ-In_2S_3, the Sr 3d spectrum (Fig. 31d) exhibits spin-orbit split peaks at approximately 132.56 eV ($3d_{5/2}$) and 134.30 eV ($3d_{3/2}$), further validating the +2 oxidation state of Sr [251]. High-resolution spectra of In 3d for pure γ-In_2S_3, illustrated in Fig. 27e, display In $3d_{5/2}$ and In $3d_{3/2}$ peaks at 444.79 eV and 452.34 eV, respectively [97,252]. The consistent spin-orbit splitting of 7.55 eV, attributed to the In-S bonding environment, remains invariant despite slight shifts in peak positions upon doping, as summarized in Table 15. These shifts towards lower binding energies suggest effective integration of the dopants into the γ-In_2S_3 lattice, indicating successful substitutional doping [138,252]. The observed redshift in In 3d binding energies post-doping is attributable to the lower electronegativity of Mg (1.31), Ca (1.00), and Sr (0.95) compared to In (1.78), resulting in increased electron density around In atoms and reduced binding energy. Moreover, the alkaline earth metal dopants, which possess fewer valence electrons and more intrinsic holes, lead to a shift in the Fermi level closer to the valence band maximum (VBM), as supported by the valence band spectra in Fig. 31c [240,253].

Table 15. In 3d and S 2p BE peak position upon doping for the synthesized materials

Samples	**In 3d BE peak position (eV)**		**S 2p BE peak position (eV)**	
	In $3d_{5/2}$	**In $3d_{3/2}$**	**$2p_{1/2}$**	**$2p_{3/2}$**
Pure γ-In_2S_3	444.79	452.34	162.48	161.34
Mg: γ-In_2S_3	444.90	452.45	162.48	161.32
Ca: γ-In_2S_3	444.56	452.11	162.52	161.43
Sr: γ-In_2S_3	444.67	452.23	162.45	161.32

Figure 31f presents high-resolution S 2p spectra for the samples, analyzed using quantum mechanically informed constraints based on the 2J + 1 rule, where J is defined as l + s (with l and s representing orbital and spin angular momentum quantum numbers, respectively). For pure γ-In_2S_3, the S $2p_{3/2}$ and S $2p_{1/2}$ peaks are observed at binding energies of 161.34 eV and 162.48 eV, respectively, with a spin-orbit splitting of 1.14 eV, corresponding to S^{2-} species [63,67,68]. Doping results in subtle shifts in the S 2p peak positions: Mg: γ-In_2S_3 exhibits a splitting of 1.16 eV, Ca: γ-In_2S_3 displays a reduced splitting of 1.09 eV, and Sr: γ-In_2S_3 shows a splitting of 1.13 eV. Notably, Ca: γ-In_2S_3 reveals a significant shift of the S 2p peaks toward higher binding energies compared to pure γ-In_2S_3, indicating electron transfer from S to In and the formation of S vacancies [69-71]. This interpretation is further supported by the diminished

intensity of the deconvoluted S 2p peaks in Ca: γ-In_2S_3, consistent with reduced S content. **Table 16** details the elemental composition and S vacancy concentrations as determined by XPS. The S vacancy concentration in Ca: γ-In_2S_3 is calculated at 3.78% relative to pure γ-In_2S_3, aligning well with results obtained from EDS analysis.

Table 16. Calculation of S_V concentration using XPS elemental composition analysis.

Samples	**In 3d (at%)**	**S 2p (at%)**	**Mg (at%)**	**Ca (at%)**	**Sr (at%)**	**S_V concentration (%)**
Pure γ-In_2S_3	39.79	60.21	-	-	-	0
Mg: γ-In_2S_3	37.61	60.32	2.07	-	-	-4.15
Ca: γ-In_2S_3	38.97	56.67	-	2.23	-	3.96
Sr: γ-In_2S_3	38.21	59.87	-	-	1.92	-2.24

Sulfur vacancy concentration calculation

The sulfur vacancy (S_V) concentration was calculated based on the difference in the S/In atomic ratio between pure γ-In_2S_3 and its doped variants Mg: γ-In_2S_3, Ca: γ-In_2S_3, and Sr: γ-In_2S_3. The calculation follows Equation (12):

$$S_V \text{ concentration } (\%) = \frac{S{:}In\ (\text{Pure } \gamma{-}In_2S_3) - S{:}In\ (\text{Doped } \gamma{-}In_2S_3)}{S{:}In\ (\text{Pure } \gamma{-}In_2S_3)} \qquad (12)$$

Elemental compositions of In and S, along with the dopants listed in **Table 16**, were obtained from XPS measurements. These values were further validated by fitting the XPS characteristic peak areas corresponding to each element.

6.3.4. Optical analysis

Understanding a material's bandgap is essential for assessing its photocatalytic performance. In this study, we employed UV-Vis spectroscopy to measure the absorbance of synthesized materials over a wavelength range of 300-1000 nm. Fig. 32a displays the optical absorption spectra of pure γ-In_2S_3, as well as its doped variants. The spectra reveal that pure γ-In_2S_3 exhibits strong optical absorption in the UV region, which gradually decreases as the wavelength extends into the visible region. Doping pure γ-In_2S_3 with Mg^{2+}, Ca^{2+}, and Sr^{2+} induces a bathochromic shift (redshift) in the absorption spectra towards the visible region, corresponding to a reduction in the optical bandgap energy (E_g). The bandgap values were

calculated using Tauc plots by extrapolating the tangent of the linear region in the plot of hν vs $(\alpha h\nu)^2$ to the energy axis, as shown in Fig. 32b. This approach is based on the equation:

$$(\alpha h\nu)^2 = A(h\nu - Eg) \qquad (12)$$

where α is the absorption coefficient, hν is the photon energy, and A is a proportionality constant [254]. The direct bandgap energy of pure γ-In_2S_3 is approximately 3.67 eV, in agreement with previous reports [100]. However, doping with Mg^{2+}, Ca^{2+}, and Sr^{2+} reduces the bandgap to 2.74 eV, 2.41 eV, and 2.91 eV, respectively. This reduction is attributed to the introduction of new energy levels within the semiconductor bandgap due to doping [243,244]. The reduced bandgap allows for an expanded light absorption spectrum, thereby enhancing the photocatalyst's optical properties. Furthermore, Fig. 32c presents the XPS valence band spectra, highlighting the valence band maximum (VBM) positions determined by extrapolating the XPS valence spectra to the x-axis [255]. The VBM positions for pure γ-In_2S_3, Mg: γ-In_2S_3, Ca: γ-In_2S_3, and Sr: γ-In_2S_3 are 3.23 eV, 2.12 eV, 1.61 eV, and 2.41 eV, respectively. Thereafter, using the formula $E_{CB} = E_g - E_{VB}$, the conduction band minimum (CBM) positions were calculated based on the obtained bandgap values, resulting in -0.44 eV, -0.62 eV, -0.80 eV, and -0.50 eV for the respective materials [256]. Additionally, Mott-Schottky measurements, as shown in Fig. 33d, were performed at 1000 Hz to investigate the electronic band structure of all four samples [138,247,257]. The flat-band potentials were determined by extrapolating the tangent to be -0.34 V, -0.52 V, -0.70 V, and -0.40 V versus NHE for pure γ-In_2S_3, Mg: γ-In_2S_3, Ca: γ-In_2S_3, and Sr: γ-In_2S_3, respectively. The positive slopes of the Mott-Schottky plots confirm the n-type semiconductor nature of all samples. Since the flat-band potential of n-type semiconductors is typically ~0.1 V more positive than the conduction band edge, the CBM were estimated at -0.44 V, -0.62 V, -0.80 V, and -0.50 V versus NHE for γ-In_2S_3, Mg: γ-In_2S_3, Ca: γ-In_2S_3, and Sr: γ-In_2S_3, respectively.

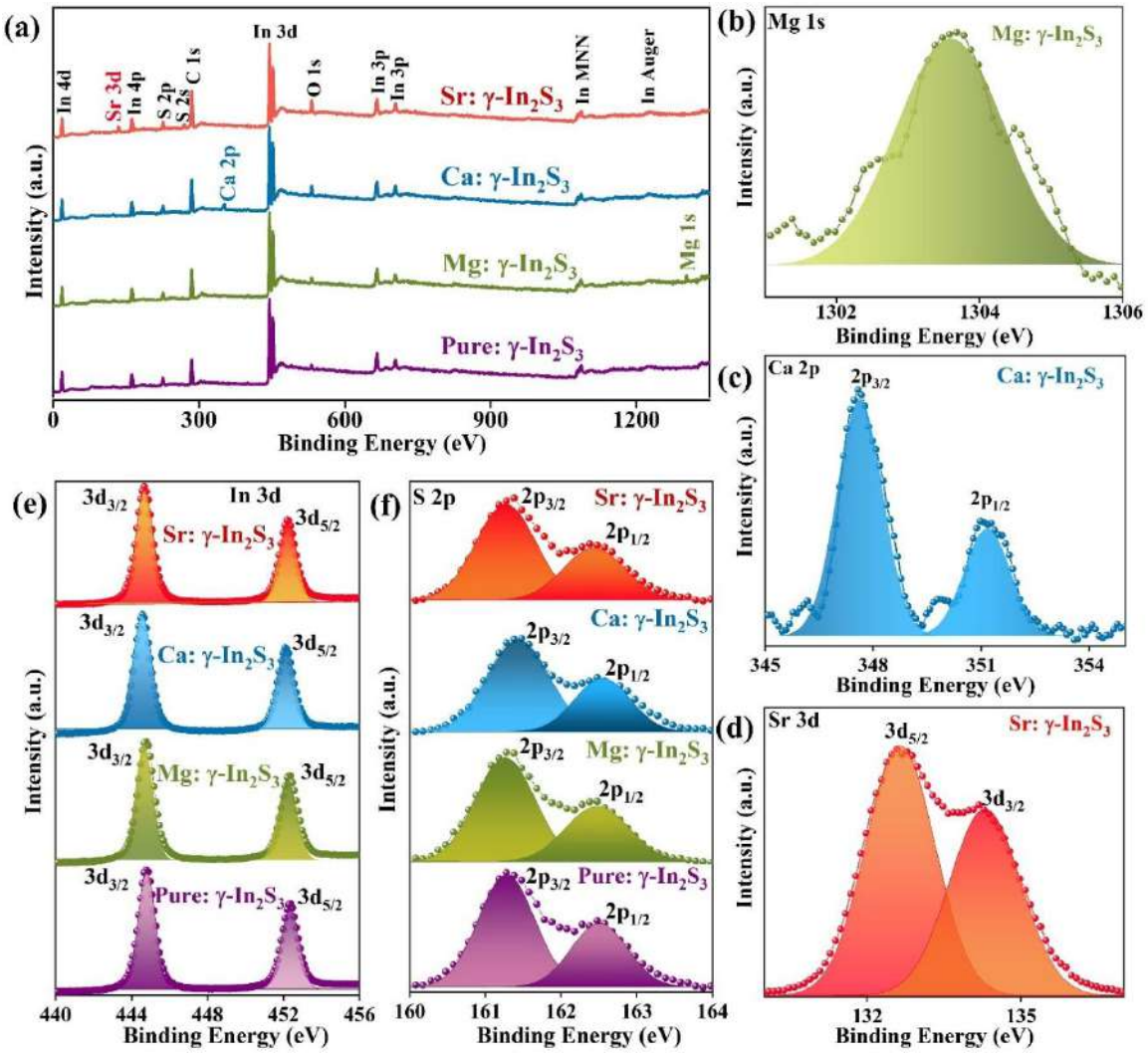

Fig. 31. (a) XPS full survey spectra of pure γ-In_2S_3, Mg: γ-In_2S_3, Ca: γ-In_2S_3, and Sr: γ-In_2S_3, (b) Mg 1s, (c) Ca 2p, (d) Sr 3d, (e) In 3d, and (f) S 2p high-resolution XPS spectra.

These results are consistent with values obtained from subtracting the bandgap from the XPS valence band position. Notably, Ca doping leads to a more negative CBM, attributed to the presence of abundant S vacancies, which enhances its suitability for photocatalytic H_2 evolution. The reduction in bandgap energy can be attributed to an increase in carrier concentration, which occupies energy states in the VB. This leads to an upward shift in the VBM, reducing the energy difference between the highest occupied molecular orbital (HOMO) in the VB and the lowest unoccupied molecular orbital (LUMO) in the CB [97,243,255]. This phenomenon, known as bandgap narrowing, is illustrated schematically in Fig. 32d.

6.3.5. Electrical analysis

Hall effect measurements using the van der Pauw configuration (Fig. 33a) were conducted to investigate the electrical properties of γ-In_2S_3 and its doped variants. Pure γ-In_2S_3 exhibited the

highest resistivity of 16.78 Ω cm. Doping with Sr^{2+}, Mg^{2+}, and Ca^{2+} progressively reduced the resistivity to 7.89 Ω cm, 5.22 Ω cm, and 2.78 Ω cm, respectively. In terms of Hall mobility, pure γ-In_2S_3 had a value of 4.4 $cm^2V^{-1}s^{-1}$, while Mg: γ-In_2S_3, Ca: γ-In_2S_3, and Sr: γ-In_2S_3 exhibited Hall mobilities of 10.4 $cm^2V^{-1}s^{-1}$, 14.1 $cm^2V^{-1}s^{-1}$, and 7.2 $cm^2V^{-1}s^{-1}$, respectively. Specifically, the Hall mobility of Ca: γ-In_2S_3 is more than three times higher than that of pure γ-In_2S_3, enabling photogenerated carriers to migrate more efficiently to the surface and thereby reducing recombination losses.

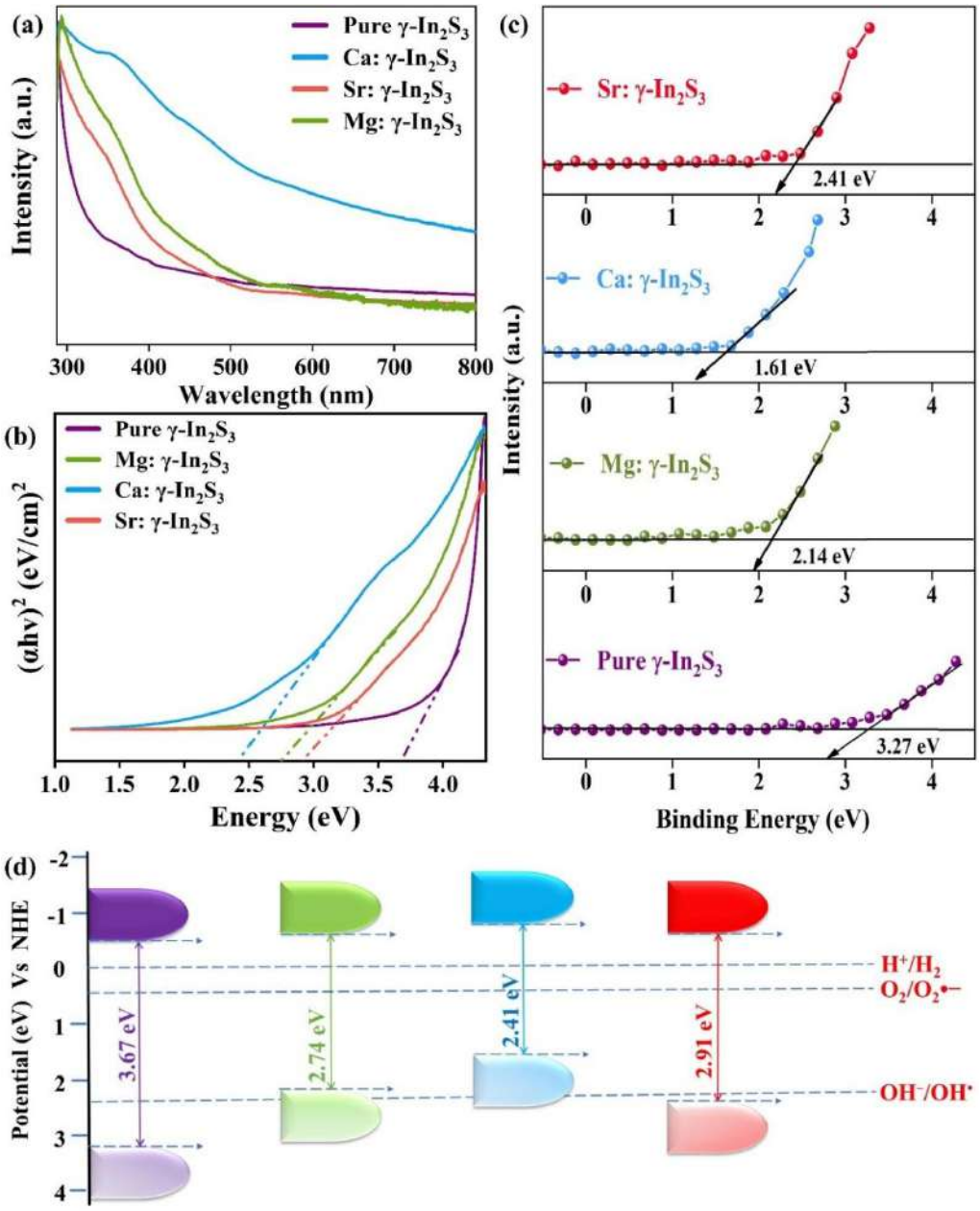

Fig. 32. (a) The absorbance spectrum, (b) Tauc plot of each curve accompanied by extrapolation lines of pure γ-In_2S_3, Mg: γ-In_2S_3, Ca: γ-In_2S_3, and Sr: γ-In_2S_3, (c) XPS Valence, and (d) Schematic illustration of band positions and redox potentials.

Subsequently, the charge carrier concentration in pure γ-In_2S_3 was found to be 1.2E17 cm^{-3}, while doping with Sr^{2+}, Mg^{2+}, and Ca^{2+} significantly increased the concentration to 6.7E18 cm^{-3}, 9.5E18 cm^{-3}, and 1.7E19 cm^{-3}, respectively. Clearly, Ca: γ-In_2S_3 exhibits the highest carrier concentration, significantly increasing the density of mobile charges available for surface reactions. To explicitly connect these transport parameters to charge-separation behavior, we quantified the charge separation efficiency using Eq. 13, which governs conductivity [258,259].

$$\sigma = q\mu n \qquad \text{Eq. 13}$$

where, σ is electrical conductivity ($S \cdot cm^{-1}$), q is the elementary charge of an electron (1.602×10^{-19} C), μ is carrier mobility ($cm^2V^{-1}s^{-1}$), n is carrier concentration (cm^{-3}).

Therefore, the calculated charge separation efficiency values are 5.28×10^{17} (Pure: γ-In_2S_3), 6.84×10^{19} (Mg: γ-In_2S_3), 6.97×10^{19} (Sr: γ-In_2S_3), and 2.40×10^{20} (Ca: γ-In_2S_3), indicating that Ca-doping enhances transport capacity by ~454 times relative to the pure sample. This trend (Ca: γ-In_2S_3 > Mg: γ-In_2S_3 > Sr: γ-In_2S_3 > pure: γ-In_2S_3) aligns with the EIS and PL results, which will be discussed in the upcoming sections. The substantially larger charge separation efficiency for Ca-doping thus reflects faster carrier drift and a greater density of mobile charges reaching surface sites before recombination, providing a direct quantitative link between improved charge mobility and carrier concentration, along with the superior photocatalytic H_2 evolution and 2,4-D degradation observed in Ca: γ-In_2S_3 [260,261]. Besides, this improvement in conductivity is closely linked to the dopant-induced modulation of the bandgap, which reduces the energy difference between the valence and conduction bands, facilitating electron excitation [254,261,262]. Furthermore, doping with Mg^{2+}, Ca^{2+}, and Sr^{2+} alters the electronic environment by redistributing electrons [263]. Electrons are transferred from the dopant sites to the In and S sites, driven by the higher electronegativities of In (1.78) and S (2.58) compared to Mg (1.31), Ca (1.0), and Sr (0.95) [264]. Additionally, the substitutional doping of Mg^{2+}, Ca^{2+}, and Sr^{2+} into In^{3+} sites, as confirmed by EDS analysis, introduces extra free electrons due to increased lattice parameters and weakened In/(Mg, Ca, Sr)-S bonds, further enhancing conductivity [265]. Notably, S vacancies in Ca: γ-In_2S_3 increase the material's electron affinity and promote photocatalytic efficiency by acting as electron traps [138,260,266]. Overall, the enhanced charge carrier mobility and improved electronic performance in the doped γ-In_2S_3 are attributed to the combined effects of dopant-induced changes in the crystal lattice and electronic environment.

The Nyquist plots from EIS (Fig. 33b) provide critical insights into electron transport resistance and charge mobilization efficiency. The semicircle radius, inversely related to charge transfer resistance, follows the order: pure γ-In_2S_3 (largest arc radius), Sr: γ-In_2S_3, Mg: γ-In_2S_3, and Ca: γ-In_2S_3 (smallest arc radius). This indicates that Ca: γ-In_2S_3 has the lowest electron transport resistance, reflecting superior conductivity and efficient charge transfer at the catalyst interface. These enhancements, attributed to improved electron migration and reduced electron-hole pair recombination, result in better charge separation [261,267]. The findings from EIS align well with Hall measurement results. As a result, Ca: γ-In_2S_3 demonstrates exceptional photocatalytic activity for H_2 evolution and 2,4-D degradation, as discussed in section 6.4. In contrast, pure γ-In_2S_3, with its larger impedance arc radius, suffers from less efficient charge separation and lower photocatalytic performance.

For a more comprehensive understanding, photoluminescence (PL) spectroscopy is crucial, as it provides valuable insights into charge carrier separation and recombination processes [257,268,269]. In our study, PL measurements were conducted to evaluate the photocatalytic performance of the as-synthesized semiconductor materials, pure: γ-In_2S_3 and Mg: γ-In_2S_3, Ca: γ-In_2S_3, and Sr: γ-In_2S_3. From Fig. 33c, the intensity of PL emission is indicative of the recombination rate of electron-hole (e^--h^+) pairs; lower emission intensity typically signifies

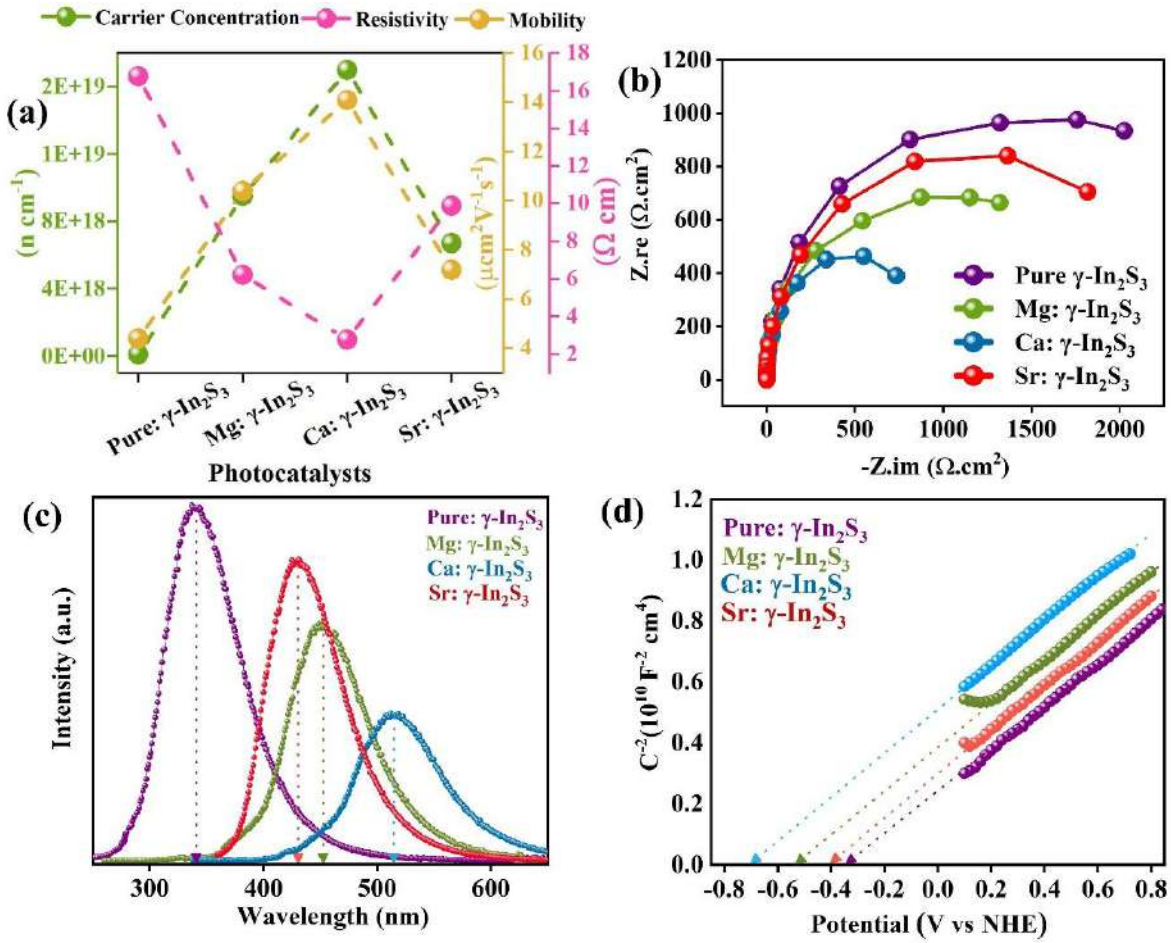

Fig. 33. Pure γ-In_2S_3, Mg: γ-In_2S_3, Ca: γ-In_2S_3, and Sr: γ-In_2S_3 (a) Hall measurements, (b) EIS Nyquist plots, (c) Photoluminescence spectra, and (d) Mott-Schottky Plot.

reduced recombination and extended carrier lifetimes. The PL emission peaks for the materials were identified at specific energies: pure γ-In_2S_3 at 341.02 eV, Mg: γ-In_2S_3 at 452.64 eV, Ca: γ-In_2S_3 at 514.39 eV, and Sr: γ-In_2S_3 at 430.57 eV, correlating with the bandgap observed in the absorption spectra. Notably, the trend in PL intensity revealed that pure γ-In_2S_3 exhibited the highest PL intensity, indicating weaker charge separation and stronger recombination. Followed by Sr: γ-In_2S_3, Mg: γ-In_2S_3, and Ca: γ-In_2S_3. Here, the lowest PL intensity is exhibited by Ca: γ-In_2S_3, indicating the most effective charge separation and minimal recombination. This behavior is attributed to S vacancies in Ca: γ-In_2S_3, which play a critical role in trapping and transporting photogenerated electrons and holes, consequently leading to a reduced recombination rate [138,260,270]. Consequently, the observed trend in PL intensity, Ca: γ-In_2S_3 < Mg: γ-In_2S_3 < Sr: γ-In_2S_3 < pure γ-In_2S_3, not only aligns well with EIS analysis but also aligns with the photocatalytic activity observed in these samples. Furthermore, the PL observations were corroborated by band alignment analysis via XPS and M-S, which indicated a more negative conduction band minimum (CBM) in Ca: γ-In_2S_3. This suggests a greater

reduction potential and an enhanced ability to produce reactive species, reinforcing the relationship between charge separation, recombination, and photocatalytic efficiency. In conclusion, employing PL spectroscopy in conjunction with EIS and Hall measurements provides a more comprehensive understanding of charge carrier behavior in photocatalysts, which is essential for assessing their efficiency and effectiveness.

6.4. Analysis of the Synthesized Nanoribbons for their Applicability in Photocatalytic H_2 Evolution and 2,4-Dichlorophenoxyacetic Acid Degradation.

This section focuses on the application of synthesized nanoribbons in photocatalytic H_2 evolution and 2,4-D degradation, corresponding to Objective 5. **Section 6.4.1** provides a comprehensive evaluation of photocatalytic H_2 generation performance, encompassing scavenger analysis, AQY, STH efficiency, and reusability assessments. **Section 6.4.2** focuses on the photocatalytic degradation of a persistent herbicide, 2,4-D, using the synthesized nanoribbons. Furthermore, extensive degradation experiments reveal the significant influence of experimental conditions, such as scavenger types, catalyst concentration, initial 2,4-D concentration, and solution pH, on the overall degradation efficiency.

6.4.1 Photocatalytic H_2 Evolution

To investigate the catalytic behavior of our samples, we conducted a photocatalytic H_2 evolution experiment using a series of as-synthesized photocatalysts: pure γ-In_2S_3, Mg: γ-In_2S_3, Ca: γ-In_2S_3, and Sr: γ-In_2S_3. Each sample was exposed to irradiation from a 300 W Xe lamp, with a 20% TEOA aqueous solution serving as a sacrificial agent for holes. The H_2 evolution profiles over time are presented in Figs. 34a and 34b. After 4 hours of irradiation, the pure γ-In_2S_3 sample produced only 142 μmol g^{-1} of H_2, with corresponding evolution rates of 35.5 μmol g^{-1} h^{-1}, indicating relatively low photocatalytic performance. This is likely due to poor charge separation and transfer efficiency, as suggested by EIS measurements. In contrast, the doped samples exhibited significantly enhanced performance. Ca: γ-In_2S_3 demonstrated the highest H_2 yield, producing 636 μmol g^{-1}, a remarkable 4.5-fold increase compared to the undoped sample. The maximum H_2 evolution rate for Ca: γ-In_2S_3 reached 159 μmol g^{-1} h^{-1}, showcasing a significant improvement attributed to multiple factors. Enhanced charge transport, the presence of electron-accumulating active sites, and electronic structure modifications facilitated by Ca^{2+} doping collectively contributed to this advancement. Moreover, the formation of Ca-S bonds during synthesis likely established efficient carrier transfer pathways, further boosting photocatalytic performance. As discussed earlier, the more

negative CBM observed from the M-S plot at -0.80 eV is optimally positioned for proton reduction, while the presence of S vacancies increases electron density, thereby enhancing the overall efficiency of the process [138]. When compared to pure γ-In_2S_3, the Mg: γ-In_2S_3 and Sr: γ-In_2S_3 showed improved H_2 evolution of 456 μmol g^{-1} and 232 μmol g^{-1}, respectively, with corresponding H_2 evolution rates of 104 μmol g^{-1} h^{-1} and 58 μmol g^{-1} h^{-1}. However, these rates were lower than that of Ca: γ-In_2S_3, likely due to higher recombination rates of photogenerated carriers and comparatively less favorable electronic structures. Among the doped samples, Sr: γ-In_2S_3 exhibited the poorest performance, attributed to its lower S vacancy density and less negative VBM position, which hindered efficient H_2 evolution. Overall, the results highlight the superior photocatalytic performance of Ca: γ-In_2S_3, emphasizing the critical role of doping in optimizing charge dynamics and electronic properties for enhanced H_2 evolution.

The amount of H_2 produced with the AQY and STH conversion efficiency at different wavelengths for Ca: γ-In_2S_3 was evaluated using a series of band-pass filters (Fig. 34c and Table 17) [271–273]. The AQY closely follows the absorption profile of Ca: γ-In_2S_3 as determined by UV-vis spectroscopy, reaching 10.47% at 400 nm and 7.92% at 420 nm, confirming that the photocatalytic reaction is driven by light absorption. Control experiments performed in the dark or without the photocatalyst showed no H_2 evolution, further demonstrating that the H_2 evolution is indeed photocatalytic. Furthermore, the STH conversion efficiency was determined to be 0.604% at 400 nm and 0.480% at 420 nm.

Table 17. Experimental parameters and the calculated AQY values for Ca: γ-In_2S_3 under monochromatic light.

λ (nm)	I (mW/cm^3)	H_2 amount (μmol)	AQY (%)	STH (%)
400 ±15	2.0	174 ± 1.7	10.47 ± 0.10 %	0.604
420 ±15	2.3	159 ± 2.5	7.92 ± 0.12 %	0.480
450 ±15	4.7	79.5 ± 1.8	1.81 ± 0.04 %	0.117
500 ±15	10.7	55.4 ± 0.5	0.49 ± 0.00 %	0.036
550 ±15	12.2	32.7 ± 1.4	0.23 ± 0.01 %	0.018
600 ±15	12.9	7.3 ± 0.9	0.05 ± 0.01 %	0.003

Thereafter, we analyzed the effects of various scavengers on the H_2 evolution performance of the best-performing Ca: γ-In_2S_3 photocatalyst, with 300 W Xe lamp (λ = 400nm) as presented in Fig. 34d. The selected scavengers included some of the most commonly used reagents: 20% TEOA (basic solution), 20% MeOH (neutral), 20% LA (acidic solution), and a mixed alkaline

solution of 0.35 M Na_2S/0.25 M Na_2SO_3. The results showed a clear variation in H_2 evolution efficiency depending on the type of scavenger. MeOH yielded the lowest H_2 evolution rate, approximately 13 μmol $g^{-1}h^{-1}$, indicating limited effectiveness as a hole scavenger in this context. The Na_2S/Na_2SO_3 solution produced slightly more H_2 at 31 μmol $g^{-1}h^{-1}$, while LA led to a further increase, reaching 52 μmol $g^{-1}h^{-1}$. TEOA, however, stood out as the most effective scavenger, achieving an H_2 evolution rate of 172 μmol $g^{-1}h^{-1}$. This enhanced activity can likely be attributed to the alkaline nature of TEOA, which increases the surface electronegativity of the catalyst, thereby improving its ability to capture photogenerated h^+ [261]. The pH of the TEOA solution (~12) contributes further by creating a favorable environment for H_2 evolution. Additionally, TEOA's relatively low oxidation potential (0.56 eV) may allow for efficient oxidation processes, promoting stronger interfacial bonding on the catalyst surface and facilitating an efficient reaction with photogenerated h^+. This, in turn, helps reduce electron-hole recombination, enhancing overall H_2 evolution. Interestingly, although the Na_2S/Na_2SO_3 solution also has an alkaline pH, its H_2 evolution was much lower than TEOA's. This reduced yield may be due to competing reduction reactions occurring between the Na_2S/Na_2SO_3 solution and the photocatalyst, which could consume active electrons that would otherwise contribute to H_2 evolution [274]. In contrast, TEOA not only acts effectively as a hole scavenger but also minimizes competing reactions, enabling a more efficient pathway for H_2 evolution on the Ca: γ-In_2S_3 catalyst.

Ensuring recurring stability is highly essential for the practical implementation of photocatalysts [142]. Thus, the stability of the best-performing Ca: γ-In_2S_3 photocatalyst was evaluated through photocatalytic H_2 evolution over five cycles of 20 hours under 300W Xe light irradiation (as shown in Fig. 34e). To establish an inert environment for the H_2 evolution reaction, the photocatalyst dispersed in solution with 3 ml of 20% TEOA was subjected to degassing and purging with N_2 gas prior to each light irradiation cycle. Notably, a slight decline in photocatalytic efficiency was observed by the third cycle, leading to the hypothesis that scavenger oxidation might be contributing to this drop. To mitigate this effect, an additional 3 ml of 20% TEOA was introduced to the reaction setup, which helped maintain H_2 evolution levels. After the fifth cycle, the Ca: γ-In_2S_3 catalyst demonstrated remarkable stability, retaining 91.3% of its original photocatalytic efficiency. To evaluate the stability of the catalyst, the photocatalyst was thoroughly washed and dried after each cycle to remove any residual substances. It was then analyzed using XRD (Fig. 35), which showed no notable alterations in the diffraction pattern. Likewise, the FESEM images (Fig. 34f) show that there were no discernible changes in the photocatalyst, suggesting that it retains its structural stability

during the process. These results, along with recycling and extended irradiation tests, confirmed that Ca: γ-In_2S_3 exhibits excellent stability and durability across multiple cycles.

A comparative study of H_2 evolution performance among various reported indium-based metal sulfide photocatalysts, including the materials synthesized in this work, is presented in Fig. 34g. Among the ternary photocatalysts examined, Pd-Vs-$ZnIn_2S_4$ exhibited the highest H_2 evolution rate of 185.6 μmol h^{-1}, highlighting the exceptional efficiency of $ZnIn_2S_4$-based systems enhanced by Pd doping [138]. In contrast, for binary systems, Ca-doped β-In_2S_3 co-doped with 1 wt% Pt exhibited a significantly enhanced H_2 evolution rate of 145 μmol h^{-1}. However, in the absence of Pt, the material showed no activity for photocatalytic H_2 evolution [46]. While this demonstrates the potential of Ca-doped β-In_2S_3 under optimized conditions, the reliance on noble metal co-catalysts such as Pt imposes substantial limitations in terms of cost, scalability, and long-term practical applicability. Other ternary materials, such as $MgIn_2S_4$, also demonstrated reasonable H_2 evolution rates, achieving up to 133.8 μmol h^{-1} under certain conditions [275]. $ZnIn_2S_4$-based doped materials, such as Mo-$ZnIn_2S_4$ (92.4 μmol h^{-1}) and Ni-$ZnIn_2S_4$ (84.3 μmol h^{-1}) [272], also exhibited decent performance. In contrast, binary systems like Pd-Vs-In_2S_3 showed a moderate amount of 58.4 μmol h^{-1} [138]. It is noteworthy that the doped γ-In_2S_3 photocatalysts synthesized in this study demonstrated remarkable improvements in H_2 evolution activity. Specifically, Ca: γ-In_2S_3 achieved an impressive H_2 evolution rate of 172 μmol h^{-1}, followed by Mg: γ-In_2S_3 at 104 μmol h^{-1} and Sr: γ-In_2S_3 at 58 μmol h^{-1}. These values represented significant enhancements over the pure γ-In_2S_3, which exhibited a lower rate of 35.5 μmol h^{-1}.

Advanced ternary systems, such as $ZnIn_2S_4$ and $MgIn_2S_4$, have demonstrated superior H_2 evolution rates, especially when combined with heterojunctions involving plasmonic metals, carbonaceous materials, or other semiconductors. In this study, we introduced alkaline earth metal-doped γ-In_2S_3 for the first time, and it exhibited improved performance as a standalone system without relying on heterojunctions or expensive noble co-dopants. Given these promising results, the incorporation of a heterojunction with the as-synthesized γ-In_2S_3-based

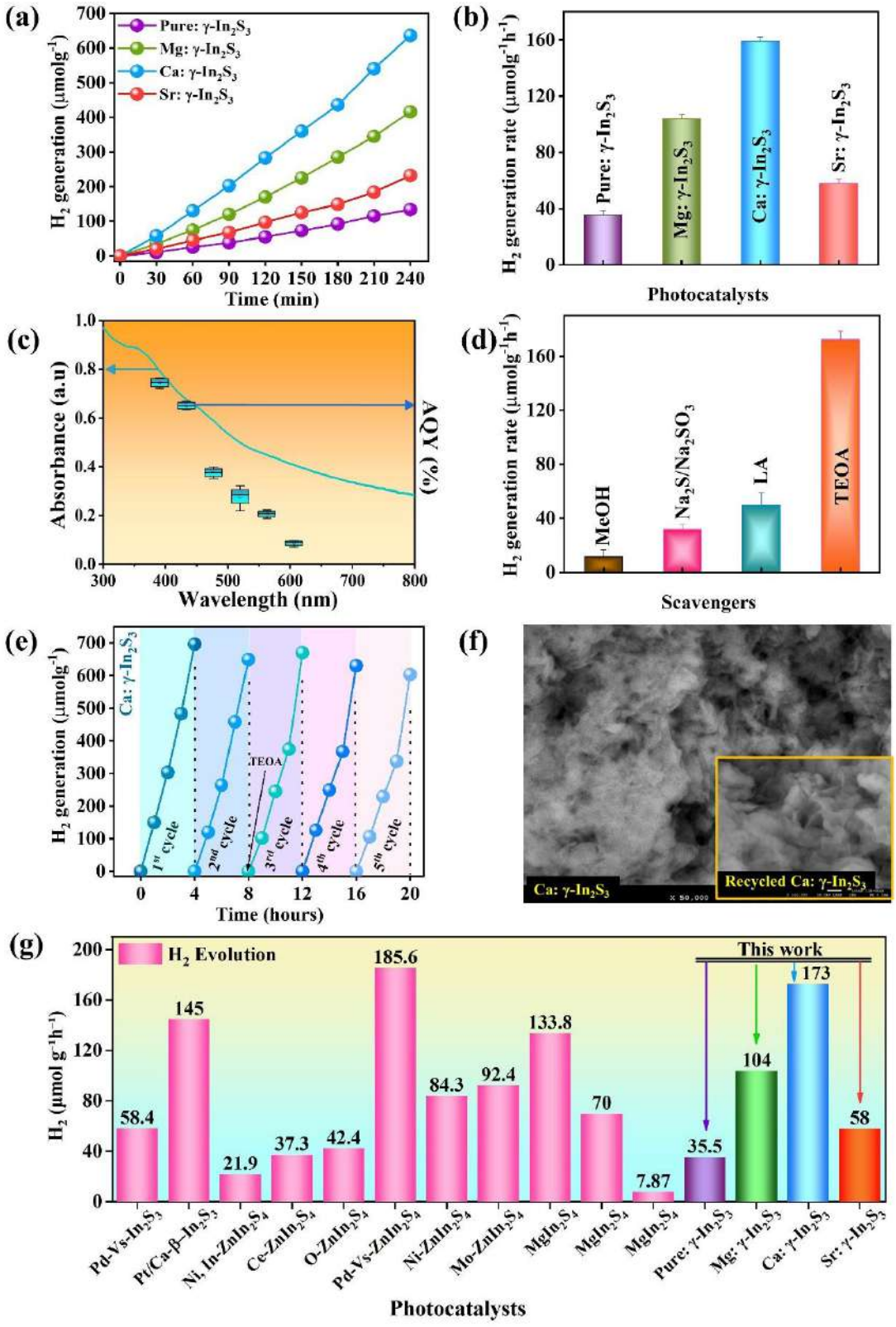

Fig. 34. (a) & (b) H_2 evolution over time and H_2 evolution rates comparison pure γ-In_2S_3, Mg: γ-In_2S_3, Ca: γ-In_2S_3, and Sr: γ-In_2S_3; (c) AQY, (d) Effect of scavengers on H_2 evolution, (e) reusability test, and (f) FESEM images of reused material after fifth cycle of best performing

Ca: γ-In_2S_3 and (g) comparison of photocatalytic H_2 evolution with the previously reported In_2S_3-based chalcogen photocatalysts.

photocatalysts could further enhance their H_2 evolution potential, offering significant improvements in a shorter timeframe. This could be an exciting avenue for future research, exploring ways to maximize the photocatalytic efficiency of γ-In_2S_3-based systems.

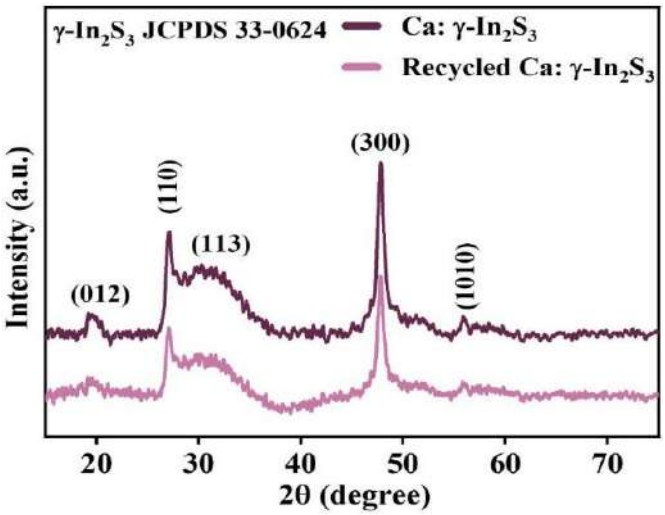

Fig. 35. XRD pattern of reused best-performing Ca: γ-In_2S_3 after the fifth cycle of photocatalytic H_2 evolution.

6.4.2. Photocatalytic Degradation of 2,4-D

The photolysis evaluation of a 40 ppm 2,4-D aqueous solution, as illustrated in Fig. 36a, was performed without the use of a photocatalyst. This study revealed that the 2,4-D molecule exhibited significant stability, remaining largely unaffected even after 240 minutes of UV-Vis irradiation. The synthesized materials were then evaluated for their photocatalytic efficiency in degrading 2,4-D under UV-Vis light. To enhance the adsorption of the herbicide onto the surface of the photocatalyst, the reaction mixture was agitated in darkness for one hour prior to the photocatalytic testing. The absorption spectra corresponding to the degradation of 2,4-D are presented in Figs. 36b - 36e, demonstrating the impact of irradiation time on pure γ-In_2S_3, Mg: γ-In_2S_3, Ca: γ-In_2S_3, and Sr: γ-In_2S_3.

The 2,4-D molecule features an aromatic ring structure with two chlorine atoms and an attached -OCH_2COOH group. This molecular arrangement facilitates conjugation between the aromatic ring and the lone pairs of electrons on the chlorine and oxygen atoms. The absorption spectra showed three distinct peaks at 282.43 nm, 228.67 nm, and 204.05 nm, corresponding to the chromophore groups of 2,4-D. Specifically, the peak at 282.43 nm is attributed to the n→π*

transitions associated with the C-Cl bonds. The peaks at 204.05 nm and 228.67 nm are linked to $\pi \rightarrow \pi^*$ transitions within the aromatic rings [141,154].

As the irradiation time increased, the intensity of all three peaks gradually diminished. Fig. 36f illustrates the relationship between the dimensionless concentration of 2,4-D (C/C_0) and irradiation time for all samples. The kinetic behavior of 2,4-D decomposition for pure γ-In_2S_3, Mg: γ-In_2S_3, Ca: γ-In_2S_3, and Sr: γ-In_2S_3 was analyzed by monitoring the maximum absorbance peak at 228.67 nm. Fig. 36g further demonstrates the impact of the initial concentration of 2,4-D on photocatalytic degradation. The degradation patterns of the herbicide followed an apparent pseudo-first-order kinetic model, as described by Eqn 14-16 [161]:

$$C = C_0 e - kt \qquad (14)$$

$$C/C_0 = e - kt \qquad (15)$$

$$-lnC/C_0 = kt \qquad (16)$$

The experimental data was validated by fitting it with an exponential curve, and nonlinear least squares methods were applied to the rate equation obtained from this fitting. From these analyses, kinetic parameters, correlation coefficients (R^2), and apparent rate constants (k_{app} min^{-1}) were calculated for all four synthesized samples. The detailed results are presented in **Table 18**, showing a strong agreement between the experimental data and the expected kinetic model.

Table 18. Kinetic parameters of 2,4-D photocatalytic degradation under UV light irradiation.

Sample	**K_{app} (min^{-1})**	**R^2**
Pure γ-In_2S_3	0.0982	0.9972
Mg: γ-In_2S_3	0.1000	0.9934
Ca: γ-In_2S_3	0.0942	0.9451
Sr: γ-In_2S_3	0.0919	0.9839

Fig. 36h presents a histogram depicting the photocatalytic degradation efficiency (η) for all four samples over the irradiation period. Specifically, the η values for pure γ-In_2S_3, Mg: γ-In_2S_3, Ca: γ-In_2S_3, and Sr: γ-In_2S_3 in degrading the aromatic peak at 228.67 nm were determined to be 78.38%, 90.72%, 95.47%, and 85.22% at 240 minutes, respectively. These results underscore the effectiveness of doping in enhancing photocatalytic performance.

The systematic introduction of Mg^{2+}, Ca^{2+}, and Sr^{2+} dopants into pure γ-In_2S_3 resulted in a progressive reduction in the bandgap, which likely contributed to the observed trend of enhanced photocatalytic degradation performance. The reduced bandgap allows a more significant portion of the incident light to have sufficient energy to induce electron excitation [106]. This suggests that the dopants play a crucial role in modifying the band structure of pure γ-In_2S_3, thereby improving its photocatalytic efficiency. Among the prepared materials, Ca: γ-In_2S_3 exhibited the smallest bandgap, leading to superior light absorption capabilities and the highest photocatalytic performance. The enhanced photocatalytic degradation observed in Ca: γ-In_2S_3 nanoribbons can be attributed to several factors. Firstly, the incorporation of Ca^{2+} into the γ-In_2S_3 lattice causes significant lattice distortion and defect formation due to the ionic radius mismatch between Ca^{2+} (0.99 Å) and In^{3+} (0.81 Å). These lattice imperfections act as effective traps for photogenerated electron-hole pairs, reducing their recombination rate and enhancing photocatalytic activity, as confirmed by PL and EIS studies [105]. Secondly, the narrowing of the bandgap increases light absorption, generating more electron-hole pairs and further boosting the photocatalytic efficiency. Thirdly, the high specific surface area suggests that Ca doping not only alters the electronic properties but also promotes surface rearrangement, thereby increasing the number of accessible active sites and facilitating better charge transfer dynamics. Additionally, S vacancies, as encountered in XPS analysis of Ca: γ-In_2S_3, facilitate the evolution of reactive oxygen species (ROS), with conduction band

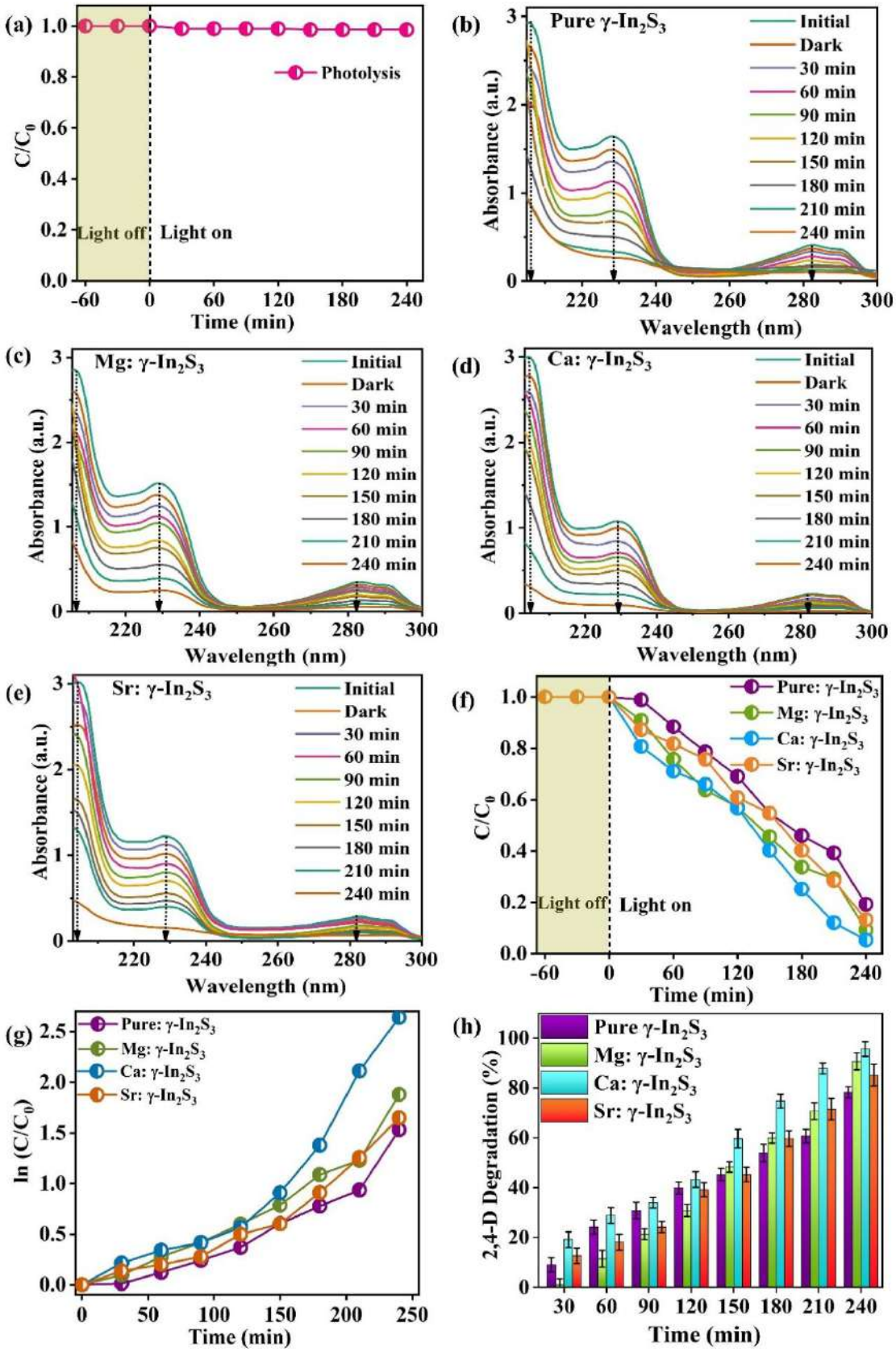

Fig. 36. (a) Photolysis, (b-e) UV absorption spectra of the degradation of 2,4-D, (f) adsorption kinetics of 2,4-D at different irradiation times, (g) kinetics of 2,4-D degradation, and (h) 2,4-D degradation efficiency of pure γ-In_2S_3, Mg: γ-In_2S_3, Ca: γ-In_2S_3, and Sr: γ-In_2S_3, respectively.

electrons reducing O_2 to $O_2^{\bullet-}$, a key agent in 2,4-D degradation [72,80]. Although the lower valence band position of Ca: γ-In_2S_3 (1.61 eV) limits OH• generation, ROS generation pathways dominate, supported by the presence of S vacancies, which is discussed in detail in the next section. This, further, along with the significantly reduced resistivity and enhanced conductivity of the material as studied from Hall measurements, underscores its superior photocatalytic performance.

6.4.2.1. Role of scavengers in photocatalytic degradation of 2,4-D.

To investigate the roles of primary reactive species, hydroxyl radicals (OH•), superoxide radicals (O_2•−), and photogenerated holes (h^+) in the photocatalytic degradation of 2,4-D, a series of radical scavenging experiments was performed using both Ca: γ-In_2S_3 and pure γ-In_2S_3. Specific scavengers were introduced at a concentration of 5 mM to selectively inhibit the activity of the target reactive species. MeOH was used to scavenge OH•, benzoquinone (BQ) to trap O_2•−, and ethylenediaminetetraacetic acid disodium salt (EDTA-2Na) to quench photogenerated h^+ [160,161,276]. Each scavenger was added to the reaction system prior to catalyst introduction, and a control experiment (blank) was conducted in parallel without any scavenger. The results for Ca: γ-In_2S_3 (Figs. 37a and 37b) showed that the degradation efficiency of 2,4-D significantly decreased upon the addition of the scavengers. Specifically, EDTA-2Na reduced the degradation efficiency from 98% (initial) to 33%, indicating that photogenerated holes are the crucial reactive species. BQ suppressed degradation to 41%, confirming the significant involvement of $O_2^{\bullet-}$ radicals. In contrast, MeOH resulted in a negligible effect, with 94% degradation, suggesting that •OH radicals play a minor role.

To validate these findings and assess possible background interferences, similar experiments were conducted using pure γ-In_2S_3 under the same reaction conditions (Figs. 37c and 37d). In the absence of scavengers, pure γ-In_2S_3 achieved a degradation efficiency of 78%. The addition of EDTA-2Na, BQ, and MeOH led to reductions in efficiency to 56.8%, 40.6%, and 37.6%, respectively. Although the degradation activity of the pure γ-In_2S_3 was lower than that of the Ca: γ-In_2S_3 photocatalyst, the suppression trends clearly indicate that •OH and O_2•− are also the primary active species in the pure γ-In_2S_3 system. The more pronounced impact of MeOH in the pure γ-In_2S_3 system (compared to the doped one) suggests a significant role for •OH radicals, followed by O_2•− and h^+. The conduction band of Ca: γ-In_2S_3 is more negative than the redox potential of the O_2/O_2•− pair (-0.33 V vs. NHE), enabling effective generation of O_2•− radicals. However, the valence band maximum (VBM) is less positive than the potential required to oxidize OH^- into OH• radicals [($OH•/OH^-$) = 1.99 V vs. NHE], preventing the

formation of OH•. In summary, the scavenging experiments reveal that both pure γ-In_2S_3 and Ca: γ-In_2S_3 nanoribbons follow the same degradation mechanism, where photogenerated h^+ and O_2•− radicals are the primary contributors for the photocatalytic degradation of 2,4-D. However, for Ca: γ-In_2S_3, OH• radicals contribute negligibly due to the insufficient valence band potential for their generation. In contrast, pure γ-In_2S_3 possesses a more positive valence band, enabling OH• formation, and the more potent inhibition observed with MeOH confirms that OH• plays a significant role alongside h^+ and O_2•− in this system.

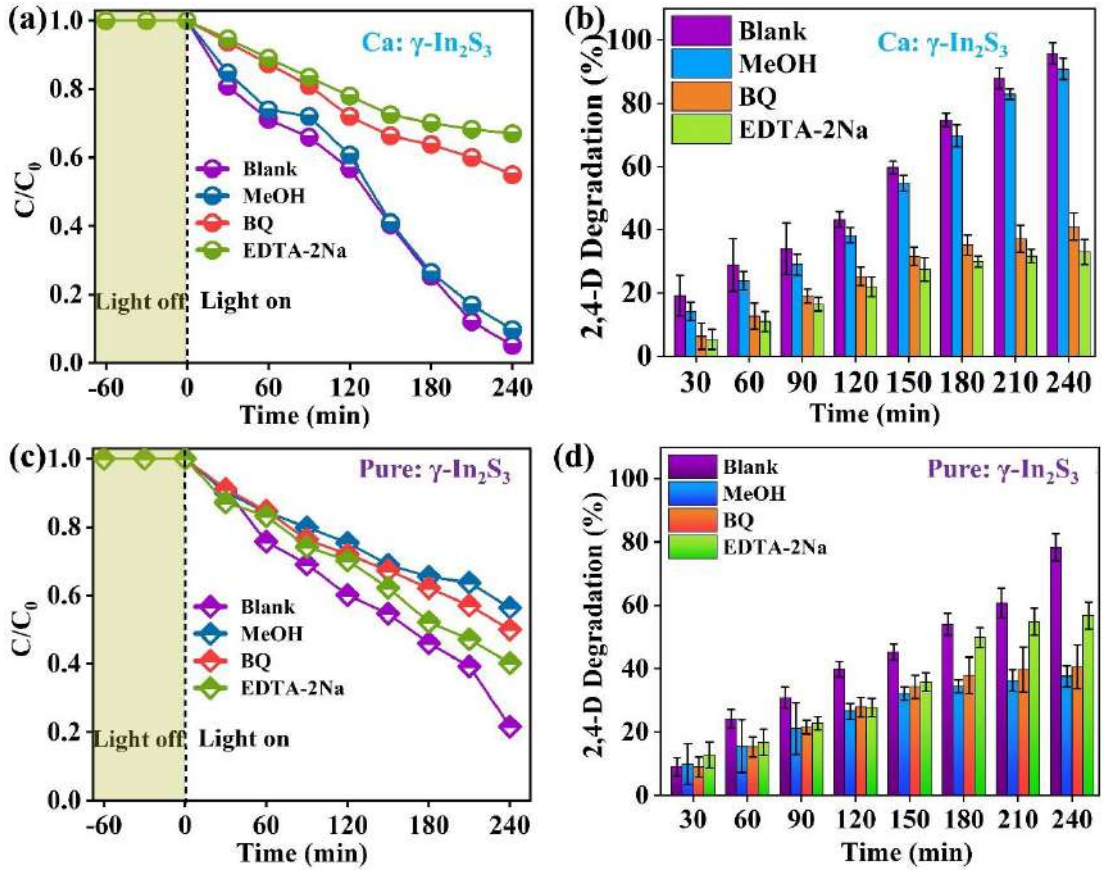

Fig. 37. Effect of scavenger on 2,4-D degradation using (a-b) the best-performing Ca: γ-In_2S_3 and (c-d) Pure: γ-In_2S_3.

6.4.2.2. Effect of varying photocatalyst concentration on photocatalytic degradation of 2,4-D.

The effect of varying Ca: γ-In_2S_3 nanoribbon dosages, specifically 20 mg, 30 mg, 40 mg, and 50 mg, on the degradation of 2,4-D (40 ppm) was evaluated and is presented in Figs. 38a and 38b. The results show that the degradation efficiency increased with catalyst dosage up to 40 mg, achieving a maximum degradation of 98.24%. However, a further increase to 50 mg resulted in a slight decline in degradation performance. This decline at higher dosages can be

attributed to several phenomena. Excess catalyst can increase the turbidity of the solution, reducing light penetration and, consequently, the effective activation of photocatalyst particles [277–279]. Furthermore, excessive catalyst loading can lead to agglomeration, which decreases the available active surface area and promotes light scattering, both of which negatively affect degradation efficiency.

To ensure consistency and provide comparative insights, the same dosage-dependent study was also carried out using pure γ-In_2S_3 (Figs. 38c and 38d). A similar trend was observed: degradation efficiency improved up to 40 mg of catalyst, after which it plateaued or slightly declined. At the optimal dosage of 40 mg, the degradation efficiencies were 83% for pure γ-In_2S_3 and 98.24% for Ca: γ-In_2S_3 nanoribbons, clearly demonstrating the enhanced photocatalytic performance imparted by Ca doping. The consistent trends observed in both Ca: γ-In_2S_3 and pure γ-In_2S_3 systems, under identical experimental conditions, confirm that the optimal photocatalyst dosage for both materials is 40 mg. This dosage was therefore selected for all subsequent experiments to ensure comparability and reproducibility.

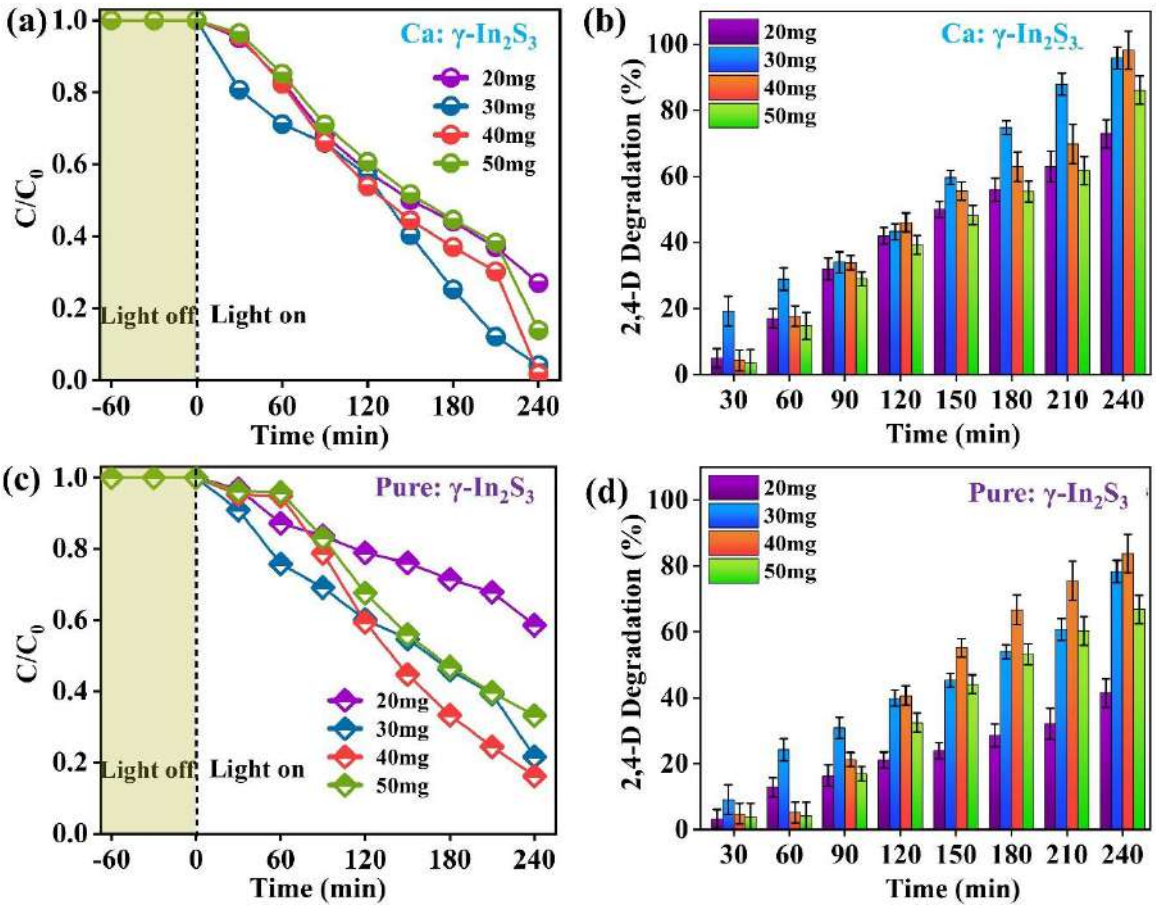

Fig. 38. Effect of varying photocatalyst on 2,4-D degradation using (a-b) the best-performing Ca: γ-In_2S_3 and (c-d) Pure: γ-In_2S_3.

6.4.2.3. Effect of varying 2,4-D initial concentration on photocatalytic degradation of 2,4-D.

To evaluate the influence of initial 2,4-D concentration on photocatalytic performance, degradation experiments were conducted using 40 mg of catalyst and varying 2,4-D concentrations of 40 ppm, 60 ppm, and 80 ppm. This study was carried out using both Ca: γ-In_2S_3 and pure γ-In_2S_3, under identical experimental conditions. As illustrated in Fig. 39a and 39b, the degradation efficiency of Ca: γ-In_2S_3 decreased as the initial 2,4-D concentration increased. After 240 minutes of light irradiation, the degradation efficiencies for 40 ppm, 60 ppm, and 80 ppm were 98.24%, 96.26%, and 62%, respectively. The minimal difference in degradation between 40 ppm and 60 ppm indicates that 40 mg of catalyst was sufficient to degrade up to 60 ppm of 2,4-D with high efficiency. However, at 80 ppm, the performance declined significantly, suggesting saturation of the catalyst's active sites and reactive species.
This reduction in degradation rate at higher concentrations of 2,4-D can be explained by the reaction dynamics between the adsorbed 2,4-D molecules and $OH^{\bullet}$ radicals formed on the surface of the Ca: γ-In_2S_3 nanoribbons. As the initial concentration of 2,4-D increases, more of it gets adsorbed on the catalyst's surface. However, at higher concentrations, the production of intermediates also increases, which then compete with the original 2,4-D molecules for adsorption sites on the catalyst. Despite the increased adsorption of 2,4-D, the concentration of $OH^{\bullet}$ radicals, which remains relatively constant due to steady light intensity, catalyst loading, and oxygen levels, does not increase proportionally. This results in a lower $OH^{\bullet}$/2,4-D ratio, leading to a reduced photocatalytic degradation rate [163,278].
Notably, Ca: γ-In_2S_3 demonstrated better performance than the undoped counterpart under all tested concentrations. When using pure γ-In_2S_3 (Figs. 39c and 39d), a similar concentration-dependent trend was observed, with degradation efficiencies of 83%, 66%, and 51% at 40 ppm, 60 ppm, and 80 ppm, respectively. However, in contrast to the doped sample, the drop in efficiency from 40 ppm to 60 ppm was more pronounced for the pure γ-In_2S_3. This performance disparity can be primarily attributed to structural differences between the two materials. On the other hand, Ca doping significantly enhances the physical characteristics of the catalyst. Ca: γ-In_2S_3 exhibits a specific surface area approximately 60% greater than that of pure γ-In_2S_3. The increased surface area facilitates better 2,4-D adsorption and provides more accessible active sites for redox reactions, contributing to the enhanced degradation performance. Moreover, improved charge separation and reduced recombination enabled by the presence of Ca further contribute to the superior photocatalytic efficiency and higher tolerance to increased 2,4-D

concentration. Based on these findings, 40 ppm and 60 ppm were selected as the standard initial concentration for pure γ-In_2S_3 and Ca: γ-In_2S_3, respectively, for subsequent pH-dependent photocatalytic experiments.

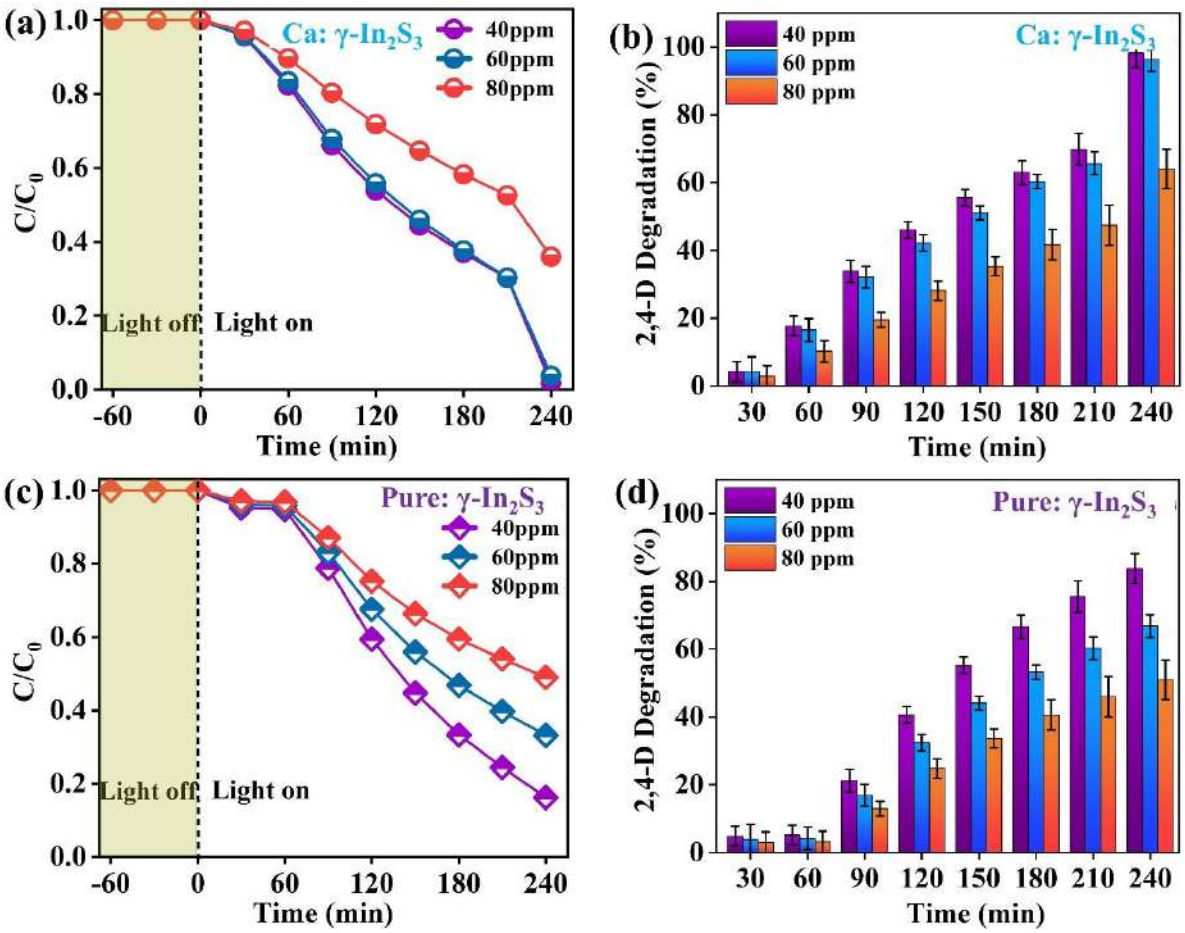

Fig. 39. Effect of initial 2,4-D concentration variations on its degradation (a-b) the best-performing Ca: γ-In_2S_3 and (c-d) Pure: γ-In_2S_3.

6.4.3.4. Effect of varying pH on photocatalytic degradation of 2,4-D.

The impact of pH on the photocatalytic degradation of 2,4-D was systematically studied across a pH range of 1 to 11, with a constant photocatalyst dosage of 40 mg Ca: γ-In_2S_3 used for 60 ppm of 2,4-D. The experiments were conducted using both Ca: γ-In_2S_3 and pure γ-In_2S_3 under identical conditions to evaluate the influence of surface charge and electrostatic interactions on photocatalytic activity. The study revealed that degradation efficiency is highly pH-dependent. As shown in Figs. 41a and 41b, the degradation efficiency while using Ca: γ-In_2S_3 peaked at pH 3, reaching 99.53%. At pH 5, efficiency remained high at 94.67% but declined at pH 7 to 76.9%. The lowest efficiencies were recorded in alkaline conditions, with 53% at pH 9 and 33% at pH 11. At pH 1, the degradation efficiency was 62.38%, which is lower than at pH 3.

This reduced efficiency can be attributed to the fact that, at pH 1, 2,4-D predominantly exists in its positively charged form.

To elucidate this trend, zeta potential (ζ-potential) measurements were carried out to assess the pH-dependent surface charge behavior of the catalysts (Fig. 40). The point of zero charge (pH_{pzc}) for Ca: γ-In_2S_3 was determined to be 5.6. Below this pH, the catalyst surface carries a positive charge, and above it, a negative charge due to deprotonation of surface hydroxyl groups. Since 2,4-D has a pKa of approximately 2.64, it exists in anionic form at pH ≥ 3. At pH 3, strong electrostatic attraction between the positively charged catalyst surface and negatively charged 2,4-D molecules enhances adsorption and subsequent degradation. At pH > 5.6, both the catalyst and 2,4-D are negatively charged, resulting in electrostatic repulsion and diminished degradation efficiency.

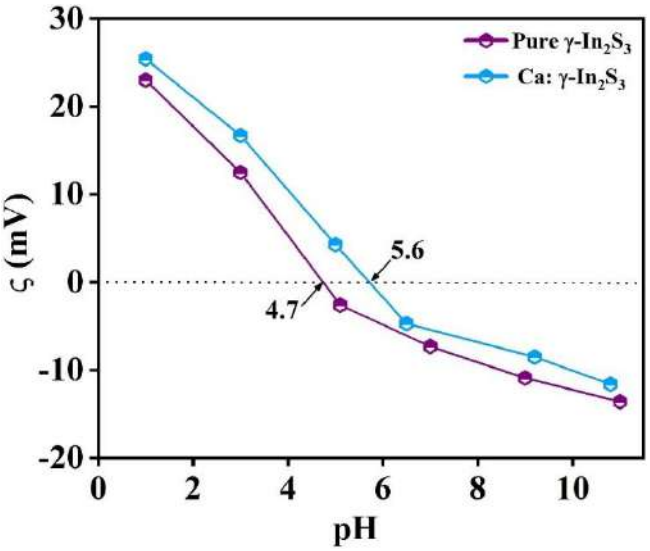

Fig. 40. Zeta Potential for estimation of Surface charge densities of pure γ-In_2S_3 and Ca: γ-In_2S_3.

Interestingly, similar pH-dependent behavior was observed for pure γ-In_2S_3, as shown in Figs. 41c and 41d. The degradation efficiencies at pH 1, 3, 5, 7, 9, and 11 were 61%, 83%, 76%, 53%, 41%, and 33%, respectively. The highest efficiency (83%) occurred at pH 3, aligning with the results from the Ca: γ-In_2S_3, though at a lower magnitude. The pH_{pzc} for pure γ-In_2S_3 was found to be 4.7, slightly lower than that of the Ca: γ-In_2S_3. At pH 3, the undoped catalyst surface is also positively charged, enabling strong electrostatic attraction with anionic 2,4-D species and efficient degradation. At pH 1, degradation was lower (61%), likely due to excess protonation disrupting surface charge stability and blocking active sites. In summary, both Ca: γ-In_2S_3 and pure γ-In_2S_3 show optimal photocatalytic degradation of 2,4-D under mildly acidic

conditions (pH 3), driven by favorable electrostatic interactions between the positively charged catalyst surfaces and anionic pollutant species [32].

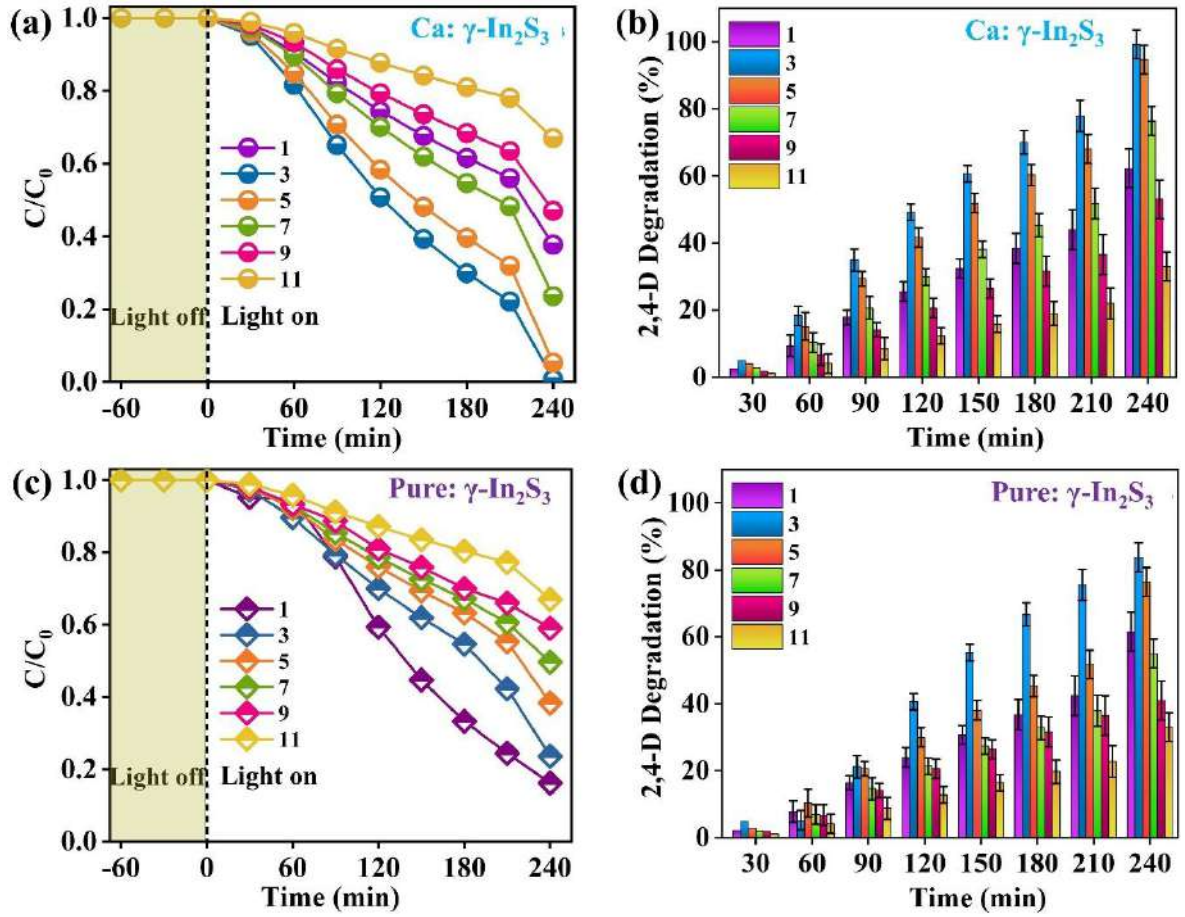

Fig. 41. Effect of pH on 2,4-D degradation (a-b) the best-performing Ca: γ-In_2S_3 and (c-d) Pure: γ-In_2S_3.

6.4.3.5. Photocatalyst reusability

Evaluating the lifespan of a photocatalyst is essential for determining its effectiveness in wastewater treatment and assessing potential cost benefits. To investigate the reusability of the photocatalyst, Ca: γ-In_2S_3 nanoribbons were tested in ten consecutive cycles of 2,4-D degradation. After each cycle, the photocatalyst was recovered, thoroughly washed, and reused without further modification. The results (Fig. 42a) showed only minor fluctuations in degradation efficiency, with a reduction of less than 2% up to the fifth cycle and a total decline of approximately 8 % by the tenth cycle. The slight decrease in activity was mainly attributed to nanoparticle aggregation during the photodegradation process and minor challenges in recovering the powder after use. Despite this, the nanoribbons demonstrated excellent photostability and reusability. XRD analysis of the samples before use, after the fifth cycle, and after the tenth cycle (Fig. 42b) revealed no significant structural changes, aside from a

slight reduction in peak intensity after the tenth cycle. This consistency in the crystal structure further confirms the outstanding stability and durability of Ca: γ-In_2S_3 nanoribbons, highlighting their strong potential for long-term application in environmental remediation.

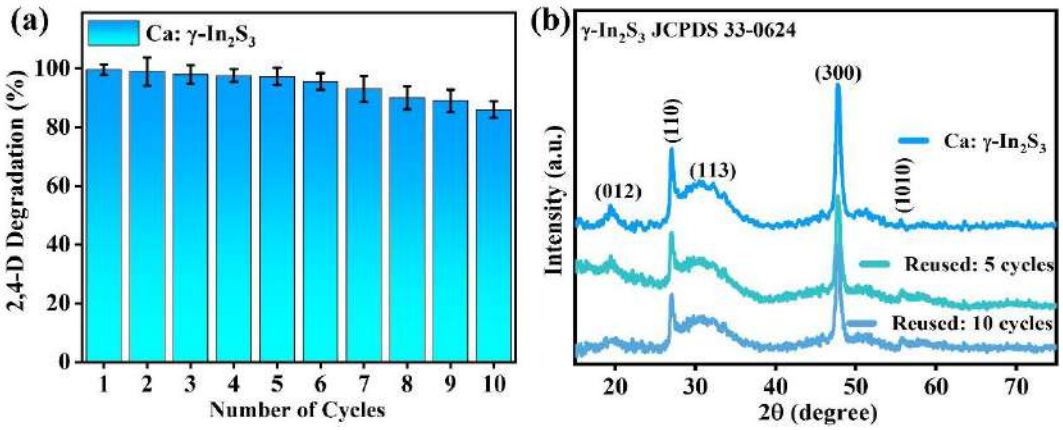

Fig. 42. (a) Photocatalytic degradation percentage for reusability tests (b) XRD of initial and reused Ca: γ-In_2S_3 nanoribbons after the fifth and tenth cycle.

6.4.3.6. Comparative Study of 2,4-D Photocatalytic Degradation with Literature.

Our research significantly contributes to the limited amount of work on the degradation of 2,4-D using In_2S_3. The only other report on this topic is our previous study. In **Table 19**, we present a comprehensive comparison of materials previously used for this purpose, covering key aspects such as pollutant quantities, degradation efficiencies, irradiation times, and reusability. Few chalcogenide-based materials have been investigated, including $ZnIn_2S_4$, Bi_2S_3, Co_9S_8, γ-In_2S_3, and Ba-doped γ-In_2S_3, which achieved photodegradation efficiencies of 30%, 12%, 15%, 77%, and 94%, respectively. Among these, $ZnIn_2S_4$ has assessed its reusability, revealing a significant drop in degradation efficiency from 30% to 3% after five cycles, indicating poor stability. In contrast, from our previous work, γ-In_2S_3 and Ba-doped γ-In_2S_3 maintained higher stability, with degradation efficiencies declining only slightly from 77% to 73% and from 94% to 93% after four cycles, respectively. However, to the best of our knowledge, there is no other report on using γ-In_2S_3 for this application.

In the current study, we extended our investigation by introducing alkaline earth metal-based dopants (Mg, Ca, and Sr) and varying several experimental conditions, including pH, photocatalyst amount, scavenger, and initial 2,4-D concentration for the best performing Ca: γ-In_2S_3. We achieved superior results using pure γ-In_2S_3 and its doped variants Mg: γ-In_2S_3, Ca: γ-In_2S_3, and Sr: γ-In_2S_3 with photodegradation efficiencies of 78.38%, 90.72%, 99.53%, and 85.22% after 240 minutes, respectively. Notably, Ca: γ-In_2S_3 proved to be particularly

effective, with a minimal decline of less than 2% in degradation efficiency after ten cycles. These promising results suggest exciting future research opportunities, including the exploration of heterojunctions or other dopants, which could further enhance the removal of 2,4-D in a shorter time frame.

Table 19. Comparative analysis of 2,4-D photodegradation using different chalcogenide-based semiconductor photocatalysts.

Sample	Amount of photocatalyst (mg)	Amount of 2,4-D (ppm)	Irradiation time (min)	η (%)	Reusability		Ref.
					η (%)	Cycles run	
$ZnIn_2S_4$	200	100	180	30	3	5	[27]
$ZnIn_2S_4$	20	30	180	30	-		[16]
Bi_2S_3	-	10	180	38.6	-		[28]
Co_9S_8	20	100	180	15	-		[30]
γ-In_2S_3	30	40	210	77	73	4	[37]
Ba-doped γ-In_2S_3	30	40	210	94	93	4	[37]
Pure γ-In_2S_3	30	40	240	78.38	-		This work
Mg: γ-In_2S_3	30	40	240	90.72	-		
Ca: γ-In_2S_3	40	60	240	99.53	91.23	10	
Sr: γ-In_2S_3	30	40	240	85.22	-		

Conclusion

In this thesis, we systematically explored both theoretical and experimental aspects of sustainable solar energy conversion systems by investigating the PV behavior of Pb-free CP SCs and the photocatalytic efficiency of doped γ-In_2S_3 nanostructures, respectively. Our research focused on advancing two complementary approaches: (i) the design and optimization of high-performance, eco-friendly $SrZrS_3$ and $BaZr_{0.96}Ti_{0.04}S_3$ SCs using novel HTLs based on c-MOFs and MPcs, and (ii) the synthesis and photocatalytic evaluation of Mg^{2+}, Ca^{2+}, and Sr^{2+} doped γ-In_2S_3 nanoribbons for H_2 fuel generation and 2,4-D degradation. The in-depth summary of the key findings from these studies is elucidated in the following sections.

1. The first study introduced an emerging class of c-MOFs as HTLs for the novel $SrZrS_3$ CP absorber for the first time. A total of 193 device configurations were simulated using Cu-MOF, NTU-9, Fe_2(DSBDC), Sr-MOF, Mn_2(DSBDC), and Cu_3(HHTP)$_2$, revealing their strong potential to enhance $SrZrS_3$ solar cell performance. Through systematic SCAPS-1D

optimization of absorber and HTL parameters, the initial PCEs of 11.03%, 11.34%, 12.66%, 13.17%, 13.25%, and 12.06% increased significantly to 30.60%, 29.78%, 28.29%, 28.44%, 28.80%, and 28.62%, respectively. These improvements were attributed to optimized electron affinity and carrier concentration, leading to reduced interface barrier heights and enhanced recombination resistances of 1.4×10^7 Ω.cm^2, 6.2×10^6 Ω.cm^2, 1.6×10^7 Ω.cm^2, 1.6×10^7 Ω.cm^2, 1.5×10^7 Ω.cm^2, and 1.7×10^7 Ω.cm^2. Further optimization of defect density and thickness increased carrier lifetime, diffusion length, and optical absorption. Notably, the best performing device with Cu-MOF HTLs showed QE enhancement from 15 % to 35 % and extended absorption from 815 nm to 910 nm, highlighting efficient NIR absorption and dual light-harvesting/charge-transport roles of the Cu-MOF layer. Comprehensive analyses, through J-V, QE, Mott-Schottky, Nyquist plots, and generation-recombination rate confirmed these enhancements. Moreover, this study also revealed the influence of back contact work function, interface properties, parasitic resistances, and operating temperature on device stability and performance.

2. The second investigation highlights the potential of MPcs, specifically, CuPc, NiPc, and ZnPc, as efficient, low-cost HTLs in $BaZr_{0.96}Ti_{0.04}S_3$ CP SCs. Through systematic optimization of both absorber and HTL parameters in FTO/SnO_2/$BaZr_{0.96}Ti_{0.04}S_3$/MPc(M = Cu, Ni, Zn)/C device structures, the PCEs were significantly enhanced from 12.16%, 13.29%, and 14.49% to 28.94%, 28.89%, and 30.12% for CuPc-, NiPc-, and ZnPc-based devices, respectively. optimization of HTL electron affinity (3.6 eV for CuPc, 3.1 eV for NiPc, and 4.0 eV for ZnPc) effectively minimized valence band offsets, reduced interfacial recombination, and induced an upward energy band shift that facilitated hole transport while suppressing electron flow. Moreover, Nyquist plot and generation rate analyses confirmed improved charge transport and a 7-9% absorption enhancement in quantum efficiency.
3. The third and fourth studies focus on experimental work, specifically synthesizing pure and Mg^{2+}, Ca^{2+}, and Sr^{2+} doped γ-In_2S_3 nanoribbons via a facile heating-up method. Structural (XRD, Raman, and HRTEM) and compositional (EDS and XPS) analyses confirmed the formation of single-phase γ-In_2S_3 and the effective incorporation of dopants, maintaining the stoichiometric In:S ratio of 2:3 with ~2 at.% of dopants. FESEM micrographs revealed well-defined nanoribbon morphology in pure and Mg: γ-In_2S_3, while showing a greater extent of aggregation in Ca: γ-In_2S_3 and Sr: γ-In_2S_3, whereas BET measurements indicated a clear enhancement in surface area upon doping. Optical (UV-Vis and PL Spectroscopy) characterizations demonstrated significant bandgap narrowing, from 3.67 eV for pure γ-

In_2S_3 to 2.74 eV (Mg), 2.41 eV (Ca), and 2.91 eV (Sr), resulting in improved visible-light absorption. Electrical properties (Mott-Schottky, EIS, and Hall measurements) confirmed improved carrier concentration, reduced recombination, and higher charge mobility across all doped samples. Thereafter systematically studied the applicability of these materials for photocatalytic H_2 fuel generation and 2,4-D degradation. Among all the samples, Ca: γ-In_2S_3 exhibited the highest photocatalytic activity, achieving an H_2 evolution rate of 636 $\mu mol \cdot g^{-1}$ in the presence of TEOA, corresponding to a 4.5-fold increase over undoped γ-In_2S_3. Photocatalytic degradation studies further confirmed its efficiency, with 99.53% removal of 2,4-D under optimal conditions (pH 3, 40 mg catalyst, 60 ppm 2,4-D). The material retained 91.3% of its H_2 evolution activity after five cycles and exhibited only an 8% reduction in degradation performance after ten cycles, indicating excellent structural and operational stability.

In summary, this thesis carries both theoretical and experimental understanding of high-efficiency solar energy materials for PV and photocatalytic applications, respectively. Theoretical results identify c-MOFs and MPcs as sustainable, high-performance HTLs for Pb-free CP SCs, offering efficient charge transport and superior stability over conventional organics like Spiro-OMeTAD. Experimentally synthesized alkaline earth metal-doped γ-In_2S_3 nanoribbons demonstrated exceptional photocatalytic activity for H_2 generation and 2,4-D degradation, showcasing their versatility and potential in the field of photocatalysis.

References

[1] Wang Q, Wang X, Li R. Energy transition and environmental sustainability: the interplay with natural resource rents and trade openness. Humanities and Social Sciences Communications. 2025 Jul 22;12(1):1-6. https://doi.org/10.1057/s41599-025-05521-4.

[2] Chee WC, Ho WS, Hashim H, Lim LK, Ab Muis Z, Nizamuddin AD, Wong KY, Overland I, Shidiq M, Pradnyaswari I. Renewable energy trade among the ASEAN countries and the road to net-zero carbon emissions. Energy Strategy Reviews. 2025 Nov 1;62:101878. https://doi.org/10.1016/j.esr.2025.101878.

[3] Jia W, Ding T, He Y. Synergistic integration of green hydrogen in renewable power systems: A comprehensive review of key technologies, research landscape, and future perspectives. Renewable and Sustainable Energy Reviews. 2026 Jan 1;226:116375. https://doi.org/10.1016/j.rser.2025.116375.

[4] Afanasev P, Askarova A, Alekhina T, Popov E, Markovic S, Mukhametdinova A, Cheremisin A, Mukhina E. An overview of hydrogen production methods: Focus on hydrocarbon feedstock. International Journal of Hydrogen Energy. 2024 Aug 12;78:805-28. https://doi.org/10.1016/j.ijhydene.2024.06.369.

[5] Monama GR, Ramohlola KE, Iwuoha EI, Modibane KD. Progress on perovskite materials for energy application. Results in Chemistry. 2022 Jan 1;4:100321. https://doi.org/10.1016/j.rechem.2022.100321.

[6] Child M, Koskinen O, Linnanen L, Breyer C. Sustainability guardrails for energy scenarios of the global energy transition. Renewable and Sustainable Energy Reviews. 2018 Aug 1;91:321-34. https://doi.org/10.1016/j.rser.2018.03.079.

[7] Chakravorty A, Roy S. A review of photocatalysis, basic principles, processes, and materials. Sustainable Chemistry for the Environment. 2024 Dec 1;8:100155. https://doi.org/10.1016/j.scenv.2024.100155.

[8] Kumar KR, Chaitanya NK, Kumar NS. Solar thermal energy technologies and its applications for process heating and power generation-A review. Journal of Cleaner Production. 2021 Feb 1;282:125296. https://doi.org/10.1016/j.jclepro.2020.125296.

[9] Wang W, Tade MO, Shao Z. Research progress of perovskite materials in photocatalysis-and photovoltaics-related energy conversion and environmental treatment. Chemical Society Reviews. 2015;44(15):5371-408. https://doi.org/10.1039/c5cs00113g.

[10] Mai H, Caruso RA. Advances in perovskite-based photovoltaics and photocatalysis: a journey fueled by ChemComm. Chemical Communications. 2024;60(86):12471-3. https://doi.org/10.1039/A902892G.

[11] Grätzel M. Photoelectrochemical cells. nature. 2001 Nov 15;414(6861):338-44.

[12] Solak EK, Irmak E. Advances in organic photovoltaic cells: a comprehensive review of materials, technologies, and performance. RSC advances. 2023;13(18):12244-69. https://doi.org/10.1039/d3ra01454a.

[13] Chen B, Yang Z, Jia Q, Ball RJ, Zhu Y, Xia Y. Emerging applications of metal-organic frameworks and derivatives in solar cells: Recent advances and challenges. Materials Science and Engineering: R: Reports. 2023 Feb 1;152:100714. https://doi.org/10.1016/j.mser.2022.100714.

[14] Sharma P, Mishra RK. Comprehensive study on photovoltaic cell's generation and factors affecting its performance: A Review. Materials for Renewable and Sustainable Energy. 2025 Apr;14(1):1-28. https://doi.org/10.1007/s40243-024-00292-5.

[15] García-Guillén A, Gutiérrez-Hinestroza M, Moreno-Alcívar L, Bravo-Montero L, Herrera-Franco G. Photovoltaic system for residential energy sustainability in Santa Elena, Ecuador. Environments. 2025 Aug 15;12(8):281. https://doi.org/10.3390/environments12080281.

[16] Van Thuan D, Ngo HL, Thi HP, Chu TT. Photodegradation of hazardous organic pollutants using titanium oxides-based photocatalytic: A review. Environmental Research. 2023 Jul 15;229:116000. https://doi.org/10.1016/j.envres.2023.116000.

[17] Sun G, Shi JW, Zou Y, Mao S, Ma D, Lv Y, Sun L, Li Z, Cheng Y. One-step synthesis of CdS/CdSe/CuS hollow nanospheres in aqueous solution for enhanced photocatalytic hydrogen evolution. Sustainable Energy & Fuels. 2020;4(7):3467-76. https://doi.org/10.1039/d0se00249f.

[18] Hussain MZ, Yang Z, Huang Z, Jia Q, Zhu Y, Xia Y. Recent advances in metal–organic frameworks derived nanocomposites for photocatalytic applications in energy and environment. Advanced Science. 2021 Jul;8(14):2100625. https://doi.org/10.1002/advs.202100625.

[19] Hota P, Das A, Maiti DK. A short review on generation of green fuel hydrogen through water splitting. International Journal of Hydrogen Energy. 2023 Jan 5;48(2):523-41. https://doi.org/10.1016/j.ijhydene.2022.09.264.

[20] Bhuiyan MM, Siddique Z. Hydrogen as an alternative fuel: A comprehensive review of

challenges and opportunities in production, storage, and transportation. International Journal of Hydrogen Energy. 2025 Feb 10;102:1026-44. https://doi.org/10.1016/j.ijhydene.2025.01.033.

[21] Shahid MU, Najam T, Helal MH, Hossain I, El-Bahy SM, El-Bahy ZM, ur Rehman A, Shah SS, Nazir MA. Transition metal chalcogenides and phosphides for photocatalytic H_2 generation via water splitting: a critical review. International Journal of Hydrogen Energy. 2024 Apr 10;62:1113-38. https://doi.org/10.1016/j.ijhydene.2024.03.139.

[22] Magnoli K, Carranza CS, Aluffi ME, Magnoli CE, Barberis CL. Herbicides based on 2, 4-D: its behavior in agricultural environments and microbial biodegradation aspects. A review. Environmental Science and Pollution Research. 2020 Nov;27(31):38501-12. https://doi.org/10.1007/s11356-020-10370-6.

[23] Girón-Navarro R, Linares-Hernández I, Teutli-Sequeira EA, Martínez-Miranda V, Santoyo-Tepole F. Evaluation and comparison of advanced oxidation processes for the degradation of 2, 4-dichlorophenoxyacetic acid (2, 4-D): a review. Environmental Science and Pollution Research. 2021 Jun;28(21):26325-58. https://doi.org/10.1007/s11356-021-13730-y.

[24 Pattappan D, Mohankumar A, Kumar RR, Palanisamy S, Lai YT, Huh YS, Shim JJ, Haldorai Y. Visible light photocatalytic activity of a FeCo metal-organic framework for degradation of acetaminophen and 2, 4-dichlorophenoxyacetic acid and a nematode-based ecological assessment. Chemical Engineering Journal. 2023 May 15;464:142676. https://doi.org/10.1016/j.cej.2023.142676.

[25] Njema GG, Kibet JK. A review of chalcogenide-based perovskites as the next novel materials: Solar cell and optoelectronic applications, catalysis and future perspectives. Next Nanotechnology. 2025 Jan 1;7:100102. https://doi.org/10.1016/j.nxnano.2024.100102.

[26] Ahmad KS, Naqvi SN, Jaffri SB. Systematic review elucidating the generations and classifications of solar cells contributing towards environmental sustainability integration. Reviews in inorganic chemistry. 2021 Mar 26;41(1):21-39.

[27] Shao S, Loi MA. The role of the interfaces in perovskite solar cells. Advanced Materials Interfaces. 2020 Jan;7(1):1901469. https://doi.org/10.1002/admi.201901469.

[28] Mdallal A, Yasin A, Mahmoud M, Abdelkareem MA, Alami AH, Olabi AG. A comprehensive review on solar photovoltaics: Navigating generational shifts, innovations, and sustainability. Sustainable Horizons. 2025 Mar 1;13:100137. https://doi.org/10.1016/j.horiz.2025.100137.

[29] Mabvuer FT, Nya FT, Dzifack Kenfack GM, Laref A. Lowering cost approach for CIGS-based

solar cell through optimizing band gap profile and doping of stacked active Layers─ SCAPS modeling. ACS omega. 2023 Jan 20;8(4):3917-28. https://doi.org/10.1021/acsomega.2c06501.

[30] Marasamy L, Aruna-Devi R, Robledo OI, Carvayar JÁ, Barragán NE, Santos-Cruz J, Mayén-Hernández SA, Contreras-Puente G, de la Luz Olvera M, de Moure Flores F. Probing the significance of RF magnetron sputtering conditions on the physical properties of CdS thin films for ultra-thin CdTe photovoltaic applications. Applied Surface Science. 2022 Feb 1;574:151640. https://doi.org/10.1016/j.apsusc.2021.151640.

[31] Arockiya-Dass KT, Sekar K, Marasamy L. Theoretical insights of degenerate ZrS_2 as a new buffer for highly efficient emerging thin-film solar cells. Energy Technology. 2023 Sep;11(9):2300333. https://doi.org/10.1002/ente.202300333.

[32] Marasamy L, Chettiar AD, Manisekaran R, Linda E, Rahman MF, Hossain MK, García CE, Santos-Cruz J, Subramaniam V, de Moure Flores F. Impact of selenization with NaCl treatment on the physical properties and solar cell performance of crack-free Cu(In,Ga)Se_2 microcrystal absorbers. RSC advances. 2024;14(7):4436-47. https://doi.org/10.1039/d3ra05829h.

[33] Oni AM, Mohsin AS, Rahman MM, Bhuian MB. A comprehensive evaluation of solar cell technologies, associated loss mechanisms, and efficiency enhancement strategies for photovoltaic cells. Energy Reports. 2024 Jun 1;11:3345-66. https://doi.org/10.1016/j.egyr.2024.03.007.

[34] Yun Y, Moon S, Kim S, Lee J. Flexible fabric-based GaAs thin-film solar cell for wearable energy harvesting applications. Solar Energy Materials and Solar Cells. 2022 Oct 1;246:111930. https://doi.org/10.1016/j.solmat.2022.111930.

[35] Rehman F, Syed IH, Khanam S, Ijaz S, Mehmood H, Zubair M, Massoud Y, Mehmood MQ. Fourth-generation solar cells: a review. Energy Advances. 2023;2(9):1239-62. https://doi.org/10.1039/d3ya00179b.

[36] Kant N, Singh P. Review of next generation photovoltaic solar cell technology and comparative materialistic development. Materials Today: Proceedings. 2022 Jan 1;56:3460-70. https://doi.org/10.1016/j.matpr.2021.11.116.

[37] Yang C, Hu W, Liu J, Han C, Gao Q, Mei A, Zhou Y, Guo F, Han H. Achievements, challenges, and future prospects for industrialization of perovskite solar cells. Light: Science & Applications. 2024 Sep 3;13(1):227. https://doi.org/10.1038/s41377-024-01461-x.

[38] Afroz M, Ratnesh RK, Srivastava S, Singh J. Perovskite solar cells: Progress, challenges, and

future avenues to clean energy. Solar Energy. 2025 Feb 1;287:113205. https://doi.org/10.1016/j.solener.2024.113205.

[39] Kojima A, Teshima K, Shirai Y, Miyasaka T. Organometal halide perovskites as visible-light sensitizers for photovoltaic cells. Journal of the american chemical society. 2009 May 6;131(17):6050-1.

[40] Rani M, Khan MM, Numan A, Khalid M, Abbas SM, Iqbal M, Mansoor MA. Breaking barriers: Addressing challenges in perovskite solar cell development. Journal of Alloys and Compounds. 2025 Jan 5;1010:177648. https://doi.org/10.1016/j.jallcom.2024.177648.

[41] Ahmed S, Gondal MA, Alzahrani AS, Parvaz M, Ahmed A, Hussain S. Recent trends and challenges in lead-free perovskite solar cells: A critical review. ACS Applied Energy Materials. 2024 Feb 7;7(4):1382-97. https://doi.org/10.1021/acsaem.3c02327.

[42] Hardy J, Fiedler H, Kennedy J. A review on the current status and chemistry of tin halide perovskite films for photovoltaics. Progress in Materials Science. 2025 Jan 25:101446. https://doi.org/10.1016/j.pmatsci.2025.101446.

[43] Wang T, Loi HL, Cao Q, Feng G, Guan Z, Wei Q, Chen C, Li M, Zhu Y, Lee CS, Yan F. Counter-Doping Effect by Trivalent Cations in Tin-Based Perovskite Solar Cells. Advanced Materials. 2024 Jul;36(30):2402947. https://doi.org/10.1002/adma.202402947.

[44] Chiara R, Morana M, Malavasi L. Germanium-based halide perovskites: materials, properties, and applications. ChemPlusChem. 2021 Jun;86(6):879-88. https://doi.org/10.1002/cplu.202100191.

[45] Raoui Y, Kazim S, Galagan Y, Ez-Zahraouy H, Ahmad S. Harnessing the potential of lead-free Sn-Ge based perovskite solar cells by unlocking the recombination channels. Sustainable Energy & Fuels. 2021;5(18):4661-7. https://doi.org/10.1039/d1se00687h.

[46] Cui Y, Yang L, Wu X, Deng J, Zhang X, Zhang J. Recent progress of lead-free bismuth-based perovskite materials for solar cell applications. Journal of Materials Chemistry C. 2022;10(44):16629-56. https://doi.org/10.1039/d2tc02643k.

[47] Raval NA, Kheraj V. Evolution and state-of-the-art development of antimony-based perovskites material-system for solar photovoltaics: A comprehensive review. Solar Energy. 2025 Jan 15;286:113128. https://doi.org/10.1016/j.solener.2024.113128.

[48] Wang C, Liu Y, Guo Y, Ma L, Liu Y, Zhou C, Yu X, Zhao G. Lead-free sodium bismuth halide

Cs_2NaBiX_6 double perovskite nanocrystals with highly efficient photoluminesence. Chemical Engineering Journal. 2020 Oct 1;397:125367. https://doi.org/10.1016/j.cej.2020.125367.

[49] Kazim MZ, Ishfaq M, Aldaghfag SA, Yaseen M, Khalid M, Dahshan A. Lead-free silver-indium based halide double perovskites for energy harvesting applications. Journal of Physics and Chemistry of Solids. 2024 Feb 1;185:111756. https://doi.org/10.1016/j.jpcs.2023.111756.

[50] Linda E, Chettiar AD, Marasamy L. Emerging class of $SrZrS_3$ chalcogenide perovskite solar cells: conductive MOFs as HTLs-A game changer?. Solar Energy Materials and Solar Cells. 2024 Dec 1;278:113204.https://doi.org/10.1016/j.solmat.2024.113204.

[51] Sun YY, Agiorgousis ML, Zhang P, Zhang S. Chalcogenide perovskites for photovoltaics. Nano letters. 2015 Jan 14;15(1):581-5. https://doi.org/10.1021/nl504046x.

[52] Sadeghi I, Ye K, Xu M, Li Y, LeBeau JM, Jaramillo R. Making $BaZrS_3$ chalcogenide perovskite thin films by molecular beam epitaxy. Advanced Functional Materials. 2021 Nov;31(45):2105563. https://doi.org/10.1002/adfm.202105563.

[53] Perera S, Hui H, Zhao C, Xue H, Sun F, Deng C, Gross N, Milleville C, Xu X, Watson DF, Weinstein B. Chalcogenide perovskites–an emerging class of ionic semiconductors. Nano Energy. 2016 Apr 1;22:129-35. https://doi.org/10.1016/j.nanoen.2016.02.020.

[54] Gupta T, Ghoshal D, Yoshimura A, Basu S, Chow PK, Lakhnot AS, Pandey J, Warrender JM, Efstathiadis H, Soni A, Osei-Agyemang E. An environmentally stable and lead-free chalcogenide perovskite. Advanced Functional Materials. 2020 Jun;30(23):2001387. https://doi.org/10.1002/adfm.202001387.

[55] Vincent Mercy EN, Srinivasan D, Marasamy L. Emerging $BaZrS_3$ and $Ba(Zr,Ti)S_3$ chalcogenide perovskite solar cells: A numerical approach toward device engineering and unlocking efficiency. ACS omega. 2024 Jan 17;9(4):4359-76. https://doi.org/10.1021/acsomega.3c06627.

[56] Niu S, Milam-Guerrero J, Zhou Y, Ye K, Zhao B, Melot BC, Ravichandran J. Thermal stability study of transition metal perovskite sulfides. Journal of Materials Research. 2018 Dec;33(24):4135-43. https://doi.org/10.1557/jmr.2018.419.

[57] Han Y, Xu J, Liang Y, Chen X, Jia M, Zhang J, Lian L, Liu Y, Li X, Shi Z. P-type conductive $BaZrS_3$ thin film and its band gap tunning via Ruddlesden-Popper $Ba_3Zr_2S_7$ and titanium alloying. Chemical Engineering Journal. 2023 Oct 1;473:145351. https://doi.org/10.1016/j.cej.2023.145351.

[58] Jaykhedkar N, Bystrický R, Sýkora M, Bučko T. Understanding the structure-band gap relationship in $SrZrS_3$ at elevated temperatures: a detailed NPT MD study. Journal of Materials Chemistry C. 2022;10(33):12032-42. https://doi.org/10.1039/d2tc02253b.

[59] Nishigaki Y, Nagai T, Nishiwaki M, Aizawa T, Kozawa M, Hanzawa K, Kato Y, Sai H, Hiramatsu H, Hosono H, Fujiwara H. Extraordinary strong band-edge absorption in distorted chalcogenide perovskites. Solar RRL. 2020 May;4(5):1900555. https://doi.org/10.1002/solr.201900555.

[60] Lee CS, Kleinke KM, Kleinke H. Synthesis, structure, and electronic and physical properties of the two $SrZrS_3$ modifications. Solid state sciences. 2005 Sep 1;7(9):1049-54.

[61] Pradhan AA, Uible MC, Agarwal S, Turnley JW, Khandelwal S, Peterson JM, Blach DD, Swope RN, Huang L, Bart SC, Agrawal R. Synthesis of $BaZrS_3$ and $BaHfS_3$ chalcogenide perovskite films using single-phase molecular precursors at moderate temperatures. Angewandte Chemie. 2023 Apr 3;135(15):e202301049. https://doi.org/10.1002/anie.202301049.

[62] Dallas P, Gkini K, Kaltzoglou A, Givalou L, Konstantakou M, Orfanoudakis S, Boukos N, Sakellis E, Tsipas P, Kalafatis A, Karydas AG. Exploring the potential of powder-to-film processing for proof-of-concept $BaZrS_3$ perovskite solar cells. Materials Today Communications. 2024 Jun 1;39:108608. https://doi.org/10.1016/j.mtcomm.2024.108608.

[63] Pindolia G, Shinde SM, Jha PK. Optimization of an inorganic lead free $RbGeI_3$ based perovskite solar cell by SCAPS-1D simulation. Solar Energy. 2022 Apr 1;236:802-21. https://doi.org/10.1016/j.solener.2022.03.053.

[64] Nie T, Fang Z, Ren X, Duan Y, Liu S. Recent advances in wide-bandgap organic-inorganic halide perovskite solar cells and tandem application. Nano-micro letters. 2023 Dec;15(1):70. https://doi.org/10.1007/s40820-023-01040-6.

[65] Hu Q, Rezaee E, Dong Q, Shan H, Chen Q, Wang L, Liu B, Pan JH, Xu ZX. P3HT/Phthalocyanine nanocomposites as efficient hole-transporting materials for perovskite solar cells. Solar Rrl. 2019 Jan;3(1):1800264. https://doi.org/10.1002/solr.201800264.

[66] Chawki N, Rouchdi M, Alla M, Fares B. Simulation and analysis of high-performance hole transport material $SrZrS_3$-based perovskite solar cells with a theoretical efficiency approaching 26%. Solar Energy. 2023 Sep 15;262:111913. https://doi.org/10.1016/j.solener.2023.111913.

[67] Dou J, Chen Q. MOFs in emerging solar cells. Chinese Journal of Chemistry. 2023 Mar 15;41(6):695-709. https://doi.org/10.1002/cjoc.202200651.

[68] Wang R, Yu W, Sun C, Chiranjeevulu K, Deng S, Wu J, Yan F, Peng C, Lou Y, Xu G, Zou G. High-hole-mobility metal-organic framework as dopant-free hole transport layer for perovskite solar cells. Nanoscale Research Letters. 2022 Jan 4;17(1):6. https://doi.org/10.1021/acsami.7b03487.

[69] Ye Y, Yin Y, Chen Y, Li S, Li L, Yamauchi Y. Metal-organic framework materials in perovskite solar cells: recent advancements and perspectives. Small. 2023 Jun;19(25):2208119. https://doi.org/10.1002/smll.202208119.

[70] D.Y. Ahn, D.Y. Lee, C.Y. Shin, H.T. Bui, N.K. Shrestha, L. Giebeler, Y.Y. Noh, S.H. Han, Novel Solid-State Solar Cell Based on Hole-Conducting MOF-Sensitizer Demonstrating Power Conversion Efficiency of 2.1%, ACS Applied Materials and Interfaces 9 (2017) 12930–12935. https://doi.org/10.1021/acsami.7b03487.

[71] Pathak A, Shen JW, Usman M, Wei LF, Mendiratta S, Chang YS, Sainbileg B, Ngue CM, Chen RS, Hayashi M, Luo TT. Integration of a (-Cu-S-) n plane in a metal-organic framework affords high electrical conductivity. Nature Communications. 2019 Apr 12;10(1):1721. https://doi.org/10.1038/s41467-019-09682-0.

[72] Mancuso JL, Hendon CH. Titanium (IV) inclusion as a versatile route to photoactivity in metal-organic frameworks. Advanced Theory and Simulations. 2019 Nov;2(11):1900126. https://doi.org/10.1002/adts.201900126.

[73] Sun L, Hendon CH, Minier MA, Walsh A, Dincă M. Million-fold electrical conductivity enhancement in Fe_2(DEBDC) versus Mn_2(DEBDC)(E= S,O). Journal of the American Chemical Society. 2015 May 20;137(19):6164-7. https://doi.org/10.1021/jacs.5b02897.

[74] Usman M, Lee CH, Hung DS, Lee SF, Wang CC, Luo TT, Zhao L, Wu MK, Lu KL. Intrinsic low dielectric behaviour of a highly thermally stable Sr-based metal-organic framework for interlayer dielectric materials. Journal of Materials Chemistry C. 2014;2(19):3762-8. https://doi.org/10.1039/c4tc00149d.

[75] Sun L, Miyakai T, Seki S, Dincă M. Mn_2(2,5-disulfhydrylbenzene-1,4-dicarboxylate): a microporous metal-organic framework with infinite (-Mn-S-)∞ chains and high intrinsic charge mobility. Journal of the American Chemical Society. 2013 Jun 5;135(22):8185-8. https://doi.org/10.1021/ja4037516.

[76] Campbell MG, Sheberla D, Liu SF, Swager TM, Dincă M. Cu_3(hexaiminotriphenylene)$_2$: an electrically conductive 2D metal-organic framework for chemiresistive sensing. Angewandte Chemie International Edition. 2015 Mar 27;54(14):4349-52.

https://doi.org/10.1002/anie.201411854.

[77] Jo YM, Lim K, Yoon JW, Jo YK, Moon YK, Jang HW, Lee JH. Visible-light-activated type II heterojunction in Cu_3(hexaiminotriphenylene)$_2$/Fe_2O_3 hybrids for reversible NO_2 sensing: critical role of π-π* transition. ACS Central Science. 2021 Jun 9;7(7):1176-82. https://doi.org/10.1021/acscentsci.1c00289.

[78] Nyiekaa EA, Aika TA, Orukpe PE, Akhabue CE, Danladi E. Development on inverted perovskite solar cells: A review. Heliyon. 2024 Jan 30;10(2). https://doi.org/10.1016/j.heliyon.2024.e24689.

[79] Danladi E, Gyuk PM, Tasie NN, Egbugha AC, Behera D, Hossain I, Bagudo IM, Madugu ML, Ikyumbur JT. Impact of hole transport material on perovskite solar cells with different metal electrode: a SCAPS-1D simulation insight. Heliyon. 2023 Jun 1;9(6). https://doi.org/10.1016/j.heliyon.2023.e16838.

[80] Rahman MF, Chowdhury M, Marasamy L, Mohammed MK, Haque MD, Al Ahmed SR, Irfan A, Chaudhry AR, Goumri-Said S. Improving the efficiency of a CIGS solar cell to above 31% with Sb_2S_3 as a new BSF: a numerical simulation approach by SCAPS-1D. RSC advances. 2024;14(3):1924-38. https://doi.org/10.1039/d3ra07893k.

[81] Ngue PG, Ngoupo AT, Abena AM, Abega FX, Ndjaka JM. Investigation of the Performance of a Sb_2S_3-Based Solar Cell with a Hybrid Electron Transport Layer (h-ETL): A Simulation Approach Using SCAPS-1D Software. International Journal of Photoenergy. 2024;2024(1):5188636. https://doi.org/10.1155/2024/5188636.

[82] Karthick S, Velumani S, Bouclé J. Experimental and SCAPS simulated formamidinium perovskite solar cells: A comparison of device performance. Solar Energy. 2020 Jul 15;205:349-57. https://doi.org/10.1016/j.solener.2020.05.041.

[83] Sun LJ, Jia YM, Yang F, Bai ZY, Xie YL. Bimetallic ZnNi co-catalyst modified g-C_3N_4 nanosheets for highly efficient photocatalytic hydrogen evolution. International Journal of Hydrogen Energy. 2025 Jan 13;98:1386-95. https://doi.org/10.1016/j.ijhydene.2024.12.057.

[84] Kanwal H, Khoja AH, Hajji Y, Shakir S, Anwar M, Liaquat R, Din IU, Bahadar A, Hleili M. Photocatalytic performance of dual-function selenium-enriched biomass-derived activated carbon as a catalyst for dye degradation and hydrogen production. International Journal of Hydrogen Energy. 2025 Feb 3;101:1288-303. https://doi.org/10.1016/j.ijhydene.2024.12.509.

[85] Josephine GS, Jayaprakash K, Suresh M, Sivasamy A. Photocatalytic degradation of 2, 4-

dicholorophenoxyacetic acid: a herbicide by nanocrystalline semiconductor material under visible light irradiation. Materials Today: Proceedings. 2019 Jan 1;17:345-53. https://doi.org/10.1016/j.matpr.2019.06.440.

[86] Uddin A, Muhmood T, Guo Z, Gu J, Chen H, Jiang F. Hydrothermal synthesis of 3D/2D heterojunctions of $ZnIn_2S_4$/oxygen-doped g-C_3N_4 nanosheet for visible light-driven photocatalysis of 2, 4-dichlorophenoxyacetic acid degradation. Journal of Alloys and Compounds. 2020 Dec 10;845:156206. https://doi.org/10.1016/j.jallcom.2020.156206.

[87] Dargahi A, Nematollahi D, Asgari G, Shokoohi R, Ansari A, Samarghandi MR. Electrodegradation of 2, 4-dichlorophenoxyacetic acid herbicide from aqueous solution using three-dimensional electrode reactor with G/β-PbO_2 anode: Taguchi optimization and degradation mechanism determination. RSC advances. 2018;8(69):39256-68. https://doi.org/10.1039/c8ra08471h.

[88] Dereumeaux C, Fillol C, Quenel P, Denys S. Pesticide exposures for residents living close to agricultural lands: A review. Environment International. 2020 Jan 1;134:105210. https://doi.org/10.1016/j.envint.2019.105210.

[89] Sánchez OA, Rodríguez JL, Barrera-Andrade JM, Borja-Urby R, Valenzuela MA. High performance of Ag/$BiVO_4$ photocatalyst for 2, 4-Dichlorophenoxyacetic acid degradation under visible light. Applied Catalysis A: General. 2020 Jun 25;600:117625. https://doi.org/10.1016/j.apcata.2020.117625.

[90] Ramos-Ramírez E, Gutiérrez-Ortega NL, Tzompantzi-Morales F, Barrera-Rodríguez A, Castillo-Rodríguez JC, Tzompantzi-Flores C, Santolalla-Vargas CE, Guevara-Hornedo MD. Photocatalytic degradation of 2, 4-Dichlorophenol on NiAl-mixed oxides derivatives of activated layered double hydroxides. Topics in Catalysis. 2020 Aug;63(5):546-63. https://doi.org/10.1007/s11244-020-01269-0.

[91] Alfred MO, Akor E, Ayeni BC, Olorunnisola CG, Unuabonah EI, Omorogie MO. Chalcogenides: recent advances in their environmental applications. Energy, Ecology, and Environment. 2025 Oct 13:1-29. https://doi.org/10.1007/s40974-025-00389-1.

[92] Alfa I, Hafeez HY, Mohammed J, Abdu S, Suleiman AB, Ndikilar CE. A recent progress and advancement on MoS_2-based photocatalysts for efficient solar fuel (hydrogen) generation via photocatalytic water splitting. International Journal of Hydrogen Energy. 2024 Jun 19;71:1006-25. https://doi.org/10.1016/j.ijhydene.2024.05.203.

[93] Siddiqui MS, Aslam M. Chalcogenides as well as chalcogenides-based nanomaterials and its

importance in photocatalysis. InChalcogenide-based nanomaterials as photocatalysts 2021 Jan 1 (pp. 33-76). Elsevier. https://doi.org/10.1016/B978-0-12-820498-6/00003-2.

[94] Linda E, Chettiar AR, Sneha V, Manisekaran R, Srinivasan D, Barcenas A, et al. Exploring the physical properties of pristine γ-In_2S_3 and its influence on Ba doping for photocatalytic degradation of 2, 4-D herbicide, Journal of Photochemistry & Photobiology, A : Chemistry 2024;456. https://doi.org/10.1016/j.jphotochem.2024.115831.

[95] Xiong J, Li H, Zhou J, Di J. Recent progress of indium-based photocatalysts: Classification, regulation and diversified applications. Coordination Chemistry Reviews. 2022 Dec 15;473:214819. https://doi.org/10.1016/j.ccr.2022.214819.

[96] Mishra SR, Gadore V, Ahmaruzzaman M. An overview of In_2S_3 and In_2S_3-based photocatalyst: characteristics, synthesis, modifications, design strategies, and catalytic environmental application. Journal of Environmental Chemical Engineering. 2024 Oct 1;12(5):113449. https://doi.org/10.1016/j.jece.2024.113449.

[97] Alhammadi S, Mun BG, Gedi S, Reddy VR, Rabie AM, Sayed MS, Shim JJ, Park H, Kim WK. Effect of silver doping on the properties and photocatalytic performance of In_2S_3 nanoparticles. Journal of Molecular Liquids. 2021 Dec 15;344:117649. https://doi.org/10.1016/j.molliq.2021.117649.

[98] Pistor P, Merino Alvarez JM, León M, Di Michiel M, Schorr S, Klenk R, Lehmann S. Structure reinvestigation of α-, β-and γ-In_2S_3. Structural Science. 2016 Jun 1;72(3):410-5. https://doi.org/10.1107/S2052520616007058.

[99] Zhang J, Ding L, Sun W, Bi W, Wu Z, Gao F. γ-In_2S_3 nanosheets-composed flowerlike nanostructure doped by Al^{3+} ions with optimal electronic structure and decreased work function of γ-In_2S_3 for CO_2 electroreduction to formate. Journal of Alloys and Compounds. 2021 Dec 31;889:161770. https://doi.org/10.1016/j.jallcom.2021.161770.

[100] Horani F, Lifshitz E. Unraveling the growth mechanism forming stable γ-In_2S_3 and β-In_2S_3 colloidal nanoplatelets. Chemistry of Materials. 2019 Feb 15;31(5):1784-93. https://doi.org/10.1021/acs.chemmater.9b00013.

[101] Diehl RO, Carpentier CD, Nitsche R. The crystal structure of γ-In_2S_3 stabilized by As or Sb. Structural Science. 1976 Apr 15;32(4):1257-60. https://doi.org/10.1107/s0567740876005062.

[102] Jebasty RM, Sjåstad AO, Vidya R. Prediction of intermediate band in Ti/V doped γ-In_2S_3. RSC advances. 2022;12(3):1331-40. https://doi.org/10.1039/d0ra08132a.

[103] Pradeev Raj K, Sadaiyandi K, Kennedy A, Sagadevan S, Chowdhury ZZ, Johan MR, Aziz FA, Rafique RF, Thamiz Selvi R, Rathina Bala R. Influence of Mg doping on ZnO nanoparticles for enhanced photocatalytic evaluation and antibacterial analysis. Nanoscale research letters. 2018 Dec;13(1):229. https://doi.org/10.1186/s11671-018-2643-x.

[104] Triyono D, Hanifah U, Laysandra H. Structural and optical properties of Mg-substituted $LaFeO_3$ nanoparticles prepared by a sol-gel method. Results in Physics. 2020 Mar 1;16:102995. https://doi.org/10.1016/j.rinp.2020.102995.

[105] Bembibre A, Benamara M, Hjiri M, Gómez E, Alamri HR, Dhahri R, Serra A. Visible-light driven sonophotocatalytic removal of tetracycline using Ca-doped ZnO nanoparticles. Chemical Engineering Journal. 2022 Jan 1;427:132006. https://doi.org/10.1016/j.cej.2021.132006.

[106] Mohamed Saadon NA, Taib NI, Loy CW, Mohamed Z. Role of Ca^{2+} doping on the enhancement of dielectric properties of $Sr_{2-x}Ca_xNiWO_6$ for energy storage device application. Scientific Reports. 2023 Jan 23;13(1):1246. https://doi.org/10.1038/s41598-023-28296-7.

[107] Guan Y, Zhang Y, Zhang Z, Zhao Y, Han H, Liu R, Wang H, Jiang B, Gong X, Zhang Y, Sun E. Band gap regulation of $LaFeO_3$ via doping Sr for efficient conversion of coke and steam. Ceramics International. 2024 Jun 15;50(12):21526-37. https://doi.org/10.1016/j.ceramint.2024.03.266.

[108] Kumar A, Kumar D, Jain N, Kumar M, Ghodake G, Kumar S, Sharma RK, Holovsky J, Saji VS, Sharma SK. Enhanced efficiency and stability of electron transport layer in perovskite tandem solar cells: Challenges and future perspectives. Solar Energy. 2023 Dec 1;266:112185. https://doi.org/10.1016/j.solener.2023.112185.

[109] Sekar K, Manisekaran R, Nwakanma OM, Babudurai M. Significance of Formamidinium Incorporation in Perovskite Composition and Its Impact on Solar Cell Efficiency: A Mini-Review. Advanced Energy and Sustainability Research. 2024 Aug;5(8):2400003. https://doi.org/10.1002/aesr.202400003.

[110] Holzhey P, Prettl M, Collavini S, Mortan C, Saliba M. Understanding the impact of surface roughness: changing from FTO to ITO to PEN/ITO for flexible perovskite solar cells. Scientific Reports. 2023 Apr 19;13(1):6375. https://doi.org/10.1038/s41598-023-33147-6.

[111] Foo S, Thambidurai M, Senthil Kumar P, Yuvakkumar R, Huang Y, Dang C. Recent review on electron transport layers in perovskite solar cells. International Journal of Energy Research. 2022 Dec;46(15):21441-51. https://doi.org/10.1002/er.7958.

[112] Swarnkar A, Mir WJ, Chakraborty R, Jagadeeswararao M, Sheikh T, Nag A. Are chalcogenide perovskites an emerging class of semiconductors for optoelectronic properties and solar cell?. Chemistry of Materials. 2019 Jan 15;31(3):565-75. https://doi.org/10.1021/acs.chemmater.8b04178.

[113] Wu N, Wu Y, Walter D, Shen H, Duong T, Grant D, Barugkin C, Fu X, Peng J, White T, Catchpole K. Identifying the cause of voltage and fill factor losses in perovskite solar cells by using luminescence measurements. Energy Technology. 2017 Oct;5(10):1827-35. https://doi.org/10.1002/ente.201700374.

[114] Rombach FM, Haque SA, Macdonald TJ. Lessons learned from spiro-OMeTAD and PTAA in perovskite solar cells. Energy & Environmental Science. 2021;14(10):5161-90. https://doi.org/10.1039/d1ee02095a.

[115] Hossain MK, Bhattarai S, Arnab AA, Mohammed MK, Pandey R, Ali MH, Rahman MF, Islam MR, Samajdar DP, Madan J, Bencherif H. Harnessing the potential of $CsPbBr_3$-based perovskite solar cells using efficient charge transport materials and global optimization. RSC advances. 2023;13(30):21044-62. https://doi.org/10.1039/d3ra02485g.

[116] Sekar K, Marasamy L, Mayarambakam S, Hawashin H, Nour M, Bouclé J. Lead-free, formamidinium germanium-antimony halide ($FA_4GeSbCl_{12}$) double perovskite solar cells: the effects of band offsets. RSC advances. 2023;13(36):25483-96. DOI: 10.1039/d3ra03102k.

[117] S. Mondal, M. Chaudhury, P. Chakrabarti, S. Maity, Band Gap-Tailored Two-Terminal Lead-Free Germanium- and Tin- Based Single-Halide Perovskite Materials for Efficient Tandem Solar Cells, (2023). https://doi.org/10.1021/acs.energyfuels.3c01258.

[118] Ghosh B, Wu B, Mulmudi HK, Guet C, Weber K, Sum TC, Mhaisalkar S, Mathews N. Limitations of $Cs_3Bi_2I_9$ as lead-free photovoltaic absorber materials. ACS applied materials & interfaces. 2018 Jan 17;10(41):35000-7. https://doi.org/10.1021/acsami.7b14735.

[119] Hossain MK, Samajdar DP, Das RC, Arnab AA, Rahman MF, Rubel MH, Islam MR, Bencherif H, Pandey R, Madan J, Mohammed MK. Design and simulation of Cs_2BiAgI_6 double perovskite solar cells with different electron transport layers for efficiency enhancement. Energy & Fuels. 2023 Feb 17;37(5):3957-79. https://doi.org/10.1021/acs.energyfuels.3c00181.

[120] Jain SM, Edvinsson T, Durrant JR. Green fabrication of stable lead-free bismuth based perovskite solar cells using a non-toxic solvent. Communications Chemistry. 2019 Aug 8;2(1):91. https://doi.org/10.1038/s42004-019-0195-3.

[121] Wang Q, Lin Z, Su J, Hu Z, Chang J, Hao Y. Recent progress of inorganic hole transport materials for efficient and stable perovskite solar cells. Nano Select. 2021 Jun;2(6):1055-80. https://doi.org/10.1002/nano.202000238.

[122] Huang D, Xiang H, Ran R, Wang W, Zhou W, Shao Z. Recent advances in nanostructured inorganic hole-transporting materials for perovskite solar cells. Nanomaterials. 2022 Jul 28;12(15):2592. https://doi.org/10.3390/nano12152592.

[123] Yang AN, Lin JT, Li CT. Electroactive and sustainable Cu-MOF/PEDOT composite electrocatalysts for multiple redox mediators and for high-performance dye-sensitized solar cells. ACS Applied Materials & Interfaces. 2021 Feb 11;13(7):8435-44. https://doi.org/10.1021/acsami.0c21542.

[124] Gao J, Miao J, Li PZ, Teng WY, Yang L, Zhao Y, Liu B, Zhang Q. A p-type Ti (IV)-based metal-organic framework with visible-light photo-response. Chemical Communications. 2014;50(29):3786-8. DOI: 10.1039/c3cc49440c.

[125] Haider G, Usman M, Chen TP, Perumal P, Lu KL, Chen YF. Electrically driven white light emission from intrinsic metal-organic framework. ACS nano. 2016 Sep 27;10(9):8366-75. https://doi.org/10.1021/acsnano.6b03030.

[126] Cotfas DT, Cotfas PA, Kaplanis S. Methods to determine the dc parameters of solar cells: A critical review. Renewable and Sustainable Energy Reviews. 2013 Dec 1;28:588-96. https://doi.org/10.1016/j.rser.2013.08.017.

[127] Marques Lameirinhas RA, Torres JP, de Melo Cunha JP. A Photovoltaic Technology Review: History, Fundamentals and Applications. Energies 2022, 15, 1823

[128] Hazeghi F, Mozaffari S, Ghorashi SM. Metal organic framework–derived core-shell CuO@ NiO nanosphares as hole transport material in perovskite solar cell. Journal of Solid State Electrochemistry. 2020 Jun;24(6):1427-38. https://doi.org/10.1007/s10008-020-04643-w.

[129] Mohamadpour F, Amani AM. Photocatalytic systems: reactions, mechanism, and applications. RSC advances. 2024;14(29):20609-45. https://doi.org/10.1039/d4ra03259d.

[130] Hassaan MA, El-Nemr MA, Elkatory MR, Ragab S, Niculescu VC, El Nemr A. Principles of photocatalysts and their different applications: a review. Topics in Current Chemistry. 2023 Dec;381(6):31. https://doi.org/10.1007/s41061-023-00444-7.

[131] Ameta SC, Ameta R, editors. Advanced oxidation processes for wastewater treatment: emerging

green chemical technology. Academic press; 2018 Feb 19. https://doi.org/10.1016/B978-0-12-810499-6.00006-1.

[132] Wang Z, Li C, Domen K. Recent developments in heterogeneous photocatalysts for solar-driven overall water splitting. Chemical Society Reviews. 2019;48(7):2109-25.. https://doi.org/10.1039/c8cs00542g.

[133] Bouzaid A, Ziat Y, Belkhanchi H. Prediction the effect of (S, Se, Te) doped $MgTiO_3$ on optoelectronic, catalytic, and pH conduct as promised candidate photovoltaic device: Ab initio framework. International Journal of Hydrogen Energy. 2025 Jan 27;100:20-32. https://doi.org/10.1016/j.ijhydene.2024.12.284.

[134] Li J, Yu Q, Zhang X, Xiong X, Jin Y, Han D, Yu B, Yao J, Dai G. Coupling CoS_2 and $CaIn_2S_4$ for efficient electron trapping and improved surface catalysis to promote solar hydrogen evolution. International Journal of Hydrogen Energy. 2024 Jan 2;51:314-26. https://doi.org/10.1016/j.ijhydene.2023.08.156.

[135] Dou Y, Gao Y, Bai B, Zheng J, Wang X, Li H, Li Y, Bu Q, Ma D, Ding F, Sun Y. Fabrication of 1D/2D CdS/Ag: $ZnIn_2S_4$ heterostructure for greatly efficacious photocatalytic H_2 production and wastewater purification. International Journal of Hydrogen Energy. 2025 Mar 14;109:453-64. https://doi.org/10.1016/j.ijhydene.2025.02.116.

[136] Xi C, Deng P, Miao D, Zhang L, Liu W, Hou Y. Improved charge transfer by binary Ni_3S_2-NiS_2 for boosting the photocatalytic hydrogen generation over g-C_3N_4. Materials Letters. 2022 Jan 15;307:131012. https://doi.org/10.1016/j.matlet.2021.131012.

[137] Xu X, Lu Q, Wu J, Mo W, Zuo L, Yang N, Xia W, Zeng X. Boosting solar driven hydrogen production rate of Cu_2S@CdS pn heterostructures and $Cu_xCd_{1-x}S$ nanorods. International Journal of Hydrogen Energy. 2024 Jan 2;51:869-79. https://doi.org/10.1016/j.ijhydene.2023.10.227.

[138] Zhang R, Jia X, Sun M, Liu X, Wang C, Yu X, Xing Y. Synergistic manipulation of sulfur vacancies and palladium doping of In_2S_3 for enhanced photocatalytic H_2 production. Journal of Colloid and Interface Science. 2025 Jan 1;677:425-34. https://doi.org/10.1016/j.jcis.2024.07.242.

[139] M. Wang, S. Shen, Effects of sacrificial reagents on photocatalytic hydrogen evolution over different photocatalysts, (2017) 5155–5164. https://doi.org/10.1007/s10853-017-0752-z.

[140] Yang S, Xu CY, Zhang BY, Yang L, Hu SP, Zhen L. Ca (II) doped β-In_2S_3 hierarchical structures for photocatalytic hydrogen generation and organic dye degradation under visible light

irradiation. Journal of Colloid and Interface Science. 2017 Apr 1;491:230-7. https://doi.org/10.1016/j.jcis.2016.12.028.

[141] Mohamed HH, Besisa DH. Eco-friendly and solar light-active Ti-Fe_2O_3 ellipsoidal capsules' nanostructure for removal of herbicides and organic dyes. Environmental Science and Pollution Research. 2023 Feb;30(7):17765-75. https://doi.org/10.1007/s11356-022-23119-0.

[142] El-Khair MA, Al-Gamal AG, Kabel KI, Gado WS, Morshedy AS. Harvesting the synergistic effect of $CuFe_2O_4$@ Ni-MOF nanomagnetic photocatalyst for enhanced visible light-driven green hydrogen production. International Journal of Hydrogen Energy. 2025 Feb 3;101:280-94. https://doi.org/10.1016/j.ijhydene.2024.12.449.

[143] Balapure A, Dutta JR, Ganesan R. Recent advances in semiconductor heterojunctions: a detailed review of the fundamentals of photocatalysis, charge transfer mechanism and materials. RSC Applied Interfaces. 2024;1(1):43-69. https://doi.org/10.1039/d3lf00126a.

[144] Abebe B, Gupta NK, Tsegaye D. A critical mini-review on doping and heterojunction formation in ZnO-based catalysts. RSC advances. 2024;14(25):17338-49. https://doi.org/10.1039/D4RA02568G.

[145] Wang G, Lv S, Shen Y, Li W, Lin L, Li Z. Advancements in heterojunction, cocatalyst, defect and morphology engineering of semiconductor oxide photocatalysts. Journal of Materiomics. 2024 Mar 1;10(2):315-38. https://doi.org/10.1016/j.jmat.2023.05.014.

[146] Bekele T, Alamnie G. The photocatalytic degradation of organic pollutants comprehensive overview. Results in Chemistry. 2025 Sep 29:102758. https://doi.org/10.1016/j.rechem.2025.102758.

[147] Gamelas SR, Tomé JP, Tomé AC, Lourenço LM. Advances in photocatalytic degradation of organic pollutants in wastewaters: harnessing the power of phthalocyanines and phthalocyanine-containing materials. RSC advances. 2023;13(48):33957-93. https://doi.org/10.1039/d3ra06598g.

[148] Hernández-Del Castillo PC, Rodríguez-González V. Efficient visible photocatalytic degradation of 4-CP herbicide using immobilized TiO_2: Ni on glass substrates. Topics in Catalysis. 2022 Aug;65(9):1139-48. https://doi.org/10.1007/s11244-022-01679-2.

[149] Cai J, Zhou M, Yang W, Pan Y, Lu X, Serrano KG. Degradation and mechanism of 2, 4-dichlorophenoxyacetic acid (2, 4-D) by thermally activated persulfate oxidation. Chemosphere. 2018 Dec 1;212:784-93. https://doi.org/10.1016/j.chemosphere.2018.08.127.

[150] Pirsaheb M, Dargahi A, Hazrati S, Fazlzadehdavil M. Removal of diazinon and 2, 4-dichlorophenoxyacetic acid (2, 4-D) from aqueous solutions by granular-activated carbon. Desalination and Water treatment. 2014 Jul 3;52(22-24):4350-5. https://doi.org/10.1080/19443994.2013.801787.

[151] Samarghandi MR, Nemattollahi D, Asgari G, Shokoohi R, Ansari A, Dargahi A. Electrochemical process for 2, 4-D herbicide removal from aqueous solutions using stainless steel 316 and graphite Anodes: optimization using response surface methodology. Separation science and technology. 2019 Mar 4;54(4):478-93. https://doi.org/10.1080/01496395.2018.1512618.

[152] Wang Y, Tian YS, Gao JJ, Xu J, Li ZJ, Fu XY, Han HJ, Wang LJ, Zhang WH, Deng YD, Qian C. Complete biodegradation of the oldest organic herbicide 2, 4-Dichlorophenoxyacetic acid by engineering Escherichia coli. Journal of Hazardous Materials. 2023 Jun 5;451:131099. https://doi.org/10.1016/j.jhazmat.2023.131099.

[153] Ismael M. Facile synthesis of NiO-loaded g-C_3N_4 heterojunction photocatalyst for efficient photocatalytic degradation of 4-nitrophenol under visible light irradiation. Journal of Photochemistry and Photobiology A: Chemistry. 2023 May 1;439:114576. https://doi.org/10.1016/j.jphotochem.2023.114576.

[154] Carvalho LM, Soares-Filho AF, Lima MS, Cruz-Filho JF, Dantas TC, Luz Jr GE. 2, 4-Dichlorophenoxyacetic acid (2, 4-D) photodegradation on WO3-TiO2-SBA-15 nanostructured composite. Environmental Science and Pollution Research. 2021 Feb;28(7):7774-85. https://doi.org/10.1007/s11356-020-11085-4.

[155] L.M. Carvalho, A.F. Soares-filho, M.S. Lima, J.F. Cruz-filho, T.C.M. Dantas, G.E. Luz, 2,4-Dichlorophenoxyacetic acid (2,4-D) photodegradation on WO3-TiO2-SBA-15 nanostructured composite, (2020).

[156] Regulacio MD, Han MY. Multinary I-III-VI_2 and I_2-II-IV-VI_4 semiconductor nanostructures for photocatalytic applications. Accounts of chemical research. 2016 Mar 15;49(3):511-9.https://doi.org/10.1021/acs.accounts.5b00535.

[157] Esmaili H, Kotobi A, Sheibani S, Rashchi F. Photocatalytic degradation of methylene blue by nanostructured Fe/FeS powder under visible light. International Journal of Minerals, Metallurgy, and Materials. 2018 Feb;25(2):244-52. https://doi.org/10.1007/s12613-018-1567-x

[158] Kaur G, Pooja D, Kumar M, Thakur A, Bala R, Kumar A. Electrochemical aspects of photocatalysis: Au@ FeS_2 nanocomposite for removal of industrial pollutant. Physical

Chemistry Chemical Physics. 2017;19(48):32412-20. https://doi.org/10.1039/c7cp06289c.

[159] Gaur R. Transition metal chalcogenides-based nanocomposite for the photocatalytic degradation of hazardous chemicals. InMultifunctional Hybrid Semiconductor Photocatalyst Nanomaterials: Application on Health, Energy and Environment 2023 Oct 12 (pp. 239-274). Cham: Springer International Publishing. https://doi.org/10.1007/978-3-031-39481-2.

[160] Qiu P, Yao J, Chen H, Jiang F, Xie X. Enhanced visible-light photocatalytic decomposition of 2, 4-dichlorophenoxyacetic acid over $ZnIn_2S_4$/g-C_3N_4 photocatalyst. Journal of hazardous materials. 2016 Nov 5;317:158-68. https://doi.org/10.1016/j.jhazmat.2016.05.069.

[161] Uddin A, Muhmood T, Guo Z, Gu J, Chen H, Jiang F. Hydrothermal synthesis of 3D/2D heterojunctions of $ZnIn_2S_4$/oxygen doped g-C_3N_4 nanosheet for visible light driven photocatalysis of 2, 4-dichlorophenoxyacetic acid degradation. Journal of Alloys and Compounds. 2020 Dec 10;845:156206. https://doi.org/10.1016/j.jallcom.2020.156206.

[162] Yang L, Sun W, Luo S, Luo Y. White fungus-like mesoporous Bi_2S_3 ball/TiO_2 heterojunction with high photocatalytic efficiency in purifying 2, 4-dichlorophenoxyacetic acid/Cr (VI) contaminated water. Applied Catalysis B: Environmental. 2014 Sep 1;156:25-34. https://doi.org/10.1016/j.apcatb.2014.02.044.

[163] Alikhani N, Farhadian M, Goshadrou A, Tangestaninejad S, Eskandari P. Photocatalytic degradation and adsorption of herbicide 2, 4-dichlorophenoxyacetic acid from aqueous solution using TiO_2/BiOBr/Bi_2S_3 nanostructure stabilized on the activated carbon under visible light. Environmental Nanotechnology, Monitoring & Management. 2021 May 1;15:100415. https://doi.org/10.1016/j.enmm.2020.100415.

[164] Gu J, Chen H, Jiang F, Wang X, Li L. All-solid-state Z-scheme Co_9S_8/graphitic carbon nitride photocatalysts for simultaneous reduction of Cr (VI) and oxidation of 2, 4-dichlorophenoxyacetic acid under simulated solar irradiation. Chemical Engineering Journal. 2019 Mar 15;360:1188-98. https://doi.org/10.1016/j.cej.2018.10.137.

[165] Jaafar NF, Jalil AA, Triwahyono S, Efendi J, Mukti RR, Jusoh R, Jusoh NW, Karim AH, Salleh NF, Suendo V. Direct in situ activation of Ag^0 nanoparticles in synthesis of Ag/TiO_2 and its photoactivity. Applied Surface Science. 2015 May 30;338:75-84. https://doi.org/10.1016/j.apsusc.2015.02.106.

[166] Ren G, Han H, Wang Y, Liu S, Zhao J, Meng X, Li Z. Recent advances of photocatalytic application in water treatment: A review. Nanomaterials. 2021 Jul 12;11(7):1804.

[167] Djebbar K, Zertal A, Sehili T. Photocatalytic degradation of 2, 4-dichlorophenoxyacetic acid and 4-chloro-2-methylphenoxyacetic acid in water by using TiO_2. Environmental technology. 2006 Nov 1;27(11):1191-7. https://doi.org/10.1080/09593332708618732.

[168] Li X, Zhou M, Pan Y. Enhanced degradation of 2, 4-dichlorophenoxyacetic acid by pre-magnetization Fe-C activated persulfate: Influential factors, mechanism and degradation pathway. Journal of Hazardous Materials. 2018 Jul 5;353:454-65. https://doi.org/10.1016/j.jhazmat.2018.04.035.

[169] Singh N, Agarwal A, Agarwal M. Numerical simulation of highly efficient lead-free all-perovskite tandem solar cell. Solar Energy. 2020 Sep 15;208:399-410. https://doi.org/10.1016/j.solener.2020.08.003.

[170] Banik S, Das A, Das BK, Islam N. Numerical simulation and performance optimization of a lead-free inorganic perovskite solar cell using SCAPS-1D. Heliyon. 2024 Jan 15;10(1). https://doi.org/10.1016/j.heliyon.2024.e23985.

[171] Kumari R, Mamta M, Kumar R, Singh Y, Singh VN. 24% efficient, simple ZnSe/Sb_2Se_3 heterojunction solar cell: an analysis of PV characteristics and defects. ACS omega. 2022 Dec 21;8(1):1632-42. https://doi.org/10.1021/acsomega.2c07211.

[172] Kowsar A, Billah M, Dey S, Debnath SC, Yeakin S, Farhad SF. Comparative study on solar cell simulators. In 2019 2nd International Conference on Innovation in Engineering and Technology (ICIET) 2019 Dec 23 (pp. 1-6). IEEE. https://doi.org/10.1109/ICIET48527.2019.9290675.

[173] Rahman MF, Chowdhury M, Marasamy L, Mohammed MK, Haque MD, Al Ahmed SR, Irfan A, Chaudhry AR, Goumri-Said S. Improving the efficiency of a CIGS solar cell to above 31% with Sb_2S_3 as a new BSF: a numerical simulation approach by SCAPS-1D. RSC advances. 2024;14(3):1924-38. https://doi.org/10.1039/d3ra07893k.

[174] Sekar K, Marasamy L, Mayarambakam S, Selvarajan P, Bouclé J. Highly efficient lead-free silver bismuth iodide (Ag_3BiI_6) rudorffite solar cells with novel device architecture: a numerical study. Materials Today Communications. 2024 Mar 1;38:108347. https://doi.org/10.1016/j.mtcomm.2024.108347.

[175] Bhardwaj KS, Rai S, Sadanand, Lohia P, Dwivedi DK. Investigating the performance of mixed cation mixed halide-based perovskite solar cells using various hole-transport materials by numerical simulation. Optical and Quantum Electronics. 2021 Nov;53(11):602. https://doi.org/10.1007/s11082-021-03262-7.

[176] Hossain MK, Uddin MS, Toki GI, Mohammed MK, Pandey R, Madan J, Rahman MF, Islam MR, Bhattarai S, Bencherif H, Samajdar DP. Achieving above 24% efficiency with non-toxic $CsSnI_3$ perovskite solar cells by harnessing the potential of the absorber and charge transport layers. RSC advances. 2023;13(34):23514-37. https://doi.org/10.1039/d3ra02910g.

[177] Kumar M, Singh A, Gill D, Bhattacharya S. Optoelectronic properties of chalcogenide perovskites by many-body perturbation theory. The Journal of Physical Chemistry Letters. 2021 Jun 1;12(22):5301-7. https://doi.org/10.1021/acs.jpclett.1c01034.

[178] Kang C, Ahsan Iqbal M, Zhang S, Weng X, Sun Y, Qi L, Tang W, Ruan S, Zeng YJ. $Cu_3(HHTP)_2$ c-MOF/ZnO Ultrafast Ultraviolet Photodetector for Wearable Optoelectronics. Chemistry–A European Journal. 2022 Nov 16;28(64):e202201705. https://doi.org/10.1002/chem.202201705.

[179] Hossain MK, Arnab AA, Samajdar DP, Rubel MH, Hossain MM, Islam MR, Das RC, Bencherif H, Rahman MF, Madan J, Pandey R. Design insights into La_2NiMnO_6-based perovskite solar cells employing different charge transport layers: DFT and SCAPS-1D frameworks. Energy & Fuels. 2023 Aug 11;37(17):13377-96. https://doi.org/10.1021/acs.energyfuels.3c02361.

[180] Kanoun MB, Ul Haq B, Kanoun AA, Goumri-Said S. Ti alloying as a route to $BaZrS_3$ chalcogenide perovskite with enhanced photovoltaic performance. Energy & Fuels. 2023 Jun 16;37(13):9548-56. https://doi.org/10.1021/acs.energyfuels.3c01272.

[181] Gan Y, Qiu G, Yan C, Zeng Z, Qin B, Bi X, Liu Y. Numerical analysis on the effect of the conduction band offset in dion–jacobson perovskite solar cells. Energies. 2023 Dec 2;16(23):7889.

[182] Arockiya Dass KT, Hossain MK, Marasamy L. Highly efficient emerging $Ag_2BaTiSe_4$ solar cells using a new class of alkaline earth metal-based chalcogenide buffers alternative to CdS. Scientific Reports. 2024 Jan 17;14(1):1473. https://doi.org/10.1038/s41598-024-51711-6.

[183] Biplab SR, Ali MH, Moon MM, Pervez MF, Rahman MF, Hossain J. Performance enhancement of CIGS-based solar cells by incorporating an ultrathin $BaSi_2$ BSF layer. Journal of Computational Electronics. 2020 Mar;19(1):342-52. https://doi.org/10.1007/s10825-019-01433-0.

[184] Bag A, Radhakrishnan R, Nekovei R, Jeyakumar R. Effect of absorber layer, hole transport layer thicknesses, and its doping density on the performance of perovskite solar cells by device simulation. Solar Energy. 2020 Jan 15;196:177-82. https://doi.org/10.1016/j.solener.2019.12.014.

[185] Hossain MK, Ishraque Toki GF, Samajdar DP, Rubel MH, Mushtaq M, Islam MR, Rahman MF, Bhattarai S, Bencherif H, Mohammed MK, Pandey R. Photovoltaic performance investigation of $Cs_3Bi_2I_9$-based perovskite solar cells with various charge transport channels using DFT and SCAPS-1D frameworks. Energy & Fuels. 2023 May 5;37(10):7380-400. https://doi.org/10.1021/acs.energyfuels.3c00540.

[186] Barman B, Ingole S. Analysis of Si back-contact for chalcogenide perovskite solar cells based on $BaZrS_3$ using SCAPS-1D. Advanced Theory and Simulations. 2023 Jul;6(7):2200820. https://doi.org/10.1002/adts.202200820.

[187] Fatima Q, Haidry AA, Hussain R, Zhang H. Device simulation of a thin-layer $CsSnI_3$-based solar cell with enhanced 31.09% efficiency. Energy & Fuels. 2023 May 3;37(10):7411-23. https://doi.org/10.1021/acs.energyfuels.3c00645.

[188] Liang Y, Zhang Y, Xu J, Ma J, Jiang H, Li X, Zhang B, Chen X, Tian Y, Han Y, Shi Z. Parametric study on controllable growth of $SrZrS_3$ thin films with good conductivity for photodetectors. Nano Research. 2023 May;16(5):7867-73.

[189] Meng W, Saparov B, Hong F, Wang J, Mitzi DB, Yan Y. Alloying and defect control within chalcogenide perovskites for optimized photovoltaic application. Chemistry of Materials. 2016 Feb 9;28(3):821-9. https://doi.org/10.1021/acs.chemmater.5b04213.

[190] Thakur N, Kumar P, Neffati R, Sharma P. Design and simulation of chalcogenide perovskite $BaZr(S,Se)_3$ compositions for photovoltaic applications. Physica Scripta. 2023 May 4;98(6):065921.

[191] Chowdhury S, Najm AS, Luengchavanon M, Holi AM, Chia CH, Techato K, Channumsin S, Salih IK. Investigating the effect of nonideal conditions on the performance of a planar Sb_2Se_3-based solar cell through SCAPS-1D simulation. Energy & Fuels. 2023 Apr 14;37(9):6722-32. https://doi.org/10.1021/acs.energyfuels.2c03593.

[192] Kumar SG, Suraj N, Pramod A, Prashanth CR, Honnavar GV. Investigating the Performance of a Wide Bandgap $BaZrS_3$ Perovskite Tandem Solar Cell. In 2023 International conference on smart systems for applications in electrical sciences (ICSSES) 2023 Jul 7 (pp. 1-6). IEEE. https://doi.org/10.1109/ICSSES58299.2023.10199943.

[193] Zhou X, Qiu L, Fan R, Zhang J, Hao S, Yang Y. Heterojunction incorporating perovskite and microporous metal–organic framework nanocrystals for efficient and stable solar cells. Nano-micro letters. 2020 Dec;12(1):80. https://doi.org/10.1007/s40820-020-00417-1.

[194] Syzgantseva MA, Stepanov NF, Syzgantseva OA. Effect of Ligand Functionalization on the Rate of Charge Carrier Recombination in Metal-Organic Frameworks: A Case Study of MIL-125. The Journal of Physical Chemistry Letters. 2021 Jan 8;12(2):829-34. https://doi.org/10.1021/acs.jpclett.0c03634.

[195] Z. Jin, X. Liu, K. Li, Y. Hu, L. Xu, B. Li, Constructing tightly integrated 2D conductive metal-organic framework/TiO_2 S-scheme heterostructure by chemical bonds for photocatalytic hydrogen evolution, International Journal of Hydrogen Energy 99 (2025) 785–792. https://doi.org/10.1016/j.ijhydene.2024.12.274.

[196] Arockiadoss KT, Chettiar AD, Linda E, Marasamy L. Boost efficiency with buffer and bottom stack optimization in $Cu_2BaSn(S,Se)_4$ solar cells by simulation. Journal of Alloys and Compounds. 2025 Jan 5;1010:177707. https://doi.org/10.1016/j.jallcom.2024.177707.

[197] Wu X, Gao W, Chai J, Ming C, Chen M, Zeng H, Zhang P, Zhang S, Sun YY. Defect tolerance in chalcogenide perovskite photovoltaic material $BaZrS_3$. Science China Materials. 2021 Dec;64(12):2976-86. https://doi.org/10.1007/s40843-021-1683-0.

[198] Shasti M, Mortezaali A. Numerical study of Cu_2O, $SrCu_2O_2$, and $CuAlO_2$ as hole-transport materials for application in perovskite solar cells. physica status solidi (a). 2019 Sep;216(18):1900337. https://doi.org/10.1002/pssa.201900337.

[199] Ranjan R, Anand N, Tripathi MN, Srivastava N, Sharma AK, Yoshimura M, Chang L, Tiwari RN. SCAPS study on the effect of various hole transport layer on highly efficient 31.86% eco-friendly CZTS based solar cell. Scientific reports. 2023 Oct 27;13(1):18411. https://doi.org/10.1038/s41598-023-44845-6.

[200] Sekar K, Marasamy L, Mayarambakam S, Hawashin H, Nour M, Bouclé J. Lead-free, formamidinium germanium-antimony halide ($FA_4GeSbCl_{12}$) double perovskite solar cells: the effects of band offsets. RSC advances. 2023;13(36):25483-96. https://doi.org/10.1039/d3ra03102k.

[201] Mora-Herrera D, Pal M. Path toward the performance upgrade of lead-free perovskite solar cells using $Cu_2ZnSn_{1-x}Ge_xS_4$ as a hole transport layer: a theoretical simulation approach. The Journal of Physical Chemistry C. 2022 Mar 28;126(13):5847-62. https://doi.org/10.1021/acs.jpcc.2c01445.

[202] Kumar M, Raj A, Kumar A, Anshul A. Computational analysis of bandgap tuning, admittance and impedance spectroscopy measurements in lead-free $MASnI_3$ perovskite solar cell device. International Journal of Energy Research. 2022 Jun 25;46(8):11456-69.

https://doi.org/10.1002/er.7942.

[203] Meskini M, Asgharizadeh S. Performance simulation of the perovskite solar cells with Ti_3C_2 MXene in the SnO_2 electron transport layer. Scientific Reports. 2024 Mar 8;14(1):5723. https://doi.org/10.1038/s41598-024-56461-z.

[204] Tress W, Leo K, Riede M. Optimum mobility, contact properties, and open-circuit voltage of organic solar cells: A drift-diffusion simulation study. Physical Review B-Condensed Matter and Materials Physics. 2012 Apr 15;85(15):155201. https://doi.org/10.1103/PhysRevB.85.155201.

[205] Du HJ, Wang WC, Zhu JZ. Device simulation of lead-free $CH_3NH_3SnI_3$ perovskite solar cells with high efficiency. Chinese Physics B. 2016 Aug 25;25(10):108802. https://doi.org/10.1088/1674-1056/25/10/108802.

[206] Kanevce A, Reese MO, Barnes TM, Jensen SA, Metzger WK. The roles of carrier concentration and interface, bulk, and grain-boundary recombination for 25% efficient CdTe solar cells. Journal of Applied Physics. 2017 Jun 7;121(21). https://doi.org/10.1063/1.4984320.

[207] Ahmad O, Rashid A, Ahmed MW, Nasir MF, Qasim I. Performance evaluation of Au/p-CdTe/Cs_2TiI_6/n-TiO_2/ITO solar cell using SCAPS-1D. Optical Materials. 2021 Jul 1;117:111105. https://doi.org/10.1016/j.optmat.2021.111105.

[208] Rahman, M.B., Miah, M.H., Khandaker, M.U. and Islam, M.A., 2023. Selection of a compatible electron transport layer and hole transport layer for the mixed perovskite $FA_{0.85}Cs_{0.15}Pb(I_{0.85}Br_{0.15})_3$, towards achieving novel structure and high-efficiency perovskite solar cells: a detailed numerical study by SCAPS-1D. *RSC advances*, *13*(25), pp.17130-17142. https://doi.org/10.1039/d3ra02170j.

[209] Moon MM, Ali MH, Rahman MF, Hossain J, Ismail AB. Design and simulation of $FeSi_2$-based novel heterojunction solar cells for harnessing visible and near-infrared light. Physica Status Solidi (a). 2020 Mar;217(6):1900921. https://doi.org/10.1002/pssa.201900921.

[210] Reza KM, Gurung A, Bahrami B, Mabrouk S, Elbohy H, Pathak R, Chen K, Chowdhury AH, Rahman MT, Letourneau S, Yang HC. Tailored PEDOT: PSS hole transport layer for higher performance in perovskite solar cells: Enhancement of electrical and optical properties with improved morphology. Journal of Energy Chemistry. 2020 May 1;44:41-50. https://doi.org/10.1016/j.jechem.2019.09.014.

[211] Lee CC, Chen CI, Liao YT, Wu KC, Chueh CC. Enhancing efficiency and stability of

photovoltaic cells by using perovskite/Zr-MOF heterojunction including bilayer and hybrid structures. Advanced Science. 2019 Mar;6(5):1801715. https://doi.org/10.1002/advs.201801715.

[212] Sekar K, Mayarambakam S. Effect of Annealed and Non-Annealed Inorganic MnS Hole-Transport Layer for Efficient $Sb_2(S,Se)_3$ Solar Cells: A Theoretical Justification. Physica Status Solidi (b). 2023 Jun;260(6):2300087. https://doi.org/10.1002/pssb.202300087.

[213] Baig H, Kanda H, Asiri AM, Nazeeruddin MK, Mallick T. Increasing efficiency of perovskite solar cells using low concentrating photovoltaic systems. Sustainable Energy & Fuels. 2020;4(2):528-37. https://doi.org/10.1039/c9se00550a.

[214] Shankar G, Kumar P, Pradhan B. Synergetically optimized perovskite subcells with a V_{OC} beyond 2V in tandem architecture. Energy & Fuels. 2023 Jun 5;37(16):12291-300. https://doi.org/10.1021/acs.energyfuels.3c00555.

[215] Shrivastav N, Madan J, Pandey R, Shalan AE. Investigations aimed at producing 33% efficient perovskite–silicon tandem solar cells through device simulations. RSC advances. 2021;11(59):37366-74. https://doi.org/10.1039/d1ra06250f.

[216] Hossain MK, Arnab AA, Das RC, Hossain KM, Rubel MH, Rahman MF, Bencherif H, Emetere ME, Mohammed MK, Pandey R. Combined DFT, SCAPS-1D, and wxAMPS frameworks for design optimization of efficient Cs_2BiAgI_6-based perovskite solar cells with different charge transport layers. RSC advances. 2022;12(54):35002-25. https://doi.org/10.1039/d2ra06734j.

[217] Wang S, Sakurai T, Wen W, Qi Y. Energy level alignment at interfaces in metal halide perovskite solar cells. Advanced Materials Interfaces. 2018 Nov;5(22):1800260. https://doi.org/10.1002/admi.201800260.

[218] D. Srinivasan, A.-D. Rasu Chettiar, S. Rajendran, H. Bencherif, P. Sasikumar, J. Ramanujam, L. Marasamy, Boosting the efficiency of $BaZrS_3$ solar cells with inorganic delafossite HTLs: A promising alternative to Spiro-OMeTAD, Inorganic Chemistry Communications 180 (2025) 114997. https://doi.org/10.1016/j.mseb.2025.118126.

[219] Polfus JM, Norby T, Bredesen R. Protons in oxysulfides, oxysulfates, and sulfides: A first-principles study of La_2O_2S, $La_2O_2SO_4$, $SrZrS_3$, and $BaZrS_3$. The Journal of Physical Chemistry C. 2015 Oct 22;119(42):23875-82. https://doi.org/10.1021/acs.jpcc.5b08278.

[220] Amjad A, Qamar S, Zhao C, Fatima K, Sultan M, Akhter Z. Numerical simulation of lead-free vacancy ordered Cs_2PtI_6 based perovskite solar cell using SCAPS-1D. RSC advances.

2023;13(33):23211-22. https://doi.org/10.1039/d3ra04176j.

[221] Shieh JT, Liu CH, Meng HF, Tseng SR, Chao YC, Horng SF. The effect of carrier mobility in organic solar cells. Journal of Applied Physics. 2010 Apr 15;107(8). https://doi.org/10.1063/1.3327210.

[222] Wang YX, Tseng SR, Meng HF, Lee KC, Liu CH, Horng SF. Dark carrier recombination in organic solar cell. Applied Physics Letters. 2008 Sep 29;93(13). https://doi.org/10.1063/1.2972115.

[223] Basyoni MS, Salah MM, Mousa M, Shaker A, Zekry A, Abouelatta M, Alshammari MT, Al-Dhlan KA, Gontrand C. On the investigation of interface defects of solar cells: lead-based vs lead-free perovskite. IEEE Access. 2021 Sep 20;9:130221-32. https://doi.org/10.1109/ACCESS.2021.3114383.

[224] D. Zheng, R. Peng, G. Wang, J.L. Logsdon, B. Wang, X. Hu, Y. Chen, V.P. Dravid, M.R. Wasielewski, J. Yu, W. Huang, Z. Ge, T.J. Marks, A. Facchetti, Simultaneous Bottom-Up Interfacial and Bulk Defect Passivation in Highly Efficient Planar Perovskite Solar Cells using Nonconjugated Small-Molecule Electrolytes, Advanced Materials 31 (2019) 1–9. https://doi.org/10.1002/adma.201903239.

[225] F. Izadi, A. Ghobadi, A. Gharaati, M. Minbashi, A. Hajjiah, Effect of interface defects on high efficient perovskite solar cells, Optik 227 (2021) 166061. https://doi.org/10.1016/j.ijleo.2020.166061.

[226] A. Jasenek, U. Rau, V. Nadenau, H.W. Schock, Electronic properties of $CuGaSe_2$-based heterojunction solar cells. Part II. Defect spectroscopy, Journal of Applied Physics 87 (2000) 594–602. https://doi.org/10.1063/1.371904.

[227] Z. Liu, B. Sun, X. Liu, J. Han, H. Ye, T. Shi, Z. Tang, G. Liao, Efficient Carbon-Based $CsPbBr_3$ Inorganic Perovskite Solar Cells by Using Cu-Phthalocyanine as Hole Transport Material, Nano-Micro Letters 10 (2018) 1–13. https://doi.org/10.1007/s40820-018-0187-3.

[228] Elanzeery H, Melchiorre M, Sood M, Babbe F, Werner F, Brammertz G, Siebentritt S. Challenge in Cu-rich $CuInSe_2$ thin film solar cells: Defect caused by etching. Physical review materials. 2019 May;3(5):055403. https://doi.org/10.1103/PhysRevMaterials.3.055403.

[229] Chawki N, Rouchdi M, Fares B. Numerical study of $BaZrS_3$ based Chalcogenide Perovskite solar cell using SCAPS-1D device simulation.

[230] Linda E, Chettiar AD, Marasamy L. Theoretical insights into high-efficiency $BaZr_{0.96}Ti_{0.04}S_3$ chalcogenide perovskite solar cells using phthalocyanine HTLs. Materials Letters. 2024 Nov 15;375:137203. https://doi.org/10.1016/j.matlet.2024.137203.

[231] Li P, Mohamed MI, Xu C, Wang X, Tang X. Electrical property modified hole transport layer (PEDOT: PSS) enhance the efficiency of perovskite solar cells: Hybrid co-solvent post-treatment. Organic Electronics. 2020 Mar 1;78:105582. https://doi.org/10.1016/j.orgel.2019.105582.

[232] Niu S, Huyan H, Liu Y, Yeung M, Ye K, Blankemeier L, Orvis T, Sarkar D, Singh DJ, Kapadia R, Ravichandran J. Bandgap control via structural and chemical tuning of transition metal perovskite chalcogenides. Advanced Materials. 2017 Mar;29(9):1604733. https://doi.org/10.1002/adma.201604733.

[233] D. Zhu, Optimization of the thermoelectric performance of layer-by-layer structured copper-phthalocyanine (CuPc) thin films doped with hexacyano-trimethylene-cyclopropane (CN6-CP), (2019) 31840–31845. https://doi.org/10.1039/c9ra06381a.

[234] Shkir M, Aldirham SH, AlFaify S, Ali AM. A novel BiOBr/rGO photocatalysts for degradation of organic and antibiotic pollutants under visible light irradiation: tetracycline degradation pathways, kinetics, and mechanism insight. Chemosphere. 2024 Jun 1;357:141934.https://doi.org/10.1016/j.chemosphere.2024.141934.

[235] Veerakumar P, Sangili A, Chen SM, Kumar RS, Arivalagan G, Firdhouse MJ, Hameed KS, Sivakumar S. Photocatalytic degradation of phenolic pollutants over palladium-tungsten trioxide nanocomposite. Chemical Engineering Journal. 2024 Jun 1;489:151127. https://doi.org/10.1016/j.cej.2024.151127.

[236] Guillemeney L, Lermusiaux L, Davidson P, Canut B, Mahler B, Abécassis B. Synthesis, structure, and gelling power of gamma-In_2S_3 nanoribbons with large aspect ratio. https://doi.org/10.1021/acs.chemmater.6b01279.

[238] Yang S, Xu CY, Zhang BY, Yang L, Hu SP, Zhen L. Ca (II) doped β-In_2S_3 hierarchical structures for photocatalytic hydrogen generation and organic dye degradation under visible light irradiation. Journal of Colloid and Interface Science. 2017 Apr 1;491:230-7. https://doi.org/10.1016/j.jcis.2016.12.028.

[239] Chen YX, Li F, Wang W, Zheng Z, Luo J, Fan P, Takeuchi T. Optimization of thermoelectric properties achieved in Cu doped β-In_2S_3 bulks. Journal of Alloys and Compounds. 2019 Apr 25;782:641-7. https://doi.org/10.1016/j.jallcom.2018.12.138.

[240] Dietrich MK, Kramm BG, Becker M, Meyer BK, Polity A, Klar PJ. Influence of doping with alkaline earth metals on the optical properties of thermochromic VO_2. Journal of Applied Physics. 2015 May 14;117(18). https://doi.org/10.1063/1.4919433.

[241] Wang C, Liu H, Wang G, Ye F, Tao S, Li X, Qiu P, Huang Z. Ni (II) doping induced lattice distortion in $Zn_3In_2S_6$/BiOBr-OV_s for boosting photocatalytic removal of antibiotics and Cr (VI) performance. Separation and Purification Technology. 2023 Nov 1;324:124457. https://doi.org/10.1016/j.seppur.2023.124457.

[242] Alsulamei A, Timoumi A. Tailoring the physical and optical properties of Sn-doped In_2S_3 thin films obtained using VTE technique. Optical Materials: X. 2022 Aug 1;15:100176. https://doi.org/10.1016/j.omx.2022.100176.

[243] Pulipaka S, Koushik AK, Deepa M, Meduri P. Enhanced photoelectrochemical activity of Co-doped β-In_2S_3 nanoflakes as photoanodes for water splitting. RSC advances. 2019;9(3):1335-40. https://doi.org/10.1039/c8ra09660k.

[244] Guo B, Liu L, Li A, Li X, Chang Y, Jiao Z, Han M. Insights into the effect of Ni doping on In_2S_3 for enhanced activity and selectivity of photocatalytic CO_2 reduction. Journal of Alloys and Compounds. 2024 Aug 15;995:174741. https://doi.org/10.1016/j.jallcom.2024.174741.

[245] Zhao B, Wang X, Zhang Y, Gao J, Chen Z, Lu Z. Synergism of oxygen vacancies, Ti^{3+} and N dopants on the visible-light photocatalytic activity of N-doped TiO_2. Journal of Photochemistry and Photobiology A: Chemistry. 2019 Sep 1;382:111928. https://doi.org/10.1016/j.jphotochem.2019.111928.

[246] A. Sharma, D. Yadav, A. Ohlan, S. Dahiya, R. Punia, A.S. Maan, Journal of Industrial and Engineering Chemistry Hydrothermally synthesized Sr-doped In_2S_3 microspheres for efficient degradation of noxious RhB pollutants in visible light exposure, Journal of Industrial and Engineering Chemistry 145 (2025) 360–371. https://doi.org/10.1016/j.jiec.2024.10.031.

[247] F. Li, X. Tang, Z. Hu, X. Li, F. Li, Y. Xie, Y. Jiang, Boosting the hydrogen peroxide production over In_2S_3 crystals under visible light illumination by gallium ions doping and sulfur vacancies modulation, Chinese Journal of Catalysis 55 (2023) 253–264. https://doi.org/10.1016/S1872-2067(23)64555-3.

[248] R. Zhang, X. Jia, M. Sun, X. Liu, C. Wang, X. Yu, Journal of Colloid And Interface Science Synergistic manipulation of sulfur vacancies and palladium doping of In_2S_3 for enhanced photocatalytic H 2 production, 677 (2025) 425–434.

[249] J.A. Joseph, S.B. Nair, S.A. Mary, S.S. John, S. Shaji, R.R. Philip, In fl uence of Magnesium Doping on the Photocatalytic and Antibacterial Properties of Hematite Nanostructures, 2100437 (2022) 1–9. https://doi.org/10.1002/pssb.202100437.

[250] Y. Chen, X. Duan, J. Li, W. Liu, S. Ren, J. Yang, Q. Liu, Hydrothermal synthesis of Ca doped β-In_2S_3 for effective dyes degradation, Advanced Powder Technology 32 (2021) 1881–1890. https://doi.org/10.1016/j.apt.2021.03.042.

[251] J. Baek, L. Thai, S. Yeon, H. Seo, Aluminum doping for optimization of ultrathin and high-k dielectric layer based on $SrTiO_3$ Journal of Materials Science & Technology Aluminum doping for optimization of ultrathin and high- k dielectric layer based on $SrTiO_3$, Journal of Materials Science & Technology 42 (2020) 28–37. https://doi.org/10.1016/j.jmst.2019.12.006.

[252] Wang Z, Miao R, He L, Guan Q, Shi Y. Green synthesis of MIL-100 (Fe) derivatives and revealing their structure-activity relationship for 2, 4-dichlorophenol photodegradation. Chemosphere. 2022 Mar 1;291:132950. https://doi.org/10.1016/j.chemosphere.2021.132950.

[253] E. Metal, B. Mg, C. Sr, B. Monolayers, First Principles Study of the Photoelectric Properties of Alkaline Earth Metal (Be/Mg/Ca/Sr/Ba)-Doped Monolayers of MoS_2, (2023).

[254] R. Aruna-Devi, L. Marasamy, S.A. Mayén-Hernández, F. De Moure-Flores, J. Santos-Cruz, Studying the impact of Mg doping on the physical properties of CdS nanocrystals for the fabrication of hybrid solar cells–based organic P3HT:PCBM polymers and inorganic Mg-doped CdS nanocrystals, International Journal of Energy Research 46 (2022) 5330–5341. https://doi.org/10.1002/er.7509.

[255] Wang L, Karuturi S, Zan L. Bi_2S_3-In_2S_3 heterostructures for efficient photoreduction of highly toxic Cr^{6+} enabled by facet-coupling and Z-scheme structure. Small. 2021 Oct;17(40):2101833.https://doi.org/10.1002/smll.202101833.

[256] Prajapati B, Roy S, Sharma S, Joshi AG, Chatterjee S, Ghosh AK. Bandgap Engineering and Signature of Ferromagnetism in $Ti_{1-x}Mn_xO_2$ Diluted Magnetic Semiconductor Nanoparticles: A Valence Band Study. physica status solidi (b). 2019 May;256(5):1800262. https://doi.org/10.1002/pssb.201800262.

[257] Sui J, Peng Z, Lu N, Qian K, Zhang X, Wei T, Li R, Yan X. Phosphorus-doped In_2S_3 with rich sulfur vacancies toward efficient photocatalytic hydrogen production from formaldehyde solution. Sustainable Energy & Fuels. 2024;8(9):2010-8. 2010–2018. https://doi.org/10.1039/d4se00123k.

[258] Jeon SJ, Zhao N, Yuan Y, Li Y. Solution-Processable and Ambient-Stable Highly Conductive p-Type Polymers Derived from Dihydropyrazine and Ethylenedioxythiophene. Advanced Functional Materials. 2025 May 5:2424664. https://doi.org/10.1002/adfm.202424664.

[259] Adnane L, Gokirmak A, Silva H. High temperature Hall measurement setup for thin film characterization. Review of Scientific Instruments. 2016 Jul 1;87(7). https://doi.org/10.1063/1.4959222.

[260] X. Chen, Y. Zhao, Z. Liu, Y. Pang, D. Wei, J. Wangchen, C. Yao, Applied Surface Science Tungsten interior doping engineering induced sulfur vacancies of MoS_2 for efficient charge transfer and nonlinear optical performance : Implications for optical limiting devices, Applied Surface Science 682 (2025) 161686. https://doi.org/10.1016/j.apsusc.2024.161686.

[261] Li J, Yao J, Yu Q, Zhang X, Carabineiro SA, Xiong X, Wu C, Lv K. Understanding the unique Ohmic-junction for enhancing the photocatalytic activity of $CoS_2/MgIn_2S_4$ towards hydrogen production. Applied Catalysis B: Environment and Energy. 2024 Aug 15;351:123950.

[262] Kaleel SG, Suhail MH, Yasser FM. Spray deposition of Cu: In_2S_3 thin films. Int. J. Emerg. Technol. Adv. Eng.. 2014;4:613-22.

[263] J. Tan, H. Ren, Z. Zhao, X. Xin, Y. Shi, D. Yang, Z. Jiang, Ca^{2+} doped metal organic frameworks for enhanced photocatalytic ammonia synthesis, Chemical Engineering Journal 466 (2023). https://doi.org/10.1016/j.cej.2023.143259.

[264] J. Feng, L. Fang, Y. Zhang, H. Zhao, Enhanced photocatalytic activity of p-nitrophenol degradation by Fe-In_2S_3 material driven by visible light, Materials Science in Semiconductor Processing 163 (2023) 107537. https://doi.org/10.1016/j.mssp.2023.107537.

[265] Jia H, Shao X, Wang YN, Zhang J, Li R, Peng T. Nickel porphyrin/$ZnIn_2S_4$ heterojunction with Ni-S highway for boosting charge separation and visible-light-driven H_2 production. Applied Catalysis B: Environment and Energy. 2024 Sep 15;353:124090.[266] M. Sheng, C. Gan, Y. Li, Z. Hu, Y. Zhang, X. Gao, X. Wang, H. Jiang, Photocatalytic degradable polymer precursor production and C–C bond synthesis with CO_2 over sulfur vacancies enriched $ZnIn_2S_4$ nanosheets, Chemical Engineering Journal 446 (2022) 136919. https://doi.org/10.1016/j.cej.2022.136919.

[267] Sun G, Tai Z, Zhang J, Cheng B, Yu H, Yu J. Bifunctional g-C_3N_4 nanospheres/CdZnS QDs S-scheme photocatalyst with boosted H_2 evolution and furfural synthesis mechanism. Applied Catalysis B: Environment and Energy. 2024 Dec 5;358:124459.

[268] Grünleitner T, Henning A, Bissolo M, Zengerle M, Gregoratti L, Amati M, Zeller P, Eichhorn J, Stier AV, Holleitner AW, Finley JJ. Real-time investigation of sulfur vacancy generation and passivation in monolayer molybdenum disulfide via in situ X-ray photoelectron spectromicroscopy. ACS nano. 2022 Dec 14;16(12):20364-75.

[269] Xue Y, Xu T, Guo Y, Song H, Wang Y, Guo Z, Li J, Zhao H, Bai X, Lai C. Amorphous/crystalline heterostructured indium (III) sulfide/carbon with favorable kinetics and high capacity for lithium storage. Advanced Composites and Hybrid Materials. 2024 Dec;7(6):213. https://doi.org/10.1039/d0cp03389h.

[270] Wang X, Bai J, Wang Y, Lu X, Zou Z, Huang J, Xu C. Sulfur vacancies-doped Sb_2S_3 nanorods as high-efficient electrocatalysts for dinitrogen fixation under ambient conditions. Green Energy & Environment. 2022 Aug 1;7(4):755-62.

[271] Quan Y, Li J, Li X, Chen R, Zhang Y, Huang J, Hu J, Lai Y. Electron-Rich Carbon Nitride with Defective Sites for Photocatalytic H2 Evolution Under Visible Light. Available at SSRN 4951308.

[272] X. Shi, L. Mao, C. Dai, P. Yang, J. Zhang, F. Dong, L. Zheng, M. Fujitsuka, H. Zheng, Inert basal plane activation of two-dimensional $ZnIn_2S_4$ via Ni atom doping for enhanced co-catalyst free photocatalytic hydrogen evolution, Journal of Materials Chemistry A 8 (2020) 13376–13384. https://doi.org/10.1039/d0ta03992f.